Large Eddy Simulation of Supersonic Combustion with Application to Scramjet Engines

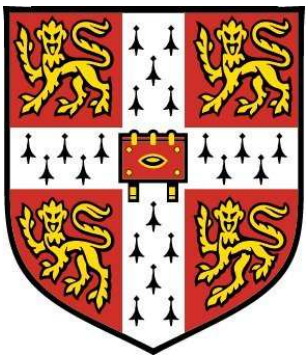

Peter Alan Thomas Cocks

Corpus Christi College

University of Cambridge

This dissertation is submitted for the degree of

Doctor of Philosophy

March 2011

To my Mum and Dad...

Acknowledgements

I would like to thank my supervisor Professor Bill Dawes for his guidance and support, both technically and financially, over the last few years. I would also like to thank my advisor Professor Stewart Cant for the many technical discussions, from which I learned a great deal, and for access to the SENGA code, which was a significant aid in the development of PULSAR. I must also thank Dr Caleb Dhanasekaran for his constant help with anything from computational resources to software compilation. I am also thankful for the support of Mary Aldridge, without whom the CFD Lab would struggle to operate.

My PhD has been funded by a Departmental EPSRC DTA studentship, for which I am very grateful. I want to separately thank the EPSRC for awarding to me a grant for time on the national supercomputer, HECToR, without which many of the simulations discussed in this thesis would not have been possible. I wish to thank Peter Benie and the University HPC support team for access to resources such at the Stokes cluster and for general help in compiling and running PULSAR on such multi-core machines. I must also thank the Department of Engineering and Corpus Christi College for their financial support, which enabled me to attend and present at two conferences.

I am very grateful to the German Research Training Group GRK 1095/2 for inviting me to multiple events throughout my PhD, from summer schools to meetings, from which I have learnt a lot. This interaction with fellow researchers in the scramjet field has been invaluable. I must also thank Professor Andrew Cutler from George Washington University for providing experimental data for the two test cases used in my work.

Many past and present members of the CFD Lab have helped me throughout my PhD and I am grateful for their guidance and insightful technical discussions. Last, but not least, I would like to thank my family for their constant support and encouragement, which made all this possible.

Abstract

This work evaluates the capabilities of the RANS and LES techniques for the simulation of high speed reacting flows. These methods are used to gain further insight into the physics encountered and regimes present in supersonic combustion. The target application of this research is the scramjet engine, a propulsion system of great promise for efficient hypersonic flight. In order to conduct this work a new highly parallelised code, PULSAR, is developed. PULSAR is capable of simulating complex chemistry combustion in highly compressible flows, based on a second order upwind method to provide a monotonic solution in the presence of high gradient physics.

Through the simulation of a non-reacting supersonic coaxial helium jet the RANS method is shown to be sensitive to constants involved in the modelling process. The LES technique is more computationally demanding but is shown to be much less sensitive to these model parameters. Nevertheless, LES results are shown to be sensitive to the nature of turbulence at the inflow; however this information can be experimentally obtained.

The SCHOLAR test case is used to validate the reacting aspects of PULSAR. Comparing RANS results from laminar chemistry and assumed PDF combustion model simulations, the influence of turbulence-chemistry interactions in supersonic combustion is shown to be small. In the presence of reactions, the RANS results are sensitive to inflow turbulence, due to its influence on mixing. From complex chemistry simulations the combustion behaviour is evaluated to sit between the flamelet and distributed reaction regimes. LES results allow an evaluation of the physics involved, with a pair of coherent vortices identified as the dominant influence on mixing for the oblique wall fuel injection method. It is shown that inflow turbulence has a significant impact on the behaviour of these vortices and hence it is vital for turbulence intensities and length scales to be measured by experimentalists, in order for accurate simulations to be possible.

Statement

This dissertation is the result of my own work and includes nothing which is the outcome of work done in collaboration with others. No parts of this dissertation have been submitted for any other qualification. This dissertation contains approximately 48,000 words and 135 figures.

Peter Cocks
March 2011

Contents

List of Figures

Nomenclature

Roman Symbols

$a_{\alpha,k}^{(l)}$	Mass based coefficients of thermochemistry polynomial
$\bar{a}_{\alpha,k}^{(l)}$	Molar based coefficients of thermochemistry polynomial
A_r	Pre-exponential factor for reaction r
A	Area
a	Speed of sound
B	Beta function parameter
C_{DES}	DES model constant
C_μ	$k-\varepsilon$ model constant
c_β	Concentration of species β
c_p	Mixture specific heat capacity at constant pressure
C_s	Smagorinsky constant
C_T, C_Y	Assumed PDF combustion model constants = 2.0
c_v	Mixture specific heat capacity at constant volume
D	Diffusion term
Da	Damköhler number

D_α	Diffusion coefficient for species α
$\widetilde{d}$	Spalart-Allmaras DES model length scale
e	Specific internal energy
E_r	Activation energy for reaction r
F_1, F_2	Menter SST model blending functions
f_a	AUSM+UP low Mach number scaling term
f_d	DDES RANS/LES blending function
G	Filter function
$\bar{g}_\alpha$	Molar Gibbs function for species α
h	Specific enthalpy
h_α	Specific enthalpy of species α
$\mathcal{H}$	Heaviside step function
I	Turbulence intensity
I_{σ_T}	Temperature variance intensity
k	Turbulence kinetic energy
k_{fr}, k_{br}	Forward and backward reaction rate constant for reaction r, respectively
K_p	AUSM+UP model constant
K_u	AUSM+UP model constant
L	Characteristic length
Le_α	Lewis number for species α
$\mathcal{L}_{ij}$	Leonard stresses

l_{ij}	Distance from centre of cell i to centre of cell j
l_m	Mixing length
L_{max}	Maximum turbulence length scale
$\widetilde{l}$	Menter SST DES model length scale
M	Mach number, or third body in the context of chemistry
$\mathcal{M}$	AUSM Mach function
M_∞	AUSM+UP free-stream Mach number
M_o	AUSM+UP reference Mach number
M_t	Turbulence Mach number
M_α	Chemical symbol for species α
$\dot{m}$	Mass flux
M_p	AUSM+UP pressure diffusion term
$\vec{n}$	Outward pointing unit normal vector
N_p	Degree of thermochemistry polynomial
N_r	Number of reactions
n_r	Temperature power constant for reaction r
N_s	Number of species
p	Static pressure
P^-	Destruction term
P	Probability density function
P^+	Production term
Pr	Prandtl number

$\mathcal{P}$	AUSM pressure function
p_u	AUSM+UP velocity diffusion term
q_j	Heat flux vector
R_α	Specific gas constant for species α
r_d	DDES RANS/LES blending parameter
Re	Reynolds number
R_{ij}	Reynolds stress tensor
R_m	Mixture specific gas constant
R^0	Universal gas constant
$\vec{r}_L, \vec{r}_R$	Vectors from centre of left and right cells, respectively, to centre of common face
$\vec{r}_{ij}$	Vector from centre of cell i to centre of cell j
S	Strain invariant
Sc	Schmidt number
S_{ij}	Strain rate tensor
τ_c	Chemical time scale
τ_K	Kolmogorov time scale
l_c	Chemical length scale
T	Temperature
$\mathcal{T}_{ij}$	Sub-test-filter stresses
$\vec{t}_{ij}$	Unit vector from centre of cell i to centre of cell j
t	Time

T^+	Dimensionless temperature
U	Characteristic velocity
u_j	Velocity vector component in direction j
u_K	Kolmogorov velocity scale
u^+	Dimensionless velocity
u_{tang}	Near wall tangential velocity
u_τ	Near wall shear velocity
$V_{\alpha,j}$	Diffusion velocity vector for species α
V	Volume
W_α	Molecular weight of species α
w	Weight for use in gradient limiter
x_j	Spatial vector component in direction j
Y_α	Mass fraction of species α
y^+	Dimensionless wall distance
y_w	Distance to nearest viscous wall
Z	Mixture fraction

Greek Symbols

α_w	Near wall eddy scaling coefficient
β_γ	Beta function parameter for species γ
β_k	L2 norm of gradient in cell k
$\beta^\star$	Menter SST model constant = 0.09
χ	Scalar dissipation rate

Δ	Filter width
δ_{ij}	Kronecker delta
Δt	Time step
δ	Delta function
Δx	Cell width
ε	Turbulence dissipation rate
η_K	Kolmogorov length scale
$\eta_{\beta,M}$	Third body efficiency of species β for third body M
Γ	Gamma function or diffusion coefficient
γ	Ratio of specific heats
κ	Kármán constant
λ	Mixture thermal conductivity
μ	Dynamic viscosity
ν	Kinematic viscosity
$\nu'_{\alpha r}, \nu''_{\alpha r}$	Molar reactant and product stoichiometric coefficients for species α in reaction r, respectively
ω	Turbulence frequency
ω_f	Fluid mechanics time scale
ψ_f, ψ_g	Flux and gradient limiters, respectively
$\dot{\omega}_\alpha$	Production rate of species α
ρ	Density
σ_T	Temperature variance

σ_Y	Sum of species mass fraction variances
τ_{ij}	Viscous stress tensor
τ_K	Kolmogorov time scale
τ_w	Wall shear stress

Subscripts

0	Stagnation property
f	Face quantity
i, j, k	Vector components
in	Inlet parameter
K	Kolmogorov parameter
l	Molecular/laminar
L	State in left hand cell
R	State in right hand cell
t	Turbulent
w	Viscous wall boundary condition

Accents

$\bar{}$	Averaged (RANS) or filtered (LES) quantity
$'$	Fluctuating quantity
$\hat{}$	Sample space variable
$\tilde{}$	Favre averaged (RANS) or favre filtered (LES) quantity
$\vec{}$	Vector

Acronyms

AUSM	Advection Upstream Splitting Method
CARS	Coherent Anti-Stokes Raman Spectroscopy
CFD	Computational Fluid Dynamics
CFL	Courant-Friedrichs-Lewy number
CV	Control Volume
DDES	Delayed Detached Eddy Simulation
DES	Detached Eddy Simulation
DNS	Direct Numerical Simulation
ILES	Implicit Large Eddy Simulation
LES	Large Eddy Simulation
PDF	Probability density function
PULSAR	Parallel Unstructured Large-eddy Simulation And Reactions
RANS	Reynolds Averaged Navier Stokes
RSM	Reynolds Stress Model
SGS	Subgrid-scale
TVD	Total Variation Diminishing
URANS	Unsteady Reynolds Averaged Navier Stokes

Chapter 1

Introduction

1.1 Background and Motivation

The desire for hypersonic flight has motivated engineers for decades to satisfy demands for high speed transport and economical access to space. In order to meet these needs and ambitions, significant advancements in propulsion technology are required. The gas turbine engines commonly employed in subsonic and low supersonic aircraft are not practical above flight Mach numbers of approximately three. Rocket engines are currently the propulsion system of choice for hypersonic flight, but suffer from poor efficiency [1] and low levels of safety. One device that holds great promise in the area of hypersonic air-breathing propulsion is the supersonic combustion ramjet (scramjet) engine.

The standard ramjet engine slows the incoming flow down to subsonic speeds in order to allow efficient mixing of air and fuel and subsequent combustion. However, as the free stream Mach number increases, the removal of a greater amount of kinetic energy from the flow incurs significant losses. Therefore, at high free stream Mach numbers the flow inside the combustion chamber is allowed to remain supersonic, leading to the creation of the supersonic combustion ramjet (scramjet).

The scramjet engine is a mechanically simple system due to its lack of moving parts. Rather than employing the active compression system found in gas turbine engines, scramjet propulsion relies on the technique of ram compression to slow

the incoming air and increase its pressure, pre-combustion. This ram compression is facilitated through a combination of the forward speed of the aircraft and the oblique shock system present at the engine inlet. However, this method of compression requires the incoming air speed to be supersonic, which is a major disadvantage for the technology in question. Flight tests to-date have used rocket propulsion to accelerate to the speeds required, but current research [2] is looking at using scramjet propulsion in combined cycle engines to provide continual thrust from takeoff to landing.

Although scramjet engines are mechanically simple, the flow physics inherent in such devices is complex and not well understood. The main challenge with scramjet propulsion is the supersonic combustion itself, since sustaining reactions in such a high velocity flow is by no means a simple task. The residence time of reactants within the combustion chamber is of the order of one millisecond [3], during which time fuel needs to be injected, efficiently mixed, fully reacted and then expanded back to free-stream conditions. Rapid mixing and combustion are important in order to reduce the required length and hence weight of the combustion chamber. However, this rapid mixing must be done as efficiently as possible, minimising losses in total pressure. Mixing is influenced by the fuel injection method employed, for which there are currently two main approaches [4]; injection at the combustor wall or injection in the core region of the combustor through the use of struts.

Wall injection can be facilitated through the use of transverse or oblique jets, as shown in Figure 1.1. Although wall normal injection achieves efficient mixing [5], significant losses in stagnation pressure are caused due to the presence of strong shocks [4]. The strength of these shocks can be reduced through the use of angled wall injection [6], with a component of the injectant momentum also contributing to the thrust. Fuel can also be injected parallel to the wall through the use of the ramp injectors, but can suffer from low levels of penetration into the combustor [4].

An example of strut injection is shown in Figure 1.2, which directly injects fuel into the core of the combustor airstream [4]. Due to the limited mixing capabilities inherent in streamwise injection, the generation of streamwise vorticity is required [7] in order for complete mixing to be achieved within the combustor length.

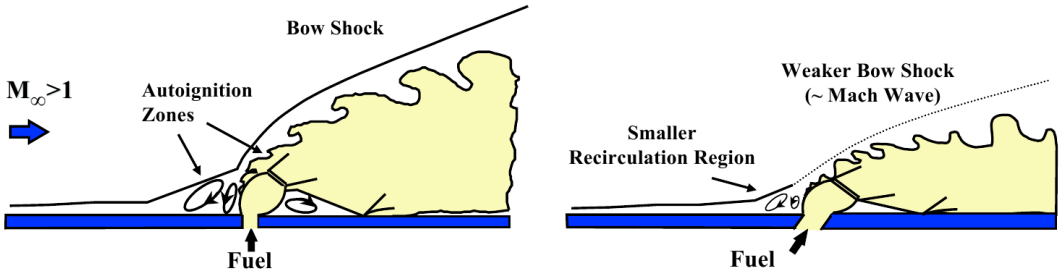

Figure 1.1: Normal (left) and oblique (right) wall injection [6]

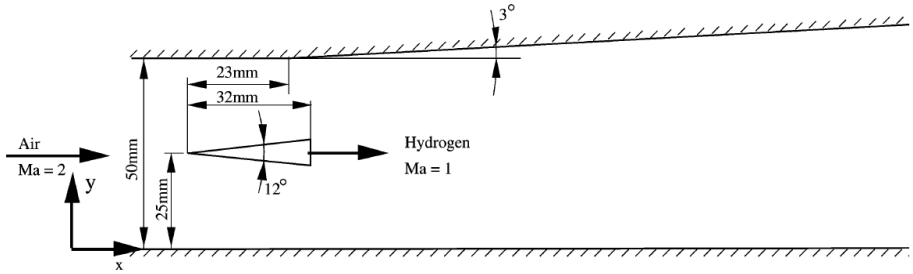

Figure 1.2: Schematic of strut based injection [8]

Due to the severe aerothermal environment in a scramjet engine and the additional drag losses introduced with strut injection of fuel, wall injection is the method of choice [9] in the flight vehicles of today and hence will be the focus of the thesis.

The first hypersonic flight of an air-breathing vehicle occurred in March, 2004, when NASA's scramjet powered, hydrogen fuelled, X-43A research vehicle reached a flight Mach number of 6.8 [10]. This was followed in November of the same year by a Mach 9.6 flight of another X-43A demonstrator [10], currently holding the Mach number record for a flight powered by an air-breathing engine. The scramjet powered phase of these flights only lasted on the order of 10 seconds, but in May, 2010, the X-51A WaveRider vehicle, powered by a Pratt & Whitney Rocketdyne hydrocarbon fuelled scramjet engine, sustained supersonic combustion at a flight Mach number of 5 for over 200 seconds [11].

Although flight tests are perhaps the best way to conduct scramjet research, they are a hugely expensive activity which to-date have resulted in vehicle destruction. Ground-based investigations are far more cost effective and constitute

the majority of supersonic combustion research carried out today. Since it is difficult to replicate the extreme conditions of hypersonic flight in ground-based facilities [12], computational methods have begun to play a major role in scramjet research and design. Accurate simulation and prediction of the complex flow physics in question presents a significant challenge to the computational methods in use today.

1.2 Turbulent Combustion Modelling

The simulation of low Mach number turbulent reacting flows is a relatively mature area of research, but the extension of the models and techniques involved to the supersonic reacting regime is still at an early stage. The instantaneous equations governing the physics of a turbulent reacting flow will be presented in Chapter 2. Techniques of varying fidelity are available to find a solution to these equations, with the most common being the DNS, LES and RANS methods briefly introduced here.

1.2.1 Direct Numerical Simulation (DNS)

DNS directly solves the instantaneous system of governing equations and is the simplest method available for the simulation of turbulent reacting flows, since no modelling contributions are required. However, for the absence of modelling to be valid DNS must capture all physical scales in the simulation, from the turbulence integral scales, right down to the small Kolmogorov and chemical scales [13]. This requirement is enabled through mesh resolution, where the cell size must be at least as small as the smallest length scale to be captured.

The mesh resolution requirements are the main obstacle to the widespread use of DNS, since there are limitations on total cell count due to the capabilities of computational resources available today. It will be shown in Chapter 2 that the Kolmogorov scales are inversely proportional to the turbulent Reynolds number to the power $\frac{3}{4}$. This means that DNS is only affordable for low Reynolds number academic research and is not suitable for the simulation of practical systems of interest.

1.2.2 Large Eddy Simulation (LES)

In order to reduce the computational expense of DNS, the mesh resolution requirements can be relaxed by directly capturing only the large scale turbulent eddies in the flow, leading to the method of large eddy simulation (LES). The minimum eddy size that can be directly captured is defined by the mesh spacing, which acts as a filter, removing the smallest scales from the solution. However, these small scales still have an influence on the large scale structures, which is included through the use of a subgrid-scale (SGS) model. These models obtain their name from the fact that they provide for the turbulent scales whose size is below (sub) the resolution of the computational grid.

Since combustion occurs at the smallest scales and since these scales are now only modelled, instantaneous reaction rates are no longer applicable and models must also be introduced to handle the physics involved in turbulence-chemistry interactions.

The size and behaviour of large scale eddies is dependent on the boundary conditions or geometrical configuration of the problem under consideration, whereas it can be shown [14] that the behaviour of subgrid-scales is more universal. The strength of LES is that the problem dependent large scales are directly captured and only the small scales, which are more suitable for a universal mathematical description, require modelling. It is the limitations of the subgrid-scale and turbulent combustion modelling which lead to limitations for the LES method.

Since the filter width should lie within the inertial range of the turbulence spectrum [14], mesh resolution requirements are still significant for LES but greatly reduced when compared to DNS. With the increase in computational power over the last decade, LES is now affordable for industrial applications.

1.2.3 Reynolds Averaged Navier Stokes (RANS)

RANS is the most traditional simulation method and is historically the most mature. Until recently, RANS was the only viable option for the modelling of practical systems due to the efficient (coarse) computational grids it employs. The RANS equations are obtained through time averaging the system of instantaneous equations, effectively creating a system which can be solved to find mean values

for the primary variables involved. However, the averaging process introduces a series of extra terms into the system of equations which require the use of turbulence models to obtain closure. Modelling is also required for the species reaction rate in order to include the effects of turbulence-chemistry interactions.

Since the full turbulence spectrum is subjected to this averaging procedure, turbulence models are very case sensitive due to the inclusion of the case dependent large scale structures. Model constants are therefore built into the turbulence model formulation, which require tuning to accurately simulate the non-universal large scales of the flow. Since tuning is required to reproduce the experimental data with which these models are validated, their extension to flight conditions or use in research where experimental data is not available, can then lead to uncertainties in the accuracy of results. However, RANS methods can often produce accurate trends and are therefore suitable for use in the initial design process in an industrial environment.

1.3 Aims of this Work

The extension of turbulence and combustion modelling to the supersonic combustion regime presents a significant challenge since the physics involved is not well understood. RANS methods are capable of providing reasonable agreement with experimental data but suffer from sensitivities to model constants such as the turbulent Prandtl and Schmidt numbers [15]. Since modelling is more universal in the LES approach and since this modelling plays a less significant role due to the direct capture of the dominant structures in the flow, LES may be capable of improving over the RANS technique commonly employed.

The aim of this research therefore is to compare the capabilities of the RANS and LES methods for the simulation of supersonic combustion, investigating the strengths and weaknesses of each approach.

Through the application of these simulation techniques, it is aimed to understand better the physics involved in supersonic combustion and to therefore understand better the efforts required to improve turbulence and combustion modelling in order to obtain accurate computational predictions in this regime. Particular attention is paid to oblique wall injection in order to understand better

the physics involved in mixing under such conditions.

These comparisons and modifications of approaches for the simulation of supersonic combustion require access to the source code of computational fluid dynamics software, ruling out any of the widely used commercial packages. Since no in-house capabilities existed for such simulations, the development of a new code, PULSAR, also forms a significant aim of this research and the numerical methods employed will be discussed in detail.

1.4 Thesis Outline

Chapter 2 reviews the field of turbulence modelling, introducing the instantaneous system of equations and the additional terms resulting from the averaging and filtering procedures used for RANS and LES, respectively. A range of turbulence and subgrid-scale models are described and the hybrid RANS-LES approach for the simulation of high Reynolds number flows is introduced.

The regime of supersonic combustion and the models available to account for turbulence-chemistry interactions are presented in Chapter 3, along with details of chemical kinetics and experimental studies of the physics involved.

The numerical methods employed in PULSAR are described in Chapter 4 and details of turbulence and combustion model implementation are provided. Methods for the discretisation of convective fluxes in supersonic reacting flows are compared, where the focus is on developing the capability of obtaining a monotonic solution. The parallel capabilities of PULSAR are also analysed.

Validation of PULSAR's mixing prediction capability is provided in Chapter 5 through the simulation of a supersonic coaxial helium jet. Capabilities of the RANS approach are evaluated and sensitivities of the results to turbulent Prandtl and Schmidt numbers are presented.

Chapter 6 demonstrates the insensitivity of the LES technique to model constants, through simulation of the coaxial jet used in Chapter 5, but evaluates the important influence of inlet turbulence parameters on the results obtained.

The SCHOLAR scramjet test case is presented in Chapter 7. The influence of turbulence-chemistry interaction modelling and chemical kinetics are investigated through RANS simulations, with computational and experimental data

being compared. An investigation into the regime of supersonic combustion is conducted and the effects of inflow turbulence and radical species concentration are evaluated. The LES method is employed to study the physics involved and sensitivities to combustion modelling and inflow turbulence are presented.

Conclusions are drawn in Chapter 8 and areas of future work are suggested.

Chapter 2

Turbulence Modelling

2.1 Introduction to Turbulence

Because of the length scales, flow rates and pressures of interest, it is known that the flow within a scramjet engine is of a turbulent nature [16]. This turbulence can play an important role in the mixing and combustion process [4] and hence accurate turbulence simulation is vital.

Turbulent flow fields are highly disordered in nature and hence notoriously difficult to accurately model. However, disordered behaviour is not the only prerequisite to a flow being defined as turbulent. All turbulent flows are rotational and exhibit high levels of vorticity, greatly enhancing the transport of mass, momentum and energy [14].

If we consider a turbulent flow of characteristic length (L) and velocity (U), we can calculate the Reynolds number, Re:

$$\mathrm{Re} = \frac{UL}{\nu} \tag{2.1}$$

where ν is the kinematic viscosity. For a supersonic combustor $\mathrm{Re} \gg 1$. Due to its rotational nature, the turbulent flow is characterised by a distribution of eddies of varying scale, where the large scale eddies are usually smaller than, but of comparable size to [17], the scale of the mean basic flow (L). The large scales are the most energetic and due to their high turbulent Reynolds number, given by:

$$\mathrm{Re_t} = \frac{U_t L_t}{\nu} \tag{2.2}$$

viscous forces are assumed negligible. The integral length (L_t) and velocity (U_t) scales are representative of the large scales of the flow. However, the large scale motions are unstable and break into smaller eddies, which take energy with them [17]. This process continues to smaller and smaller scales until they are small enough for the Reynolds number, based on their characteristic length and velocity, to be of the order of unity [14]. This Reynolds number is too low to cause eddy instabilities and hence these are the smallest scales possible in the flow, called the Kolmogorov length scale. At these scales, viscous forces dominate and the transfer of energy is through this dissipative mechanism [17].

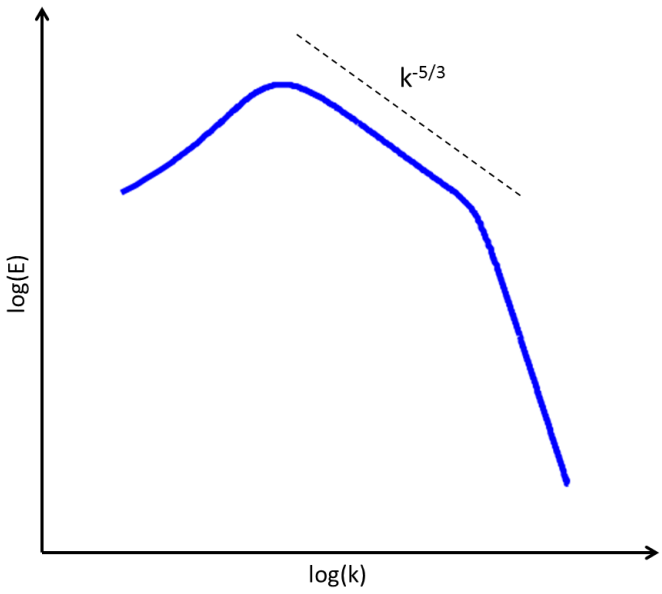

Figure 2.1: Generic energy spectrum, with energy E and frequency k.

This process is called the energy cascade and Figure 2.1 shows a generic energy spectrum. The large (low frequency) scales contain the most energy and this decreases down to the small dissipative eddies. One distinguishing feature of the energy spectrum is the *inertial* range, with a gradient of $k^{-5/3}$ which is obtained through dimensional analysis [18]. Through the introduction of density into this

dimensional analysis Ingenito and Bruno [19] suggested the rate of decay in a supersonic reacting flow is higher, leading to a steeper gradient of $k^{-8/3}$. This faster decay is said to be brought about by baroclinic and dilatational effects [19] and it is suggested [20] that the baroclinic effects also play a role in the enhancement of fuel-air mixing. Due to the steeper decay of the inertial range in compressible flows, the smallest scales are found to be larger than would be expected under incompressible conditions [19].

Although the mean effect of the small scales is the dissipation of energy away from the large scales, the intermittent transfer of energy from the small to the large scales is also possible [21] and is known as *backscatter*. The backscatter magnitude can be significant and can therefore play a significant role in turbulent flow behaviour.

The following relations [22] can be used to find the Kolmogorov length (η_K), time (τ_K) and velocity (u_K) scales from the large eddy (integral scale) properties:

$$\eta_K = L_t \mathrm{Re}_t^{-\frac{3}{4}} \tag{2.3}$$

$$\tau_K = T_t \mathrm{Re}_t^{-\frac{1}{2}} \tag{2.4}$$

$$u_K = U_t \mathrm{Re}_t^{-\frac{1}{4}} \tag{2.5}$$

where T_t is the large eddy turnover time. It can be seen from the above relations that, for the same large eddy properties, an increase in the turbulent Reynolds number results in a reduction of the Kolmogorov length, time and velocity scales [22]. However, the turbulent Reynolds number does not affect the structure of the large or small scales; it just defines the size ratio between them [17].

It was therefore hypothesised by Kolmogorov [23], that the *structure* of the smallest scales is independent of the turbulent Reynolds number and can be thought of as universal in all flows. The large scales are highly dependent on both system geometry and boundary conditions; hence large variations in eddy structure can occur [14; 17]. This is well shown by the experimental study of Saddoughi and Veeravalli [24] presented in Figure 2.2. It can clearly be seen that

the large scales are highly dependent on the boundary conditions of the flow, whereas data for the small scales (high wave numbers) collapses nicely for all cases.

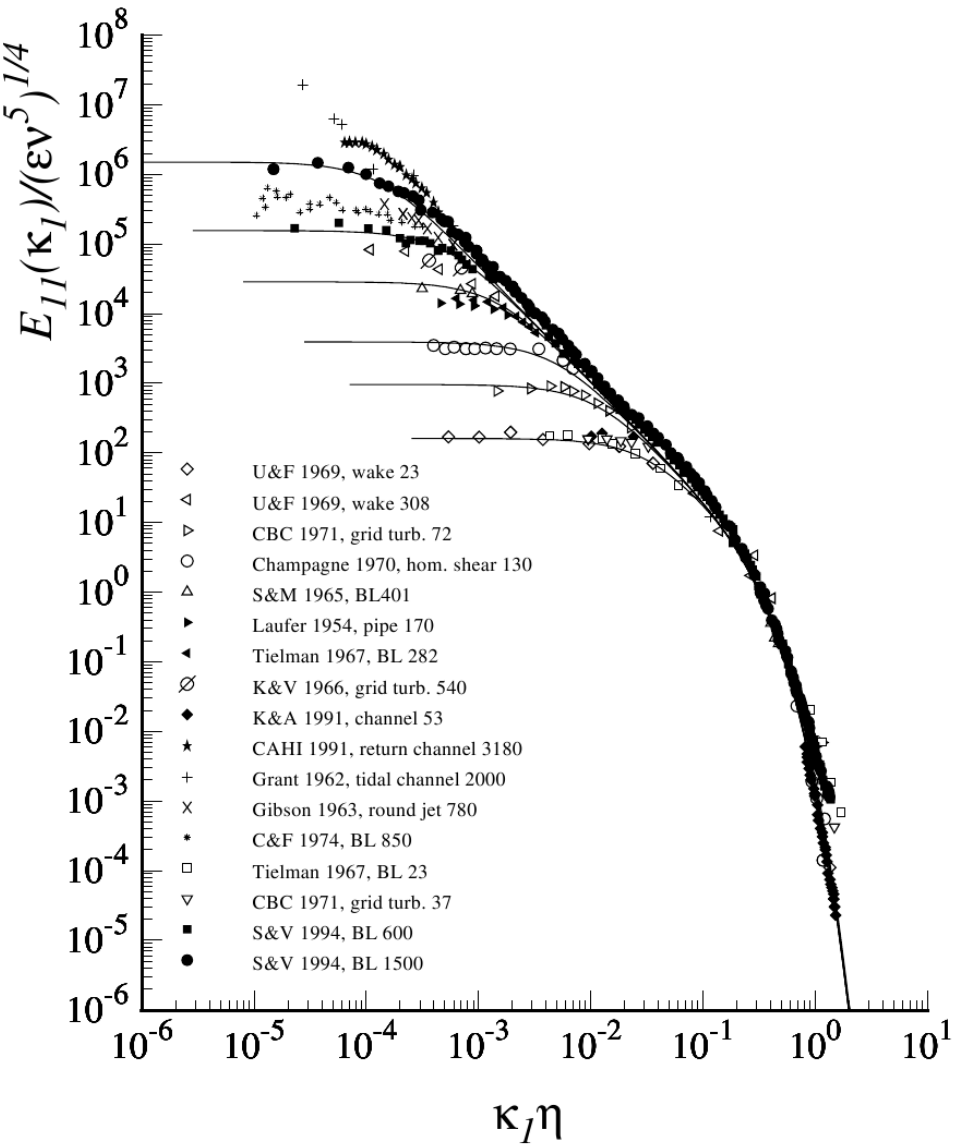

Figure 2.2: One dimensional energy spectra for different experimental cases, showing problem dependent large scales and universal small scales [24].

2.2 Governing Equations

A system of equations exists which governs the physics of a chemically reactive fluid, namely the instantaneous continuity, momentum, energy and species transport equations. Since the application in question is a high Mach number flow with heat release, the compressible form of the equations is used.

The continuity equation handles the conservation of mass and is defined as:

$$\frac{\partial \rho}{\partial t} + \frac{\partial \rho u_j}{\partial x_j} = 0 \tag{2.6}$$

where ρ is the fluid density, t is time, u_j is the velocity in direction j and x_j is the spatial vector. The momentum equation is defined as:

$$\frac{\partial \rho u_i}{\partial t} + \frac{\partial \rho u_i u_j}{\partial x_j} = -\frac{\partial p}{\partial x_i} + \frac{\partial \tau_{ij}}{\partial x_j} \tag{2.7}$$

where p is the static pressure and τ_{ij} is the viscous stress tensor, given by:

$$\tau_{ij} = 2\mu_l \left(S_{ij} - \frac{1}{3}\frac{\partial u_k}{\partial x_k}\delta_{ij} \right) \tag{2.8}$$

where μ_l is the molecular viscosity and δ_{ij} is the Kronecker delta. The strain rate is defined as:

$$S_{ij} = \frac{1}{2}\left(\frac{\partial u_i}{\partial x_j} + \frac{\partial u_j}{\partial x_i} \right) \tag{2.9}$$

The energy equation is given by:

$$\frac{\partial \rho e_0}{\partial t} + \frac{\partial \rho u_j h_0}{\partial x_j} = -\frac{\partial q_j}{\partial x_j} + \frac{\partial \tau_{ij} u_i}{\partial x_j} \tag{2.10}$$

where q_j is the heat flux vector. The specific stagnation internal energy, e_0, and specific stagnation enthalpy, h_0, are defined as:

$$e_0 = h - \frac{p}{\rho} + \frac{1}{2}u_i u_i \tag{2.11}$$

$$h_0 = e_0 + \frac{p}{\rho} \tag{2.12}$$

with the specific static enthalpy, h, given by:

$$h = \sum_{\alpha=1}^{N_s} Y_\alpha h_\alpha \tag{2.13}$$

where Y_α and h_α are the mass fraction and specific enthalpy of species α, respectively, and N_s is the number of chemical species. The calculation of h_α and other thermodynamic properties is to be discussed in chapter 4.

The species transport equation is defined using the species mass fraction:

$$\frac{\partial \rho Y_\alpha}{\partial t} + \frac{\partial \rho u_j Y_\alpha}{\partial x_j} = \dot{\omega}_\alpha - \frac{\partial \rho V_{\alpha,j} Y_\alpha}{\partial x_j}, \qquad \alpha = 1, \ldots, N_s - 1 \tag{2.14}$$

where $\dot{\omega}_\alpha$ is the reaction rate for species α. $V_{\alpha,j}$ is the j component of the diffusion velocity for species α, which can be described using Fick's law [25]:

$$V_{\alpha,j} Y_\alpha = -D_\alpha \frac{\partial Y_\alpha}{\partial x_j} \tag{2.15}$$

where the species diffusion coefficient, D_α, is defined as:

$$D_\alpha = \frac{\lambda}{\rho c_p Le_\alpha} \tag{2.16}$$

with the Lewis number, Le_α, assumed to be constant for each species. λ and c_p are the thermal conductivity and specific heat capacity at constant pressure of the mixture, respectively.

Only $N_s - 1$ species transport equations are required due to the compatibility condition:

$$\sum_{\alpha=1}^{N_s} Y_\alpha = 1 \tag{2.17}$$

meaning Y_{N_s} can be found from:

$$Y_{N_s} = 1 - \sum_{\alpha=1}^{N_s - 1} Y_\alpha \tag{2.18}$$

It is this set of instantaneous equations (2.6, 2.7, 2.10 and 2.14) which could be solved using the Direct Numerical Simulation (DNS) technique, with all phys-

ical scales captured and no modelling contributions required. However, the mesh requirements for such a simulation are very high, with required cell size to be of the order of the Kolmogorov length scale, restricting such simulations to low Reynolds number flows. For reacting cases mesh resolution requirements are even higher since the cell size is required to be of the order of the smallest chemical length scale [13]. Methods exist to reduce the computational expense involved in solving the system of governing equations, with the most popular being the averaging and filtering techniques used in the RANS and LES approaches, respectively.

2.3 Reynolds Averaged Navier Stokes (RANS)

For many engineering applications it is unnecessary to resolve all physical length scales, since it is often only the mean properties of the flow which are of interest. Therefore, in order to significantly reduce the computational time required for a DNS calculation, the instantaneous governing equations can be averaged in time to produce the Reynolds Averaged Navies Stokes (RANS) equations. The time averaging of a quantity ϕ is defined as:

$$\bar{\phi} = \frac{1}{T}\int_{t}^{t+T} \phi\left(\tau\right) d\tau \tag{2.19}$$

where T is a time scale much greater than any physical time scales in the flow. The Reynolds Averaged Navier Stokes equations are obtained when this averaging is applied to the instantaneous system of equations and they describe the evolution of mean quantities [14].

2.3.1 Favre Averaging

The averaging process introduces extra terms into the system of equations, which will be discussed in detail shortly. In order to avoid the introduction of extra terms into the continuity equation the standard Reynolds averaging of Equation 2.19 can be replaced by Favre averaging [26; 27], defined as:

$$\tilde{\phi} = \frac{\overline{\rho\phi}}{\bar{\rho}} \tag{2.20}$$

where the overbar and tilde indicate Reynolds averaged and Favre averaged quantities, respectively. An instantaneous quantity can be decomposed into a mean and fluctuating contribution:

$$\phi = \tilde{\phi} + \phi^{'} \tag{2.21}$$

with the fluctuations denoted by $^{'}$. Although the averaged equations describe the evolution of mean quantities and although $\widetilde{\phi^{'}} = 0$ [25], when the averaging process is applied to the product of more than one variable, extra terms are introduced into the system of equations since it can be shown that:

$$\widetilde{\phi\theta} = \widetilde{\phi}\widetilde{\theta} + \widetilde{\phi^{'}\theta^{'}} \tag{2.22}$$

where, $\widetilde{\phi^{'}\theta^{'}}$ is not equal to zero [25]. Applying Favre averaging to the instantaneous system of equations (2.6, 2.7, 2.10 and 2.14), the compressible RANS equations can be obtained:

$$\frac{\partial\bar{\rho}}{\partial t} + \frac{\partial\bar{\rho}\tilde{u}_j}{\partial x_j} = 0 \tag{2.23}$$

$$\frac{\partial\bar{\rho}\tilde{u}_i}{\partial t} + \frac{\partial\bar{\rho}\tilde{u}_i\tilde{u}_j}{\partial x_j} = -\frac{\partial\bar{p}}{\partial x_i} + \frac{\partial\bar{\tau}_{ij}}{\partial x_j} - \frac{\partial\bar{\rho}\widetilde{u_i^{'}u_j^{'}}}{\partial x_j} \tag{2.24}$$

$$\frac{\partial\bar{\rho}\widetilde{e_0}}{\partial t} + \frac{\partial\bar{\rho}\tilde{u}_j\widetilde{h_0}}{\partial x_j} = \frac{\partial}{\partial x_j}\left(\bar{\tau}_{ij}\tilde{u}_{ij} + \overline{\tau_{ij}u_i^{'}} - \bar{q}_j - \overline{\rho u_j^{'}h_0^{'}}\right) \tag{2.25}$$

$$\frac{\partial\bar{\rho}\tilde{Y}_\alpha}{\partial t} + \frac{\partial\bar{\rho}\tilde{u}_j\tilde{Y}_\alpha}{\partial x_j} = \bar{\dot{\omega}}_\alpha - \frac{\partial}{\partial x_j}\left(\overline{\rho V_{\alpha,j}Y_\alpha} + \bar{\rho}\widetilde{u_j^{'}Y_\alpha^{'}}\right) \tag{2.26}$$

Although it may be the mean properties of the flow which are of interest, the influence of turbulent fluctuations on this mean flow is still of great importance. This influence arises in the system of equations through the extra terms generated by the averaging process and they require modelling to obtain system closure.

2.3.2 Closure

The turbulent Reynolds stress term, $\widetilde{\bar{\rho}u_i''u_j''}$, in the momentum equation is often modelled using the concept proposed by Boussinesq [28], where the turbulent stresses are proportional to gradients in mean velocity:

$$-\widetilde{\bar{\rho}u_i''u_j''} = 2\mu_t\left(\tilde{S}_{ij} - \frac{1}{3}\frac{\partial\tilde{u}_k}{\partial x_k}\delta_{ij}\right) - \frac{2}{3}\bar{\rho}k\delta_{ij} \tag{2.27}$$

with k being the mean turbulence kinetic energy per unit mass, defined as:

$$k = \frac{1}{2}\widetilde{u_i''u_i''} \tag{2.28}$$

The $\frac{2}{3}\rho k\delta_{ij}$ term is often neglected, but may be non-negligible in high speed flows [29], so is included here.

The mean stagnation energy is defined as:

$$\widetilde{e}_0 = \widetilde{h} - \frac{\widetilde{p}}{\bar{\rho}} + \frac{1}{2}\widetilde{u}_i\widetilde{u}_i + k \tag{2.29}$$

where, again, the turbulence kinetic energy is included.

The turbulence kinetic energy gradient can can be used to approximate the molecular diffusion term in the time averaged energy equation [30]:

$$\frac{\partial\overline{\tau_{ij}u_i''}}{\partial x_j} \approx -\frac{\partial}{\partial x_j}\left(\mu_l\frac{\partial\widetilde{k}}{\partial x_j}\right) \tag{2.30}$$

and the mean heat flux vector is defined as:

$$\bar{q}_j = -\overline{\lambda\frac{\partial T}{\partial x_j}} + \sum_{\alpha=1}^{N_s}\overline{\rho V_{\alpha,j}Y_\alpha h_\alpha} \tag{2.31}$$

where the heat conduction and energy flux due to gradients in species mass fraction can respectively be approximated as:

$$\overline{\lambda\frac{\partial T}{\partial x_j}} \approx \lambda\frac{\partial\widetilde{T}}{\partial x_j} \tag{2.32}$$

$$\sum_{\alpha=1}^{N_s} \overline{\rho V_{\alpha,j} Y_\alpha h_\alpha} \approx -\sum_{\alpha=1}^{N_s} \bar{\rho} D_\alpha \tilde{h}_\alpha \frac{\partial \tilde{Y}_\alpha}{\partial x_j} \tag{2.33}$$

In order to model the turbulent flux of stagnation enthalpy, $\overline{\rho u_j^{'} h_0^{'}}$, the fluctuating stagnation enthalpy, $h_0^{'}$, needs to be defined. Subtracting Equation 2.29 from Equation 2.12, the following is obtained:

$$h_0^{'} = h^{'} + \tilde{u}_i u_i^{'} + k^{'} \tag{2.34}$$

giving

$$\widetilde{\bar{\rho} u_j^{'} h_0^{'}} = \widetilde{\bar{\rho} u_j^{'} h^{'}} + \bar{\rho} \tilde{u}_i \widetilde{u_i^{'} u_j^{'}} + \widetilde{\bar{\rho} u_j^{'} k^{'}} \tag{2.35}$$

The second term can easily be found once the turbulent Reynolds stresses are known. The turbulent enthalpy flux and turbulent kinetic energy flux, along with the turbulent diffusion term from the time-average species transport equation, can all be modelled using the gradient diffusion approximation [30]:

$$\widetilde{\bar{\rho} u_j^{'} h^{'}} = -\frac{\mu_t c_p}{Pr_t} \frac{\partial \widetilde{T}}{\partial x_j} \tag{2.36}$$

$$\widetilde{\bar{\rho} u_j^{'} k^{'}} = -\frac{\mu_t}{\sigma_k} \frac{\partial \widetilde{k}}{\partial x_j} \tag{2.37}$$

$$\widetilde{\bar{\rho} u_j^{'} Y_\alpha^{'}} = -\frac{\mu_t}{Sc_t} \frac{\partial \widetilde{Y}_\alpha}{\partial x_j} \tag{2.38}$$

where σ_k is a model constant whilst Pr_t and Sc_t and the turbulent Prandtl and Schmidt numbers, respectively. Terms involving μ_t will usually dominate over the laminar terms in the mean transport equations and sensitivities of RANS to the choice of Pr_t and Sc_t will be investigated in Chapter 5.

Modelling of the mean reaction rate, $\bar{\dot{\omega}}$, will be the subject of Chapter 3 since a wide range of methods are available.

Studying the approximations presented for modelling the additional terms, other than model constants, it is just the turbulent viscosity which is unknown. It is the job of the turbulence model to find its value and obtain closure for the system of equations.

2.3.3 Turbulence Models

Turbulence models of varying degrees of complexity exist, from simple mixing length approaches to full Reynolds stress formulations. Central to most turbulence models is the Boussinesq approximation of Equation 2.27, but the Reynolds stress model attempts to overcome the limitations of this concept.

2.3.3.1 Mixing Length Model

A mixing length turbulence model consists of a simple algebraic expression defining the turbulent viscosity. Prandtl's mixing length model can be defined as [31]:

$$\mu_t = \bar{\rho} l_m^2 \left| \left(\frac{\partial \widetilde{u}_i}{\partial x_j} + \frac{\partial \widetilde{u}_j}{\partial x_i} \right) \frac{\partial \widetilde{u}_i}{\partial x_j} \right| \tag{2.39}$$

where l_m is the mixing length. Simple algebraic formulae can be used to describe the mixing length and the mixing length model can be applied with good success to basic flows such as the plane mixing layer. However, it is difficult to use this low order model in more complex flows where the definition of the required mixing length is not straightforward. Although the mixing length model does provide a spatially varying turbulent viscosity due to proportionality to the mean velocity gradient, more sophisticated turbulence models have been developed which handle the transport of turbulence properties. Differential equations handle the effects of transport through convection and diffusion and the effects of production and destruction of these turbulence properties can also be modelled.

2.3.3.2 One Equation Models

Models exist which provide these capabilities through use of a single differential equation. The Spalart-Allmaras model [32] is one example of this, which solves a transport equation for the kinematic eddy viscosity ($\tilde{\nu}$):

$$\frac{\partial \rho \tilde{\nu}}{\partial t} + \frac{\partial \rho u_j \tilde{\nu}}{\partial x_j} = D_{\tilde{\nu}} + P_{\tilde{\nu}}^{+} - P_{\tilde{\nu}}^{-} \tag{2.40}$$

where $D_{\tilde{\nu}}$, $P_{\tilde{\nu}}^{+}$ and $P_{\tilde{\nu}}^{-}$ are the terms modelling diffusion, production and destruc-

tion, respectively. The turbulent viscosity can be found from:

$$\mu_t = \rho\tilde{\nu} f_{\nu 1} \tag{2.41}$$

where $f_{\nu 1}$ is a wall damping function. Away from the wall this damping function is unity and the kinematic eddy viscosity ($\widetilde{\nu}$) is simply equal to the kinematic viscosity (ν_t). The Spalart-Allmaras turbulence model performs well in external aerodynamic and boundary layer flows [33] but, similarly to the mixing length model, one equation turbulence models require an algebraic expression for the turbulence length scale. This means they can perform poorly in complex flows, where the turbulence length scale can vary and is harder to define. The Spalart-Allmaras turbulence model has also been shown to perform poorly in round jets and round wakes [34], but is robust and does not require any low Reynolds number modifications.

2.3.3.3 Two Equation Models

Two equation turbulence models can be used to remove the requirements for an algebraic expression for the turbulence length scale. The turbulence length scale can then be calculated on the fly, from a combination of the two variables for which differential transport equations are provided. Various turbulence models of this sort are available; the three most common are briefly discussed here.

$\underline{k-\varepsilon}$

The most widely used and validated two equation turbulence model is the $k-\varepsilon$ model [35; 36], where transport equations for the turbulence kinetic energy (k) and the turbulence dissipation rate (ε) are employed:

$$\frac{\partial \rho k}{\partial t} + \frac{\partial \rho u_j k}{\partial x_j} = D_k + P_k^+ - P_k^- \tag{2.42}$$

$$\frac{\partial \rho \varepsilon}{\partial t} + \frac{\partial \rho u_j \varepsilon}{\partial x_j} = D_\varepsilon + P_\varepsilon^+ - P_\varepsilon^- \tag{2.43}$$

The turbulent viscosity is given by:

$$\mu_t = \rho C_\mu \frac{k^2}{\varepsilon} \tag{2.44}$$

where C_μ is a model constant. The turbulence length scale can now be calculated using [33]:

$$L_t = \frac{k^{\frac{3}{2}}}{\varepsilon} \tag{2.45}$$

Although the $k-\varepsilon$ turbulence model is capable of producing good results for free shear layer flows [33] it is not capable of accurately predicting separation or the viscous region near a wall [37]. For boundary layer flows, the addition of low Reynolds number damping functions (such as that by Chien [38]) is required, but these make the differential equations numerically stiff through the introduction of additional source terms, and hence difficult to solve.

$\underline{k-\omega}$

The $k-\omega$ turbulence model of Wilcox [37] was developed to improve over the $k-\varepsilon$ model for the calculation of boundary layers in adverse pressure gradient flows. For the $k-\omega$ turbulence model, a transport equation for the turbulence frequency (ω) is used instead of for the turbulence dissipation rate:

$$\frac{\partial \rho\omega}{\partial t} + \frac{\partial \rho u_j \omega}{\partial x_j} = D_\omega + P_\omega^+ - P_\omega^- \tag{2.46}$$

The k equation (2.42) is only modified with a change of variables in the destruction term (P_k^-), through use of the simple relation between k, ε and ω:

$$\beta^\star \omega = \frac{\varepsilon}{k} \tag{2.47}$$

where $\beta^\star$ is a model constant. The turbulent viscosity is given by:

$$\mu_t = \frac{\rho k}{\omega} \tag{2.48}$$

The $k-\omega$ turbulence model is numerically robust, since the addition of low Reynolds number damping functions is not required. The model is able to ac-

curately predict mildly separated flows, but can prove sensitive to free-stream values of ω (i.e. inlet boundary condition values). However, these sensitivities have been improved by recent modifications to the model [39].

Menter SST

The Menter SST turbulence model [40] attempts to improve upon the $k-\varepsilon$ and $k-\omega$ formulations by combining the two, using the strengths of the $k-\omega$ model near the wall and the $k-\varepsilon$ model in the free-stream. Still only two transport equations are required, due to the simple relationship between the three variables (Equation 2.47), but blending functions are used to smoothly transition between the two turbulence models outside of the boundary layer. The turbulent viscosity is given by:

$$\mu_t = \frac{\rho k}{\max(a_1\omega, \widetilde{S}F_2)} \tag{2.49}$$

where F_2 is one such blending function and S is the strain invariant, defined as:

$$S = \sqrt{2S_{ij}S_{ij}} \tag{2.50}$$

2.3.3.4 Reynolds Stress Model

Two-equation turbulence models have been found to perform well for many industrially relevant flows [33] and so have been widely used and validated. However, such models require the presence of velocity gradients in order to generate eddy viscosity, meaning away from shear layers no Reynolds stresses are calculated. Also, when significant velocity gradients exist in more than one direction the two-equation approach may be unsuitable, and led to the development of the Reynolds-stress model (RSM) [41].

Rather than employing the Boussinesq assumptions of Equation 2.27, the RSM employs a transport equation for each Reynolds stress. Since the turbulent stress tensor is symmetric, six additional transport equations are required for $\widetilde{u_1'^2}$, $\widetilde{u_2'^2}$, $\widetilde{u_3'^2}$, $\widetilde{u_{12}'}$, $\widetilde{u_{13}'}$ and $\widetilde{u_{23}'}$:

$$\frac{\partial \rho \widetilde{u_i' u_j'}}{\partial t} + \frac{\partial \rho u_k \widetilde{u_i' u_j'}}{\partial x_k} = D_{ij} + P_{ij}^{+} - P_{ij}^{-} + \Theta_{ij} \tag{2.51}$$

where, subscript 1 corresponds to the x-direction (u-velocity), 2 to the y-direction (v-velocity) and 3 to the z-direction (w-velocity). D_{ij}, P_{ij}^{+}, P_{ij}^{-} and Θ_{ij} are the diffusion, production, dissipation and pressure-strain terms [41], respectively. Due to the increased complexity of this approach and due to the attempt at directly modelling each Reynolds-stress, the RSM is often referred to as a second order closure for the RANS equations.

Models are required for the diffusion, dissipation and pressure strain terms. An additional transport equation, for the turbulence dissipation rate (ε), is required for this modelling, bringing the total number of additional differential equations to seven. This means the Reynolds-stress model is very computationally expensive compared to the zero, one and two equation turbulence models previously discussed.

In order to model the turbulent fluxes arising in the energy and species transport equations, the turbulent viscosity can be used, as before. The turbulence kinetic energy can be calculated from the three normal stresses using Equation 2.28 and this, in addition to the availability of the turbulence dissipation rate, means the turbulence viscosity can be calculated as for the $k-\varepsilon$ turbulence model, from Equation 2.44.

2.3.3.5 Model Constants

Since the turbulence model is required to account for all physical length scales in a RANS environment, empirically tuned constants are employed to deal with the problem dependent large scales of the flow. The eddy viscosity will dwarf the molecular viscosity and hence it is the turbulent transport terms in the RANS system of equations which will play the dominant role. Constants such as the turbulent Prandtl and Schmidt numbers therefore have a significant influence on the computational results obtained.

The Prandtl number is the ratio of momentum (viscous) and heat transport and is linked to the species Lewis number through the relation:

$$Sc_\alpha = PrLe_\alpha = \frac{\mu_l}{\rho D_\alpha} \tag{2.52}$$

where Sc_α is the species Schmidt number, which is the ratio of momentum and molecular diffusion. The turbulent Prandtl and Schmidt numbers are therefore the turbulent equivalent, involving turbulent transport and diffusion rather than the molecular properties defined here. The turbulent Schmidt number will be assumed constant for all species.

Significant tuning of such constants is therefore required in order to accurately simulate the problem dependent large scales of the flow. This can be successful if experimental data is available to aid the tuning process, but it can often be time consuming. For cases where experimental data is not available, it is difficult to place a great deal of trust into the accuracy of the results obtained. It is therefore difficult to use the RANS method in certain areas of research and extrapolation of numerical methods from lab based experiments to full flight conditions can provide unreliable results. The sensitivities of RANS to the modification of certain model constants will be demonstrated in Chapter 5.

However, the RANS method is computationally efficient and is capable of predicting trends in the physics of a given problem.

2.3.4 Unsteady RANS (URANS)

The time step, Δt, used to iterate the numerical methods employed is defined by the CFL number:

$$\Delta t = \frac{\mathrm{CFL} \cdot \Delta x}{|u| + a} \tag{2.53}$$

where Δx is the minimum length of the cell, u the flow velocity and a the speed of sound. This approach ensures a hypothetical particle cannot move more than Δx in a single time step. A maximum CFL number will exist to define stability, which is dependent upon the method employed for time integration.

Although the time-dependent terms are present in the RANS equations (2.23-2.26), they are not solved in a time accurate manner when a steady state solution is required. In order to accelerate convergence to a steady state, variable time

steps are often employed whereby each computational cell uses a time step dependent on its own minimum size and flow properties. However, steady RANS methods struggle to predict flows involving massive separation [42]. If the physics involved in a particular simulation are not of a steady nature, a time-accurate simulation is required to capture the transient behaviour, where a global time step is used for every computational cell, leading to the Unsteady RANS (URANS) formulation.

It is intended that the URANS approach mimics the large scale dynamics of the flow [42]. Such simulations can be ensemble averaged to provide reasonable predictions for mean flow variables, however rms predictions are often in poor agreement with experimental data.

The behaviour of the URANS technique can be demonstrated through the simulation of the flow around a square cylinder [43]. Figure 2.3 displays the vorticity magnitude, clearly showing the unsteady vortical structure is captured in the simulation. However, it can be seen that the solution is smooth since, due to the averaging process, only a single frequency is captured in the solution and hence there is a lack of turbulent fluctuating data in the results.

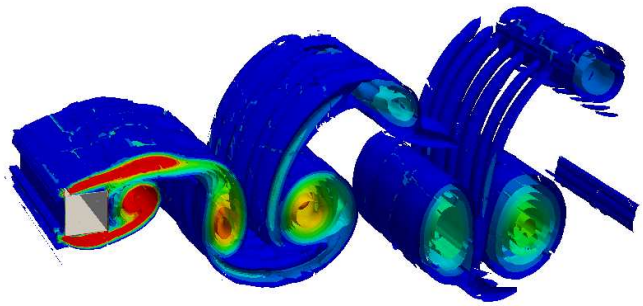

Figure 2.3: Vorticity magnitude contours from a square cylinder URANS simulation

The steady RANS approach is not suitable for the simulation of the square cylinder test case, due to its transient behaviour. The resulting solution is dependent upon the disparity in free-stream cell size and a steady state solution may never be reached.

2.4 Large Eddy Simulation (LES)

Large eddy simulation aims to improve over the RANS technique by attempting to directly capture some of the turbulent scales present in a given flow. It can be considered as an intermediate between RANS and DNS, since similarly to DNS direct resolution of turbulent structures is attempted; however, DNS of high Reynolds number flows is not currently possible, so a coarser mesh is employed. This mesh acts as a low-pass filter in Fourier space, removing the high wave number (small length scale) eddies from the solution. These smaller eddies still play an important role in the physics, providing overall dissipation to the large scale structures, and this must now be modelled. In RANS, models are used to account for all turbulent scales in the flow; now they are only used to account for the smaller turbulent structures. Due to the more universal behaviour of these small scales, the development of widely applicable models is more straightforward.

LES can be compared to the Reynolds averaged approach through the simulation of the square cylinder test case presented in the previous section. It can be seen from Figure 2.4 that the turbulent nature of the wake is far better captured with the LES technique, with a range of turbulent scales present.

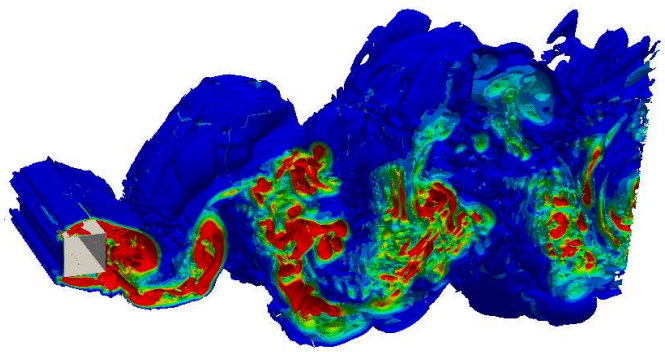

Figure 2.4: Vorticity magnitude contours from a square cylinder large eddy simulation

2.4.1 Favre Filtering

Since the mesh acts as a filter on the turbulence, the equations for LES can be obtained by applying a filter to the instantaneous governing equations. A filtered variable is defined as:

$$\bar{\phi}(x) = \int_D \phi(x^\star) G(x - x^\star) \mathrm{d}x^\star \tag{2.54}$$

where $G(x - x^\star)$ is the filter function. Finite volume LES can be thought of as using a top-hat filter in physical space. The top-hat filter is a sharp cutoff filter, where the turbulent structures are either big enough to be captured by the mesh, or they are not [14]:

$$G(x) = \begin{cases} 1/\Delta & \text{if } |x| \leq \Delta/2 \\ 0 & \text{otherwise} \end{cases} \tag{2.55}$$

where Δ is the filter width. In order to be able to capture the large scale eddies of the flow on a given computational mesh, the filter width must lie within the inertial range of the turbulence spectrum.

Similarly to Favre averaging, Favre filtering is used to obtain the compressible form of the governing equations, in order to avoid the introduction of additional terms into the continuity equation. Equation 2.20 is also used to define a Favre filtered variable ($\widetilde{\phi}$), where the overbar now corresponds to the filtering defined in Equation 2.54.

Since LES directly resolves the large scales of the flow, which are random in nature by definition, statistical methods are required to analyse the resulting data. The mean and rms values can respectively be defined as:

$$\widetilde{\phi}_{mean} = \frac{1}{N_{mean}} \sum_{i=1}^{N_{mean}} \widetilde{\phi}_i \qquad \widetilde{\phi}_{rms} = \sqrt{\frac{1}{N_{rms}} \sum_{j=1}^{N_{rms}} (\widetilde{\phi} - \widetilde{\phi}_{mean})^2} \tag{2.56}$$

where N_{mean} and N_{rms} are the number of iterations over which the mean and rms values are calculated, respectively. The number of iterations needs to be large enough to allow the statistical data to reach a steady state.

Although Favre filtering is conceptually different to the Favre averaging process and the resulting system of equations has a different physical meaning, they are visually identical to those presented in Section 2.3 and so will not be repeated here. This makes it relatively straightforward to convert a URANS code into one capable of conducting large eddy simulations. The only modification required is the way in which the turbulent viscosity is calculated, with this parameter now referred to as the subgrid-scale (SGS) viscosity (μ_{SGS}). This subgrid viscosity is responsible for modelling the dissipation that the small (subgrid) scales provide to the large scale turbulence.

There are currently two main approaches to modelling this subgrid dissipation, whereby the subgrid viscosity can either be explicitly calculated using a subgrid-scale model or it can be neglected, with the required dissipation being implicitly provided by the numerical dissipation of an upwind scheme.

2.4.2 Explicit Subgrid-Scale (SGS) Models

Subgrid-scale models of varying degrees of complexity are available to provide the dissipation required. Rather than explicitly filtering the solution, as implied by Equation 2.54, implicit filtering is applied by the computational grid. The filter width provided by a given computational grid therefore plays a significant role in subgrid-scale modelling; the smaller the filter width, the larger the range of scales captured by the mesh and the lower the requirements for subgrid viscosity, but the higher the computational cost.

The filtering operation of Equation 2.54 assumes a constant filter width so that it commutes with the operation of differentiation [44]. However, in complex geometries where unstructured grids are employed it is difficult to keep the mesh spacing and hence filter width constant. There are two main methods for calculating a spatially varying filter width, with the cube root of the cell volume often being used:

$$\Delta = \sqrt[3]{\delta_x \delta_y \delta_z} = \sqrt[3]{\text{volume}} \tag{2.57}$$

where, δ_x, δ_y and δ_z are the cell dimensions in the x, y and z directions, respectively. However, for a non-isotropic grid, it is reasonable to state that the smallest

turbulent eddy that a computational grid is capable of capturing, is that with size greater than the maximum dimension of a cell [45]:

$$\Delta = \max(\delta_x, \delta_y, \delta_z) \tag{2.58}$$

This would provide the same filter width as Equation 2.57 on a regular structured grid, but significantly different for a grid containing elongated cells. Although Equation 2.58 has a physical background, it can generate significantly higher levels of subgrid viscosity and the use of 2.57 can aid the growth of shear layer instabilities, encouraging the transition to turbulence [46] when high aspect ratio cells are present. The influence on results of the choice of filter width will be investigated in Chapter 6.

2.4.2.1 Smagorinsky model

The most straightforward and also most widely used subgrid-scale model, is that developed by Smagorinsky [47]:

$$\mu_{SGS} = \rho \left(C_s \Delta\right)^2 |\tilde{S}| \tag{2.59}$$

where, C_s is a model constant. This model was obtained by assuming the subgrid-scales are in equilibrium, meaning the production and destruction of energy is balanced. This assumption is used in the detached eddy simulation approach, to be discussed in Section 2.4.4.3, in order to obtain a Smagorinsky like eddy viscosity model.

Due to the model's simplicity, it is easy to implement and is computationally efficient. However, results can be heavily dependent on the model constant used [48], with values in the approximate range 0.1-0.2 found to be most appropriate, depending on the application in question. In complex flows, where different flow physics may be encountered in different regions of the computational domain, it is restrictive to require C_s to remain constant in space.

The Smagorinsky model is also purely dissipative and therefore is not capable of modelling backscatter.

2.4.2.2 Dynamic model

The range of values found for the Smagorinsky constant implies the subgrid scales are not as universal as initially thought. This led to the development of the dynamic SGS eddy viscosity model by Germano et al. [48], where the Smagorinsky constant is calculated on-the-fly using information from the smallest resolved turbulent eddies, and is allowed to vary in space and time.

Moin et al. [49] modified the dynamic model for compressible flows. The methodology employed to calculate the dynamic Smagorinsky constant is briefly discussed here. It can be shown that the subgrid stress can be defined as:

$$\tau_{ij} = \bar{\rho}(\widetilde{u_i u_j} - \widetilde{u}_i \widetilde{u}_j) \tag{2.60}$$

with the tilde and bar here representing Favre and spatially filtered variables, respectively. Expanding these Favre filtered expressions gives:

$$\tau_{ij} = \overline{\rho u_i u_j} - \frac{\overline{\rho u_i}\,\overline{\rho u_j}}{\bar{\rho}} \tag{2.61}$$

The dynamic model applies a second filter to the resolved scales in order to use spectral data from the resolved field. This second filter is referred to as a test filter and the sub-test-filter stresses can be defined as:

$$\mathcal{T}_{ij} = \widehat{\overline{\rho u_i u_j}} - \frac{\widehat{\overline{\rho u_i}}\,\widehat{\overline{\rho u_j}}}{\hat{\bar{\rho}}} \tag{2.62}$$

where $\widehat{\ }$ refers to a filtered variable at the test-filter width, $\widehat{\Delta}$, which is larger than the mesh filter width, Δ.

Now, the stresses for the scales between the test and grid filter (denoted by the shaded region in Figure 2.5), called the Leonard stresses, $\mathcal{L}_{ij}$, are calculated as the difference between the sub-test-filter stresses and test-filtered subgrid stresses:

$$\mathcal{L}_{ij} \equiv \mathcal{T}_{ij} - \hat{\tau}_{ij} \tag{2.63}$$

which, through reverting back to Favre filtered variables, is given by:

$$\mathcal{T}_{ij} - \hat{\tau}_{ij} = \widehat{\bar{\rho}\widetilde{u}_i \widetilde{u}_j} - \frac{1}{\hat{\bar{\rho}}}(\widehat{\bar{\rho}\widetilde{u}_i}\,\widehat{\bar{\rho}\widetilde{u}_j}) \tag{2.64}$$

Using a Smagorinsky model for both the sub-test-filter stresses, $\mathcal{T}_{ij}$, and the subgrid stresses, $\hat{\tau}_{ij}$, it can be shown that [49] Equation 2.64 can provide a formulation for the dynamic constant. All data on the right hand side is readily available from the resolved data. The spatially filtered density and Favre filtered velocity data is provided by the grid filtered data. The test-filtered data can then be found by averaging neighbouring values of grid filtered data, effectively applying a larger spatial filter.

The dynamic model is capable of generating negative values for this constant and so allowing for backscatter.

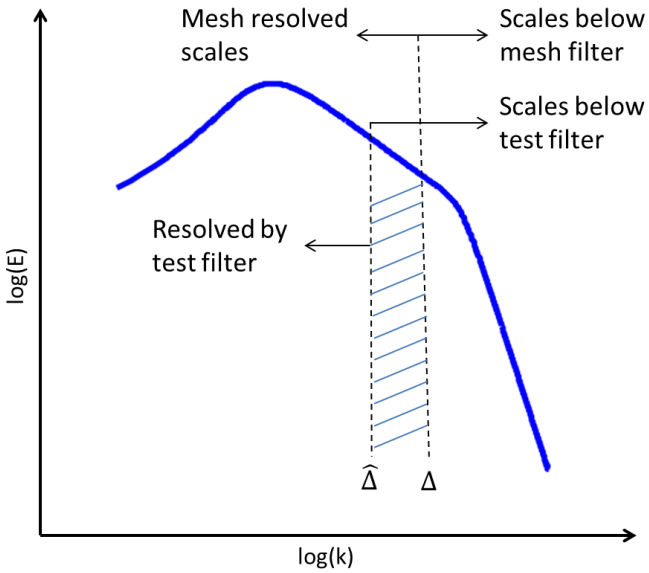

Figure 2.5: Turbulence energy spectrum showing mesh and test filters

2.4.3 Implicit LES

It will be presented in Chapter 4 that for the accurate simulation of supersonic combustion a high order upwind scheme is required to capture flow discontinuities in a monotonic fashion. Garnier et al. [50] investigated the effect of using a SGS model in combination with a shock capturing scheme, for the LES of compressible flows. It was concluded that the addition of a SGS model to shock-capturing

methods is unnecessary and inconvenient, since the dissipation provided by the shock-capturing schemes is on its own greater than that provided by the SGS model. This type of SGS model free LES leads into the realm of implicit LES (ILES), where the numerical dissipation needed to model the sub-grid scales is provided by the numerical methods employed.

Implicit LES can be thought of as under-resolved DNS, since it is the instantaneous set of governing equations which are solved on a grid too coarse to capture the smallest scales of the flow. No modelling is provided for the subgrid scales since it is claimed [51] that the intrinsic dissipation of an upwind scheme can mimic the effect of a SGS model. Fureby and Grinstein [52] and Fureby [53] compared the implicit and explicit LES approaches through the simulation of both a free shear layer and rearward facing step. It was concluded that the concept of LES is virtually independent of the method employed, as long as grid resolution is high enough to ensure that the minimum resolved scales are in the inertial range of the turbulence spectrum.

Despite encouraging results using the implicit LES approach, its use is often the topic of debate because the dissipation employed lacks the complex physical meaning provided by explicit SGS models. It is also not well understood how well the implicit approach handles complex combustion, since only the instantaneous reaction rate ($\dot{\omega}$) is solved and no modelling for turbulence chemistry interaction is provided. In order for turbulence chemistry interactions to be modelled, subgrid properties such as the turbulence length scale would be needed (see Chapter 3) for which an explicit SGS model is required.

2.4.4 Wall Bounded LES

Since the application of this work is to be the simulation of a supersonic combustor, which is a wall bounded internal aerodynamics problem, it is important to study the modelling requirements for the LES of boundary layer flows. As previously stated, the resolution of a computational mesh must be such that the cutoff wave number should be somewhere in the inertial range of the turbulence spectrum. For this to be the case, it can be shown [54] that, far from a wall in the free-stream, the mesh resolution requirements (number of cells, N_{free}) are

proportional to the turbulent Reynolds number as:

$$N_{free} \propto \mathrm{Re}_t^{0.6} \tag{2.65}$$

However, near the wall, where the effects of viscosity are important, the required resolution for a LES is much more demanding [55] since important near wall vortical structures scale with wall units. It is therefore not only in the wall normal directions that significant resolution is required (as would be the case in RANS), but also in the two wall parallel directions, significantly increasing the mesh resolution requirements. The number of cells required to accurately resolve this region (N_{wall}) is proportional to the turbulent Reynolds number [54] as:

$$N_{wall} \propto \mathrm{Re}_t^{2.4} \tag{2.66}$$

This places significant restrictions on the affordability of fully resolved wall bounded LES, especially for the very high Reynolds number flows that are to be studied. It is therefore necessary to investigate ways to relax these restrictions, by not resolving the near wall turbulent structures but by applying models which provide the correct boundary layer behaviour (e.g. separation) and apply the correct shear stresses to the free-stream flow.

2.4.4.1 Wall Functions

Early large eddy simulations [56; 57] of wall bounded high Reynolds number flows employed the wall functions often used with the RANS equations, in order to reduce the near wall resolution requirements. Wall functions assume the presence of a near wall logarithmic layer which can be used to calculate the shear stress to be applied to the fluid in a near wall cell. However, in practical engineering applications the assumption that a logarithmic layer exists often does not hold [54] due to the presence of severe favourable and adverse pressure gradients, along with regions of separation.

2.4.4.2 Two Layer Model

The two layer model is a zonal approach originally proposed by Balaras and Benocci [58], which solves the Reynolds averaged boundary layer equations on a fine wall normal mesh, which is embedded on a coarser LES mesh, reducing the computational demands of a fully resolved large eddy simulation. The main assumption is a weak coupling between the near wall and outer layer regions, where the LES solution provides velocity values to the inner layer calculation and the inner layer provides shear stresses for the outer layer flow. Although the two layer model has been applied with success and can improve significantly over the wall function approach, the location at which the inner layer communicates with the LES zone must be specified by the user and requires prior knowledge of the final solution, which may not be available.

2.4.4.3 DES

It is also possible to solve the full system of Reynolds averaged Navier Stokes equations in the near wall region, dramatically reducing the computational cost of fully resolved LES by relaxing the requirements on mesh spacing, particularly in the directions parallel to the surface. Standard RANS turbulence models can therefore be used, with a transition to LES occurring away from the surface. There is a stronger coupling between the RANS and LES regions than in the two layer approach, since all required fluxes are calculated across this boundary. There can however be a discontinuous eddy viscosity profile due to the transition from RANS to SGS turbulence models. However, the severity of this transition can be controlled through the choice of blending between the two regions.

One choice can be to apply an explicit blending function between a RANS turbulence model with strong near wall modelling capabilities and a separate SGS model for the free-stream, as was done by Baurle and Edwards [15] for a supersonic coaxial jet. The choice of blending function and the location at which this blending occurs, can have a significant impact on the accuracy of the near wall modelling and resultant skin friction values.

Another approach for blending the near wall and free-stream regions is to transition the length scale in the RANS model to one based on mesh spacing.

This effectively transitions the RANS turbulence model to an SGS model for use in LES. This length scale modification is used in detached eddy simulation and will be the focus here. Details for the whole spectrum of wall modelling approaches are available in the comprehensive reviews of Piomelli [54], Piomelli and Balaras [59] and Cabot and Moin [55].

Detached eddy simulation (DES) was developed by Spalart et al. [60] and is a hybrid RANS-LES method which makes use of a single turbulence model for both the near wall RANS regions and the free-stream LES calculations. DES was originally formulated with the Spalart-Allmaras turbulence model due to its robust nature and suitability for modelling boundary layer flows. It is possible to transform this turbulence model into a Smagorinsky type SGS model by balancing the production and destruction terms in the transport equation for kinematic eddy viscosity (2.40), giving:

$$c_{b1}\widetilde{S}\widetilde{\nu} = c_{w1}\left(\frac{\widetilde{\nu}}{d}\right)^2 \tag{2.67}$$

where, c_{b1} and c_{w1} are model constants and, critically, d is the RANS turbulence length scale given by the distance to the nearest wall, y_w. Through some manipulation and use of Equation 2.41 this becomes:

$$\mu_t \propto \rho\widetilde{S}d^2 \tag{2.68}$$

Through comparison to Equation 2.59 it is straightforward to see that a Smagorinsky type model can be achieved through alteration of the turbulence length scale from d in the RANS region to $C_{DES}\Delta$ in the free-stream, where C_{DES} is a model constant. The transition between these length scales is made possible through the introduction of a new variable $\widetilde{d}$, in place of d, in the kinematic eddy viscosity transport equation, defined as:

$$\widetilde{d} = \min\left(y_w, C_{DES}\Delta\right) \tag{2.69}$$

This assumes that the production and destruction terms are dominant in an equilibrium flow (i.e. the diffusion term is negligible) and so they can be equated to form the Smagorinsky like model.

This new length scale acts as a sharp switching function between the RANS and LES approaches and is dependent upon mesh resolution and the method used to calculate the filter width. Special care needs to be taken when designing the grid on which a DES is to be conducted [61] in order to ensure transition to LES occurs outside of the boundary layer. The recommended filter width [45] is that given by Equation 2.58.

DES is not restricted to use with the Spalart-Allmaras turbulence model and Strelets [45] formulated a version which uses the Menter SST turbulence model, citing its good performance in boundary layer calculations and separation prediction as to why it would make an ideal candidate for RANS modelling in the near wall region. Equations 2.45 and 2.47, can be combined to define the RANS length scale as:

$$l_{k-\omega} = \frac{k^{\frac{1}{2}}}{\beta^{\star}\omega} \tag{2.70}$$

Again, it is required that for an equilibrium free-stream flow the k and ω transport equations are modified such that the turbulent viscosity of the Menter SST turbulence model reduces to a Smagorinsky like form. For simplicity, Strelets [45] suggested a modification to just the diffusion term in the k equation (2.42), from

$$D_k = \rho\beta^{\star}k\omega = \frac{\rho k^{\frac{3}{2}}}{l_{k-\omega}} \tag{2.71}$$

to

$$D_{k,DES} = \frac{\rho k^{\frac{3}{2}}}{\widetilde{l}} \tag{2.72}$$

where, $\widetilde{l}$ is the DES turbulence length scale, given as:

$$\widetilde{l} = \min\left(l_{k-\omega}, C_{DES}\Delta\right) \tag{2.73}$$

Since the Menter SST turbulence model transitions between the $k-\varepsilon$ and $k-\omega$ turbulence models using a blending function F_1, it is possible the subgrid viscosity could be calculated using either model, since the transition between

models may not coincide with the transition to LES. For this reason, there exists a C_{DES} constant for each model, and that used in the calculation for $\widetilde{l}$ must be found using the blending function:

$$C_{DES} = (1 - F_1)\, C_{DES}^{k-\varepsilon} + F_1 C_{DES}^{k-\omega} \tag{2.74}$$

However, use of the $k - \varepsilon$ model is more likely since the $k - \omega$ turbulence model is only active near the wall.

These model constants were tuned by simulating the decay of homogeneous isotropic turbulence and were found to be $C_{DES}^{k-\varepsilon} = 0.61$ and $C_{DES}^{k-\omega} = 0.78$. For DES with the Spalart-Allmaras turbulence model C_{DES} was tuned to a value of 0.65.

2.4.4.4 DDES

The need to design the computational mesh to ensure switching from RANS to LES occurs outside of the boundary layer can often be problematic, since the required mesh spacing may not be possible due to geometric constraints, required free-stream resolution or simply because knowledge of the flow field is not known prior to mesh generation. If the wall parallel mesh spacing is small enough to cause transition from RANS to LES inside the boundary layer, but is not fine enough to resolve the turbulent streaks, a reduction in the Reynolds stresses are obtained. This is because the reduction in turbulent viscosity from the SGS model is not replaced by resolved shear stresses due to lack of mesh resolution [62]. This leads to an erroneous prediction of the skin friction at the wall.

This reliance on mesh design lead to the birth of the delayed detached eddy simulation (DDES) method [62], which modifies the switching position through use of flow field quantities such as velocity gradients and the turbulent viscosity. Concentrating on the Menter SST form of DES, the turbulence length scale (Equation 2.73) can be modified through the introduction of the function f_d:

$$\widetilde{l} = l_{k-\omega} - f_d \max\left(0, l_{k-\omega} - C_{DES}\Delta\right) \tag{2.75}$$

which can be defined as:

$$f_d = 1 - \tanh\left([8_{r_d}]^3\right) \tag{2.76}$$

where r_d is a function of viscosity and velocity gradients:

$$r_d = \frac{\mu_t + \mu_l}{\rho\sqrt{\frac{\partial U_i}{\partial x_j}\frac{\partial U_i}{\partial x_j}}\kappa^2 y_w^2} \tag{2.77}$$

with κ being the Kármán constant. The blending function f_d is designed to be equal to 1 in the LES region and 0 elsewhere. As well as ensuring the transition from RANS to LES occurs outside of the boundary layer, this blending function also provides a smoother transition, removing the discontinuity in eddy viscosity.

Introducing a blending function based on flow variables also means the switching position is less sensitive to the filter width than is the case with DES. The strict requirement to use Equation 2.58 for the filter width can therefore be relaxed and the more conventional filter width given by Equation 2.57 can also be considered. The effects of using these two filter widths will be investigated in Chapter 6.

2.4.4.5 Transition Region Turbulence

Although the methods mentioned above make the large eddy simulation of high Reynolds number wall bounded flows affordable, there are significant drawbacks to under-resolving the near wall region. In areas of separation, the turbulent structures from the outer region of the boundary layer, which should be shed into the free-stream, will not be present since they are not resolved. This can cause a delay in the transition to turbulence and development of eddy structures in the LES regime, which for high Mach number flows could therefore occur significantly further downstream of separation than experienced in practise; this behaviour will be discussed in more detail in Chapter 6.

Reynolds stresses in the near wall region are supported by the modelling effort applied there and the Reynolds stresses in the free-stream are supported by the presence of turbulent eddies [54]. However, in the transition region between the two, where these turbulent eddies may not exist, errors can occur in the Reynolds stress calculation. It is therefore important to try and assist the development of

these turbulent eddies in the transition region between the modelled near wall region and LES free-stream domain.

Various methods for accelerating the development of these eddies have been developed [54]. If the flow does not contain massively separated regions which can themselves introduce instabilities that will naturally grow with the solution, some sort of perturbation is required in regions of mild separation in order to encourage eddy development. For hybrid RANS-LES techniques, Keating and Piomelli [63] introduced stochastic forcing in the transition region in order to generate small-scale fluctuations. Turbulent fluctuations applied to the inlet of the solution domain are also possible, with the method of Kempf et al. [64] capable of generating coherent structures on unstructured grids.

Chapter 3

Combustion Modelling

The averaging and filtering processes applied to the system of governing equations generates the reaction rate source term $\overline{\dot{\omega}}$. Unfortunately, the instantaneous reaction rate, $\dot{\omega}$, cannot be employed for this averaged or filtered quantity since

$$\overline{\dot{\omega}(\rho, T, Y)} \neq \dot{\omega}(\bar{\rho}, \widetilde{T}, \widetilde{Y}) \tag{3.1}$$

due to its non-linear nature [25]. Therefore, a model is required in order to handle the turbulence-chemistry interactions and provide $\overline{\dot{\omega}(\rho, T, Y)}$.

3.1 Supersonic Combustion

In order to aid combustion model selection, it is important to try and understand the regime in which supersonic combustion occurs. However, due to the coupling of reactions, turbulence and shock waves, the flow physics in a scramjet combustor is complex and hence not well understood.

Balakrishnan and Williams [65] declared the turbulent Reynolds number, Re_t, and Damköhler number, Da, the most significant parameters for defining the supersonic combustion regime. The turbulent Reynolds number is defined by Equation 2.2 using integral scale properties, which can be calculated from turbulence model variables. The Damköhler number is the ratio of turbulence time scale, T_t, to chemical time scale, τ_c:

$$\mathrm{Da} = \frac{T_t}{\tau_c} \tag{3.2}$$

where the turbulence time scale is defined as the integral scale turnover time, which can be calculated from turbulence model parameters:

$$T_t = \frac{1}{\beta^\star \omega} \tag{3.3}$$

Since the instantaneous reaction rate, $\dot{\omega}_\alpha$, is the production rate of ρY_α, the chemical time scale, τ_c, can be defined as:

$$\tau_c = \frac{\rho}{\dot{\omega}_\alpha} \tag{3.4}$$

where the averaged or filtered quantities, $\bar{\rho}$ and $\overline{\dot{\omega}_\alpha}$, should be used in RANS and LES, respectively.

Two limits on the Damköhler number are $\mathrm{Da} \gg 1$ and $\mathrm{Da} \ll 1$, which correspond to fast and slow chemistry compared to mixing, respectively. Simplifications to reaction rate modelling can be made in both limiting situations, with infinitely fast chemistry applicable for high Damköhler numbers and well stirred reactor modelling used for those much less than unity.

The diagram shown in Figure 3.1 is often used to try and describe the regime in which supersonic combustion occurs. The separate regimes displayed are to be discussed.

A Damköhler number, Da_K, based on the Kolmogorov time scale, τ_K, can also be defined, which is given by:

$$\mathrm{Da}_K = \frac{\tau_K}{\tau_c} \tag{3.5}$$

and using the definition of τ_K given in Equation 2.4 it can be shown that:

$$\mathrm{Da}_K = \frac{T_t \mathrm{Re}_t^{-\frac{1}{2}}}{\tau_c} = \mathrm{Da}\mathrm{Re}_t^{-\frac{1}{2}} \tag{3.6}$$

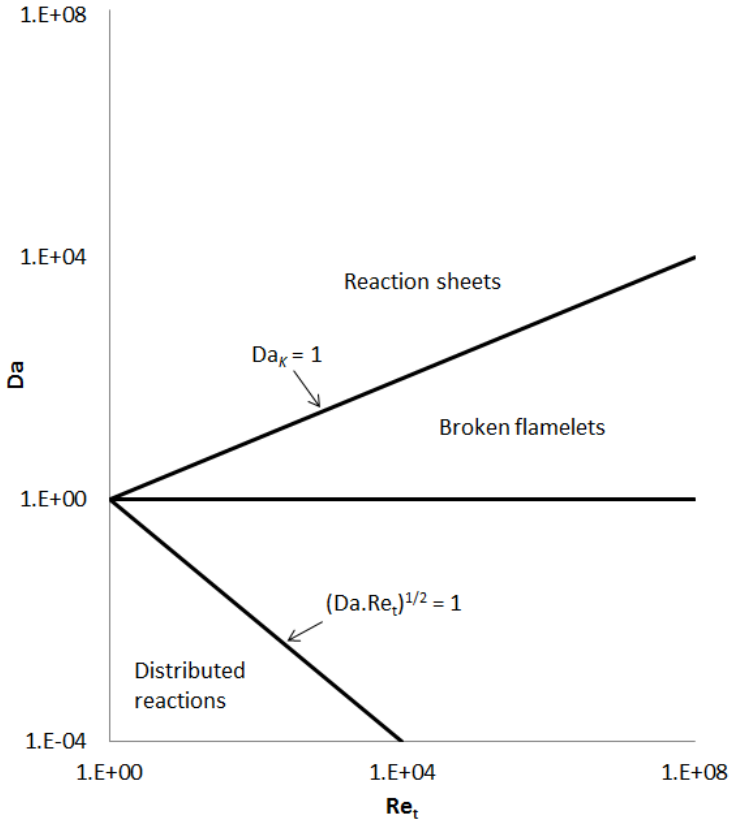

Figure 3.1: Regime diagram: Log-log plot of Damköhler number versus turbulent Reynolds number

Alternative definitions are available for the Kolmogorov length and time scales [22] in terms of the turbulence dissipation rate, ε:

$$\eta_K = \left(\frac{\nu^3}{\varepsilon}\right)^{\frac{1}{4}} \tag{3.7}$$

$$\tau_K = \left(\frac{\nu}{\varepsilon}\right)^{\frac{1}{2}} \tag{3.8}$$

Combining Equations 3.7 and 3.8 gives:

$$\mathrm{Da}_K = \frac{\eta_K^2}{\nu \tau_c} \tag{3.9}$$

and defining the chemical length scale as [66] $l_c = (\nu\tau_c)^{\frac{1}{2}}$, the square root of the Kolmogorov Damköhler number can be shown to be equal to the ratio of Kolmogorov to chemical length scales:

$$\sqrt{\mathrm{Da}_K} = \frac{\eta_K}{l_c} \tag{3.10}$$

Through use of Equation 2.3, the ratio of the integral and chemical length scales can also be shown to be:

$$\frac{L_t}{l_c} = \sqrt{\mathrm{DaRe}_t} \tag{3.11}$$

Lines of unity Damköhler number, Kolmogorov Damköhler number and integral to chemical length scale ratio are shown in Figure 3.1, which define some of the different reaction regimes possible. Above the unity Da_K line, all turbulence length scales are larger than the chemical length scale, resulting in the reaction sheets regime where the turbulent eddies cannot enter and disrupt the reaction zone, but only wrinkle it. The region between the $\mathrm{Da} = 1$ and $\mathrm{Da}_K = 1$ lines can be described as the broken flamelet regime [66], where the reaction sheets may be wrapped around the large eddies used to define Da, but extinguished in the small eddies. Between the $\mathrm{Da} = 1$ and $(\mathrm{DaRe}_t)^{1/2} = 1$ lines the degree to which turbulence structures can enter the reaction zone increases, until the $(\mathrm{DaRe}_t)^{1/2} = 1$ line is reached, beyond which all turbulence length scales are smaller than the chemical length scale, causing distributed reactions to occur.

Figure 3.2 places the supersonic combustion regimes proposed by Balakrishnan and Williams [65] and Ingenito and Bruno [19] on the diagram described. Balakrishnan and Williams analysed the conditions in a possible scramjet engine flight envelope, showing high turbulent Reynolds numbers are most likely with chemical reactions proceeding at a rate faster than the large scale mixing. Ingenito and Bruno extracted data from a large eddy simulation of the SCHOLAR scramjet test case using 1-step chemistry. The possibility of lower turbulent Reynolds and Damköhler numbers than predicted by Balakrishnan and Williams is suggested, indicating finite reaction rates may be important in the supersonic combustion regime.

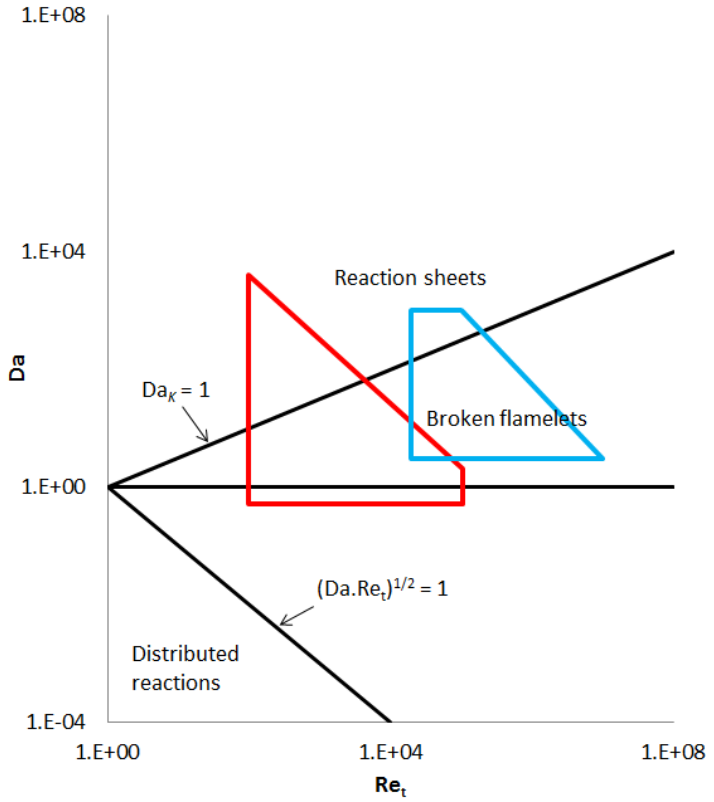

Figure 3.2: Supersonic combustion regimes proposed by Balakrishnan and Williams (light blue) and Ingenito and Bruno (red)

Flight Mach number and geometrical configuration would influence the regimes proposed; Balakrishnan and Williams investigated flight Mach numbers up to 25 and the conditions in the SCHOLAR scramjet test case corresponding to a flight Mach number of 7. The Mach number would influence the levels of stagnation enthalpy and hence reaction rates, along with combustor residence times and turbulent Reynolds numbers. Engine geometry and method of fuel injection would also influence mixing, leading to changes in the Damköhler number through alteration of the corresponding turbulence time scales and reaction rates.

Both studies suggest the broken flamelets regime is the most likely, but the wide range of Damköhler numbers proposed by Ingenito and Bruno, coupled with the additional influence of compressibility effects, makes this conclusion uncertain. Berglund et al. have applied LES to two different strut injector scramjet test

cases, for which it was concluded from experimental data that combustion occurs in the flamelet regime for one [67] and with distributed reactions well outside the flamelet regime in another [68], suggesting test case geometry and boundary conditions can play a significant role in the regime achieved.

Through analysis of high Mach number compressibility effects on the rate of reaction, Ingenito and Bruno suggest a modification to the position of the $\mathrm{Da}_K = 1$ and $(\mathrm{DaRe}_t)^{1/2} = 1$ lines on the regime diagram, shifting them both upwards to higher Damköhler numbers. However, this appears somewhat contradictory to the compressibility effects on turbulence that are discussed in Section 2.1. If the smallest scales in supersonic combustion are indeed larger than those defined by the Kolmogorov length scale, the reaction sheet regime would be applicable at lower Damköhler numbers than implied in Figure 3.1, since just below the $\mathrm{Da}_K = 1$ line there would be no small scales to enter and disrupt the reaction zone.

Effects such as compressibility and the need to model finite rate reactions due to low residence times, even if the Damköhler numbers do not support such requirements, significantly complicate the physics involved in supersonic combustion. Modelling of such physics may not be as straightforward as the extension of knowledge and models from the subsonic regime and a deeper understanding of the interactions involved is required.

3.2 Laminar Chemistry

Finite rate reactions can be simulated through the use of multi-step chemical systems of the form:

$$\sum_{\alpha=1}^{N_s} \nu'_{\alpha r} M_\alpha \Leftrightarrow \sum_{\alpha=1}^{N_s} \nu''_{\alpha r} M_\alpha, \quad r = 1, \ldots, N_r \tag{3.12}$$

where N_r and N_s are the number of reactions and species in the chemical mechanism, respectively. M_α is the chemical symbol for species α with $\nu'_{\alpha r}$ and $\nu''_{\alpha r}$ being the molar reactant and product stoichiometric coefficients for species α in reaction r, respectively. The $\Leftrightarrow$ symbol implies a reversible reaction.

Using such chemical reactions, the instantaneous reaction rate for species α,

$\dot{\omega}$, which appears as a source term in the instantaneous species transport equation (2.14), can be defined as:

$$\dot{\omega}_\alpha = W_\alpha \sum_{r=1}^{N_r} \left[\left(\nu''_{\alpha r} - \nu'_{\alpha r} \right) \left(k_{fr} \prod_{\beta=1}^{N_s} c_\beta^{\nu'_{\beta r}} - k_{br} \prod_{\beta=1}^{N_s} c_\beta^{\nu''_{\beta r}} \right) \right] \tag{3.13}$$

where W_α is the molecular weight of species α and c_β is the species concentration, given by:

$$c_\beta = \frac{\rho Y_\beta}{W_\beta}. \tag{3.14}$$

k_{fr} and k_{br} are the forward and backward reaction rate constants for reaction r, respectively, for which an Arrhenius expression is used:

$$k_{fr} = A_r T^{n_r} \exp\left(-\frac{E_r}{R^0 T} \right) \tag{3.15}$$

where A_r is the pre-exponential factor and E_r is the activation energy, for reaction r. It is the exponential term in this equation which causes the significant non-linearity of the system, which makes turbulent reacting flows so difficult to model [22].

It should be noted that the process of radical recombination generates sufficient energy to cause the reaction product to decompose back into the original radical species [69]. The addition of a third body, M, to such reactions is therefore required in order to absorb the excess energy, giving:

$$\sum_{\alpha=1}^{N_s} \nu'_{\alpha r} M_\alpha + M \Leftrightarrow \sum_{\alpha=1}^{N_s} \nu''_{\alpha r} M_\alpha + M, \quad r = 1, \ldots, N_r \tag{3.16}$$

which leads to a modified reaction rate equation given by:

$$\dot{\omega}_\alpha = W_\alpha \sum_{r=1}^{N_r} \left[\left(\nu''_{\alpha r} - \nu'_{\alpha r} \right) \left(k_{fr} c_M \prod_{\beta=1}^{N_s} c_\beta^{\nu'_{\beta r}} - k_{br} c_M \prod_{\beta=1}^{N_s} c_\beta^{\nu''_{\beta r}} \right) \right] \tag{3.17}$$

with the third body concentration, c_M, defined as:

$$c_M = \sum_{\beta=1}^{N_s} \eta_{\beta,M} c_\beta \tag{3.18}$$

where $\eta_{\beta,M}$ is the third body efficiency of species β for third body M. The modified equation for the instantaneous reaction rate can be universally used, with c_M set to unity for steps not involving a third body reaction.

It is this instantaneous reaction rate, $\dot{\omega}_\alpha$, which will be referred to as laminar chemistry. The instantaneous reaction rate can directly be employed in DNS for calculation of the reaction rate term in the species transport equation, since the influence of all turbulence structures on the flame is directly captured. Unfortunately the picture is significantly more complex for the mean and filtered systems of equations, where a model is required in order to handle the turbulence-chemistry interactions and calculate $\overline{\dot{\omega}(\rho, T, Y)}$.

3.3 Turbulence-Chemistry Interaction Modelling

Since the physics involved in supersonic combustion is still not well understood the current trend for reaction rate modelling is to attempt the extension of methods designed for subsonic combustion to the supersonic combustion regime. Although the regime diagram of Figure 3.2 implies the flamelet regime is most likely, as discussed in Section 3.1 further regimes may also be applicable.

Central to many combustion models is the use of the probability density function (PDF) to find mean variables from the instantaneous values:

$$\overline{\phi} = \int \phi P(\hat{\phi}) \mathrm{d}\hat{\phi} \tag{3.19}$$

where $P(\hat{\phi})$ is the PDF for the variable ϕ and the integration is carried out over the sample space variable $\hat{\phi}$. A PDF is defined so that the probability that $\hat{\phi} < \phi < \hat{\phi} + \mathrm{d}\hat{\phi}$ is $P(\hat{\phi})\mathrm{d}\hat{\phi}$ [22].

3.3.1 Flamelet Model

The flamelet model has been applied [8; 67; 70] to the simulation of supersonic combustion because of the assumptions made on reactions occurring in the flamelet regime. The flamelet approach simplifies combustion modelling through use of geometrical concepts; assuming the flame is thin compared to other scales of the flow.

Supersonic combustion in a scramjet engine is non-premixed in nature, due to the injection of pure fuel directly into the combustion chamber. The mixture fraction Z is introduced for the flamelet model, which is a conserved scalar taking the value of 0 in regions of pure oxidiser and 1 in regions of pure fuel. Because it is a conserved scalar, the mixture fraction denotes the mass fraction of fluid originating in the fuel stream of the flow [22], at any point in the domain. The flame is assumed to take the shape of the iso-contour of the stoichiometric value for the mixture fraction, Z_{st}.

Instantaneous mass fractions, temperatures and densities are set as functions of the mixture fraction. Their mean values can therefore be calculated using the PDF method in Equation 3.19, where the mixture fraction is set as the sample space variable:

$$\overline{\phi} = \int \phi(Z) P(\hat{Z}) \mathrm{d}\hat{Z} \tag{3.20}$$

In order to take finite rate chemistry effects into account, Zheng and Bray [70] introduced a strain rate parameter, whilst the scalar dissipation rate has also been used [67]. The instantaneous properties can then be set as functions of both the mixture fraction and rate parameter variables, with flamelet libraries correspondingly defined. The mean variables can now be calculated from:

$$\overline{\phi} = \int \phi(Z, \chi) P(\hat{Z}, \hat{\chi}) \mathrm{d}\hat{Z} \mathrm{d}\hat{\chi} \tag{3.21}$$

where χ is the rate parameter in question. However, in order to carry out the integration, statistical independence between the two variables of the joint PDF is assumed:

$$P(Z,\chi) = P(Z)P(\chi) \tag{3.22}$$

where the shape of each PDF is presumed.

Zheng and Bray confirmed the importance of finite rate effects in supersonic combustion through comparison of the joint PDF method with that in Equation 3.20. It was concluded that the combustor residence times are so low due to the high velocities present that the reactions may fail to reach completion [70]. It was also shown that the Kolmogorov based Damköhler number was below unity throughout the reaction zone for the test case simulated. Recalling the regime diagram in Figure 3.1, this suggests assumptions of flamelet type behaviour for the Evans et al. [71] test case are reasonable.

So, in summary; the flamelet model employs transport equations for non-reacting scalars and uses the PDF method to obtain the mean variables of the flow rather than directly attempting to evaluate the mean reaction rate in the transport equation of a reactive scalar. Assumptions are made on the structure of the flame using a geometrical approach, assuming that it is thin. However, since other regimes are possible in supersonic reacting flows the flamelet model may be limited in its applicability.

3.3.2 Probability Density Function Approach

Rather than employing the PDF method to evaluate the mean properties of the flow through use of the mixture fraction and flamelet libraries, the PDF method can be used to directly evaluate the mean reaction rate, using a joint PDF of temperature and composition:

$$\bar{\dot{\omega}} = \int \dot{\omega}\left(\hat{T}, \hat{c}_1, \ldots, \hat{c}_{N_s}\right) P\left(\hat{T}, \hat{c}_1, \ldots, \hat{c}_{N_s}\right) \mathrm{d}\hat{T}\mathrm{d}\hat{c}_1, \ldots, \mathrm{d}\hat{c}_{N_s} \tag{3.23}$$

This approach does not make use of the mixture fraction variable and makes no assumptions on the regime in which combustion occurs. Two methods exist to evaluate the joint PDF, either by evaluation through the solution of a PDF transport equation or by making assumptions on the PDF shape.

3.3.2.1 Transported PDF

An evolution equation for the joint PDF of thermochemical scalars, such as the species mass fraction and enthalpy of the flow, can be derived. This equation has the significant advantage of including the species reaction rate in closed form [72]. Modelling for this term is therefore no longer required and the instantaneous reaction rate in Equation 3.17 can be used. However, an unclosed term for mixing does arise, for which a model is required. Due to the high dimensionality of a transport equation for the joint PDF of multiple scalars, the use of finite difference methods for its solution is very expensive [73]. Lagrangian particle methods however scale linearly with the dimensionality of the PDF [73] and Pope first introduced [74] a Monte Carlo method for the efficient solution of the PDF transport equations.

Since the PDF can be used to contain statistical information for any flow variable, transport equations for the joint PDF of velocity can also be derived. In a similar fashion to the reaction rate calculations, this equation circumvents the gradient-diffusion assumption for turbulence transport modelling [73], since these transport processes appear closed in the PDF evolution equation.

Möbus et al. [75] employed a Monte Carlo method for the solution of a transport equation for the joint PDF of velocity, enthalpy and species mass fraction, for the simulation of a high speed reacting flow. Results were compared to a similar method employing a joint PDF of just enthalpy and species mass fraction, using standard turbulence modelling to obtain the required Reynolds stresses. Good agreement with experimental data was obtained, with the joint PDF including velocity providing the best results. However, the computational cost is very high when compared to conventional finite volume approaches, particularly when the dimensionality of the PDF is increased further through inclusion of the velocity variables. Although the Lagrangian particle method provides an efficient approach for the solution of the PDF evolution equation, on the order of 100 particles are required per computational cell [75] in order to obtain the required statistics. Therefore, for practical problems of interest where computational meshes containing millions of cells are required, the transported PDF method can be prohibitively expensive despite the significant advantage of the

reaction rate appearing in closed form. This cost is exacerbated in LES, due to the high mesh resolution requirements.

3.3.2.2 Assumed PDF

In an attempt to reduce the high computational costs of the transported PDF method, which allows the PDF to evolve in time and space, the shape of the PDF can be assumed. However, it is difficult to form a mathematical definition for the joint PDF of temperature and composition so statistical independence is presumed between the temperature, species mass fraction and density:

$$P\left(\hat{\rho}, \hat{T}, \hat{Y}_1, \ldots, \hat{Y}_{N_s}\right) = P_T(\hat{T}) P_Y(\hat{Y}_1, \ldots, \hat{Y}_{N_s}) \delta(\hat{\rho} - \bar{\rho}) \tag{3.24}$$

The assumed PDF combustion model is the most widely applied for the simulation of supersonic combustion [76; 77; 78], where a clipped Gaussian profile is employed for the temperature PDF and the multivariate β-PDF of Girimaji [79; 80] is used for species mass fractions. To define each of these assumed PDFs, both the mean variables (temperature and species mass fractions) and a higher order moment are required. The higher order moments are obtained through the introduction of two transport equations [77] for the temperature variance, σ_T, and sum of species mass fraction variances, σ_Y:

$$\begin{aligned} \frac{\partial \bar{\rho}\sigma_T}{\partial t} + \frac{\partial \bar{\rho}\tilde{u}_j\sigma_T}{\partial x_j} &= \frac{\partial}{\partial x_j}\left[\left(\gamma\frac{\mu}{Pr} + \frac{\mu_t}{Pr_t}\right)\frac{\partial \sigma_T}{\partial x_j}\right] + 2\frac{\mu_t}{Pr_t}\left(\frac{\partial \tilde{T}}{\partial x_j}\right)^2 \\ &- C_T\gamma\bar{\rho}\sigma_T\omega_f - 2(\gamma-1)\bar{\rho}\sigma_T\frac{\partial \tilde{u}_j}{\partial x_j} + \frac{1}{c_v}2T'\sum_{\alpha=1}^{N_k}\dot{\omega}_\alpha h_{f\alpha} \end{aligned} \tag{3.25}$$

$$\begin{aligned} \frac{\partial \bar{\rho}\sigma_Y}{\partial t} + \frac{\partial \bar{\rho}\tilde{u}_j\sigma_Y}{\partial x_j} &= \frac{\partial}{\partial x_j}\left[(D + D_t)\frac{\partial \sigma_Y}{\partial x_j}\right] + 2\sum_{\alpha=1}^{N_k}\bar{\rho}D_t\frac{\partial \tilde{Y}_\alpha}{\partial x_j}\frac{\partial \tilde{Y}_\alpha}{\partial x_j} \\ &- C_Y\bar{\rho}\sigma_Y\omega_f + 2\sum_{\alpha=1}^{N_k}\overline{\dot{\omega}_\alpha Y'_\alpha} \end{aligned} \tag{3.26}$$

where,

$$\sigma_T = \widetilde{T''^2}, \quad \sigma_Y = \sum_{\alpha=1}^{N_s} \widetilde{Y''^2} \tag{3.27}$$

ω_f is the fluid mechanics timescale and the model constants C_T and C_Y are set to 2.0, as in [77]. It is the occurrence of the fluid mechanics timescale which requires the use of a two equation turbulence model, which is capable of defining such flow properties through use of:

$$\omega_f = \frac{1}{\beta^\star \omega} \tag{3.28}$$

The source terms at the end of each variance transport equation, which contain the species reaction rate variables, could also be modelled using an assumed PDF approach. However, highly erroneous results are obtained if this is done [77] and so they are usually neglected.

The multivariate β-PDF of Girimaji is used to reduce the computational cost, since it combines all the mass fraction variances into a single variable, σ_Y. If a PDF was defined for every single species, an additional transport equation would be required for the variance of each mass fraction, leading to a large computational cost when complex chemical mechanisms are employed.

Baurle and Girimaji [78] attempted to model temperature-composition correlations which are neglected through the assumption of statistical independence in Equation 3.24, but little improvement over the method presented here was obtained.

The assumed PDF approach is also used in the flamelet model, as described in Section 3.3.1, but rather than applying it to calculate the mean reaction rate the mean species mass fractions are obtained from the mixture fraction variable. The assumption of a certain shape for the mixture fraction PDF is somewhat robust, since the mixture fraction is a non-reacting transported scalar. A large body of knowledge is available for such fluid processes, showing the assumption of such PDFs to be reasonable [22]. However, the application of assumed PDFs to reacting scalars is less robust and particularly in supersonic combustion there is no evidence known to the author of such PDFs arising in practice.

However, the assumed PDF approach for calculating the mean reaction rate is still widely applied in supersonic combustion research due to its increased computational efficiency over the transported PDF method and lack of assumptions on flame structure and reaction rates. This model is even applicable to both premixed and non-premixed combustion [81]. It has been shown [77] that accurate results can be obtained for both the mean quantities of the flow and the rms values calculated from the variance transport equations, for a supersonic reacting coaxial hydrogen jet [82].

3.3.3 Other Models

Other models which have been applied to the simulation of supersonic combustion to handle the turbulence-chemistry interactions are the linear eddy mixing (LEM) model [83] and the partially stirred reactor (PaSR) model [68], which have both been employed under an LES framework. Neither makes assumptions on the shape of the reaction zone, as is done in the flamelet model, but the PaSR model does assume that Kolmogorov length scales are present in order to model the subgrid mixing.

In the LEM model an unfiltered species transport equation is solved on a fine one-dimensional sub-mesh grid. Due to the one-dimensionality, subgrid stirring is simulated through a stochastic procedure called triplet mapping. The big advantage of the LEM model for reacting flows is that the species reaction rate appears in closed form in the one-dimensional equation to be solved. The LEM model has been applied to the simulation of supersonic mixing by Sankaran and Menon [84] and Génin and Menon [85] and to reacting flow by Génin et al. [86] and Ghodke et al. [83], with success. However, since the resolution of the sub-mesh grid must be fine enough to directly capture all scales of the flow (as in DNS), this approach is very computationally expensive. Methods to reduce the computational cost of such simulations are being attempted [83].

3.4 Combustion Model Influence

Since supersonic combustion is not well understood, the role of turbulence-chemistry interactions under such conditions is unknown. In order to investigate such physics, the laminar chemistry approach can be used to neglect any interactions not captured by the computational mesh and results compared to those from a combustion model designed to provide for such interactions.

This has been done by Gerlinger et al. [76] for the simulation of a supersonic laboratory hydrogen jet flame, through comparison of the laminar chemistry approach to the assumed PDF combustion model. It was found that very comparable results are achieved from both approaches, suggesting that the influence of turbulence-chemistry interactions is minimal.

Möbus et al. [75] compared a finite volume laminar chemistry simulation to the results from two transported PDF calculations, for two supersonic hydrogen jet flames. Again, it was found that only small differences in the results were obtained, in particular for the radial profiles of pressure and species mass fraction. Although some improvements were gained through the use of a joint PDF of velocity, enthalpy and composition, minimal improvements over laminar chemistry were obtained when employing a standard turbulence model in combination with a joint PDF of only enthalpy and composition, suggesting the method chosen for turbulence modelling may have a more significant influence over the results obtained than the approach employed to handle the turbulence-chemistry interactions. Results from all three simulations were however in reasonable agreement with the experimental data, again suggesting the influence of turbulence-chemistry interactions is minimal.

The influence of these interactions in a realistic scramjet combustor geometry was investigated by Keistler et al. [87], where results from laminar chemistry and a variable Prandtl and Schmidt number combustion model were compared. It was concluded that turbulence-chemistry interactions play an important role in supersonic combustion, however the results from the combustion model employed are in far worse agreement with experimental data than those from laminar chemistry, for which a reasonable comparison is obtained. Further work on the importance of these interactions in realistic geometries is required.

Due to the finite volume laminar chemistry simulations somewhat surprisingly providing results in good agreement with experimental data, the modelling of turbulence chemistry interactions is often neglected [88; 89; 90].

3.5 Chemical Kinetics

Since finite rate effects play an important role in supersonic combustion, either from the short residence times of reactants within the combustor or the possibility of low Damköhler numbers, it is important to evaluate the influence of chemical kinetics on computational results. The computational cost introduced through the use of complex mechanisms with a large number of species and reaction steps must also be taken into account when a selection of the chemical kinetics model is to be made.

The most widely used mechanisms for the simulation of supersonic hydrogen combustion are those of Jachimowski, with two mechanisms consisting of 9 species and 19 reactions from 1988 [91; 92] and 1992 [93] and a reduced mechanism [94] of just 7 species and 7 reactions, commonly employed. The complex mechanism of O'Conaire et al. [95], which consists of 9 species and 21 reactions, is perhaps considered the most comprehensive description of hydrogen chemical kinetics due to its wide range of validation and inclusion of pressure effects through the use of Troe parameters. More computationally efficient descriptions of the chemistry are also available, with the 4 species single-step mechanism of Marinov et al. [96] and the 5 species 2-step mechanism of Rogers and Chinitz [97]. It should be noted that the number of species listed for each mechanism includes N_2, for which reactions are not included.

Gerlinger et al. [98] conducted a comprehensive comparison of the prediction capabilities for all mechanisms discussed above, apart from the 2-step model. A supersonic lifted flame was simulated with the ignition delays calculated for each mechanism and radial profiles of the temperature and mass fraction statistics evaluated. It was concluded that, due to the neglect of radical species, both the temperatures and ignition delay times predicted by the 1-step mechanism are in poor agreement with experimental data and hence it should not be used. It was found that as long as conditions are not close to the ignition limit then the

reduced Jachimowski mechanism is in good agreement with both the 1988 and 1992 full Jachimowski mechanisms, which are both in turn in good agreement with the more comprehensive mechanism of O'Conaire. This suggests that significant savings in computational cost can be made by using the reduced mechanism. It should be noted that results were sensitive to the concentration of radical species at the inflow to the domain, so studies should be conducted to evaluate this whenever employing detailed chemistry.

Berglund et al. [68] compared results from 1-step, 2-step and 7-step chemical mechanisms for the large eddy simulation of strut injection into a realistic scramjet combustor geometry. The combustion for this test case was experimentally evaluated to be in the low Damköhler number distributed reactions regime. It was found that the induction time (defined as the time taken for the temperature to increase 100K from the initial state) for the 1-step mechanism is much shorter than the turbulence time scales, resulting in a corrugated flame which tends not to interact with the turbulence scales of the flow, corresponding to high Damköhler number combustion. The poor agreement of the 1-step mechanism corresponds to the short ignition delay times found by Gerlinger et al., as discussed above. However, for the 2-step and 7-step mechanisms the induction times were found to be of the same order of magnitude as the time scales of the flow, leading to a flame that can be wrinkled by the vortical structures present. It is also noted that the behaviour of the more complex mechanisms are in much better agreement with a 19-step chemical kinetics model, with respect to the induction times calculated. When studying computational results for the distribution of the OH radical and wall pressure distributions Berglund et al. found the 1-step mechanism (OH distribution was calculated using chemical equilibrium) to again be in poor agreement with experimental data, whilst the 7-step mechanism provided the best agreement. The 2-step mechanism provided results in reasonable qualitative and quantitative agreement.

The choice of chemical mechanism can obviously have a significant impact on the reaction rate calculations and hence it is important to study such influences to ensure accurate computational results are obtained.

3.6 Experimental Studies

Detailed experimental studies of supersonic combustion are limited, due to both the difficulties and costs involved in carrying out such research. The high stagnation enthalpy conditions experienced in hypersonic flight are difficult to replicate in ground based facilities and run times can be limited. Although limited in detail and number, since supersonic combustion research is an active field in countries such as the US, Australia, Japan, Germany and France, to name a few, a range of experimental studies have been conducted. A basic overview is given here of the most widely used sets of experimental data, but this review is by no means exhaustive.

The supersonic reacting hydrogen coaxial jet of Evans et al. [71] has been used by Zheng and Bray [70] and Gerlinger et al. [75; 76] for computational studies into supersonic reacting flows. Radial profiles of mean pitot pressure and species mass fractions (H_2O, H_2, O_2 and N_2) are available at several locations down the axis of the jet. This is a simple test case which can provide useful validation for computational techniques, but unknowns about it's geometrical configuration and setup provide a degree of uncertainty.

More detailed experimental data is available for the supersonic reacting hydrogen coaxial jet of Cheng et al. [82], which has been used by a number of authors for the validation of computational methods [75; 76; 77; 78]. Simultaneous measurements of the major species (H_2O, H_2, O_2 and N_2), OH radical concentrations and temperature were made, providing both mean and variance data. An experiment conducted on the same burner by Dancey [99] provides measurements for the mean and fluctuating velocities in two directions. Unfortunately, geometrical information for the burner is limited to sketches in the relevant papers, introducing significant uncertainties into computational studies when the whole burner is to be simulated. There is also limited information about the radical concentrations in the jet co-flow, which Gerlinger et al. [98] found to be a significant uncertainty in the computational setup.

A supersonic jet test case for which both geometrical data and detailed measurements are available is that by Cutler et al. [100]. However, this is a non-reacting coaxial jet, using helium as the test gas to simulate the supersonic com-

pressible shear layer mixing experienced in a scramjet combustor fuelled by hydrogen. Probes are used to measure the radial profiles of total temperature, pitot pressure and composition at several locations down the axis of the jet. RELIEF velocimetry is used to measure mean and fluctuating axial velocity profiles and schlieren visualisation is employed. Detailed co-ordinates for the contours which make up the central jet and co-flow surfaces are available.

Another non-reacting test case is that of wall injection into a supersonic cross-flow, where the injected fluid is air. Both normal and oblique injection experiments have been conducted, with the most widely used being the wall normal test case, with velocity measurements available from Santiago et al. [101] and scalar mixing data from [102]. Such test cases can be employed to study the physics of injection into a scramjet combustor and to analyse the capabilities of numerical methods for their simulation. Reacting experiments of wall normal injection are also available, such as that by Ben-Yakar et al. [103], for which OH-PLIF measurements are available.

As well as supersonic coaxial jet and wall injection experiments, measurements of the reacting flow within realistic scramjet combustor geometries are also available. The SCHOLAR test case is perhaps the most widely used, with data available for both normal wall injection [104] and angled injection at 30 degrees to the horizontal [105]. A dual-pump CARS technique is employed to simultaneously measure composition and temperature, with static pressure measurements made on all four walls of the combustor. However, not enough data is collected using the CARS technique for reliable mean values to be evaluated, so profiles are obtained using best-fit techniques. Also, no information on the concentration of radical species entering the combustor is provided.

There is a distinct need for detailed measurements of a supersonic combustion experiment, providing reliable profiles of the mean and fluctuating values of composition, temperature and velocity components, along with geometry, in order to evaluate the ability of turbulence and combustion models to capture the physics involved. However, it is difficult to make such measurements in a scramjet combustor due to its wall bounded nature. Laboratory jet flames such as the Evans et al. and Cheng et al. experiments are attractive for their simplicity, aiding both the experimental data collection and affordability for numerical

simulations. Cutler et al. [106] are working on such an experiment, using the dual-pump CARS technique to obtain the required temperature and composition statistical data. An interferometric Rayleigh scattering technique is being built into the dual-pump CARS method [107], for simultaneous measurements of velocity. However, results are not currently available for this test case.

It should be noted that measurements of turbulence length and velocity scales were not made in any of the experiments discussed. The importance of such data is to be demonstrated throughout this thesis.

Chapter 4

Numerical Methods and Implementation

4.1 Introduction to PULSAR

In order to carry out computational research into supersonic combustion a parallel code capable of simulating high speed flows and finite rate complex chemistry combustion is required. It is possible various commercial codes could provide these capabilities, but the lack of detailed information on model implementation and the ability for model development is prohibitive. When conducting LES studies, a significant number of commercial licenses would be required for large parallel computations and hence the use of such software is not practical from the point of view of cost.

Various in-house codes were in existence at the start of this research but none were suitable for the application in question. A parallel code (pNEWT) for non-reacting turbo-machinery simulations and a serial code (McUNNEWT) for premixed combustion research were the prominent tools in the CFD Lab at the time.

Therefore, development of a new in-house code was required for the simulation of supersonic combustion. This code has been named PULSAR (Parallel Unstructured Large-eddy Simulation And Reactions). The starting point for PULSAR was the pNEWT in-house code developed by Professor Bill Dawes. Significant

modifications were made to every element of the solver, the development of which is the topic of discussion for this chapter.

4.2 Finite Volume Method

In CFD, the governing equations of fluid flow are solved over the domain in question using a distribution of control volumes known as a mesh. The governing equations presented in Chapter 2 can be solved in an iterative manner on this computational mesh through use of the finite volume method. The equations can be described using a partial differential equation of the form:

$$\frac{\partial \rho\phi}{\partial t} + \frac{\partial \rho u_j \phi}{\partial x_j} = \frac{\partial}{\partial x_j}\left(\Gamma \frac{\partial \phi}{\partial x_j}\right) + S_\phi \tag{4.1}$$

where ϕ becomes 1, u_i, h_0 and Y_α for the continuity, momentum, energy and species transport equations, respectively. In order as displayed, the four terms in the equation 4.1 are the transient term, convective term, diffusive term and source term, where Γ corresponds to a diffusion coefficient. The starting point for the finite volume method is the integral form of this equation:

$$\int_{CV} \frac{\partial \rho\phi}{\partial t} \mathrm{d}V + \int_{CV} \frac{\partial \rho u_j \phi}{\partial x_j} \mathrm{d}V = \int_{CV} \frac{\partial}{\partial x_j}\left(\Gamma \frac{\partial \phi}{\partial x_j}\right) \mathrm{d}V + \int_{CV} S_\phi \mathrm{d}V \tag{4.2}$$

where the integration is carried out over each control volume (CV). Through the application of Gauss's divergence theorem:

$$\int_{CV} \frac{\partial \beta_j}{\partial x_j} \mathrm{d}V = \oint (\vec{n}.\vec{\beta}) \mathrm{d}A \tag{4.3}$$

volume integrals can be re-cast as integrals over the surface of the control volume, where $\vec{n}$ is the outward pointing unit normal vector to a cell face of area A, giving:

$$\frac{\partial}{\partial t}\int_{CV} \rho\phi \mathrm{d}V + \oint \vec{n}.(\rho\vec{u}\phi) \mathrm{d}A = \oint \vec{n}.\left(\Gamma \frac{\partial \phi}{\partial x_j}\right) \mathrm{d}A + \int_{CV} S_\phi \mathrm{d}V \tag{4.4}$$

Assuming infinitesimal values for the time step, cell volumes and face areas,

this can be written as the flux sum over all cell faces to define the change in conserved variable over the corresponding time step:

$$\Delta(\rho\phi)_{CV} = \frac{\Delta t}{\Delta V_{CV}} \left(\sum_{f=1}^{nfaces} \vec{n}_f . \left(\Gamma \nabla \phi\right)_f \Delta A_f + (S_\phi \Delta V)_{CV} - \sum_{f=1}^{nfaces} \vec{n}_f . (\rho \vec{u} \phi)_f \Delta A_f \right) \tag{4.5}$$

and an iterative method can then be used to solve for the conserved variables over multiple time steps, n:

$$\phi_{n+1} = \frac{(\rho\phi)_n + \Delta(\rho_n \phi_n)}{\rho_{n+1}} \tag{4.6}$$

where $\Delta(\rho_n \phi_n)$ is the change in $\rho\phi$ calculated using data from time step n.

Geometric data for the normal unit vectors and areas for the faces of each cell in the computational mesh are therefore required. For clarity later, the inviscid and viscous fluxes through face f are respectively defined as:

$$\vec{n}_f . (\rho \phi \vec{u})_f \Delta A_f \tag{4.7}$$

$$\vec{n}_f . \left(\Gamma \nabla \phi\right)_f \Delta A_f \tag{4.8}$$

where f corresponds to a quantity at the centre of a cell face. Calculation of the $(\rho\phi\vec{u})_f$ and $(\Gamma\nabla\phi)_f$ face quantities is the job of the specific discretisation scheme employed. Determination of the $\frac{\partial p}{\partial x_i}$ source term in the momentum equation can be absorbed into the inviscid flux calculation.

4.3 Data Structure

When the computational domain is divided into finite volumes (cells) there is the choice to store the conserved variables at either the vertices of the cell or the cell centre (see Figure 4.1), leading to the cell-vertex and cell-centred data structures,

respectively. The implementation of numerical methods differs between each approach and their respective advantages and disadvantages are often debated. A comprehensive comparison of the two techniques was recently presented in [108; 109].

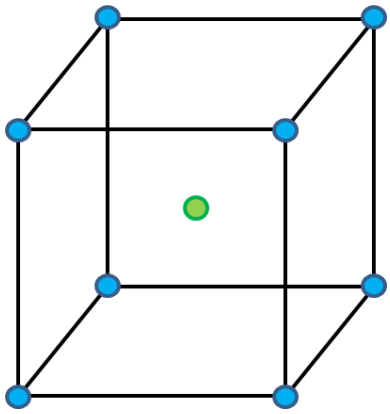

Figure 4.1: Data storage locations. Cell-vertex (blue) and cell-centre (green).

PULSAR employs a cell-centred data structure but pNEWT uses cell-vertex storage for the conserved variables and hence significant modifications were made to the data structure to convert PULSAR to the cell-centred equivalent.

When a computational domain is meshed into finite volumes, the cell size is dependent upon the length scales of the flow physics to be captured and most mesh generators used today provide a choice for cell topology. For a given length scale, it is much more efficient to discretise a domain using hexahedral cells from the point of view of cell count, with savings of the order of four times made compared to their tetrahedral counterparts. However, the vertex count is comparable when using both hexahedral and tetrahedral cell topologies. Therefore, when moving from a cell-vertex to a cell-centred data structure it is very important from the point of efficiency to ensure the code is capable of handling meshes containing hexahedral elements. pNEWT operates on solely tetrahedral meshes and so significant effort was put into ensuring PULSAR could operate on mixed grids, containing any mix of tetrahedral, hexahedral, prismatic and pyramidal cell topologies.

The commercial package ANSYS ICEM CFD is used for mesh generation,

and although PULSAR does have mixed grid capabilities all meshes used for test cases presented throughout this thesis are purely hexahedral.

The data structure modification was further complicated by the parallel capabilities of the code, which are further discussed in Section 4.11.

4.4 Inviscid Fluxes

The inviscid terms in the governing equations are those describing convection:

$$\frac{\partial \rho u_j}{\partial x_j} \quad \frac{\partial \rho u_i u_j}{\partial x_j} \quad \frac{\partial \rho u_j h_0}{\partial x_j} \quad \frac{\partial \rho u_j Y_\alpha}{\partial x_j} \tag{4.9}$$

As discussed in Section 4.2, through application of Gauss's divergence theorem to the integral form of these terms there is the need to calculate face fluxes containing face values $(\rho\phi\vec{u})_f$, where the following will be assumed:

$$(\rho\phi\vec{u})_f = (\rho\phi)_f \vec{u}_f \tag{4.10}$$

and $\vec{n}_f.\Delta A_f$ can be defined as an area vector $\vec{A}_f$ which splits the face area into area projections in the three component directions $(A_{x,f}, A_{y,f}, A_{z,f})$. The $(\rho\vec{u})_f \cdot \vec{A}_f$ term which is common to all convective flux terms can be defined as the face mass flux, $\dot{m}_f$:

$$(\rho\vec{u})_f.\vec{A}_f = \dot{m}_f \tag{4.11}$$

There are many discretisation methods available to calculate the face data required, with each method having its own numerical properties. It is therefore important to understand the physics involved in the problem to be simulated in order to select a discretisation method which provides the numerical properties desired.

4.4.1 Desirable Properties

The simulation of supersonic combustion is computationally challenging due to the presence of discontinuities provided by shock waves, flame fronts and species

transport. These flow phenomena result in high gradient regions and a computational method is required which can accurately predict this in a stable fashion.

4.4.1.1 Monotonicity

The most desirable property of a numerical scheme to be used for the calculation of the inviscid fluxes is that of monotonicity. As will be shown, certain discretisation techniques can cause spurious oscillations in the presence of discontinuities. These spurious oscillations can pollute the solution and cause numerical instabilities. Oscillations in temperature can also cause non-physical ignition to occur. A numerical scheme is required which can accurately capture high gradient regions in a monotone (smooth) fashion.

The total variation diminishing (TVD) criterion [33] is often applied to the development of numerical methods in order to obtain a monotonic solution. However, this can often be an over-restrictive requirement, proving detrimental to the numerical accuracy.

4.4.1.2 High Order of Accuracy

High order accurate methods are desirable in order to obtain sharp resolution of the flow physics encountered. Low dissipation methods are also extremely important when employing the LES technique. Since the large turbulent structures are directly captured, low levels of numerical dissipation are required to prevent these structures from being prematurely destroyed.

However, since unstructured computational meshes are employed the use of extended stencils to achieve higher order of accuracy is not possible. Unstructured meshes are used in order to handle complex geometries with an industrial focus, for which computational cost is of primary concern. Therefore, no attempt has been made to increase the accuracy of computational methods in PULSAR above second order.

4.4.2 Discretisation Techniques

The performance of an upwind scheme for the simulation of discontinuous flows will be investigated and compared to the centred discretisation approach. Test

cases are chosen which replicate a discontinuous flow field, which are characteristic of the physics encountered in a scramjet combustor.

4.4.2.1 Centred Scheme

The pNEWT solver uses a centred scheme for the discretisation of the inviscid fluxes, which is inherently unstable and therefore requires the addition of artificial dissipation [110] in order for convergence to be obtained.

The face quantities required for the flux calculations are found through a simple average of the neighbouring cell centred variables:

$$\phi_f = \frac{\phi_L + \phi_R}{2} \tag{4.12}$$

where L and R correspond to the respective left and right states, as shown in Figure 4.2.

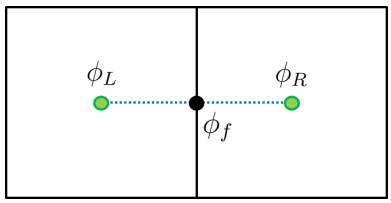

Figure 4.2: Left and right states used to calculate face data for the centred discretisation method.

The mass flux can therefore be defined as:

$$\dot{m}_f = \sum_{i=1}^{3} \left(\frac{\rho_L u_{iL} + \rho_R u_{iR}}{2} A_i \right) \tag{4.13}$$

with the complete discretisation of Equation 4.7, given by:

$$f_{\phi f} = \dot{m}\phi_f \tag{4.14}$$

The pressure gradient source term for the i momentum equation can be included through the addition of:

$$\left(\frac{p_L + p_R}{2}\right) A_i \tag{4.15}$$

to the i momentum face flux calculations.

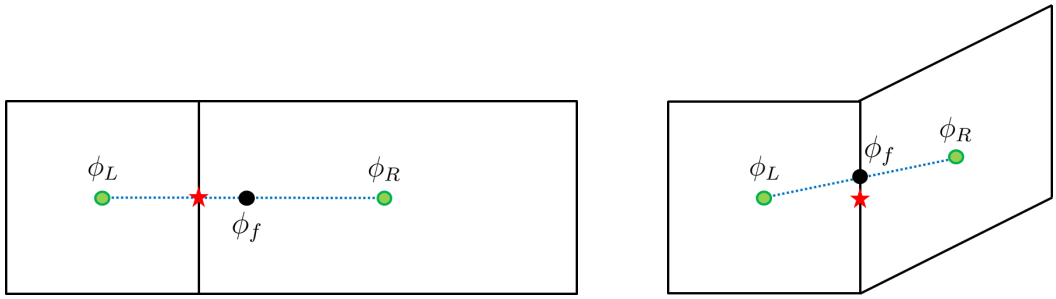

Figure 4.3: Disadvantages of the centred scheme on a non-regular mesh. Black dot corresponds to half way between cell centres and red star corresponds to centre of face.

This method is second order accurate on regular grids. However, if the mesh is irregular and the half way point between the neighbouring cell centres does not coincide with the centre of the face, as shown by the stretched and skewed cells in Figure 4.3, the order of accuracy of the simple average in Equation 4.12 is reduced.

4.4.2.2 Test case: Discontinuity Capturing - Centred

In order to assess the monotonic properties of discretisation schemes, a propagating discontinuity can be simulated. Often, a discontinuous pressure field is employed in order to replicate a shock wave, however a discontinuous species mass fraction field is to be used here to show that the monotonic solution of any discontinuous conserved variable is of great importance.

Figure 4.4 shows the initial state of the test case, where an axial velocity of 150 ms^{-1} propagates a discontinuity of pure nitrogen into a field of pure oxygen. The domain is $0.5m$ in length, $0.05m$ in height and $0.0015m$ in depth, discretised by regular hexahedral elements of $0.5mm$, totalling 300,000 cells. A time step of 4×10^{-7} seconds is used and the computational results are compared to the analytical solution after 1500 iterations.

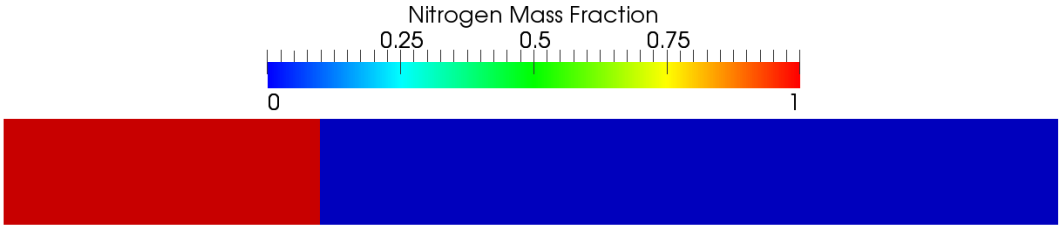

Figure 4.4: Initial conditions for the mass fraction discontinuity test case

It can be seen from Figures 4.5 and 4.6 that the centred scheme causes spurious oscillations near the mass fraction discontinuity. These numerical oscillations are known as Gibb's phenomenon [111] and can cause unphysical predictions to occur or can grow and destabilise the solution. For this test case these oscillations cause the prediction of erroneous values for species mass fraction, but near discontinuities in a scramjet combustor these oscillations could arise for any conserved variable. Oscillations in density lead to oscillations in temperature, as will be shown in section 4.4.3.3, which could cause non-physical ignition to occur in a reacting simulation.

4.4.2.3 AUSM+

In order to avoid the production of spurious oscillations in discontinuous regions of the flow an upwind method can be used. The Roe scheme [112] is commonly employed, which belongs to the flux-difference splitting family of upwind methods. However, the Roe scheme requires the formulation of a Roe matrix which can become impractically complicated [113] when an undefined number of additional transport equations are introduced for the species mass fractions. The flux-vector splitting family of schemes are computationally less expensive than their flux-difference splitting counterparts and do not require the formulation of such matrices, but often provide a reduced level accuracy [114].

An advection upstream splitting method (AUSM) family of schemes has been developed by M.-S. Liou, where the AUSM+ scheme [113] has been shown to provide comparable accuracy to the Roe scheme, for a reduced computational expense. AUSM+ is an improvement on the original AUSM method [114].

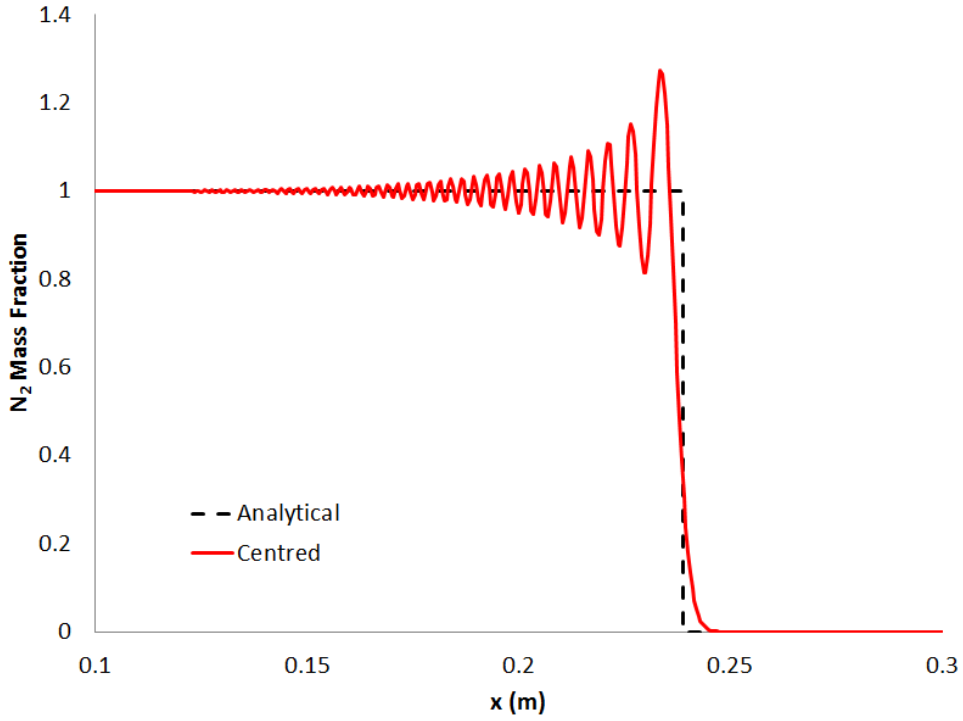

Figure 4.5: Capability of the centred scheme for discontinuity capturing

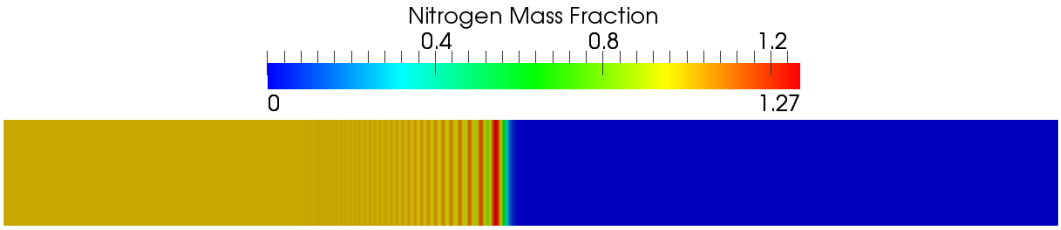

Figure 4.6: Nitrogen mass fraction profile when using the centred scheme

For simplicity, the AUSM+ approach is to be briefly presented by assuming a one dimensional system of governing equations, but is easily extendable to the fully three dimensional system presented in Chapter 2. The flux-vector splitting definition corresponds to the separation of the inviscid fluxes into convective and pressure terms:

$$\vec{F}_{invis} = \vec{F}_c + \vec{P} \tag{4.16}$$

with

$$\vec{F}_c = \rho M a \begin{pmatrix} 1 \\ u \\ h_0 \\ Y_\alpha \end{pmatrix} = \rho M a \vec{\phi}, \qquad \vec{P} = \begin{pmatrix} 0 \\ p \\ 0 \\ 0 \end{pmatrix} \tag{4.17}$$

where M is the Mach number and a is the speed of sound, since

$$M = \frac{u}{a} \tag{4.18}$$

The numerical convective face flux can therefore be defined as:

$$f_{\phi f} = \rho_f M_f a_f \phi_f A_f + p_f A_f \tag{4.19}$$

where $\rho_f M_f a_f A_f$ is the mass flux, $\dot{m}$.

It is the definition of the face values for Mach number and pressure which make up the core of the AUSM family of schemes. The face Mach number is defined as:

$$M_f = \mathcal{M}^+(M_L) + \mathcal{M}^-(M_R) \tag{4.20}$$

where M_L and M_R correspond to the Mach numbers for the left and right cells, defined using the face value for the speed of sound:

$$M_{L/R} = \frac{u_{L/R}}{a_f} \tag{4.21}$$

The $\mathcal{M}$ function is defined as:

$$\mathcal{M}^{\pm}(M) = \begin{cases} \frac{1}{2}(M \pm |M|) & \text{if } |M| \geq 1 \\ \mathcal{M}^{\pm}_{\beta}(M) & \text{otherwise} \end{cases} \tag{4.22}$$

with

$$\mathcal{M}^{\pm}_{\beta}(M) = \pm\frac{1}{4}(M \pm 1)^2 \pm \beta(M^2-1)^2, \quad -\frac{1}{16} \leq \beta \leq \frac{1}{2} \tag{4.23}$$

The face pressure is calculated using:

$$p_f = \mathcal{P}^{+}(M_L)p_L + \mathcal{P}^{-}(M_R)p_R \tag{4.24}$$

and the $\mathcal{P}$ function is defined as:

$$\mathcal{P}^{\pm}(M) = \begin{cases} \frac{1}{2M}(M \pm |M|) & \text{if } |M| \geq 1 \\ \mathcal{P}^{\pm}_{\alpha}(M) & \text{otherwise} \end{cases} \tag{4.25}$$

with

$$\mathcal{P}^{\pm}_{\alpha}(M) = \frac{1}{4}(M \pm 1)^2(2 \mp M) \pm \alpha M(M^2-1)^2, \quad -\frac{3}{4} \leq \alpha \leq \frac{3}{16} \tag{4.26}$$

It should be noted that Equation 4.23 differs slightly from that in reference [113], due to an error in the original paper. That presented here is correct [115]. The terms involving α and β correspond to the higher order extension of the original AUSM scheme. For simplicity, the numerical speed of sound will be calculated as a simple average of the left and right states:

$$a_f = \frac{a_L + a_R}{2} \tag{4.27}$$

where the speed of sound for a cell is defined as:

$$a_{L/R} = \sqrt{\gamma_{L/R}\frac{p_{L/R}}{\rho_{L/R}}} \tag{4.28}$$

The face value of the conserved variables is defined through simple upwinding:

$$\phi_f = \begin{cases} \phi_L & \text{if } M_f \geq 0 \\ \phi_R & \text{otherwise} \end{cases} \tag{4.29}$$

The use of neighbouring cell centred data for the left and right states corresponds to a first order upwind method. Extension to higher orders will be discussed in Section 4.4.3.

4.4.2.4 AUSM+UP

The AUSM family of upwind schemes was developed for use in density based solvers for the solution of high Mach number flows. However, it is often important to ensure a numerical method is applicable over a wide range of flow regimes [116]. Not only is it useful for a compressible flow solver to be applicable to the solution of low speed problems, but high Mach number flows may also contain low speed regions. Scramjet combustors may contain regions of separation to aid flame-holding or the simulation of converging diverging nozzles used in experimental apparatus to accelerate the flow to supersonic speeds may be required. Computational techniques are therefore needed which can simultaneously handle the simulation of these high and low speed regimes.

The AUSM and AUSM+ schemes are known to produce oscillations in pressure under low Mach number conditions [116]. This may be due to the presence of a low speed region or may simply occur in directions of corresponding low velocity, even if the speed of the bulk flow is high (i.e. velocity component perpendicular to main flow direction may be small).

This behaviour led to the development of the AUSM+UP scheme, which is applicable at all speeds. Essentially, this scheme was developed through application of a low Mach number series expansion to the governing system of equations. Modified equations for M_f and p_f were created, which effectively lead to the addition of diffusion terms to damp oscillations under low Mach number conditions.

The new face Mach number is expressed as:

$$M_f = \mathcal{M}^+(M_L) + \mathcal{M}^-(M_R) + M_p \tag{4.30}$$

which is identical to Equation 4.20 with the addition of a pressure diffusion term, M_p, defined as:

$$M_p = -\frac{K_p}{f_a}\max(1 - \sigma\bar{M}^2, 0)\frac{p_R - p_L}{\rho_f a_f^2} \tag{4.31}$$

where K_p and σ are model constants with bounds $0 \leq K_p \leq 1$ and $\sigma \leq 1$. This diffusion term is only activated in low Mach number regions of the flow through the $\max(1 - \sigma\bar{M}^2, 0)$ term, where $\bar{M}$ can be interpreted as the mean local Mach

number:

$$\bar{M}^2 = \frac{u_L^2 + u_R^2}{2a_f^2} \tag{4.32}$$

The term f_a is introduced to properly scale the diffusion with flow speed. It is defined in terms of a reference Mach number, M_o:

$$f_a(M_o) = M_o(2 - M_o) \tag{4.33}$$

where

$$M_o^2 = \min(1, \max(\bar{M}^2, M_\infty^2)) \tag{4.34}$$

M_∞ is the free-stream, or cut-off, Mach number, used to avoid f_a tending to zero. Since the test cases to be presented in this thesis will consist of supersonic core flows, f_a will usually become unity, providing zero scaling contribution.

The face pressure is modified in a similar manner, with the addition of a velocity diffusion term, p_u, to Equation 4.24:

$$p_f = \mathcal{P}^+(M_L)p_L + \mathcal{P}^-(M_R)p_R + p_u \tag{4.35}$$

with

$$p_u = -K_u\mathcal{P}^+(M_L)\mathcal{P}^-(M_R)(\rho_L + \rho_R)(f_a a_f)(u_R - u_L) \tag{4.36}$$

where K_u is a model constant. The p_u diffusion term is only active in subsonic regions of the flow, since at Mach numbers above unity either $\mathcal{P}^+(M_L)$ or $\mathcal{P}^-(M_R)$ becomes zero to obtain a one sided approximation.

It is the addition of the velocity and pressure diffusion terms, p_u and M_p, to the AUSM+ scheme which gives AUSM+UP its name. The values employed for the AUSM+UP model constants are presented in Table 4.1.

Since regions of subsonic flow exist in test cases to be presented in Chapters 5 6 and 7, and since the diffusion terms do not play a detrimental role in supersonic flow regimes due to the switching employed, the AUSM+UP scheme is the upwind method of choice.

Variable	Value
α	$\frac{3}{16}$
β	$\frac{1}{8}$
K_p	$\frac{1}{4}$
K_u	$\frac{3}{4}$
σ	1.0

Table 4.1: Model constants used for the AUSM family of schemes [116].

4.4.2.5 Test case: Discontinuity Capturing - Upwind

The test case of Section 4.4.2.2 is again simulated, now using a first order AUSM+UP upwind scheme. It can be seen from Figure 4.7 that the introduction of an upwind scheme prevents the generation of spurious oscillations and provides a monotonic solution for the discontinuity in question.

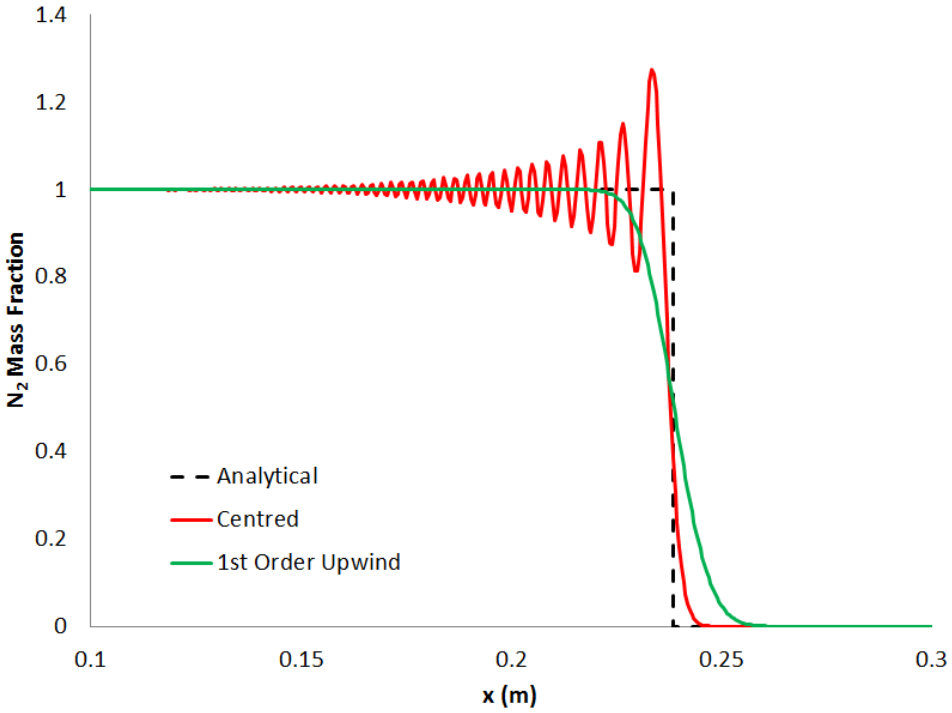

Figure 4.7: Capability of the 1st order upwind scheme for discontinuity capturing

However, it can be seen that the first order upwind method is very dissipative, severely smoothing the discontinuity. Higher order methods are required in order for a sharper resolution to be obtained. This first order method would not be suitable for a large eddy simulation since it would rapidly dissipate the large scale structures of the flow.

4.4.3 Linear Interpolation

In order to obtain a more accurate solution, it is possible to extend the upwind scheme to higher orders using interpolation of cell-centred data to cell faces. The extension of the AUSM+UP scheme to second order of accuracy using a linear interpolation method is to be demonstrated.

As discussed, it is the face data that is required for the inviscid flux calculations. The centred scheme approximates this through a simple average of neighbouring cell-centred data and the first order upwind method simply sets the face data equal to the cell-centred data in the upwind cell. In order to increase the accuracy of the AUSM+UP scheme, the cell-centred data can be interpolated to the centre of the face using gradient information for the variables concerned.

As can be seen from Figure 4.8, this interpolation generates new values for the left and right states, which are simply used in place of the left and right cell-centred data of the first order method.

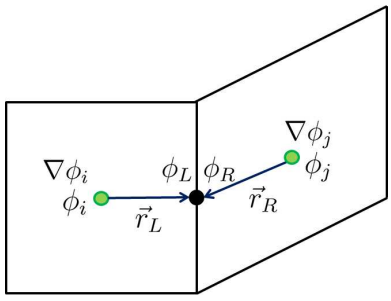

Figure 4.8: Linear interpolation approach

The interpolation procedure for the new left and right values can be mathematically described as:

$$\begin{aligned} \phi_L &= \phi_i + \nabla\phi_i \cdot \vec{r}_L \\ \phi_R &= \phi_j + \nabla\phi_j \cdot \vec{r}_R \end{aligned} \tag{4.37}$$

where $\vec{r}_L$ and $\vec{r}_R$ are the vectors to the face centre from the left and right cell centres, respectively, and $\nabla\phi_i$ is the gradient of variable ϕ at cell centre i. The weighted least squares method described later in Section 4.5.1 is employed for the gradient calculation.

However, in high gradient regions this interpolation can produce erroneous results, with the generation of spurious oscillations. A limiter is therefore required to control the addition of the interpolated data to the cell centred values. Either a flux limiter, ψ_f, which directly scales the interpolation:

$$\begin{aligned} \phi_L &= \phi_i + \psi_f(\nabla\phi_i \cdot \vec{r}_L) \\ \phi_R &= \phi_j + \psi_f(\nabla\phi_j \cdot \vec{r}_R) \end{aligned} \tag{4.38}$$

or a gradient limiter, ψ_g, which modifies the gradient data used in the interpolation:

$$\begin{aligned} \phi_L &= \phi_i + \psi_g(\nabla\phi_i) \cdot \vec{r}_L \\ \phi_R &= \phi_j + \psi_g(\nabla\phi_j) \cdot \vec{r}_R \end{aligned} \tag{4.39}$$

can be used. A flux limiter simply varies between 1 in smooth regions of the flow and 0 in high gradient regions, resorting back to the first order upwind method near discontinuities. The gradient limiter modifies the gradient data through a weighted average of neighbouring gradient values. Since gradient limiters are capable of achieving second order accuracy right up to a discontinuity [117], they will be the focus here.

When increasing the order of accuracy through use of the linear interpolation approach, the computational cost is significantly increased over the first order upwind method. Additional calculations are required in order to obtain the gradient data and then to conduct the limiting and interpolation procedures. However, for a viscous simulation, where the gradient data is also required for the viscous flux calculations (see Section 4.5), the additional cost of the increased order of accuracy is not so severe, as shown in Table 4.2.

	% increase
Inviscid	222
Viscous	54

Table 4.2: Percentage increase in computational cost of inviscid and viscous flow calculations for the second order upwind method with Van Rosendale gradient limiter, over the 1st order upwind scheme.

4.4.3.1 Gradient Limiter

It is possible to modify the gradient employed in the interpolation calculation in such a way as to avoid the generation of spurious interpolated data. This is known as gradient limiting and the gradient limiter presented here is based on that of Van Rosendale [117]. The limited gradient for cell i, $\nabla\phi_i|_l$, is calculated through a weighted sum of all unlimited neighbouring cell-centred gradient values:

$$\psi_g(\nabla\phi_i) = \nabla\phi_i|_l = \sum_{j=1}^{N_i} w_{i,j}\nabla\phi_j \tag{4.40}$$

where N_i is the number of neighbouring cells (e.g. 6 for a hexahedral cell) plus one:

$$N_i = N_{neighbours} + 1 \tag{4.41}$$

The plus one is present to ensure the unlimited gradient value for cell i is also included in the calculation.

The weight $w_{i,j}$, applied to the gradient in cell j in the calculation of the reconstructed gradient value for cell i, is given by:

$$w_{i,j} = \frac{\prod_{k\neq j}^{N_i}\beta_k + \epsilon}{\sum_{l=1}^{N_i}\prod_{k\neq l}^{N_i}\beta_k + N_i\epsilon} \tag{4.42}$$

where β_k is the square of the L2-norm of the gradient in question:

$$\beta_k = \|\nabla\phi_k\|^2 = \left(\frac{\partial\phi}{\partial x}\bigg|_k\right)^2 + \left(\frac{\partial\phi}{\partial y}\bigg|_k\right)^2 + \left(\frac{\partial\phi}{\partial z}\bigg|_k\right)^2 \tag{4.43}$$

and the small number ϵ avoids division by zero, with the N_i factor in the denominator satisfying the constraint that:

$$\sum_{j=1}^{N_i} w_{i,j} = 1 \tag{4.44}$$

The weights are calculated in this way so that if a cell-centred gradient in cell j is significantly larger than those in other neighbouring cells, the corresponding $\prod_{k \neq j}^{N_i} \beta_k$ term will be relatively small, since it does not include the large squared L2-norm for this gradient. This results in a small weighting, $w_{i,j}$, and resulting small contribution from cell j to the limited gradient for use in the cell i interpolation.

This procedure has the property that near discontinuities the reconstructed gradient uses information just from one side of the discontinuity, avoiding the generation of spurious oscillations whilst still achieving second order of accuracy [117]. This gradient limiter therefore behaves in a similar fashion to the more expensive essentially non-oscillatory (ENO) scheme [118].

4.4.3.2 Test case: Discontinuity Capturing

The test case of Section 4.4.2.2 is re-used to demonstrate the increase in accuracy obtained through use of the linear interpolation method with the Van Rosendale gradient limiter. It can be seen from both Figure 4.9 and Figure 4.10 that the introduction of linear interpolation provides a sharper resolution of the mass fraction discontinuity when compared to the first order upwind method, whilst still maintaining a monotonic solution.

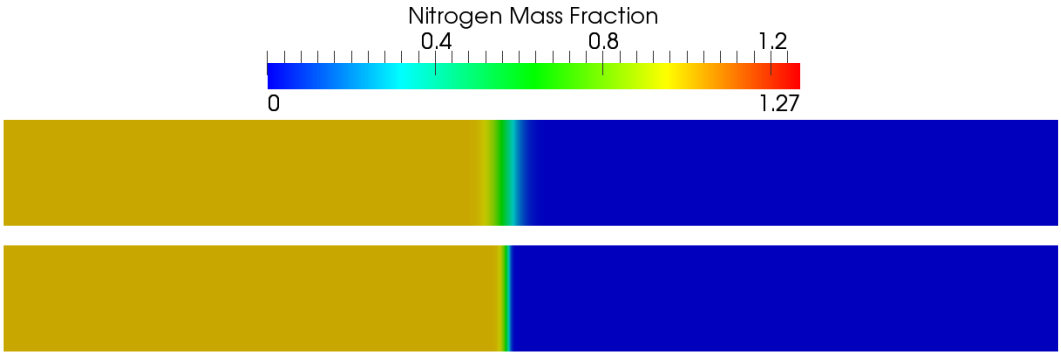

Figure 4.9: Resolution comparison for 1st order upwind (top) and second order upwind with Van Rosendale gradient limiter (bottom), schemes

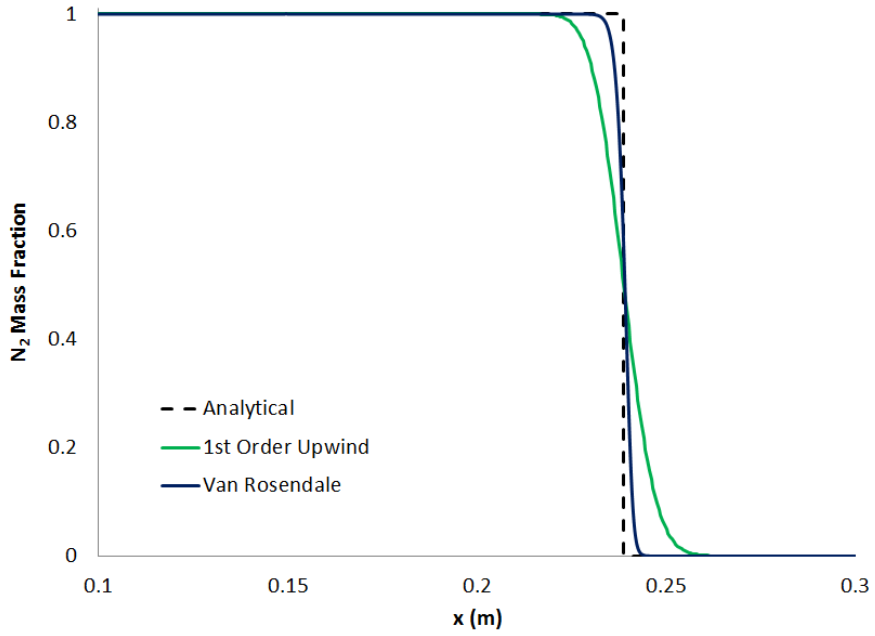

Figure 4.10: Capabilities of the higher order upwind method for discontinuity capturing

4.4.3.3 Test case: Sod's Shock Tube Problem

Another test case, which shows some important features of the Van Rosendale gradient limiter and provides the capability to compare the higher order upwind and central discretisations in subsonic smooth regions of the flow, is Sod's shock tube problem.

This test case consists of a fully enclosed domain with discontinuous initial conditions. As is shown in Figure 4.11, the initial profile consists of two regions separated by a hypothetical diaphragm. Table 4.3 provides the initial conditions for this test case showing that region 1 and region 4 are high and low pressure regions, respectively. The test gas is pure air.

Initiation of a simulation with such initial conditions corresponds to this diaphragm bursting and the characteristics of the resulting flow, for which an analytical solution is available, are also shown in Figure 4.11. An expansion fan separates regions 1 and 2 and initially propagates to the left, and a contact dis-

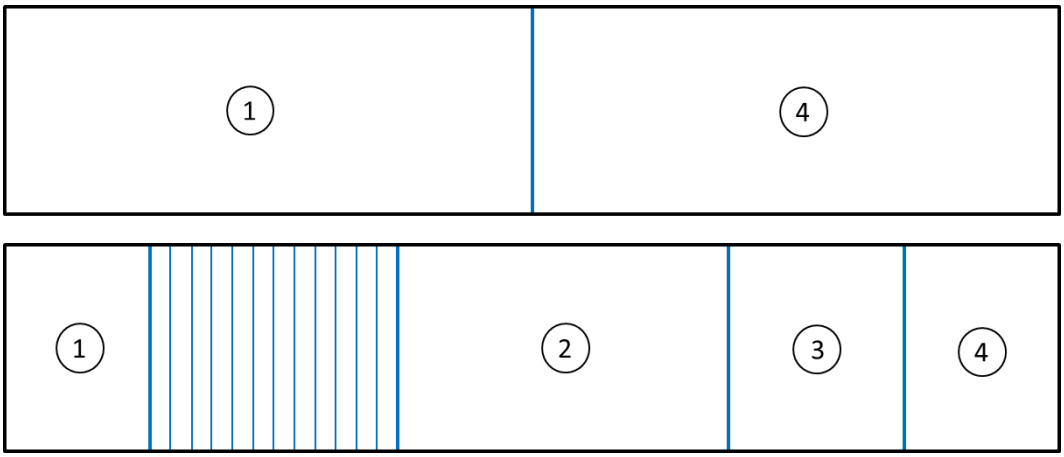

Figure 4.11: Initial conditions and analytical solution profile for Sod's shock tube problem

	Region 1	Region 4
Pressure (bar)	10	1
Temperature (K)	520	416
Velocity (m/s)	0	0

Table 4.3: Initial conditions for Sod's shock tube problem.

continuity separating regions 2 and 3 and a shock wave separating regions 3 and 4 initially propagate to the right.

The same mesh as used for the mass fraction discontinuity test case is employed here, but inviscid wall boundary conditions are used in place of the inlet and outlet. A time step of 1.6×10^{-7} seconds is now employed and the computational and analytical solutions are compared after 1500 iterations, which is before the shock wave has reached the end wall. The AUSM+UP and central schemes are employed for discretisation of the inviscid fluxes.

Figure 4.12 shows the resulting pressure distribution, where the monotonic improvement over the centred scheme, through use of upwind methods, can again clearly be seen at the shock location. Two regions are highlighted on this plot, namely the top and bottom of the expansion fan. At the top of the expansion fan it can be seen that the AUSM+UP upwind method with linear interpolation

and the Van Rosendale gradient limiter, is more accurate than the second order centred scheme. However, at the bottom of the expansion fan, for the higher order upwind scheme, a small undershoot can be seen in the solution. This undershoot is due to the fact that the Van Rosendale gradient limiter does not obey the strict TVD criterion. However, the magnitude of this oscillation is small and is deemed acceptable.

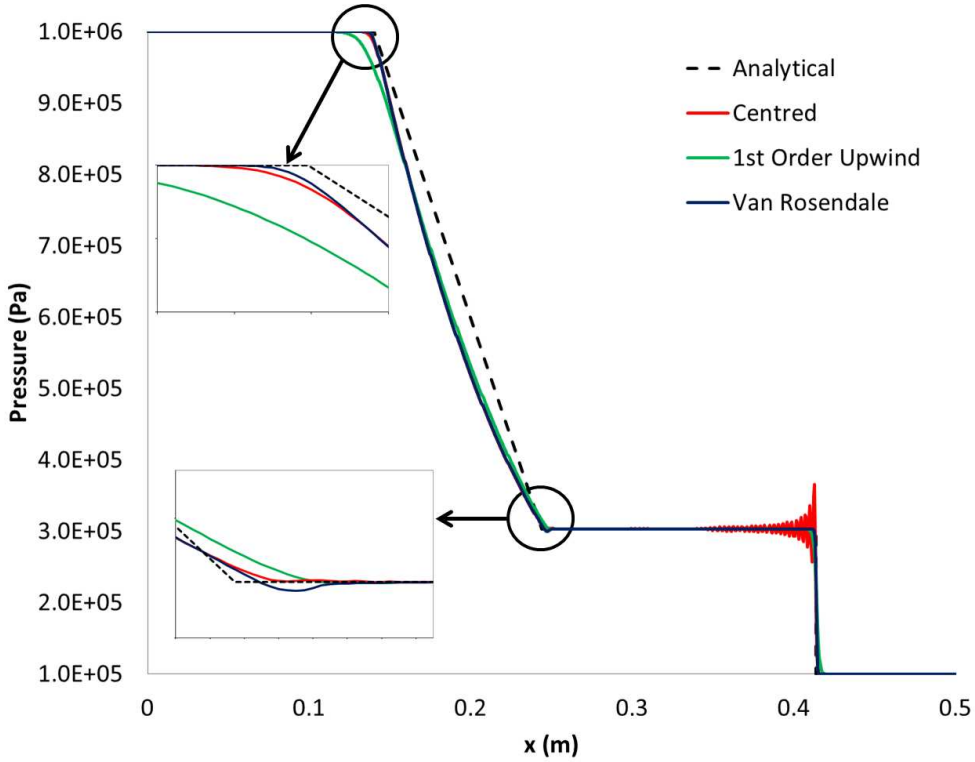

Figure 4.12: Pressure profile for Sod's shock tube problem, after 1500 iterations

As an aside, to further demonstrate why the centred scheme is unsuitable for discretisation of the inviscid fluxes in supersonic combustion, Figure 4.13 shows the resulting oscillations in the temperature profile, which could cause unphysical ignition to occur. Oscillations at both the contact discontinuity and shock wave are visible, caused by oscillations in density at these locations.

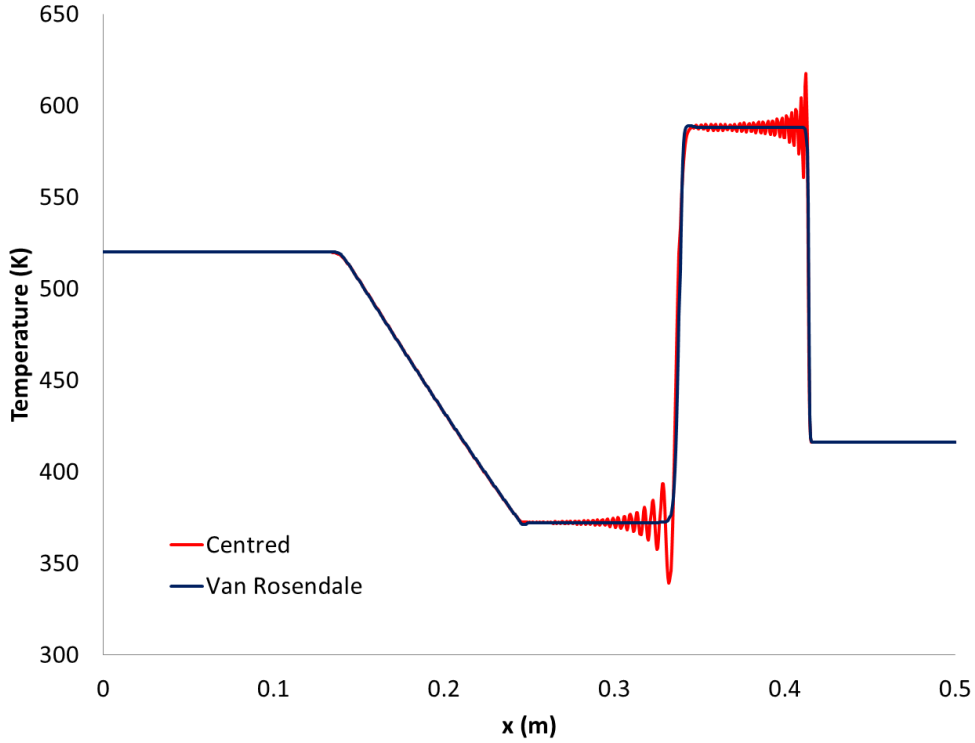

Figure 4.13: Temperature profile for Sod's shock tube problem, after 1500 iterations

4.5 Viscous Fluxes

The calculation of the viscous flux in Equation 4.8 requires calculation of face data for both the diffusion terms and gradient vectors. Simple averaging of the neighbouring cell centred data is used to calculate the face values for the scalar diffusion coefficients so the focus of this section is on the more complex calculations for face values of the gradient data.

4.5.1 Gradient Reconstruction

Cell-centred gradient data is required for calculation of the viscous fluxes and is also used in the linear interpolation method for higher order upwind inviscid flux discretisation. Green-Gauss and least-squares methods are commonly employed

for the gradient reconstruction. However, the Green-Gauss approach can provide highly inaccurate results on mixed grids [119], particularly when a cell-centred data structure is used [120]. The least-squares approach is capable of providing accurate results on arbitrary mesh types, independent of the data structure employed, and is therefore the method of choice for gradient reconstruction in PULSAR.

For highly anisotropic grids, such as those found in regions close to a viscous wall or in a shear layer, the least-squares method can underestimate the gradients by up to an order of magnitude [120]. It is therefore important to apply weights, w_{ij}, to contributions from neighbouring cells and the inverse distance weighting approach is employed:

$$w_{ij} = \frac{1}{l_{ij}} \tag{4.45}$$

Figure 4.14 shows a typical region of stretched cells. Through use of the inverse distance weighting method, where l_{ij} is the distance between cell centres, cells A and C provide a greater contribution to the gradient calculation, significantly improving results from the least-squares method on anisotropic meshes.

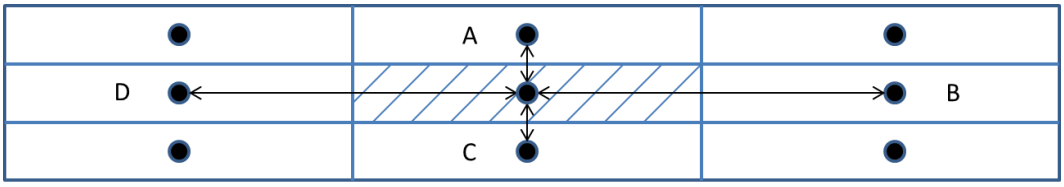

Figure 4.14: Stencil for least-squares gradient reconstruction in shaded cell. Anisotropic grid displayed.

The weighted least-squares procedure for gradient reconstruction is quite involved and is provided in the Appendix of [120].

4.5.2 Discretisation Technique

Face values for the diffusion coefficient, or any other scalar quantities required for the viscous flux, is calculated using the centred approach of Equation 4.12. The

centred approach is also employed for the calculation of the face gradient values, $\nabla\phi_f$, where it is natural to take a simple average of the neighbouring data:

$$\overline{\nabla\phi} = \frac{\nabla\phi|_i + \nabla\phi|_j}{2} \tag{4.46}$$

However, on regular hexahedral grids this simple average can lead to decoupling of the solution [121] and subsequent generation of spurious oscillations. In order to avoid this decoupling, modifications similar to those introduced by Rhie and Chow [122] for pressure-velocity coupling in the Euler equations, can be applied to Equation 4.46:

$$\nabla\phi_f = \overline{\nabla\phi} - \left[\overline{\nabla\phi}\cdot\vec{t_{ij}} - \left.\frac{\partial\phi}{\partial l}\right|_{ij}\right]\vec{t_{ij}} \tag{4.47}$$

where

$$\left.\frac{\partial\phi}{\partial l}\right|_{ij} = \frac{\phi_j - \phi_i}{l_{ij}} \tag{4.48}$$

and the distance between the centres of cells i and j, l_{ij}, and corresponding vector, $\vec{r_{ij}}$, are used to define the unit vector, $\vec{t_{ij}}$.

$$\vec{t_{ij}} = \frac{\vec{r_{ij}}}{l_{ij}} \tag{4.49}$$

4.6 Turbulence Model

The Menter SST turbulence model is chosen for the calculation of both the eddy viscosity in a RANS simulation and also the sub-grid viscosity for LES, using a DDES hybrid RANS-LES approach.

This two equation model is capable of providing the turbulence length scales required for use in combustion model source terms whilst combining the good near wall and free-stream properties of the $k-\omega$ and $k-\varepsilon$ models, respectively.

4.6.1 RANS

Although there is a transition from a $k-\omega$ to a $k-\varepsilon$ turbulence model away from the wall through use of a blending function, F_1, only two transport equations for k and ω are required due to the simple relationship with ε, given by Equation 2.47:

$$\frac{\partial \bar{\rho} k}{\partial t} + \frac{\partial \bar{\rho} \tilde{u}_i k}{\partial x_i} = \tilde{P} - \beta^{\star} \bar{\rho} \omega k + \frac{\partial}{\partial x_i} \left[\left(\mu + \sigma_k \mu_t \right) \frac{\partial k}{\partial x_i} \right] \tag{4.50}$$

$$\begin{aligned} \frac{\partial \bar{\rho} \omega}{\partial t} + \frac{\partial \bar{\rho} \tilde{u}_i \omega}{\partial x_i} &= \frac{\bar{\rho} \alpha}{\mu_t} \tilde{P} - \beta \bar{\rho} \omega^2 + \frac{\partial}{\partial x_i} \left[\left(\mu + \sigma_\omega \mu_t \right) \frac{\partial \omega}{\partial x_i} \right] \\ &+ 2 \left(1 - F_1 \right) \frac{\bar{\rho} \sigma_{\omega 2}}{\omega} \frac{\partial k}{\partial x_i} \frac{\partial \omega}{\partial x_i} \end{aligned} \tag{4.51}$$

In the standard $k-\omega$ model [37], the dynamic eddy viscosity is calculated from:

$$\mu_{t,k-\omega} = \frac{\rho k}{\omega} \tag{4.52}$$

However, for adverse pressure gradient regions of a boundary layer this formulation leads to a severe over-prediction of the shear stress [123]. A better model for the eddy viscosity in these regions is given by:

$$\mu_{t,adverse} = \frac{\rho a_1 k}{S} \tag{4.53}$$

The eddy viscosity for the Menter SST turbulence model is therefore chosen as the minimum of $\mu_{t,k-\omega}$ and $\mu_{t,adverse}$. However, in order to restrict the use of the adverse pressure gradient modification to inside the boundary layer, a second blending function, F_2, is introduced:

$$\mu_t = \frac{\bar{\rho} a_1 k}{max \left(a_1 \omega, S F_2 \right)} \tag{4.54}$$

The blending function, F_1, used to transition between the $k-\omega$ and $k-\varepsilon$ turbulence models, is given as:

$$F_1 = \tanh \left(arg_1^4 \right) \tag{4.55}$$

where

$$arg_1 = min\left(arg_2, \frac{4\bar{\rho}\sigma_{\omega 2}k}{\mathrm{CD}_{k\omega}y_w^2}\right) \tag{4.56}$$

with

$$arg_2 = max\left(\frac{\sqrt{k}}{\beta^\star\omega y_w}, \frac{500\mu_l}{y_w^2\bar{\rho}\omega}\right) \tag{4.57}$$

and

$$\mathrm{CD}_{k\omega} = max\left(2\bar{\rho}\sigma_{\omega 2}\frac{1}{\omega}\frac{\partial k}{\partial x_i}\frac{\partial \omega}{\partial x_i}, 10^{-10}\right) \tag{4.58}$$

The second blending function, F_2, is given by:

$$F_2 = \tanh\left(arg_2^2\right) \tag{4.59}$$

The production term used in the two transport equations is defined as:

$$P = \bar{\rho}\widetilde{u_i'u_j'}\frac{\partial \tilde{u}_i}{\partial x_j} \tag{4.60}$$

where the turbulent stresses, $\bar{\rho}\widetilde{u_i'u_j'}$, are given by the Boussinesq approximation of equation 2.27. In order to prevent the buildup of turbulence in stagnation regions a limiter is applied to this production term, giving:

$$\tilde{P} = min\left(P, 10\beta^\star\bar{\rho}k\omega\right) \tag{4.61}$$

All model constants are provided in Table 4.4. The constants appearing in the k and ω transport equations are made up of a blend of the constants for the $k-\omega$ and $k-\varepsilon$ turbulence models. For example, the constant σ_k is defined as:

$$\sigma_k = \sigma_{k1}F_1 + \sigma_{k2}(1 - F_1) \tag{4.62}$$

α_1	$\frac{5}{9}$	α_2	0.44
β_1	0.075	β_2	0.0828
σ_{k1}	0.85	σ_{k2}	1
$\sigma_{\omega 1}$	0.5	$\sigma_{\omega 2}$	0.856
κ	0.41	a_1	0.31
$\beta^\star$	0.09		

Table 4.4: Model constants for the Menter SST turbulence model.

4.6.2 DDES

The Menter SST turbulence model is also used as the sub-grid scale model under a DDES framework. Transitioning from a RANS model near the wall to a sub-grid scale model in the free-stream is enabled through a simple modification to the turbulence length scale in the k equation destruction term:

$$\frac{\partial \bar{\rho} k}{\partial t} + \frac{\partial \bar{\rho} \tilde{u}_i k}{\partial x_i} = \tilde{P} - \frac{\bar{\rho} k^{\frac{3}{2}}}{\widetilde{l}} + \frac{\partial}{\partial x_i}\left[(\mu + \sigma_k \mu_t)\frac{\partial k}{\partial x_i}\right] \tag{4.63}$$

Specific details of model length scales, $\widetilde{l}$, and the blending employed were provided in Section 2.4.4.

4.6.3 Wall Distance

The distance to the nearest wall, y_w, required for the Menter SST turbulence model is found using a simple search procedure. For each cell, every wall boundary point is searched to find the smallest distance to a viscous boundary. As one might expect, this procedure is computationally expensive and more efficient methods are available [124]. However, these efficient methods are more complicated to implement, so the speed-up of the searching procedure was attempted.

Computational costs are brought down to a reasonable level through fully parallel operation, whereby only wall distance calculations for the cells on each partition are required. In order for this calculation to be performed only once, the results are output to a data file which can be quickly read in for subsequent runs of a simulation.

As an example, the time required to calculate the wall distances for the LES

mesh of the wall bounded combustor flow to be presented in Chapter 7 is approximately 460 seconds. The mesh consists of 36.8M cells and is partitioned onto 2640 processors, giving approximately 17,000 cells per partition. The calculations were performed on the HECToR cluster. This one-off computational time is considered acceptable.

4.6.4 Compressibility Corrections

For highly compressible flows, corrections can be applied to the turbulence model in order to reduce the eddy viscosity to more realistic levels. Scaling is applied to the destruction source terms in both the k and ω equations, by modifying the $\beta^\star$ and β coefficients to:

$$\beta^\star_{cc} = \beta^\star[1 + \xi^* F(M_t)] \tag{4.64}$$

$$\beta_{cc} = \beta - \beta^\star \xi^* F(M_t) \tag{4.65}$$

where $\beta^\star_{cc}$ and β_{cc} are the new scaled coefficients to be used in the turbulence model transport equations. ξ^* and $F(M_t)$ are defined by the particular compressibility correction employed, where M_t is the turbulence Mach number, defined as:

$$M_t^2 = \frac{2k}{a^2} \tag{4.66}$$

with a being the speed of sound. The Sarkar, Wilcox and Zeman compressibility corrections [125] are implemented in PULSAR:

Sarkar compressibility correction:

$$\xi^* = 1, \qquad F(M_t) = M_t^2 \tag{4.67}$$

Wilcox compressibility correction:

$$\xi^* = 2, \qquad F(M_t) = \max(M_t^2 - M_{to}^2, 0) \tag{4.68}$$

where M_{to} is a cut-off Mach number equal to 0.25.

Zeman compressibility correction:

$$\xi^* = \frac{3}{4}, \qquad F(M_t) = \left[1 - e^{-\frac{1}{2}(\gamma+1)(M_t+M_{to})^2/\Lambda^2}\right] \mathcal{H}(M_t - M_{to}) \tag{4.69}$$

where $M_{to} = 0.1\sqrt{2/(\gamma+1)}$ and $\Lambda = 0.6$.

4.7 Boundary Conditions

Correct specification of boundary conditions on the flow in question is of significant importance in order to accurately replicate the physics encountered in reality. Inlet, outlet and surface boundary conditions are applied for simulations throughout this research.

4.7.1 Inlet

The eigenvalues of the one-dimensional Euler equations are given as:

$$u - a$$
$$u$$
$$u + a$$

where u is the flow velocity and a is the speed of sound, and define the directions in which information can propagate. The methods employed for specification of inlet boundary conditions therefore depend on the Mach number of the incoming flow.

4.7.1.1 Supersonic

For inlet Mach numbers above unity, information can only propagate downstream since all eigenvalues are positive. Therefore, all flow parameters must be specified at the inlet plane. PULSAR requires specification of the stagnation pressure $p_{0,in}$, static pressure p_{in} and stagnation temperature $T_{0,in}$. The static temperature T_{in}, velocity normal to the inlet V_{in} and density ρ_{in}, can then be calculated from:

$$T_{in} = T_{0,in}\left(\frac{p_{in}}{p_{0,in}}\right)^{\frac{\gamma-1}{\gamma}} \tag{4.70}$$

$$V_{in} = \sqrt{2c_p(T_{0,in} - T_{in})} \tag{4.71}$$

$$\rho_{in} = \frac{p_{in}}{RT_{in}} \tag{4.72}$$

where γ and R are dependent upon temperature and composition.

4.7.1.2 Subsonic

For an inlet Mach number below unity the inlet velocity is lower than the speed of sound and the $u-a$ eigenvalue is negative, meaning information can propagate in both the up and downstream directions. For this reason, one of the boundary variables must be interpolated from inside the domain. In PULSAR the outgoing Riemann invariant,

$$R^- = u_{i,c} \cdot n_i - \frac{2a_c}{\gamma_c - 1} \tag{4.73}$$

is used to specify the speed of sound at the inlet [119], a_{in}:

$$a_{in} = \frac{-R^-(\gamma_c - 1)}{(\gamma_c - 1)\cos^2\theta + 2}\left\{1 + \cos\theta\sqrt{\frac{[(\gamma_c - 1)\cos^2\theta + 2]a_0^2}{(\gamma_c - 1)(R^-)^2} - \frac{\gamma_c - 1}{2}}\right\} \tag{4.74}$$

where the subscripts c and 0 correspond to data at the centre of the computational cell inside the domain and stagnation values, respectively, and θ is the flow angle relative to the boundary. The stagnation temperature and pressure are prescribed for the inlet, and the static temperature is calculated from:

$$T_{in} = T_{0,in}\left(\frac{a_{in}^2}{a_0^2}\right) \tag{4.75}$$

allowing the inlet pressure, velocity and density to be calculated from Equations 4.70, 4.71 and 4.72, respectively.

4.7.1.3 Turbulence

Boundary conditions for the k and ω variables used in the Menter SST turbulence model also need to be specified at the inlet plane, with the following range of variables recommended [126]:

$$\frac{10^{-5}\mu_l V_{in}}{\rho_{in} L_{k-\omega}} < k_{in} < \frac{0.1\mu_l V_{in}}{\rho_{in} L_{k-\omega}} \tag{4.76}$$

$$\frac{V_{in}}{L_{k-\omega}} < \omega_{in} < \frac{10 V_{in}}{L_{k-\omega}} \tag{4.77}$$

where $L_{k-\omega}$ is a prescribed length scale.

Turbulent inlets are also possible, where coherent structures are convected into the domain through specification of velocity fluctuations. The method employed to generate this turbulent velocity data is described in Section 4.10.

4.7.2 Outlet

Similarly to the inlet boundary condition, the method used to handle outlet flows depends on the outlet Mach number. In PULSAR, for supersonic flows, the required boundary data is simply interpolated from inside the domain using a first order, zero gradient approach.

For subsonic flow one variable needs to be prescribed at the outlet to deal with the negative $u - a$ eigenvalue. The static pressure, p_{out}, is the variable applied and all other boundary data is interpolated from inside the domain in the same fashion as for supersonic conditions.

4.7.3 Wall

The presence of viscous surfaces can have a significant impact on the physics of a flow, due to the no-slip condition at the wall. Since scramjet combustors provide a wall bounded problem, the accurate modelling of the physics involved is of paramount importance. Viscous surfaces apply a shear stress to the near wall fluid and can also provide a heat flux through use of isothermal boundary conditions. Correct modelling of turbulent boundary layers also requires the correct boundary condition application for the k and ω variables.

4.7.3.1 Velocity

A flow tangential to a solid surface encounters a viscosity dominated region called a boundary layer, where the velocity tends to zero at the wall, called the no-slip condition. The structure of a high Reynolds number flat plate zero pressure gradient boundary layer can be described in terms of non-dimensional numbers for wall distance (y^+) and velocity (u^+), where

$$y^+ = \frac{\rho y_w u_\tau}{\mu} \tag{4.78}$$

$$u^+ = \frac{u_{tang}}{u_\tau} \tag{4.79}$$

with

$$u_\tau = \sqrt{\frac{|\tau_w|}{\bar{\rho}}} \tag{4.80}$$

y_w is the wall normal distance from the viscous surface to the centre of the near wall cell, u_τ is the shear velocity, τ_w is the wall shear stress and u_{tang} is the velocity in the near wall cell, tangential to the surface.

Figure 4.15 shows the profile from a flat plate zero pressure gradient boundary layer simulation. It can be seen that close to the wall there is a linear region, called the *viscous sublayer*, where y^+ scales directly with u^+. The linear region is valid up to a y^+ value of approximately 10, but above a y^+ of about 6 the errors in this linear assumption begin to grow.

For $30 < y^+ < 1000$ the boundary layer profile is well represented by a *log-law* [127], where u^+ is proportional to the log of y^+, given as:

$$u^+ = \frac{1}{\kappa}\ln(Ey^+) \tag{4.81}$$

where κ is the von Kármán constant, taken as 0.41, and E is a constant taken as 9.5. However, in the range $10 < y^+ < 30$ there exists a *buffer layer*, which does not obey either the linear or log laws. Above a y^+ of approximately 1000 exists the outer region of the boundary layer.

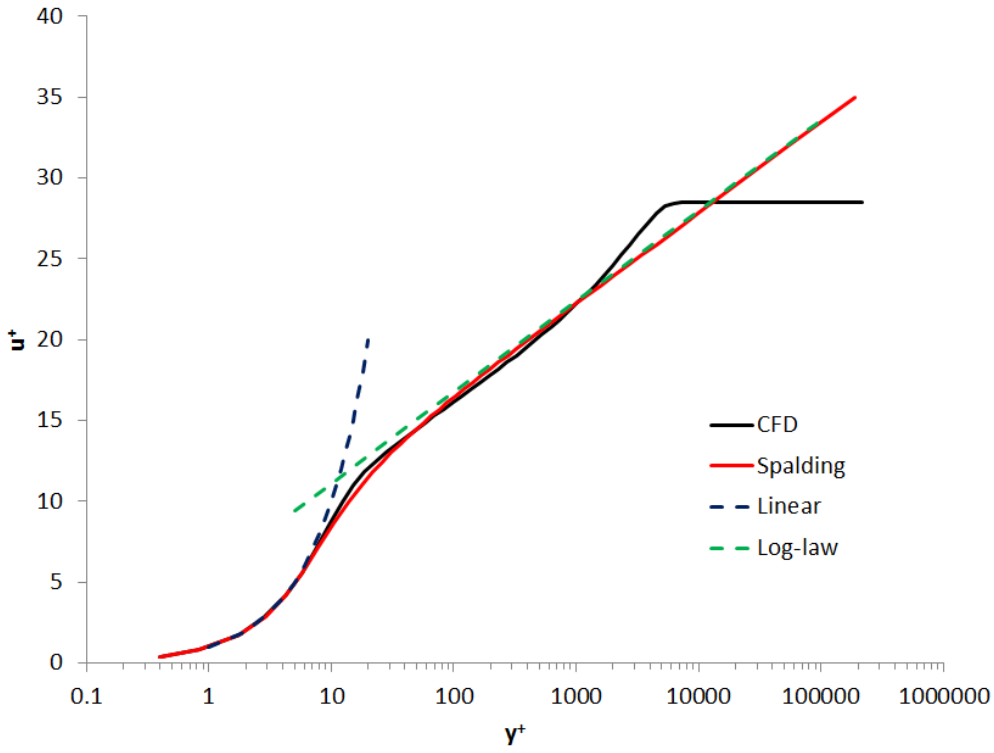

Figure 4.15: Dimensionless profile for a flat plate zero pressure gradient boundary layer.

It is the wall shear stress, τ_w, which is required to be applied as a boundary condition to the momentum equations. Through manipulation of Equations 4.79 and 4.80 this wall shear stress can be given as:

$$\tau_w = \bar{\rho} \left(\frac{u^+}{u_{tang}} \right)^2 \tag{4.82}$$

It can be seen from this equation that as long as the u^+ value and flow properties for the near wall cell are known, the shear stress can be found.

As can be seen in Figure 4.15, Spalding [128] developed a single equation which is capable of continuously defining the viscous, buffer and log-law regions:

$$y^+ = u^+ + 0.1108 \left[e^{0.41u^+} - 1 - 0.41u^+ - \frac{(0.41u^+)^2}{2!} - \frac{(0.41u^+)^3}{3!} \right] \tag{4.83}$$

An iterative Newton-Raphson method can be applied to find the y^+ and u^+ values for the near wall cell. Once the y^+ and u^+ values have been obtained, u_τ can be found from Equation 4.78 or 4.79 and subsequently the wall shear stress from Equation 4.82.

However, the application of a log-law collapses under more complex flow conditions [54]. In the presence of physics such as pressure gradients or shock-wave boundary layer interactions it is recommended that the near-wall cell has a y^+ of less than 5 [61], so that the assumptions of linearity in the viscous sublayer are used to calculate the wall shear stress, rather than the now invalid law of the wall.

4.7.3.2 Temperature

Adiabatic and isothermal wall boundary conditions are implemented into PULSAR. Using the isothermal boundary condition, constant temperature walls can be used to calculate the levels of heat flux, $\dot{q}_w$, into the near wall cell. The heat flux is defined as [129]:

$$\dot{q}_w = \frac{\bar{\rho} c_p (T_w - \widetilde{T}) u_\tau}{T^+} \tag{4.84}$$

where T^+ is the dimensionless variable for temperature, T_w is the specified wall temperature and $\widetilde{T}$ is the temperature in the near wall cell. Similarly to the velocity boundary conditions, a linear relationship between T^+ and y^+ is assumed to exist near to the wall:

$$T^+ = y^+ \mathrm{Pr}_l \tag{4.85}$$

and a log relationship away from the wall:

$$T^+ = \frac{1}{\widetilde{\kappa}} \ln(\widetilde{E} y^+) \tag{4.86}$$

Once T^+ is known, the heat flux can be found from Equation 4.84. Since y^+ is already know from the velocity boundary conditions, iterative methods are not required here. Determination of T^+ for near wall cells inside the viscous sublayer is straightforward through use Equation 4.85. For y^+ values in the log-law region,

rather than attempting to determine the variables $\widetilde{\kappa}$ and $\widetilde{E}$ in Equation 4.86, the temperature and velocity log laws are combined to produce [129]:

$$T^+ = \frac{\kappa}{\widetilde{\kappa}}(u^+ + P) \tag{4.87}$$

where P is the pee function:

$$P = \frac{1}{\kappa}\ln\left(\frac{\widetilde{E}}{E}\right) \tag{4.88}$$

empirically given by [130]:

$$P = 9.24(\widetilde{\sigma}^{\frac{3}{4}} - 1)[1 + 0.28e^{-0.007\widetilde{\sigma}}] \tag{4.89}$$

with

$$\widetilde{\sigma} = \frac{\mathrm{Pr}_l}{\mathrm{Pr}_t} \tag{4.90}$$

4.7.3.3 Turbulence

In order to correctly define the near wall distribution of eddy viscosity, boundary conditions are required for k and ω. A simple zero flux boundary condition is applied at the wall for the k equation, but solutions for ω in the near wall linear and logarithmic regions are respectively given by [131]:

$$\omega_{lin} = \frac{80\mu_l}{\bar{\rho}y_w^2} \tag{4.91}$$

and

$$\omega_{log} = \frac{1}{0.3\kappa}\frac{u_{\tau,blend}}{y_w} \tag{4.92}$$

where $u_{\tau,blend}$ is a blending of the shear velocity values from the linear and logarithmic regions:

$$u_{\tau,blend} = \sqrt[4]{u_{\tau,lin}^4 + u_{\tau,log}^4} \tag{4.93}$$

with

$$u_{\tau,lin} = \frac{u_{tang}}{y^+} \tag{4.94}$$

and

$$u_{\tau,log} = \frac{u_{tang}\kappa}{\ln(Ey^+)} \tag{4.95}$$

For small y^+ this blending tends to the linear value and for large y^+ to the logarithmic value. Similarly, a smooth blending can then be used to define the near wall cell value, ω_w:

$$\omega_w = \sqrt{\omega_{lin}^2 + \omega_{log}^2} \tag{4.96}$$

4.8 Combustion

Implementation of reaction rate modelling is not the only concern when developing a code to be used for simulations of combustion. The underlying thermodynamics is also of paramount importance and both will be discussed here.

4.8.1 Thermo-chemistry

The stagnation specific internal energy equation introduced in Chapter 2, reproduced here for clarity:

$$\widetilde{e}_0 = \widetilde{h} - \frac{\widetilde{p}}{\bar{\rho}} + \frac{1}{2}\widetilde{u}_i\widetilde{u}_i + k$$

handles the thermodynamics of the flow. The influence of chemical composition on the thermodynamics is clearer when the energy equation is re-written as:

$$\widetilde{e}_0 = \sum_{\alpha=1}^{N_s} \widetilde{Y}_\alpha h_\alpha - R_m\widetilde{T} + \frac{1}{2}\widetilde{u}_i\widetilde{u}_i + k \tag{4.97}$$

where the definition of static enthalpy from Equation 2.13 and the ideal gas law have been employed, with R_m being the mixture value for the specific gas constant, given by:

$$R_m = \sum_{\alpha=1}^{N_s} \widetilde{Y}_\alpha R_\alpha. \tag{4.98}$$

and R_α being the specific gas constant for species α. The only remaining unknown in Equation 4.97 is the specific enthalpy for each species, h_α. Since a reacting flow encounters large variations in temperature, the constant specific heat assumptions of a perfect gas can not be used and so h_α must be defined through use of the integral form:

$$h_\alpha = \int_{T_{ref}}^{T} c_{p\alpha} \mathrm{d}T + h_\alpha^{ref} \tag{4.99}$$

where $c_{p\alpha}$ is the mass-based specific heat capacity at constant pressure for species α and h_α^{ref} is the value of h_α at the reference temperature T_{ref}. For a semi-perfect gas the specific heat capacity can be described through use of a polynomial in temperature [132]:

$$c_{p\alpha} = \sum_{k=1}^{N_p} a_{\alpha,k}^{(l)} \widetilde{T}^{k-1} \tag{4.100}$$

where $a_{\alpha,k}^{(l)}$ are the coefficients of the polynomial with degree N_p, for species α in temperature interval l. Performing the integration over successive temperature intervals, it can be shown [132] that:

$$h_\alpha = \sum_{k=1}^{N_p} \frac{a_{\alpha,k}^{(l)}}{k} \widetilde{T}^k + a_{\alpha,N_p+1}^{(l)} \tag{4.101}$$

Inserting this into Equation 4.97 and arranging terms into corresponding powers of T, a polynomial for the temperature can be formed:

$$\begin{aligned} 0 \;=\; & \left[\left(\frac{1}{2} \widetilde{u}_i \widetilde{u}_i + k - e_0 \right) + \sum_{\alpha=1}^{N_s} \widetilde{Y}_\alpha a_{\alpha,N_p+1}^{(l)} \right] \\ + \; & \left[\sum_{\alpha=1}^{N_s} \widetilde{Y}_\alpha \left(a_{\alpha,1}^{(l)} - R_\alpha \right) \right] \widetilde{T} + \sum_{k=2}^{N_p} \left[\sum_{\alpha=1}^{N_s} \widetilde{Y}_\alpha \frac{a_{\alpha,k}^{(l)}}{k} \right] \widetilde{T}^k \end{aligned} \tag{4.102}$$

Employing the same Newton-Raphson iterative method as used for Equation 4.83, the solution to this equation can be found, providing the temperature. The corresponding pressure can be found through use of the ideal gas equation:

$$\bar{p} = \bar{\rho} R_m \widetilde{T} \tag{4.103}$$

and the temperature dependent dynamic molecular viscosity is given by:

$$\mu_l = \frac{\lambda}{c_p} Pr_l \tag{4.104}$$

where λ is the mixture thermal conductivity, which can be found using the following relationship [132]:

$$\frac{\lambda}{c_p} = A_\lambda \left(\frac{\widetilde{T}}{T_{ref}} \right)^r \tag{4.105}$$

with A_λ, r and T_{ref} being constants.

The molar polynomial coefficients, $\bar{a}^{(l)}_{\alpha,k}$, are provided by the CHEMKIN database and the mass based coefficients, $a^{(l)}_{\alpha,k}$, are calculated from:

$$a^{(l)}_{\alpha,k} = \frac{R^0}{W_\alpha} \bar{a}^{(l)}_{\alpha,k} \tag{4.106}$$

where R^0 is the universal gas constant.

4.8.2 Assumed PDF Combustion Model

As discussed in Chapter 3, the assumed PDF combustion model is used to find the mean reaction rate through integration of the instantaneous reaction rate,

$$\bar{\dot{\omega}} = \int \dot{\omega} \left(\hat{\rho}, \hat{T}, \hat{Y}_1, \ldots, \hat{Y}_{N_s} \right) P \left(\hat{\rho}, \hat{T}, \hat{Y}_1, \ldots, \hat{Y}_{N_s} \right) \mathrm{d}\hat{\rho} \mathrm{d}\hat{T} \mathrm{d}\hat{Y}_1, \ldots, \mathrm{d}\hat{Y}_{N_s}$$

where statistical independence is assumed between temperature, composition and density:

$$P \left(\hat{\rho}, \hat{T}, \hat{Y}_1, \ldots, \hat{Y}_{N_s} \right) = P_T(\hat{T}) P_Y(\hat{Y}_1, \ldots, \hat{Y}_{N_s}) \delta(\hat{\rho} - \bar{\rho})$$

With the instantaneous reaction rate given by Equation 3.17, this leads to

$$\bar{\dot{\omega}}_\alpha = W_\alpha \sum_{r=1}^{N_r} \left[\left(\nu''_{\alpha r} - \nu'_{\alpha r} \right) \left(\overline{k_{fr}} \overline{c_M^{\nu_{Mr}} \prod_{\gamma=1}^{N_s} c_\gamma^{\nu'_{\gamma r}}} - \overline{k_{br}} \overline{c_M^{\nu_{Mr}} \prod_{\gamma=1}^{N_s} c_\gamma^{\nu''_{\gamma r}}} \right) \right] \tag{4.107}$$

where

$$\overline{k_r} = \int_0^\infty k_r(\hat{T}) P_T(\hat{T}) \mathrm{d}\hat{T} \tag{4.108}$$

and

$$\overline{c_M^{\nu_{Mr}} \prod_{\gamma=1}^{N_s} c_\gamma^{\nu_{\gamma r}}} = \int \hat{c}_M^{\nu_{Mr}} \prod_{\gamma=1}^{N_s} \hat{c}_\gamma^{\nu_{\gamma r}} P_Y(\hat{Y}_1, \ldots, \hat{Y}_{N_s}) \mathrm{d}\hat{Y}_1, \ldots, \mathrm{d}\hat{Y}_{N_s} \tag{4.109}$$

with

$$\hat{c}_M^{\nu_{Mr}} \prod_{\gamma=1}^{N_s} \hat{c}_\gamma^{\nu_{\gamma r}} = \sum_{\gamma=1}^{N_s} \left(\frac{\eta_{\gamma,M} \bar{\rho} \hat{Y}_\gamma}{W_\gamma} \right)^{\nu_{Mr}} \prod_{\gamma=1}^{N_s} \left(\frac{\bar{\rho} \hat{Y}_\gamma}{W_\gamma} \right)^{\nu_{\gamma r}} \tag{4.110}$$

where ν_{Mr} is unity if third body reactions are present in reaction r and zero otherwise and $\hat{}$ corresponds to sample space variables.

4.8.2.1 Clipped Gaussian PDF

Numerical integration is required in order to evaluate the mean reaction rate constant in Equation 4.108, since no analytical solution is available. The instantaneous reaction rate constant is integrated with a Gaussian PDF for temperature:

$$P_T(\hat{T}) = \frac{1}{\sqrt{2\pi\sigma_T}} \exp \left[-\frac{(\hat{T} - \widetilde{T})^2}{2\sigma_T} \right] \tag{4.111}$$

where $\widetilde{T}$ and σ_T are the mean and variance values.

However, the integration limits on $\hat{T}$ of 0 and ∞ cause problems in the evaluation of $k_r(\hat{T})$, since the Arrhenius expression is not valid at very low or very

high temperatures [76]. Therefore, the integration is modified to

$$\overline{k_r} = \int_{\hat{T}_{min}}^{\hat{T}_{max}} k_r(\hat{T}) P_T(\hat{T}) \mathrm{d}\hat{T} = T_1 \tag{4.112}$$

where a clipped Gaussian profile [133] is employed with $\hat{T}_{min}$ and $\hat{T}_{max}$ equal to 300K and 3000K, respectively:

$$P_T(\hat{T}) = \frac{1}{\sqrt{2\pi\sigma_T}} \exp\left[-\frac{(\hat{T}-\widetilde{T})^2}{2\sigma_T}\right]\left[\mathcal{H}(\hat{T}-T_{min}) - \mathcal{H}(\hat{T}-T_{max})\right] + A_1\delta(\hat{T}-T_{min}) + A_2\delta(\hat{T}-T_{max}) \tag{4.113}$$

A_1 and A_2 are the areas under the PDF below and above the T_{min} and T_{max} limits, respectively. They are lumped at the two extremes through use of the delta function, in order to stay consistent with Equation 4.111.

On-the-fly numerical integration is computationally expensive and so the look-up table approach is preferred. At the start of a simulation matrices of mean forward and backward reaction rate constants are evaluated over a user-defined range of temperature and temperature variance values. The user also defines the matrix density, by specifying the number of rows and columns (number of temperature and variance values) to use. The composite Simpsons rule is employed to integrate the reaction rate constant for each matrix entry. The sample space from 300K to 3000K is split into 1000 intervals in order to capture PDFs of a sharp nature.

During a simulation, linear interpolation between four tabulated values is used to find the required mean reaction rate constant from simulated temperature and temperature variance values.

4.8.2.2 Multivariate Beta PDF

The multivariate beta PDF of Girimaji [79; 80] is employed for the species mass fraction PDF:

$$P_Y(\hat{Y}_1,\ldots,\hat{Y}_{N_s}) = \frac{\Gamma(\sum_{\gamma=1}^{N_s}\beta_\gamma)}{\prod_{\gamma=1}^{N_s}\Gamma(\beta_\gamma)}\left[\delta\left(1-\sum_{\gamma=1}^{N_s}\hat{Y}_\gamma\right)\prod_{\gamma=1}^{N_s}\hat{Y}_\gamma^{\beta_\gamma-1}\right] \tag{4.114}$$

where δ and Γ are the delta and Gamma functions, respectively. An analytical solution is available [76] for this beta PDF to evaluate the integration in Equation 4.109, defined as:

$$\overline{c_M^{\nu_{Mr}}\prod_{\gamma=1}^{N_s}c_\gamma^{\nu_{\gamma r}}} = T_2T_3T_4 \tag{4.115}$$

with

$$T_2 = \bar{\rho}^{\nu_{Mr}}\prod_{\gamma=1}^{N_s}\left(\frac{\bar{\rho}}{W_\gamma}\right)^{\nu_{\gamma r}} = \bar{\rho}^{m_r}\prod_{\gamma=1}^{N_s}\left(\frac{1}{W_\gamma}\right)^{\nu_{\gamma r}} \tag{4.116}$$

$$T_3 = \left[\sum_{\gamma=1}^{N_s}\frac{\eta_\gamma}{W_\gamma}(\beta_\gamma+\nu_{\gamma r})\right]^{\nu_{Mr}} \tag{4.117}$$

$$T_4 = \frac{\prod_{\gamma=1}^{N_s}\prod_{k=1}^{\nu_{\gamma r}}(\beta_\gamma+\nu_{\gamma r}-k)}{\prod_{l=1}^{m_r}(B+m_r-l)} \tag{4.118}$$

where

$$m_{fr} = \nu^{Mr} + \sum_{\gamma}^{N_s}\nu'_{\gamma r}, \qquad m_{br} = \nu^{Mr} + \sum_{\gamma}^{N_s}\nu''_{\gamma r} \tag{4.119}$$

and the Beta function parameters are

$$\beta_\gamma = \widetilde{Y}_\gamma B, \qquad B = \frac{\sum_{\gamma=1}^{N_s}\widetilde{Y}_\gamma(1-\widetilde{Y}_\gamma)}{\sigma_Y} - 1 \tag{4.120}$$

where $\widetilde{Y}$ and σ_Y are the mean and variance for the species mass fraction.

4.8.2.3 Mean Reaction Rate

Feeding Equations 4.112 and 4.115 into Equation 4.107, the mean reaction rate can finally be evaluated as:

$$\bar{\dot{\omega}}_\alpha = W_\alpha \sum_{r=1}^{N_r} \left[\left(\nu''_{\alpha r} - \nu'_{\alpha r} \right) \left(T_{1f} T_{2f} T_{3f} T_{4f} - T_{1b} T_{2b} T_{3b} T_{4b} \right) \right] \tag{4.121}$$

4.8.2.4 Backward Reaction Rate Constant

Evaluation of the forward rate constant for reaction r, k_{fr}, is straightforward from the definition of Equation 3.15, using data from the chosen chemical mechanism. However, evaluation of the backward reaction rate constant, k_{br}, is a little more involved.

The backward reaction rate constant is found from [132]:

$$\ln k_{br} = \ln k_{fr} + \sum_{\alpha=1}^{N_s} (\nu''_{\alpha r} - \nu'_{\alpha r}) \left(\frac{\bar{g}_\alpha}{R^0 T} + \ln \frac{p_{ref}}{R^0} - \ln T \right) \tag{4.122}$$

where $\bar{g}_\alpha$ is the molar Gibbs function for species α and p_{ref} is the thermodynamic reference pressure. The molar Gibbs function can be expressed using polynomial coefficients:

$$\frac{\bar{g}_\alpha}{R^0 T} = \frac{\bar{a}^{(L)}_{\alpha, N_p+1}}{T} - \bar{a}_{\alpha,1} \ln T + (\bar{a}^{(L)}_{\alpha,1} - \bar{a}^{(L)}_{\alpha, N_p+2}) - \sum_{k=2}^{N_p} \frac{\bar{a}^{(L)}_{\alpha,k}}{k(k-1)} T^{k-1} \tag{4.123}$$

where the polynomial coefficients are provided by the CHEMKIN database. The thermodynamic reference pressure is a user supplied value but is taken as 1 bar for all reacting simulations presented.

4.9 Temporal Discretisation

Significant effort has been applied to the implementation of an upwind method for the discretisation of the inviscid fluxes, in order to ensure a monotonic solution for a discontinuous flow field. However, it is also possible [134] that spurious

oscillations can be introduced by the scheme employed for the temporal discretisation. For this reason, a three-step third order TVD Runge-Kutta scheme [134] is implemented in PULSAR, given by:

$$\begin{aligned}(\rho\phi)^{(1)} &= (\rho\phi)^n + \Delta t L((\rho\phi)^n) \\ (\rho\phi)^{(2)} &= \frac{3}{4}(\rho\phi)^n + \frac{1}{4}(\rho\phi)^{(1)} + \frac{2}{3}\Delta t L((\rho\phi)^{(1)}) \\ (\rho\phi)^{n+1} &= \frac{1}{3}(\rho\phi)^n + \frac{2}{3}(\rho\phi)^{(2)} + \frac{2}{3}\Delta t L((\rho\phi)^{(2)})\end{aligned} \tag{4.124}$$

for a differential equation of the form

$$\frac{\partial \rho\phi}{\partial t} = L(\rho\phi) \tag{4.125}$$

where $\Delta t L((\rho\phi)^i)$ is the change in conserved variable $\rho\phi$ at step i, given by equation 4.5.

This scheme has a maximum stable CFL number of 1. Although there are Runge-Kutta schemes with maximum CFL numbers above 1, theoretically allowing larger time steps to be used, due to the stiffness of the reacting species transport equations a CFL number below unity is in practice required for stability. Therefore, this scheme is used to make use of its TVD properties, third order of accuracy and efficient three-step formulation.

4.10 Turbulence Initialisation

The generation of turbulent structures in LES, either for initialisation purposes or turbulent inlet boundary conditions, is often desired. Fourier transform methods are often used, where a specific turbulence spectrum can be prescribed. However, due to the use of unstructured meshes by PULSAR, this approach is not possible. Instead, the method of Kempf et al. [64] is implemented, which is capable of generating turbulence for arbitrary geometries with a prescribed Reynolds stress tensor and turbulence length scales.

As a starting point, a different Gaussian profile of random numbers is applied to all three velocity components, u_i. To account for the variations in cell size,

the prescribed velocities in each cell are multiplied by square root of the volume of the cell. These velocities are then diffused to form turbulent structures of a prescribed length scale, through use of the following diffusion equation:

$$\frac{\partial u_i}{\partial t} = D\frac{\partial^2 u_i}{\partial x_j^2} \tag{4.126}$$

This equation can be solved using a simple iterative method with prescribed time step, Δt, and number of steps, n, where the diffusion coefficient, D, can be found from:

$$D = \frac{L_t^2}{2\pi n \Delta t} \tag{4.127}$$

where L_t is the required turbulence length scale. This length scale does not need to be constant throughout the domain and in particular it is useful to be able to prescribe a variable length scale for wall bounded flows. Near wall eddies can be scaled with distance from the wall, while a maximum free-stream length scale, L_{max}, (corresponding to the integral length scale) is prescribed. This results in the following definition for the spatially varying length scale used to calculate a spatially varying diffusion coefficient:

$$L_t = \min(L_{max}, \alpha_w y_w) \tag{4.128}$$

where α_w is a constant used to scale the near wall eddies with wall distance.

Once the random numbers have been diffused to form turbulent structures the required Reynolds stresses can be applied through use of a transformation by Lund et al. [135], forming the final velocity field $u_{i,L}$:

$$\begin{aligned} u_{x,L} &= a_{11}u_x \\ u_{y,L} &= a_{21}u_x + a_{22}u_y \\ u_{z,L} &= a_{31}u_x + a_{32}u_y + a_{33}u_z \end{aligned} \tag{4.129}$$

where the Reynolds stress tensor, R_{ij}, is applied through the tensor a_{ij}:

$$a_{ij} = \begin{bmatrix} \sqrt{R_{11}} & 0 & 0 \\ R_{21}/a_{11} & \sqrt{R_{22} - a_{21}^2} & 0 \\ R_{31}/a_{11} & (R_{32} - a_{21}a_{31})/a_{22} & \sqrt{R_{33} - a_{31}^2 - a_{32}^2} \end{bmatrix} \tag{4.130}$$

When using such turbulence profiles as inlet conditions to large eddy simulations, the prescribed Reynolds stresses and length scales can have a significant impact on the resulting flow. Therefore, knowledge of experimental turbulence properties is of paramount importance for accurate computational results. In Chapter 6, the influence of prescribed Reynolds stresses and near wall scaling parameter α_w, on the results of a LES study of a supersonic coaxial jet, is investigated.

4.11 Parallel Capabilities

In order to run on multiple processors the computational mesh must be decomposed so that each processor has its own subset of the domain on which to solve the governing fluid flow equations. The ParMETIS [136] code is used for domain decomposition.

In order to allow the computation of fluid flow between partitions a single layer of overlapping halo cells is used and parallel communication is enabled through the implementation of the message passing interface (MPI). The results presented in this thesis could not have been obtained without these parallel capabilities due to the significant computational requirements. Two high performance clusters were used for the simulations.

4.11.1 Stokes

Stokes is a 42 node cluster in the Department of Engineering at the University of Cambridge. Each node has two Intel Xeon E5540 quad-core processors and 24Gb of DDR3 memory, giving a total of 336 cores on the machine. An InfiniBand network is used for inter-node communication. Each job submitted is limited to 36 hours of run time.

4.11.2 HECToR

The HECToR XT6 machine is the UK national supercomputing service which consists of 464 compute blades housed in 20 cabinets. Each blade has four nodes with each node having two 12-core AMD Opteron 2.1GHz Magny Cours processors, giving a total of 44,544 cores over the machine. Each 12-core processor has access to 16Gb of shared memory. Each job submitted is limited to 12 hours of run time.

The XT6 machine started life with each processor coupled to a Cray SeaStar2 routing and communications chip, but this has recently been upgraded to the Cray Gemini interconnect.

4.11.3 Scaling

The scalability of PULSAR has been evaluated using the HECToR cluster. This study corresponds to a *strong* scaling study, whereby the size of the computational mesh is held constant and split between an increasing number of cores, starting with 264 and 528 cores and then increasing the number of cores by 528 up to a maximum of 4224. The computational mesh for the SCHOLAR large eddy simulation to be presented in Chapter 7 is used, consisting of 36.8M hexahedral elements. A reacting simulation using the assumed PDF combustion model with second order upwind spatial and three step Runge-Kutta temporal discretisations is conducted.

The normalised speed of a simulation is calculated as the time per iteration for the 264 core calculation, over the time per iteration for the x core simulation in question,

$$\text{Normalised Speed} = \frac{t_{iter,264}}{t_{iter,x}} \tag{4.131}$$

where the iteration time is calculated as an averaged of the first 300 time steps.

Figure 4.16 shows the scaling performance of PULSAR on the HECToR XT6 machine before and after the Gemini interconnect upgrade. It can be seen that with the upgraded communication between nodes, the scaling is improved. The time per iteration was also improved, which reduced from 18.1s to 16.4s for the 264 core simulation.

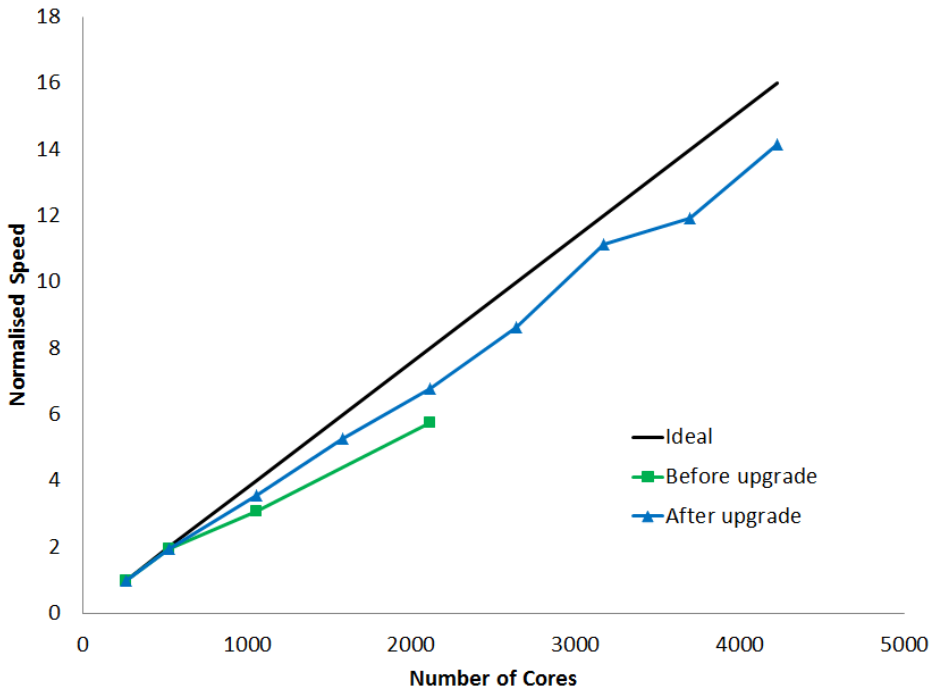

Figure 4.16: Strong scaling of PULSAR on the HECToR XT6 cluster, before and after interconnect upgrade

Chapter 5

Supersonic Non-Reacting Coaxial Jet - RANS

After development of a new code, significant validation is required. Since PULSAR is to be used for the simulation of combustion, validation of its mixing prediction capabilities is of primary importance. This analysis is more straightforward for non-reacting flows, hence a non-reacting coaxial jet is simulated for this purpose. Results are to be presented for the simulation of a supersonic coaxial helium jet, since this test case was developed with the validation of CFD software in mind, particularly the validation of codes to be used in the simulation of supersonic combustion. Therefore, as well as providing validation for PULSAR, this test case can simultaneously be used to investigate the capabilities of computational methods for the simulation of mixing in a scramjet combustor.

5.1 Description

The experiment in question [100] was conducted at NASA Langley Research Center. As can be seen from Figure 5.1, the coaxial jet assembly consists of both a central jet and a co-flow. Both jets have an exit Mach number of 1.8 (see Figure 5.2), but since the central jet consists mostly of helium (see Figure 5.3) its density is much lower than that of the air co-flow, giving it a much higher speed of sound and therefore a much higher exit velocity (see Figure 5.4).

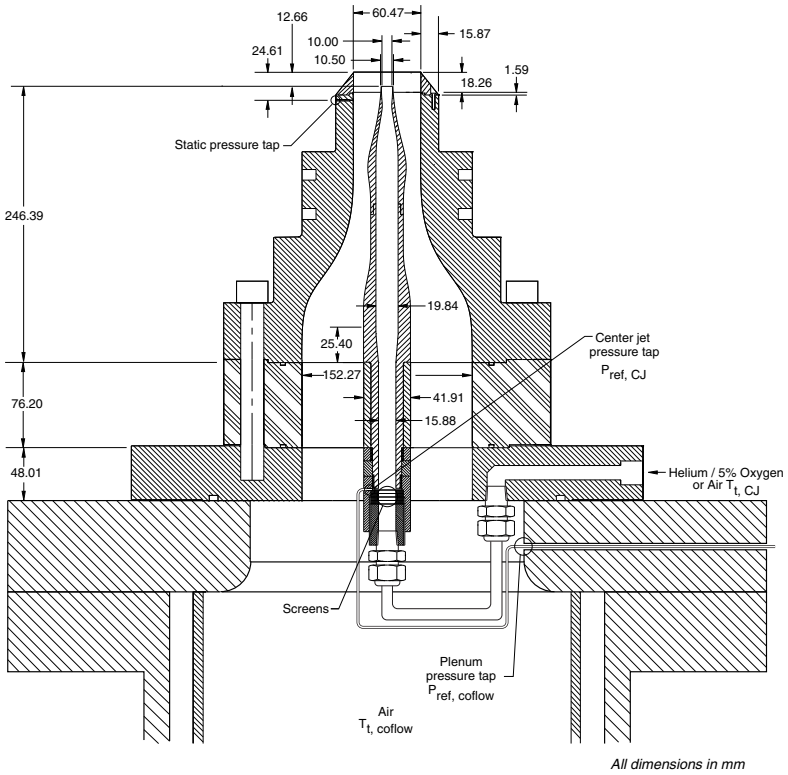

Figure 5.1: Coaxial jet assembly [100]

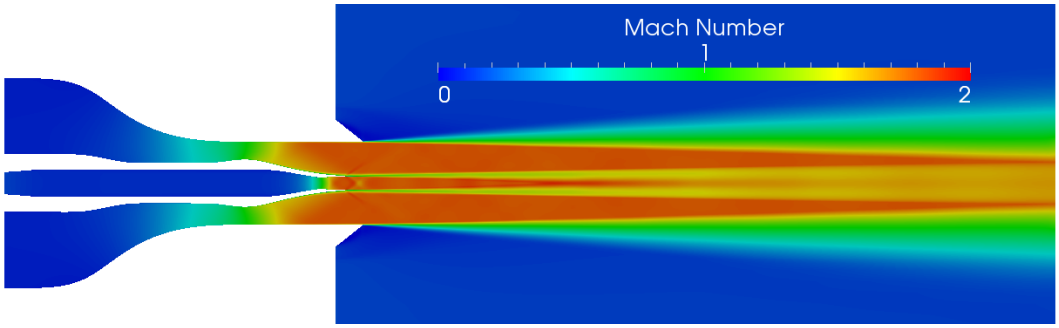

Figure 5.2: Mach number profile

This generates a compressible shear layer between the central and co-flow jets [100], as would be found in a scramjet combustor due to fuel injection into a supersonic flow. The use of helium for the central jet is to replicate the light gas fuel hydrogen and to simulate the subsequent mixing process, avoiding the need

for the simulation of combustion when using this test case for code validation.

The remaining mass fraction of 0.2961 for the central jet is oxygen, which corresponds to a mole fraction of just 0.05. This oxygen is added to the central jet to allow the use of an oxygen flow-tagging technique for non-intrusive velocity measurements.

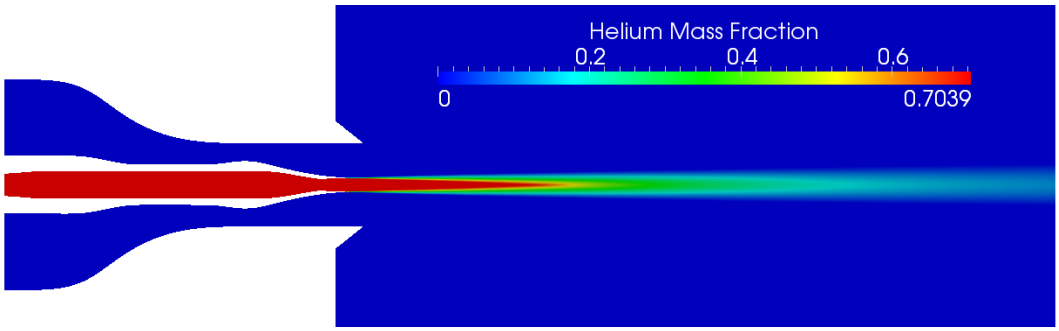

Figure 5.3: Helium mass fraction profile

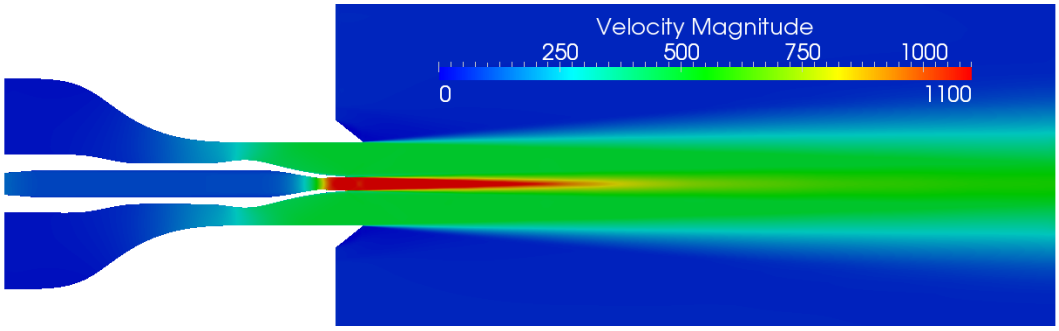

Figure 5.4: Velocity magnitude profile, m/s

5.1.1 Experimental Data

Both mean and rms values for the axial component of velocity were obtained using the Raman excitation plus laser-induced electronic fluorescence (RELIEF) technique. The flow was also probed to obtain pitot pressure, total temperature and gas concentration measurements.

Since the concentration measurements were actually measurements for mole fraction of the centre jet gas, they are effectively normalised measurements for helium, which have been processed to provide both mole and mass fraction profiles. For direct comparisons of experimental and computational data, the numerical helium mass fractions, $Y_{He,CFD}$, should be normalised by the centre jet helium mass fraction:

$$Y_{He,norm} = \frac{Y_{He,CFD}}{0.7039} \tag{5.1}$$

Pitot pressure, mole fraction and velocity measurements are available at 14 locations down the axis of the jet. However, the locations for velocity data do not correspond to the locations at which pitot pressure and concentration measurements were taken. The experimental profiles are in the radial direction across the jet.

Since the flow is supersonic, some post-processing is required to convert the static pressure data from numerical computations to pitot pressure measurements. Figure 5.5 shows the resulting pitot probe bow shock, which can be assumed to be a normal shock on its centreline.

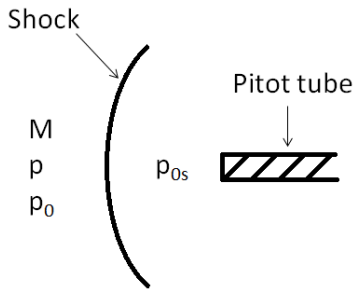

Figure 5.5: Pitot tube shock schematic

The pitot pressure, p_{pitot}, can therefore be calculated from the free-stream static pressure, p, and Mach number, M:

$$p_{pitot} = p_{0s} = p\left(\frac{\gamma+1}{2}M^2\right)^{\frac{\gamma}{\gamma-1}}\left(\frac{2\gamma}{\gamma+1}M^2 - \frac{\gamma-1}{\gamma+1}\right)^{\frac{1}{1-\gamma}} \tag{5.2}$$

where p_{0s} is the post-shock stagnation pressure. However, in subsonic regions of

the flow the pitot pressure is equivalent to the free-stream stagnation pressure, p_0:

$$p_{pitot} = p_0 = p\left(1 + \frac{\gamma - 1}{2}M^2\right)^{\frac{\gamma}{\gamma-1}} \tag{5.3}$$

5.1.2 Computational Mesh

Figure 5.6 shows the mesh used for the RANS simulations. ANSYS ICEM CFD is used to generate a three-dimensional mesh using the multi-block technique, employing O-grids to handle the coaxial nature of the problem. The mesh is purely hexahedral and contains 3.8M cells.

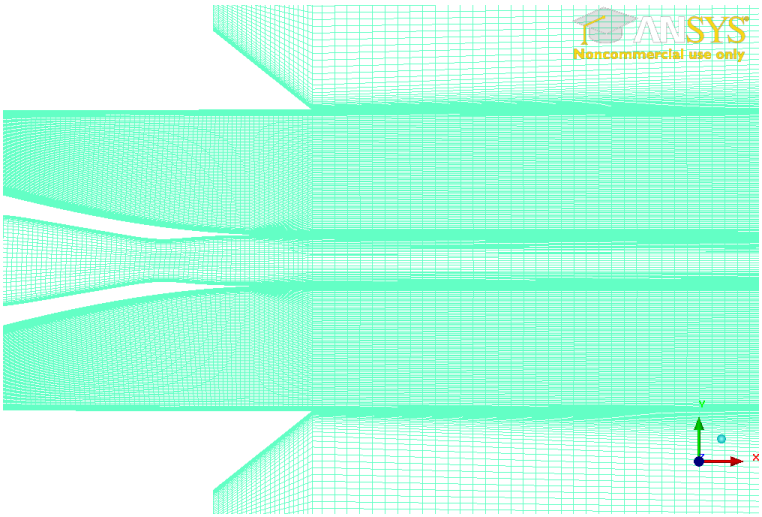

Figure 5.6: Slice through RANS mesh at z = 0, near the jet exit

Due to the use of O-grids, boundary layer cells far from the centreline of the jet can have very high aspect ratios. This problem is encountered for the boundary layer cells in the co-flow jet and therefore the wall normal spacing was relaxed in this region. For the co-flow surfaces the near wall spacing transitions from 0.5mm at inlet to 2×10^{-6}m near the jet exit. However, for the central jet a near wall spacing of 2×10^{-6}m is uniformly used. This means the y^+ values in the co-flow are mostly outside the viscous sublayer, as shown by Figure 5.7, with Spalding's equation used to obtain the wall shear stress. For the central jet the

y^+ values are less than three everywhere, with the near wall cells lying inside the linear region of the boundary layer.

A total of 24 cells are used across the 0.25mm central jet tip and the axial spacing in the free-stream is equal to 2.5mm. The mesh downstream of the jet extends 0.5m (50 central jet diameters) and 0.44m (44 central jet diameters) in the axial and radial directions, respectively. The large radial extent ensures the presence of the far-field boundary does not have an influence on the jet behaviour.

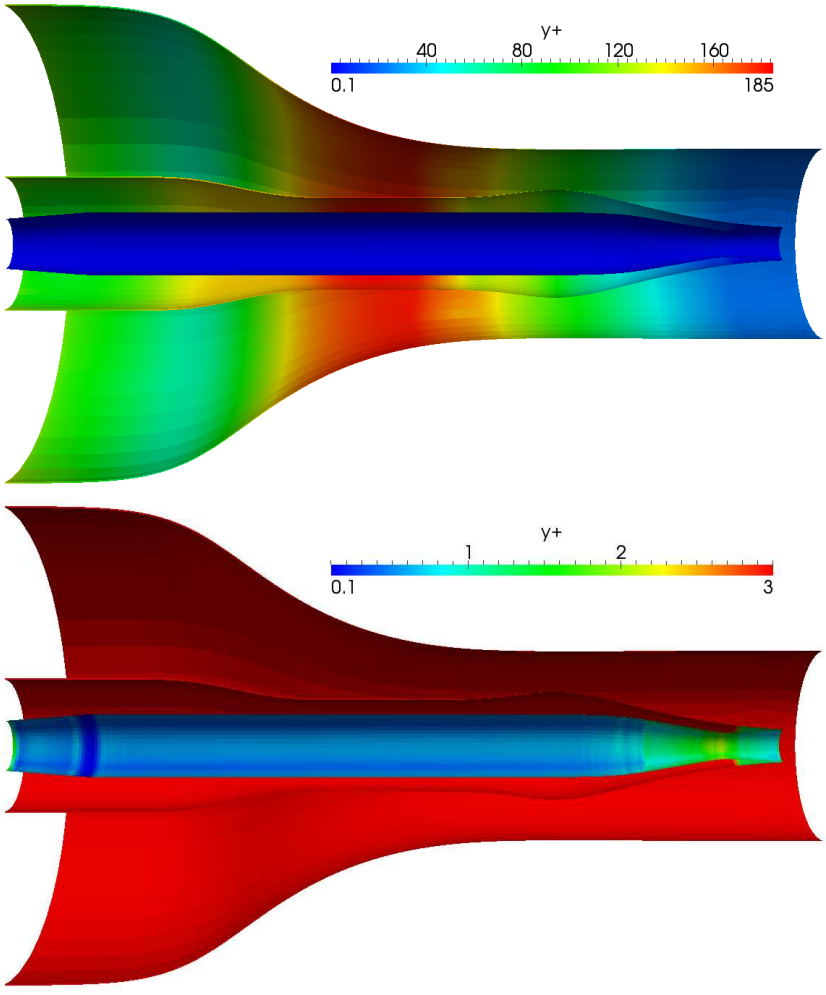

Figure 5.7: y^+ values: Scaled to show distributions for the co-flow (top) and central (bottom) jet surfaces

5.1.3 Boundary Conditions

Although the jets have an exit Mach number above unity, this is caused by flow acceleration through a converging diverging nozzle. All three inlets to the domain therefore have subsonic boundary conditions. The inlet stagnation properties and flow composition data are presented in Table 5.1.

	Centre Jet	Co-flow Jet	Ambient
Stagnation pressure, p_0 (Pa)	628300	580000	101325
Stagnation temperature, T_0 (K)	306.0	300.0	294.6
Y_{He}	0.7039	0.0000	0.0000
Y_{O_2}	0.2961	0.2300	0.2300
Y_{N_2}	0.0000	0.7700	0.7700

Table 5.1: Coaxial jet inlet boundary conditions.

The inlet boundary conditions for the k and ω turbulence model variables are:

$$k_{in} = \frac{0.001 \mu U_\infty}{\rho L_{ref}} \tag{5.4}$$

$$\omega_{in} = \frac{5 U_\infty}{L_{ref}} \tag{5.5}$$

where the reference length is set to 1mm, to be on the order of the tip thickness.

The outlet boundary analyses whether to apply subsonic or supersonic conditions, since the outlet boundary in the outer shear layer between the co-flow and ambient air will transition between these two regimes. For supersonic outlet Mach numbers the boundary values are simply interpolated from inside the domain. For subsonic outlet Mach numbers an exit static pressure of 101325 Pa is applied.

The no-slip condition is applied to all jet surfaces and an inviscid condition is applied to the far-field boundary.

5.1.4 Computational Methods

The AUSM+UP scheme is used for the spatial discretisation, with second order of accuracy achieved through use of linear interpolation with the Van Rosendale

gradient limiter. The three-step, third order TVD Runge Kutta method is used for temporal integration, with a CFL number of 0.5. The Menter SST turbulence model is employed with constant values for the turbulent Prandtl and Schmidt numbers.

Since convergence acceleration methods, such as multi-grid, are not implemented in PULSAR and since this shear layer jet is diffusion dominated, the computational solution may still be changing between time steps even after residuals appear to have leveled out. For this reason, monitoring points are used to study the change in variables over time. Once variables such as the species mass fraction, temperature, pressure and velocity have achieved a steady state, numerical convergence can be declared. An example of this convergence monitoring can be seen in Figure 5.8, which is the convergence history for the helium mass fraction, down the centre-line of the jet at an axial location of 0.3m, for the fine mesh to be presented in Section 5.2.5.

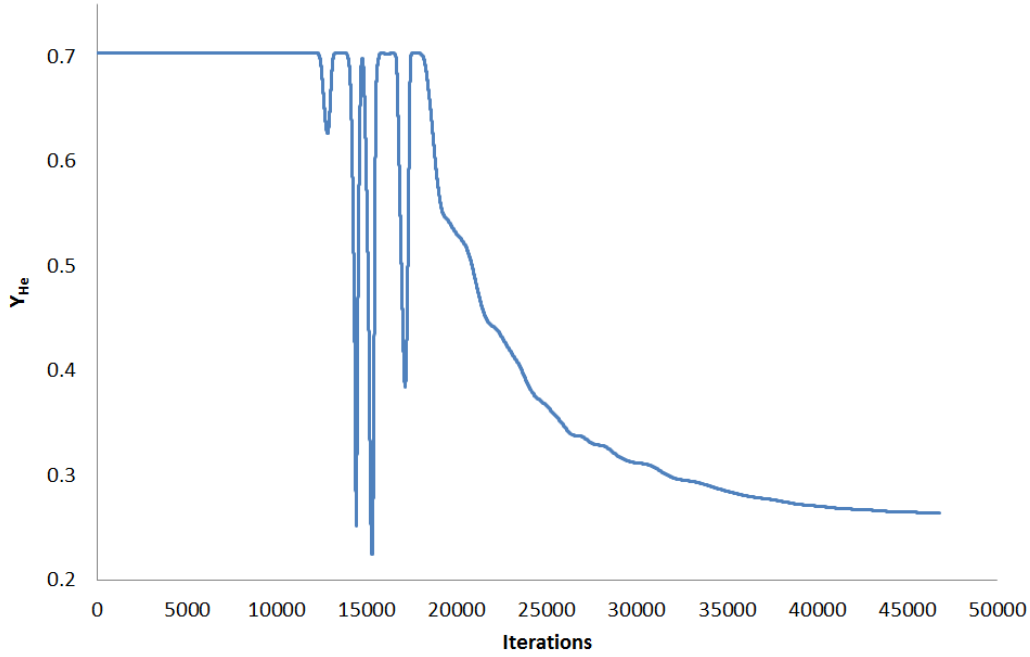

Figure 5.8: Convergence studied through data from monitor point

Simulations are carried out on 24 cores of the Stokes cluster. After initialisation with an inviscid solution, convergence is obtained in approximately 60 hours after approximately 45,000 iterations.

5.2 Results

Due to the presence of an inner shear layer between the central and co-flow jets and an outer shear layer between the co-flow and ambient air, this coaxial jet is diffusion dominated. Since validation of the species mixing prediction capabilities of PULSAR is a primary objective, the turbulent diffusion term in the species transport equation (Equation 2.38) will play an important role in the simulations; replicated here for clarity:

$$\frac{\mu_t}{Sc_t}\frac{\partial \widetilde{Y_\alpha}}{\partial x_j}$$

It is therefore sensible to first investigate the influence on computational results of model parameters in this term.

5.2.1 Turbulent Schmidt Number

Since the species diffusion term is proportional to the inverse of the turbulent Schmidt number, it is important to investigate how sensitive the computational results are to changes in this model constant. Keeping the turbulent Prandtl number fixed at 0.9 for now, but choosing two values for the turbulent Schmidt number of 0.7 and 1.0, these sensitivities can be investigated.

It can be seen from Figure 5.9 that for both turbulent Schmidt number values good agreement with experimental data for normalised helium mass fraction is obtained near the jet exit, but at locations further downstream a gross over prediction of the spreading rate of the central jet is obtained.

Increasing the turbulent Schmidt number to 1.5 provides computational results which are in better agreement with the experimental data, but it is generally accepted that Schmidt numbers far above 1 are too high.

Figure 5.10 shows the influence of varying turbulent Schmidt number on the

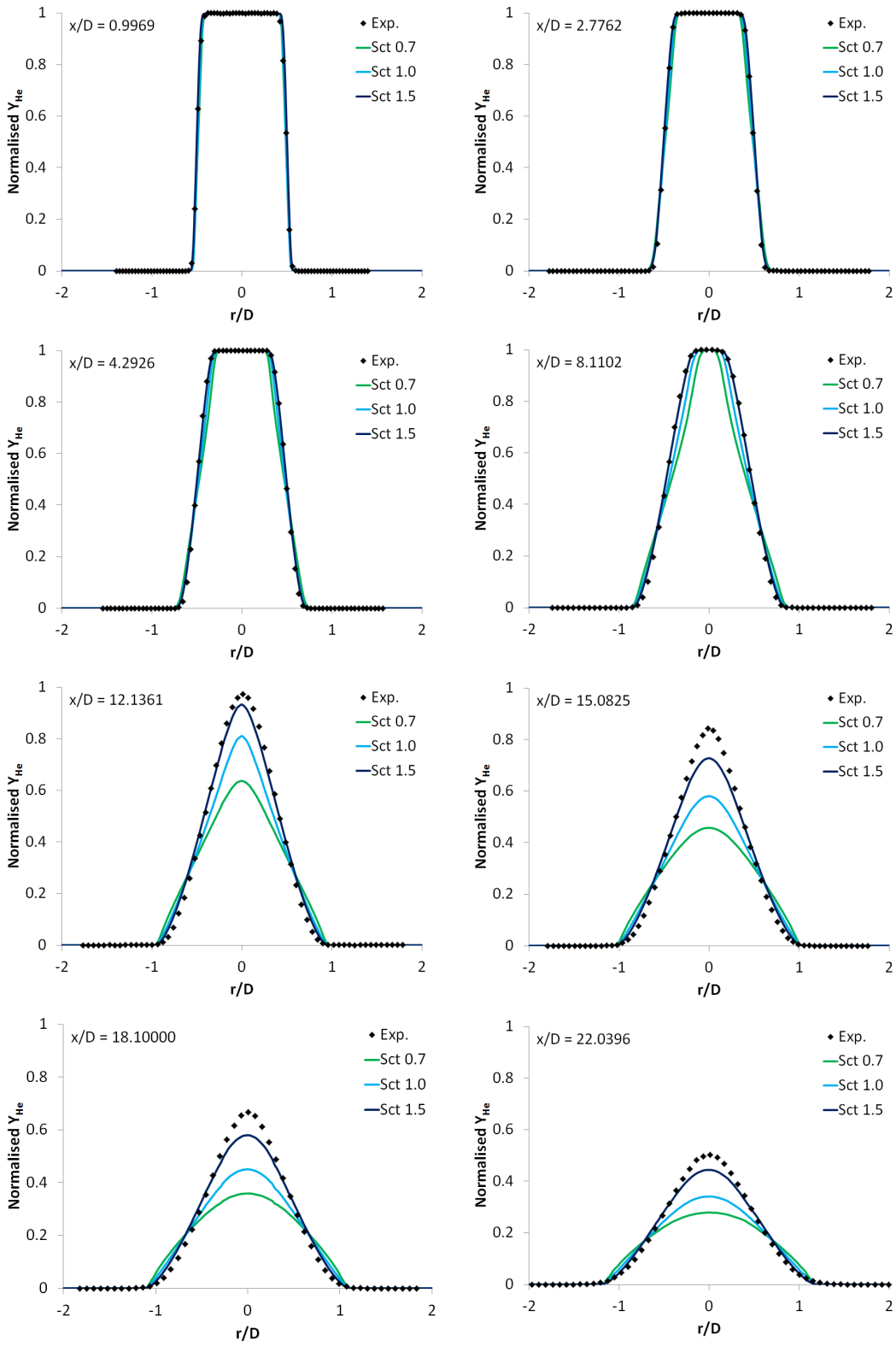

Figure 5.9: Radial (r) profiles of normalised helium mass fraction at several axial (x) locations, with varying Schmidt number and a Prandtl number of 0.9

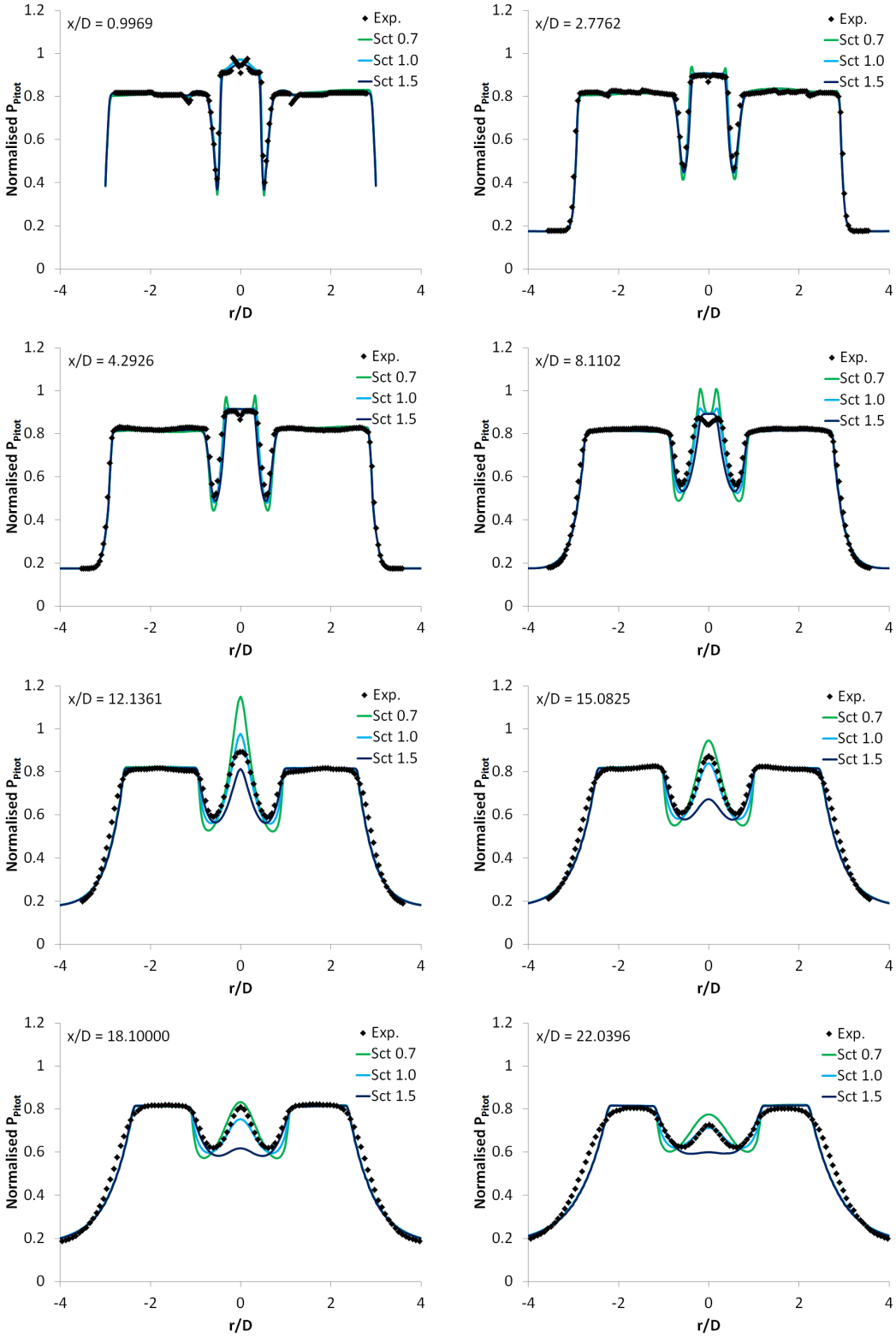

Figure 5.10: Radial (r) profiles of normalised pitot pressure at several axial (x) locations, with varying Schmidt number and a Prandtl number of 0.9

pitot pressure profiles, where the normalised pitot pressure is defined as:

$$p_{pitot,norm} = \frac{p_{pitot}}{580000} \tag{5.6}$$

with 580000 Pa corresponding to the stagnation pressure at the co-flow inlet.

It can be seen that variations in the turbulent Schmidt number have a similar influence on the pitot pressure profiles as for the species mass fraction. The results can be explained by analysing the magnitude of the species diffusion coefficient, where small turbulent Schmidt numbers correspond to high levels of diffusion corresponding high losses in stagnation pressure.

However, none of the results presented are satisfactory, since it is a turbulent Schmidt number of 1.0 which gives the best agreement with experimental data for the pitot pressure but a corresponding poor agreement with experimental data for the helium mass fraction.

5.2.2 Compressibility Correction

Looking back at the species turbulent diffusion term, it can be seen there is also a dependence on the eddy viscosity, which can be scaled through application of compressibility corrections to the turbulence model. Compressibility corrections reduce the levels of eddy viscosity in regions of high turbulence Mach number, as discussed in Section 4.6.4.

Figure 5.11 compares computational results using the Sarkar, Zeman and Wilcox compressibility corrections, to experimental data. The turbulent Prandtl and Schmidt numbers are held constant at 0.9 and 1.0, respectively.

It can be seen that all compressibility corrections improve the mixing prediction when compared to results from the simulation without corrections applied, but to varying degrees. The Wilcox compressibility correction provides the smallest improvement due to the fact that it is only triggered in regions of the flow which have a turbulence Mach number above 0.25. It can be seen from Figure 5.12 that, because of the high speed of sound due to the low density of helium, only small regions of the central jet flow satisfy this criteria. Although excellent agreement with experimental data is obtained at x/D = 12.1361, further downstream of this location the Wilcox compressibility correction is not activated for

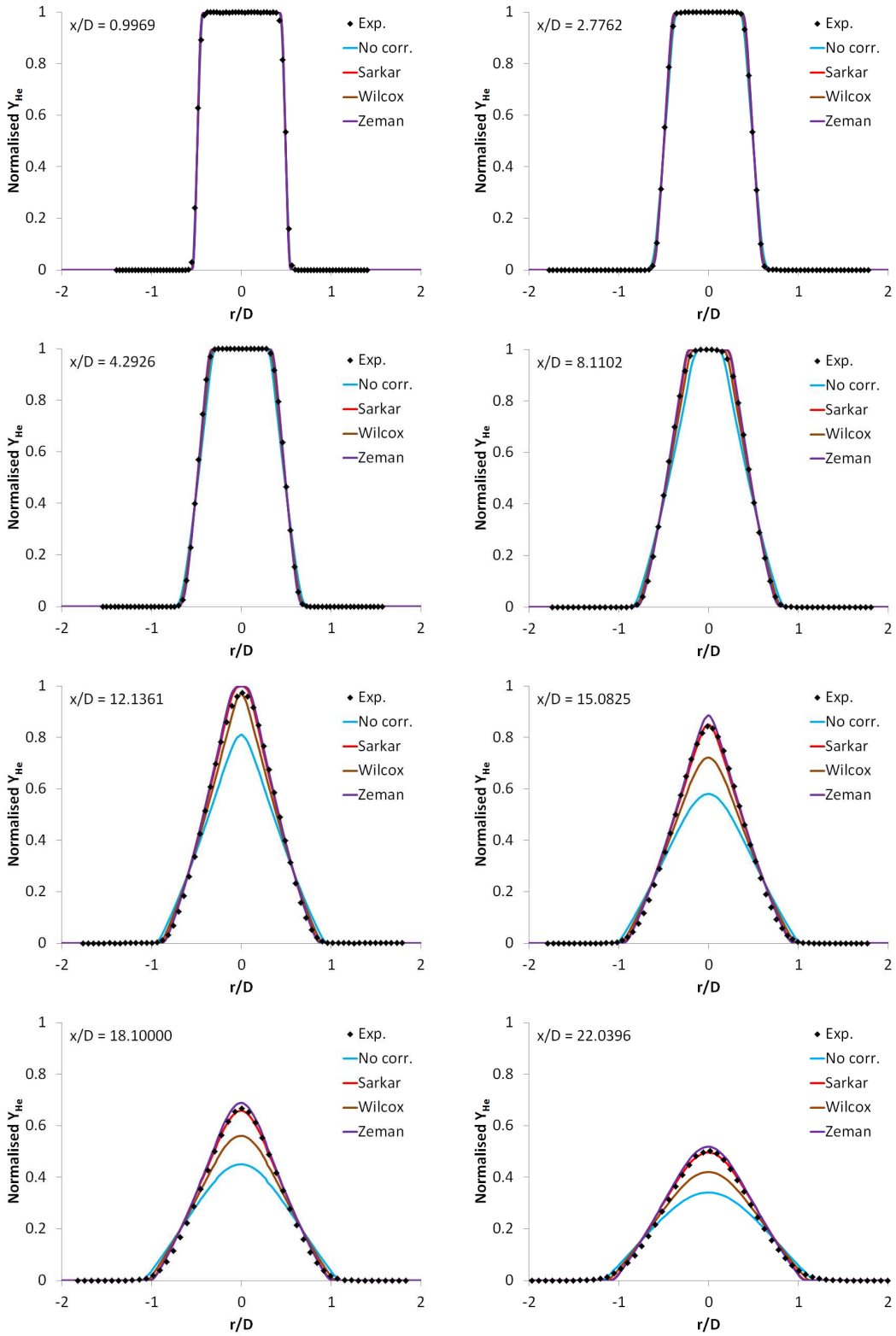

Figure 5.11: Radial (r) profiles of normalised helium mass fraction at several axial (x) locations, with different compressibility corrections and turbulent Schmidt and Prandtl numbers of 1.0 and 0.9, respectively

the inner shear layer and hence no further improvements are visible. The Sarkar compressibility correction gives the best agreement with experimental data, but of course these results could all be scaled through alteration of the turbulence Schmidt number.

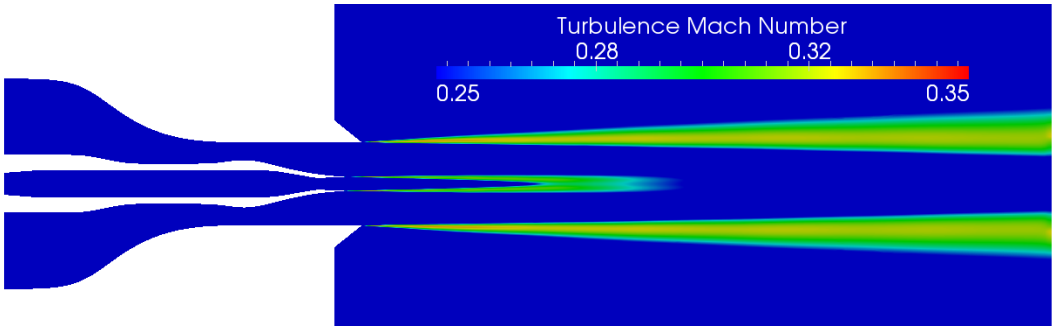

Figure 5.12: Turbulence Mach number profile

Figure 5.13 shows that the introduction of a compressibility correction has a significant impact on the pitot pressure predictions, having a detrimental effect on the accuracy of the results obtained. Again this is due to the reduction in the species diffusion coefficient causing a reduction in stagnation pressure loss but also because the scaled eddy viscosity is also present in the turbulent diffusion term for the energy equation:

$$\frac{\mu_t c_p}{Pr_t}\frac{\partial \widetilde{T}}{\partial x_j}$$

with a reduction in the eddy viscosity also causing a reduction in the stagnation energy, and hence pressure, loss.

5.2.3 Turbulent Prandtl Number

This turbulent energy diffusion term also introduces the influence of the turbulent Prandtl number on the results obtained. Figure 5.13 also demonstrates the significant influence of the variation of this model constant on the pitot pressure profiles. Decreasing the turbulent Prandtl number from 0.9 to 0.5 provides a

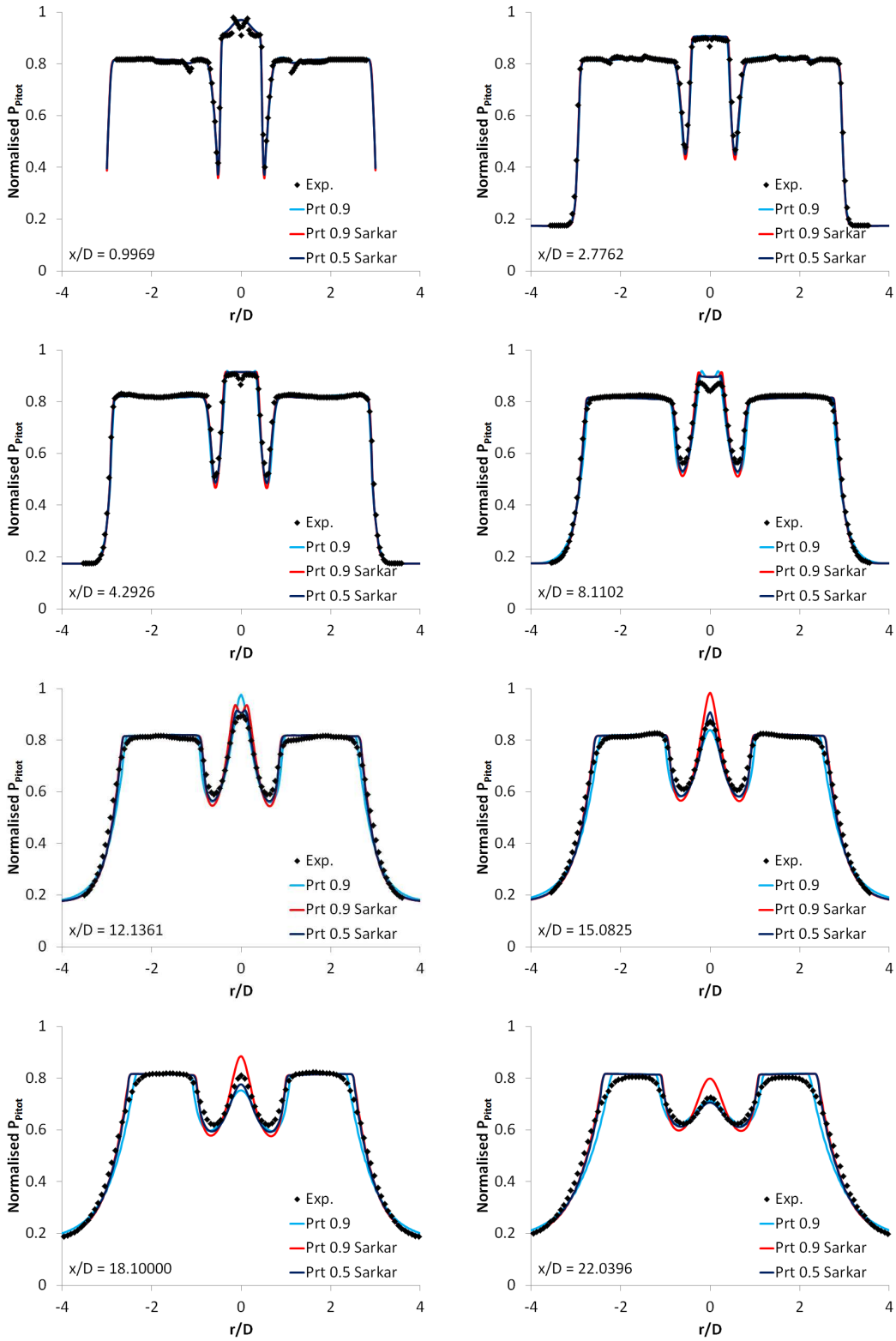

Figure 5.13: Radial (r) profiles of normalised pitot pressure at several axial (x) locations, showing the influence of the Sarkar compressibility correction and variation of the turbulent Prandtl number, with the turbulence Schmidt number held constant at 1.0

better agreement with experimental data, when the turbulent Schmidt number is held constant at 1.0 and the Sarkar compressibility correction is employed.

Since the turbulent Prandtl number does not arise in the species transport equation, the influence of its alteration on the species mass fraction distribution is minimal, as shown in Figure 5.14.

5.2.4 Velocity Distribution

The computational setup has been tuned to give good agreement with experimental data for composition and pitot pressure profiles. With the turbulent Schmidt number and turbulent Prandtl number held constant at 1.0 and 0.5, respectively, and the Sarkar compressibility correction employed to scale the eddy viscosity, computational predictions for the mean and fluctuating velocity components can be evaluated.

Experimental data is only available for the axial velocity component and it can be seen in Figure 5.15 that reasonable agreement is obtained with computational results for the mean values, however there is some disagreement with the magnitude of the central jet velocity at several locations down its axis.

The Boussinesq approximation in Equation 2.27 used to calculate the Reynolds stress tensor can be employed to estimate the levels of fluctuating velocity:

$$\sqrt{\widetilde{u_i'u_j'}} = \sqrt{\frac{\frac{2}{3}\bar{\rho}k\delta_{ij} - 2\mu_t\left(\tilde{S}_{ij} - \frac{1}{3}\frac{\partial\tilde{u}_k}{\partial x_k}\delta_{ij}\right)}{\bar{\rho}}} \tag{5.7}$$

as was done by Baurle and Edwards [15]. Another basic approximation can also be obtained from the turbulence kinetic energy of Equation 2.28:

$$\sqrt{\widetilde{u_i'u_i'}} = \sqrt{\frac{2k}{3}} \tag{5.8}$$

where the 3 comes from summation over all three velocity directions.

The Boussinesq approximation is capable of providing direction dependent rms velocities due to the presence of the strain tensor, $\tilde{S}_{ij}$, whereas the rms velocities calculated from the turbulence kinetic energy are isotropic due to its scalar nature.

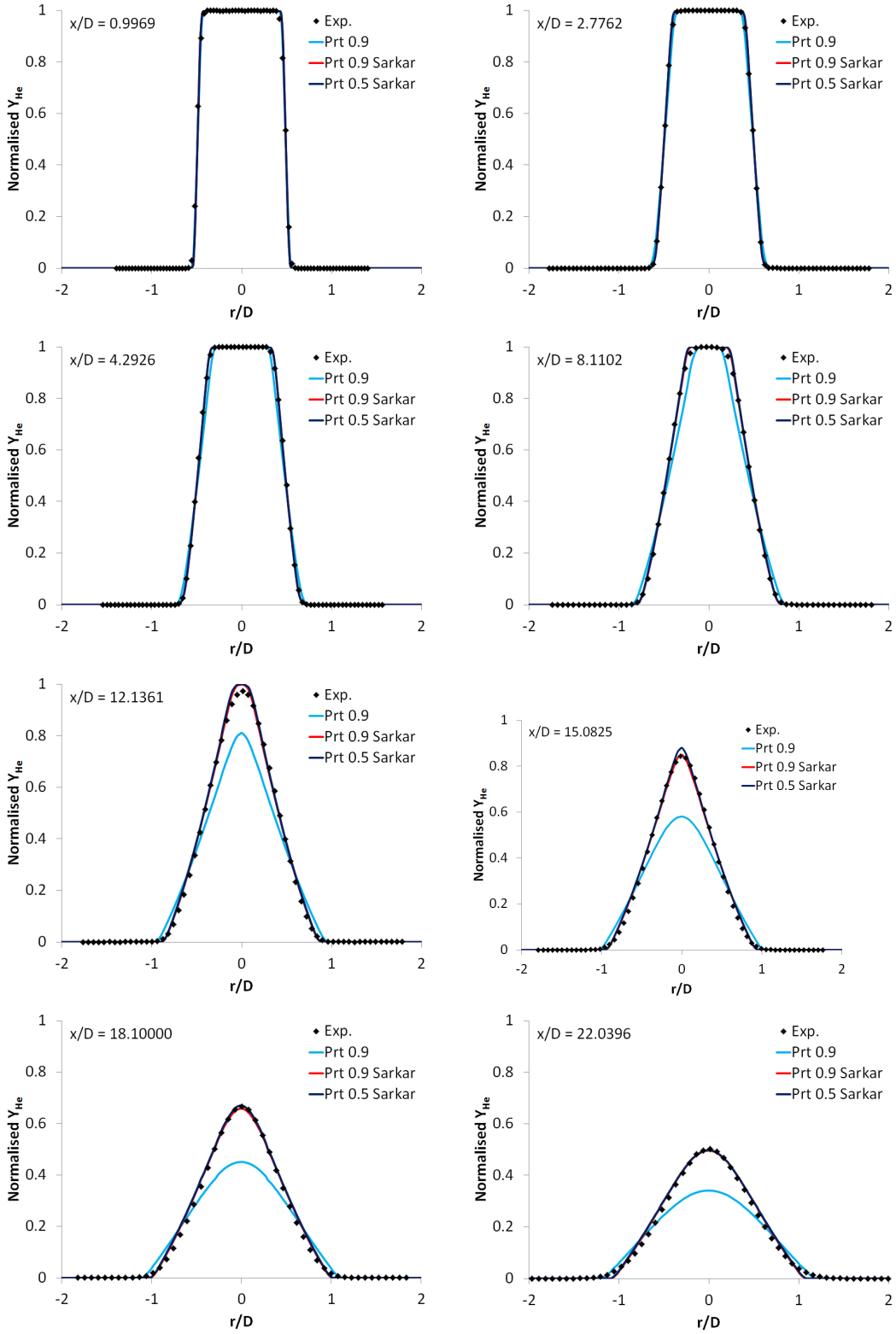

Figure 5.14: Radial (r) profiles of normalised helium mass fraction at several axial (x) locations, with different turbulent Prandtl numbers and the turbulent Schmidt equal to 1.0

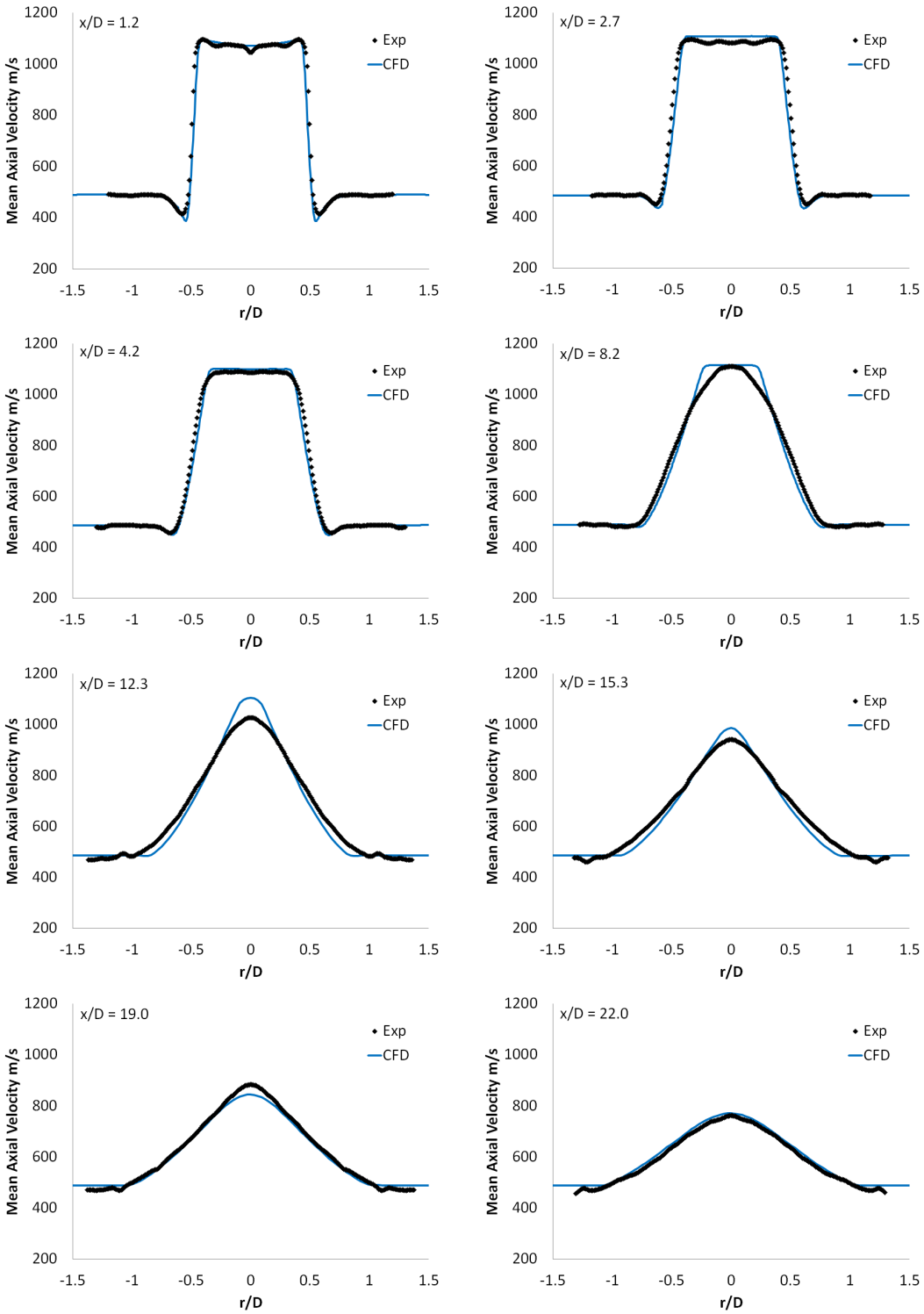

Figure 5.15: Radial (r) profiles of mean axial velocity at several axial (x) locations.

Figure 5.16 compares the Boussinesq and turbulence kinetic energy approximations to the rms axial velocity with experimental data. It can be seen that both approximations are capable of providing good predictions for the magnitude of the peaks in the rms velocity data and the general profile is well captured. However, there is poor agreement with experimental data for the centre of the central and co-flow jets. The agreement starts to improve for the central jet profile at an axial location of x/D = 15.3 but remains poor in the co-flow.

In order to investigate why the Boussinesq and turbulence kinetic energy approaches give comparable predictions for the axial rms velocity, the magnitude of the terms in the Boussinesq approximation can be compared, with the turbulence kinetic energy, strain and divergence terms respectively defined as:

$$\frac{2}{3}\bar{\rho}k, \quad 2\mu_t\frac{\partial\tilde{u}}{\partial x}, \quad \frac{2}{3}\mu_t\left(\frac{\partial\tilde{u}}{\partial x}+\frac{\partial\tilde{v}}{\partial y}+\frac{\partial\tilde{w}}{\partial z}\right) \tag{5.9}$$

Figure 5.17 clearly shows the turbulence kinetic energy term dominates the Boussinesq approximation at all axial locations and explains why comparable approximations to the rms axial velocity are found from the Boussinesq and turbulence kinetic energy approaches. This confirms the importance of including the turbulence kinetic energy term in both the Boussinesq approximation and mean stagnation energy equation (2.29).

The reason for the poor agreement with experimental data in the central and co-flow jet core regions can be explained by Figure 5.18 which shows the absence of turbulence kinetic energy in these areas, since it is concentrated in high velocity gradient shear layer regions. Once the central jet shear layers merge at the centreline, better agreement with experimental data for the core region is obtained. This is due to the Boussinesq approximation requiring the presence of velocity gradients to become active.

In order to see if the directional strain term plays a more significant role in the Boussinesq approximation for the transverse rms velocities, the corresponding values are compared to the turbulence kinetic energy approximation in Figure 5.19. It can be seen that both approaches are again in excellent agreement, confirming the turbulence kinetic energy term in Equation 5.7 dominates in all directions. The Boussinesq approximation therefore produces isotropic Reynolds stresses for

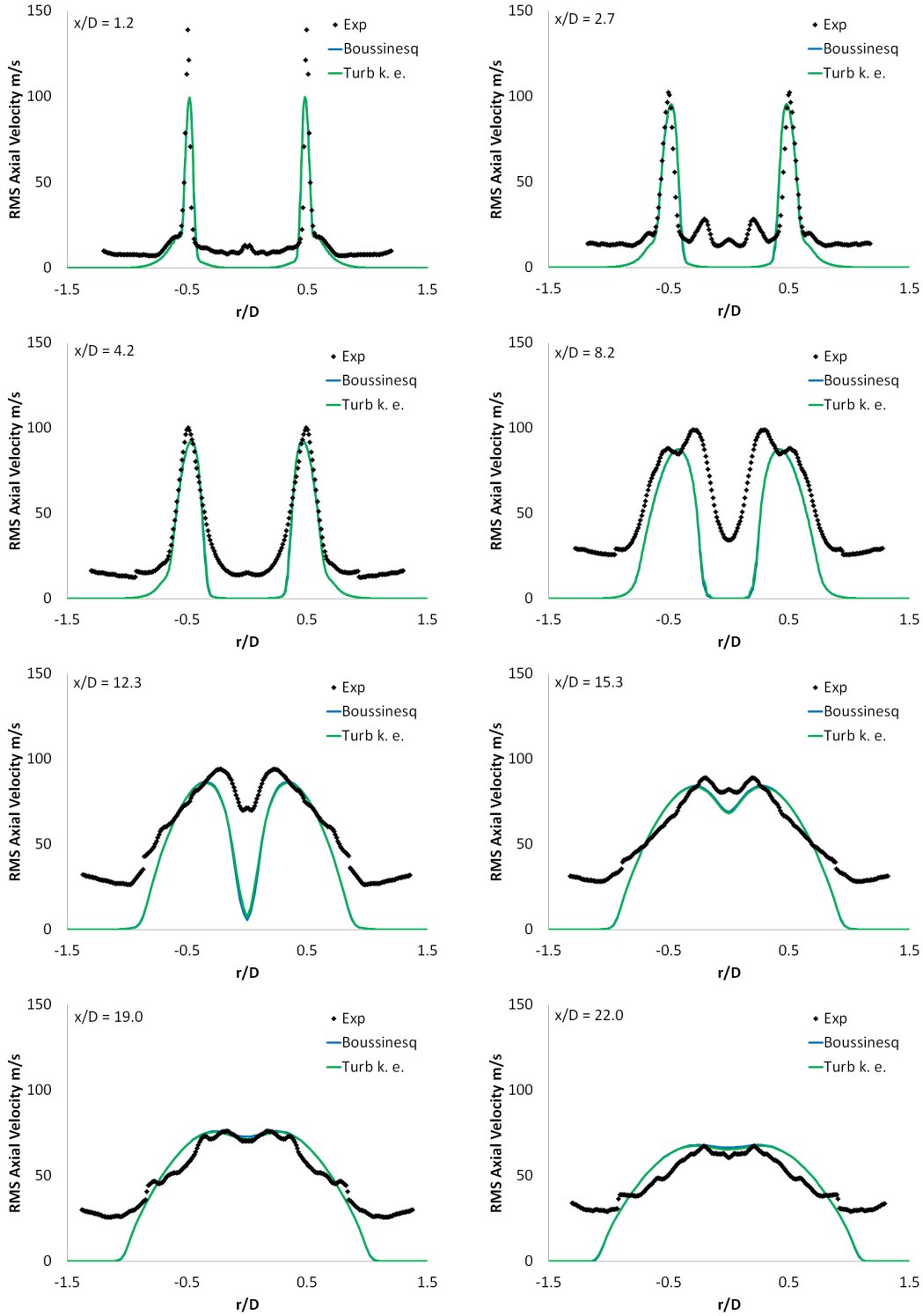

Figure 5.16: Radial (r) profiles of the axial rms velocity, comparing the Boussinesq and turbulence kinetic energy approximations to experimental data at several axial (x) locations.

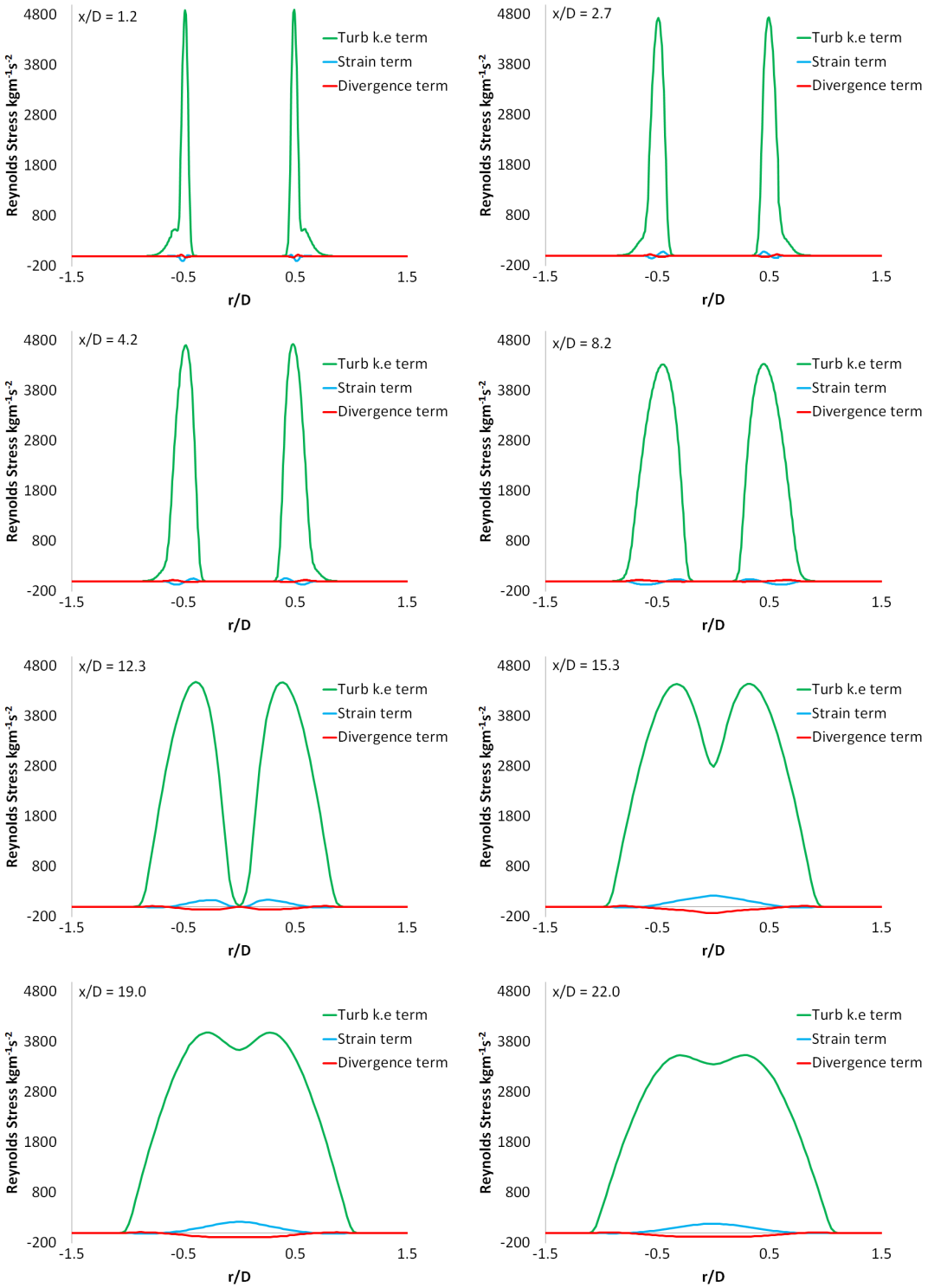

Figure 5.17: Radial (r) profiles of the terms involved in the Boussinesq approximation to the Reynolds stress.

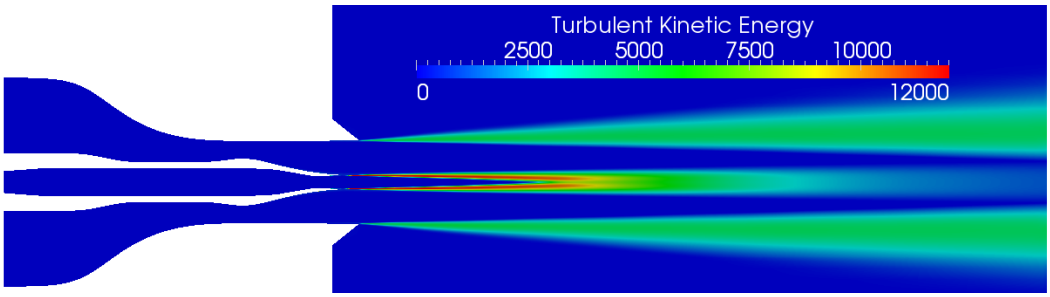

Figure 5.18: Turbulence kinetic energy profile

the test case in question; unfortunately no experimental data is available for rms velocities in the y and z directions to confirm whether this behaviour is correct.

5.2.5 Mesh Convergence

In order to check mesh convergence for the RANS results presented, a simulation is conducted on a finer mesh, which is discussed in more detail in Chapter 6. The fine mesh contains 22.2M hexahedral cells and the simulation was run on 128 cores of the Stokes cluster.

Figures 5.20 and 5.21 compare normalised helium mass fraction and pitot pressure profiles, where 'coarse' corresponds to the mesh presented in Section 5.1.2 and 'fine' for the LES mesh of Chapter 6. The turbulent Prandtl and Schmidt numbers are held constant at 0.9 and 1.0, respectively, and the Sarkar compressibility correction is employed. It can be seen that minimal differences are present between the two sets of data, confirming mesh convergence for the RANS results obtained.

5.3 Summary

The sensitivities of RANS to choices in model constant values has been presented. Although it appears these model constants can be tuned to give accurate results, different model constants would be required for the simulation of different test cases, since they scale the eddy viscosity which is used to model the problem dependent large scales of the flow. It is therefore very difficult to obtain accurate

results using RANS methods in a research environment, where the experimental data required to tune model constants may not be available. It is particularly difficult to use these methods for combustion research due to sensitivities of the turbulent diffusion of reacting species to the turbulent Schmidt number.

However, it should be stated that although computational accuracy appears sensitive to the choice of values for the model constants, RANS methods are capable of predicting the correct trends in the results obtained and can therefore still have an important role to play in early stage design activities.

In order to avoid the problems presented with constant turbulent Schmidt and Prandtl numbers, models attempting to vary these parameters in space and time have been attempted [137]. However, these methods can be expensive to use through the introduction of additional transport equations and still suffer from modelling constraints. It is more desirable to employ a computational method which is less sensitive to the choice of such parameters, through reducing the modelling effort and attempting to directly capture a higher level of the physics involved; for example LES.

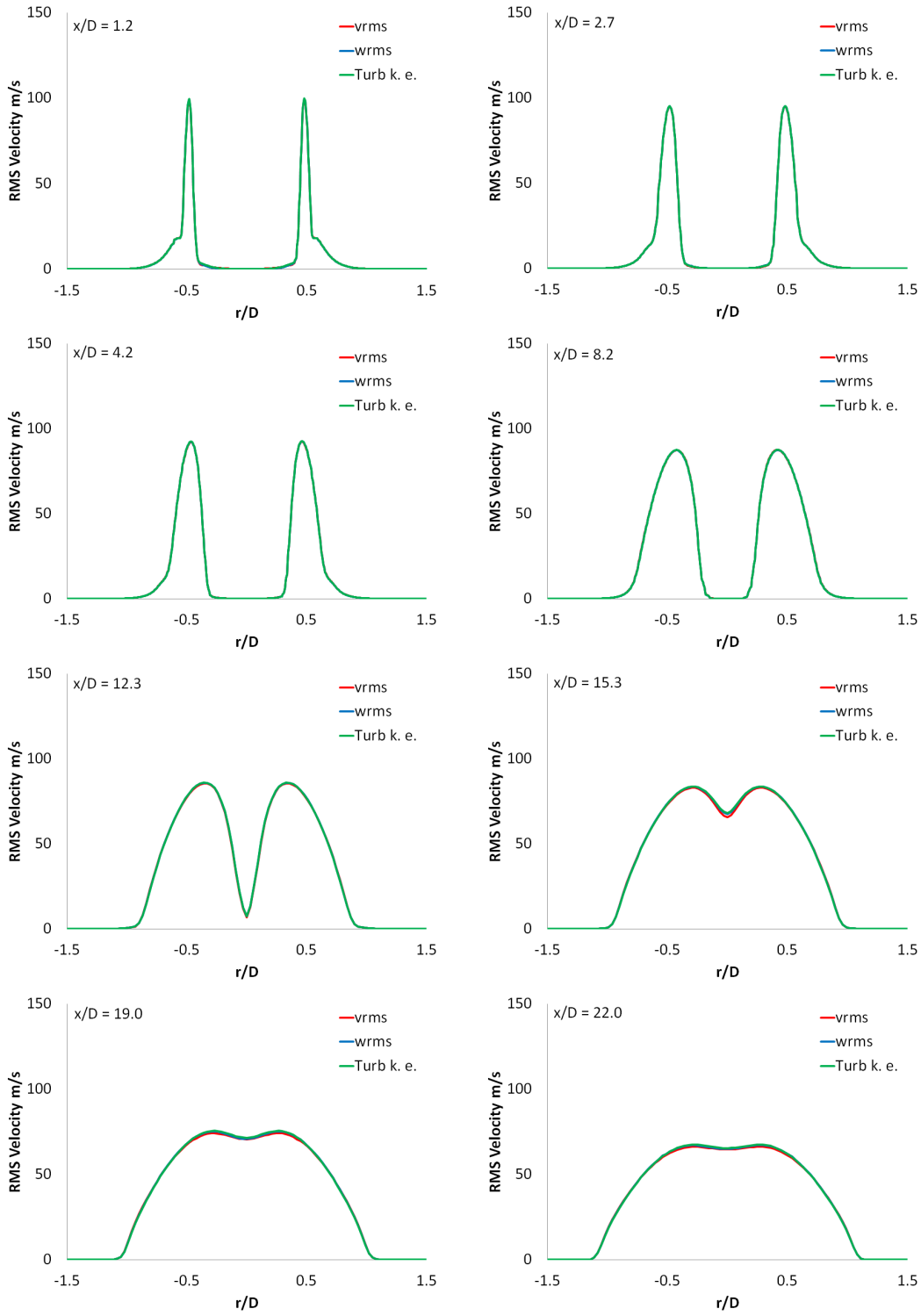

Figure 5.19: Radial (r) profiles of the transverse rms velocities, comparing the Boussinesq (red and blue) and turbulence kinetic energy approximations at several axial (x) locations.

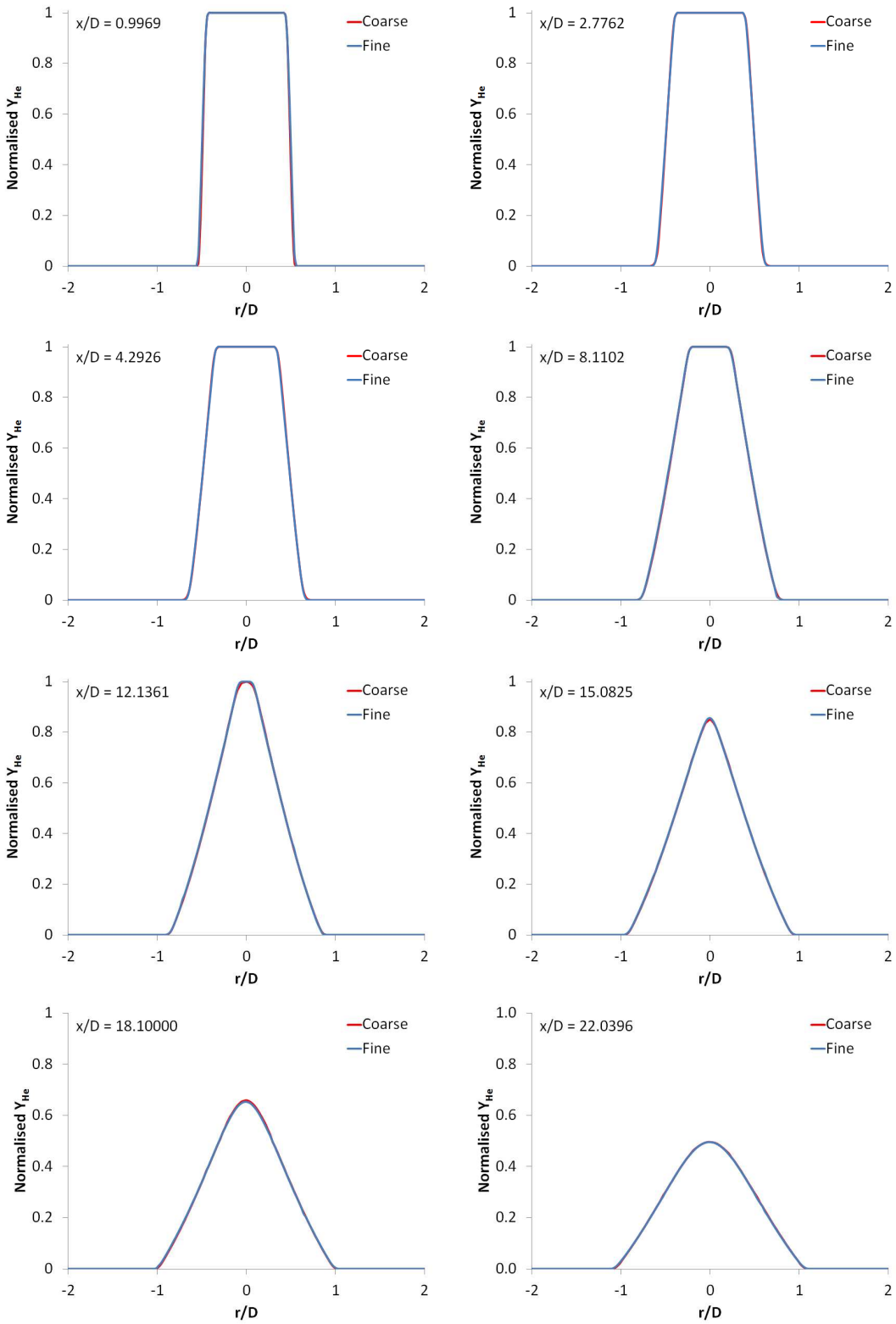

Figure 5.20: Helium mass fraction profiles confirming mesh convergence

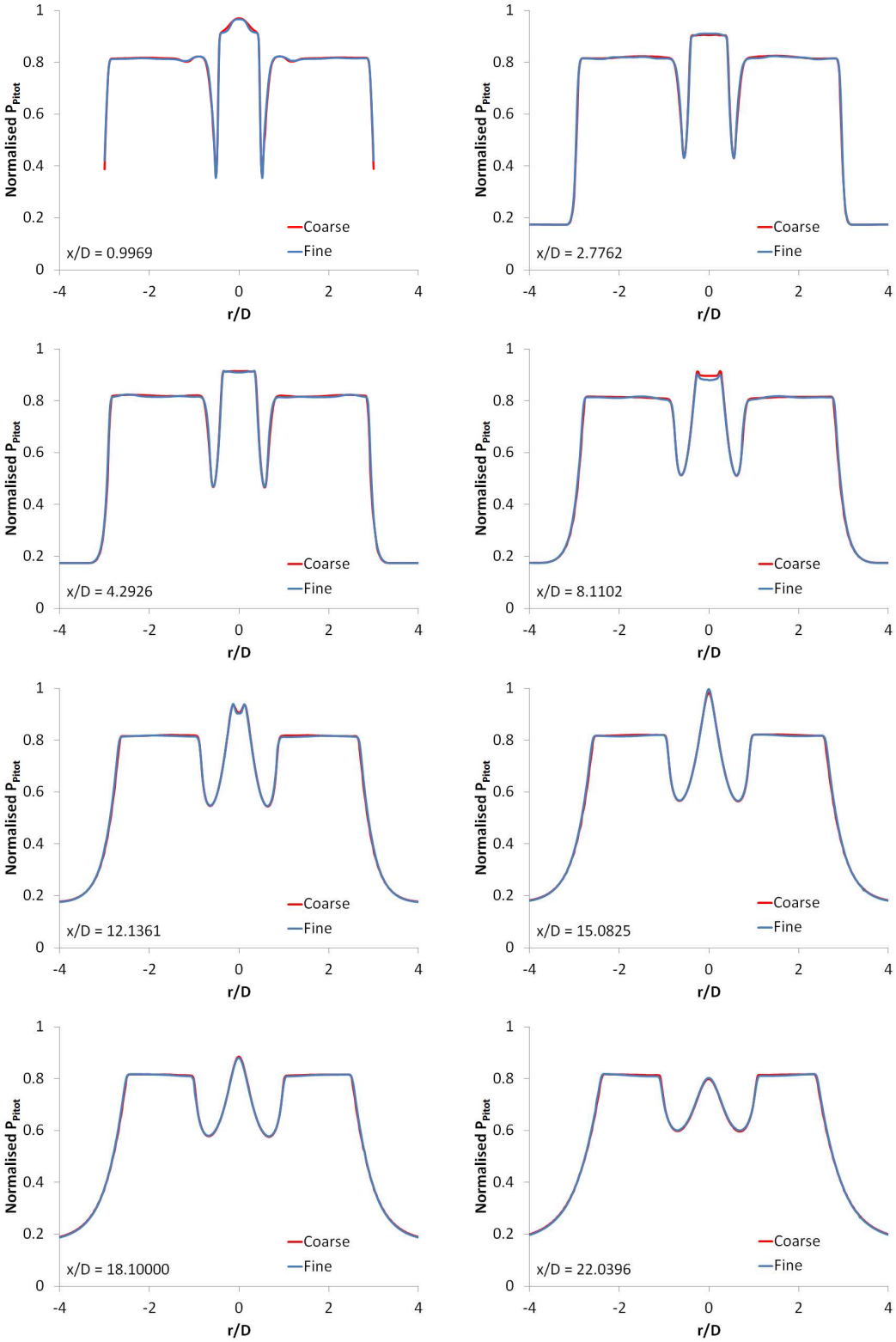

Figure 5.21: Pitot pressure profiles confirming mesh convergence

Chapter 6

Supersonic Non-Reacting Coaxial Jet - LES

Since LES directly captures the problem dependent large scales of the flow and applies modelling solely to the more universal small scales, the influence of empirical constants and their tuning requirements should be reduced, when compared to RANS. Due to a smaller range of the turbulence spectrum being accounted for through the modelling process, the levels of modelled viscosity are lower, meaning the turbulent transport terms in the Favre filtered system of equations play a less dominant role in computations. Computational results should therefore prove less sensitive to variations in the turbulence Prandtl and Schmidt numbers, improving over the deficiencies of the RANS approach. LES should also generate more physically meaningful results and provide the capability of extracting mean and fluctuating statistical data.

In order to investigate this hypothesis, large eddy simulations of the non-reacting coaxial jet introduced in Chapter 5, are presented. Baurle and Edwards [15] compared results from RANS and LES for the test case in question, but did not investigate the influence of the turbulent Prandtl and Schmidt numbers on the LES results. Poor agreement was obtained with experimental data for the LES ensemble averaged data, possibly due to the low levels of SGS viscosity employed.

6.1 Delayed Detached Eddy Simulation

Due to the high Reynolds numbers encountered in high speed flows, the delayed detached eddy simulation (DDES) hybrid RANS-LES method is used to reduce near wall computational costs. The Menter SST turbulence model is used in both the near wall RANS region and as the sub-grid scale model in the free-stream.

6.1.1 Computational Mesh

In order to further minimise the computational cost, the extent of the computational domain in the axial direction is reduced from that used in the RANS simulations of Chapter 5. The distance from the central jet tip to the domain outlet is now 0.27m, which is large enough to contain all experimental data points.

The y^+ distributions in Figure 5.7 can be used to design an efficient but accurate near wall mesh. In order for these time accurate simulations to be affordable the near wall spacing is slightly relaxed, since it is this dimension which governs the time step to be used. The central jet near wall cell size is fixed at 6.0×10^{-6}m for its entire length. Again, in order to avoid the generation of very high aspect ratio cells on the curved surfaces of the co-flow jet (due to the o-grid blocking mesh employed) the near wall cell size transitions from the inlet to the jet exit plane. The near wall spacing at the inlet is set to 0.5mm which linearly transitions to 6.0×10^{-6}m and 1.0×10^{-5}m half way down the jet length, for the inner and outer surfaces of the co-flow, respectively. They then linearly transition again to 3.0×10^{-6}m and 6.0×10^{-6}m, respectively, before the jet exit plane. It can be seen in Figure 6.1 that a y^+ of approximately four exists over the majority of the viscous surfaces, lying within the linear viscous sublayer. This provides sufficient resolution whilst allowing a computationally efficient time step to be used. A time step of 3.075×10^{-9}s is required to achieve computational stability.

The axial mesh spacing is set to 0.25mm in order to try and obtain isotropic cells in the central and co-flow jet core regions, as shown in Figure 6.2. Since turbulent structures are three dimensional in nature it is advantageous to use isotropic cells and simplifies the implicit filtering operation and choice of filter

width calculation. However, due to the meshing method employed, high aspect ratio cells can not be avoided in the shear layer regions and their impact on the computational results will be investigated. A purely hexahedral o-grid multi-block mesh is employed, resulting in 22.22M cells, with 12 cells used to resolved the central jet tip.

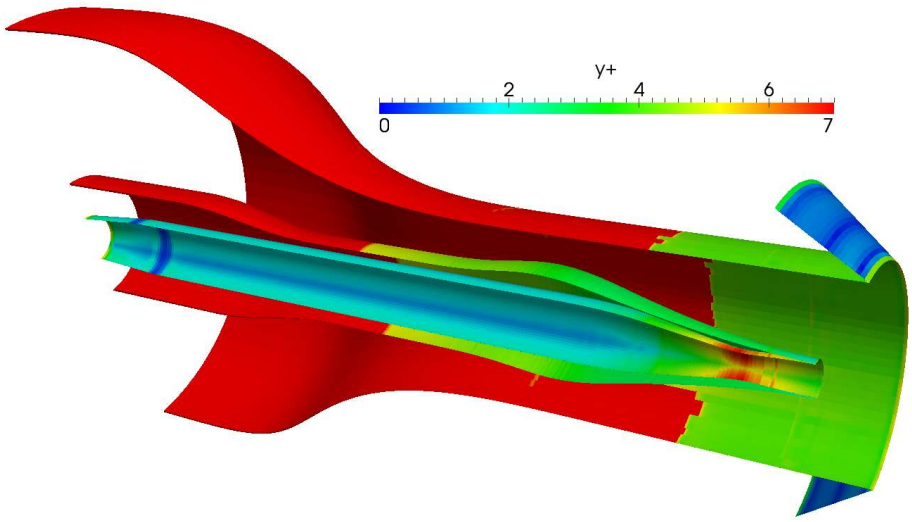

Figure 6.1: y^+ distribution for coaxial jet DDES

6.1.2 Boundary Conditions

The same steady state boundary conditions used in the RANS simulations of the previous Chapter are employed here. The simulations are initialised with a steady state solution, mapped from the coarser RANS mesh onto the fine mesh described above.

6.1.3 Computational Methods

Again, the second order AUSM+UP scheme with the Van Rosendale gradient limiter is used for the spatial discretisation and the third order three step TVD Runge-Kutta scheme for temporal integration.

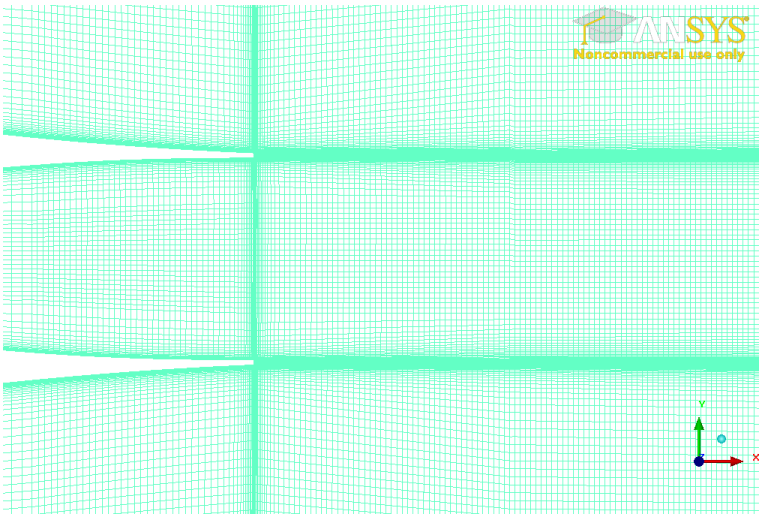

Figure 6.2: Fine DDES mesh, showing high aspect ratio cells in the shear layer regions and isotropic cells elsewhere.

6.1.4 Results

Figure 6.3 shows an instantaneous image from a simulation employing the DDES method. It can be seen that there is a significant delay before the inner shear layer transitions to turbulent behaviour. Through comparison of this image with the experimental schlieren in Figure 6.4 it can be seen that the jet is significantly more turbulent in reality.

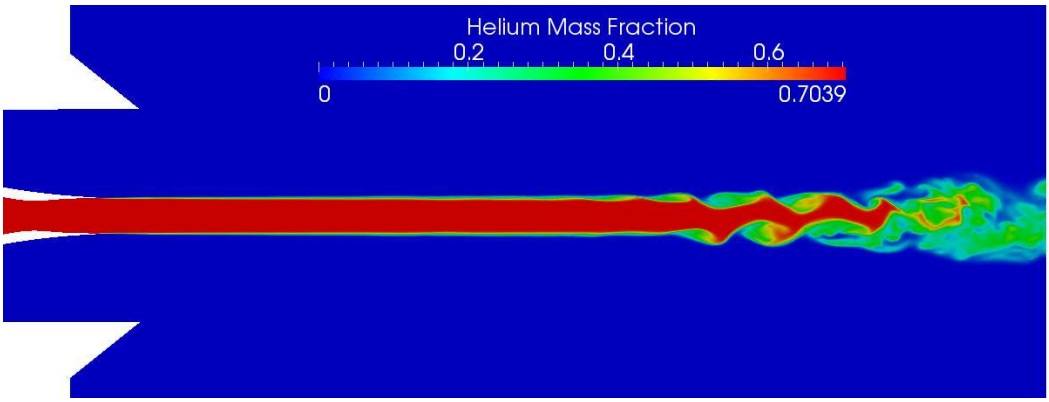

Figure 6.3: Instantaneous helium mass fraction distribution for coaxial jet DDES

Because the jet is lacking in transient behaviour, it is easy to see that the ensemble averages would be in poor agreement with experimental data and therefore need not be calculated. In fact, at the axial locations of x/D = 12.1361 and x/D = 15.0825, due to the lack of turbulent motion, the instantaneous profiles can be compared with experimental results. It can be seen from Figure 6.5 that a significant under-prediction of the spreading rate of the jet exists, suggesting enhanced turbulent mixing is required closer to the nozzle exit.

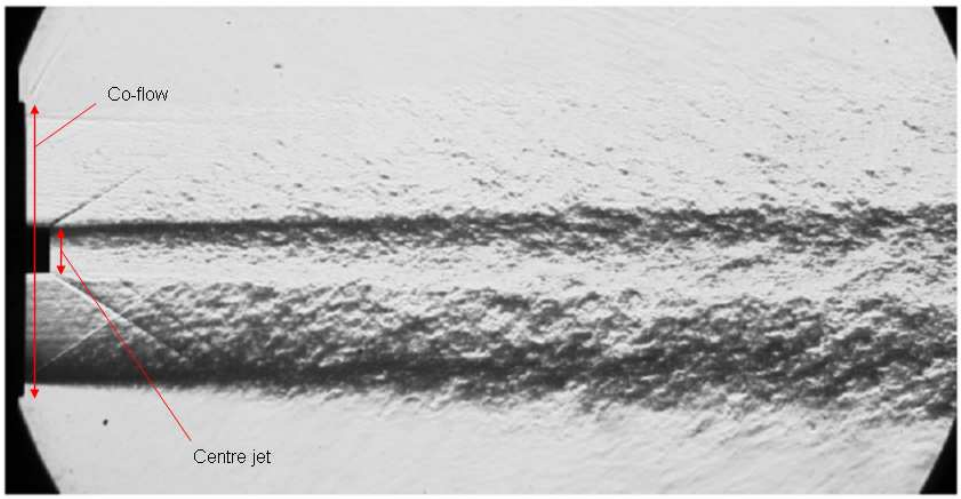

Figure 6.4: Experimental schlieren image [100], with angled shroud removed

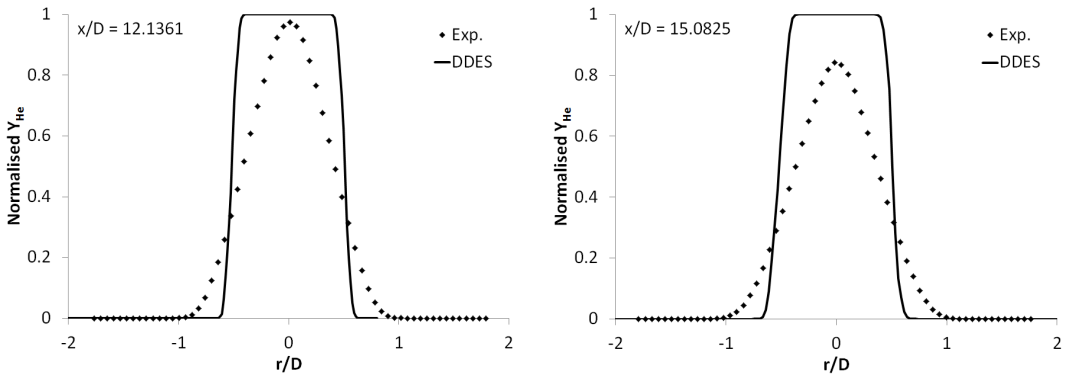

Figure 6.5: Radial (r) profiles of normalised helium mass fraction at two axial (x) locations for the DDES

This behaviour was also encountered by Baurle and Edwards [15] who needed to use a very low value for the Smagorinsky constant in their SGS model in order to encourage jet-breakup. However, this resulted in an over-prediction of the spreading rate of the jet and hence another solution to this problem is required.

It is possible the levels of numerical dissipation provided by the second order upwind scheme contribute to this result. However, in order to try and limit the levels of subgrid viscosity in the simulation, the filter width in Equation 2.57 employing the cube root of the cell volume, is used. Due to the presence of high aspect ratio cells in the shear layer regions, the use of this filter width should provide a significantly reduced subgrid viscosity compared to Equation 2.58.

Since the sub-grid model employed aims to mimic the purely dissipative Smagorinsky SGS model, the absence of backscatter capabilities could play a role in the lack of generation of shear layer instabilities. It is possible movement of energy towards the large scales could provide the shear layer perturbations required to initiate jet-breakup.

The high axial velocity of the central jet severely exacerbates this delayed transition problem. Any perturbations to the shear layer near the jet exit are rapidly convected downstream, travelling a significant distance before being amplified to cause the required shear layer instabilities.

Since the near wall regions are modelled using the RANS approach, there is no resolved turbulent content in the boundary layers. Since these boundary layers separate to form the shear layers of the flow, they are unable to provide the perturbations required to initiate jet-breakup. This is not a new problem; Keating and Piomelli [63] employed stochastic forcing at the boundary between the RANS and LES regions in order to increase the levels of resolved stresses at the interface. Alternatively, it has been suggested [15] that the introduction of turbulence structures at the inlet may help the jet transition. The influence of the addition of coherent structures to the computational domain will be investigated.

6.2 Turbulence Inflow

Turbulence data is often provided at domain inlets; however, this is not feasible for the jet in question due to the wide range of velocities encountered. Although

high velocities exist at the nozzle exits due to the supersonic conditions there, the velocities at the domain inlets are subsonic and below $100ms^{-1}$ (see Figures 5.2 and 5.4). For temporal accuracy a global time step is used, meaning it could take hundreds of thousands of iterations just for the turbulence information provided at the inlet to reach the jet exit plane and the coherent structures may even have been significantly dissipated by this time. The magnitude of the velocity fluctuations at the inlet may also be required to be on the order of 50% of mean inlet velocities in order to obtain turbulent intensity values of a few percent at jet exit, possibly leading to simulation stability issues. For these reasons, a method which enables this turbulence information to be provided closer to the jet exits is implemented in PULSAR and this approach is employed here.

The definition of the input turbulence requires knowledge of the experimental turbulence intensity and length scales. Since this data is not available, estimates must be made.

6.2.1 Computational Approach

The position of the turbulence inlet plane is somewhat arbitrarily chosen to be 1.15cm (1.15 central jet exit diameters) upstream of the central jet tip, as indicated in Figure 6.6. Turbulent fluctuations are imposed by modifying numerical fluxes through the corresponding cell faces at this location, where the fluctuating data is generated prior to the simulation.

In order to generate this fluctuating data a slice is taken through the mesh at the chosen location, as demonstrated in Figure 6.6. This slice is then extruded in the axial direction (perpendicular to its plane), to generate two cylindrical shaped domains. These domains are meshed with hexahedral cells, and the mesh used for the plane parallel to the extracted slice must correspond to the mesh used for the jet geometry at this location, but an evenly space distribution is used in the axial direction, as shown by Figure 6.7.

Approximately 400,000 cells are used for the central jet domain and 1.6M for the co-flow. 200 layers of 0.5mm cells are employed in the axial direction, giving a total domain length of 0.1m. This corresponds to 10 central jet diameters and is deemed sufficient to avoid problems with repetition of inlet fluctuating data.

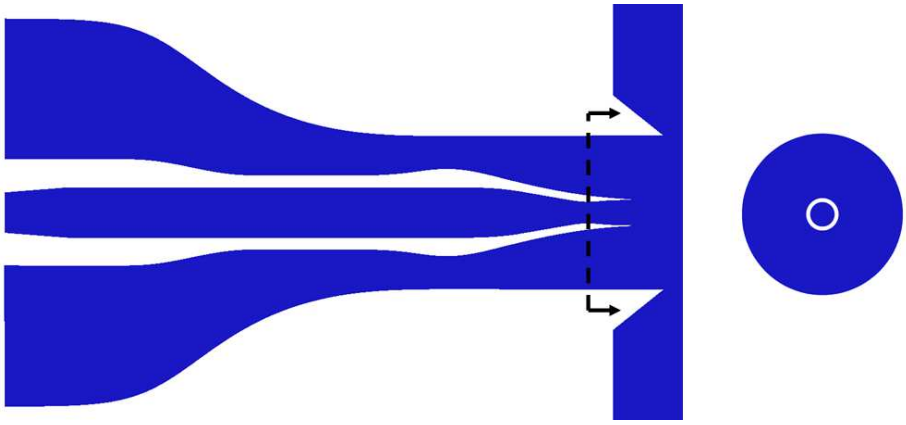

Figure 6.6: Location of turbulence inlet plane and corresponding geometry cross-section

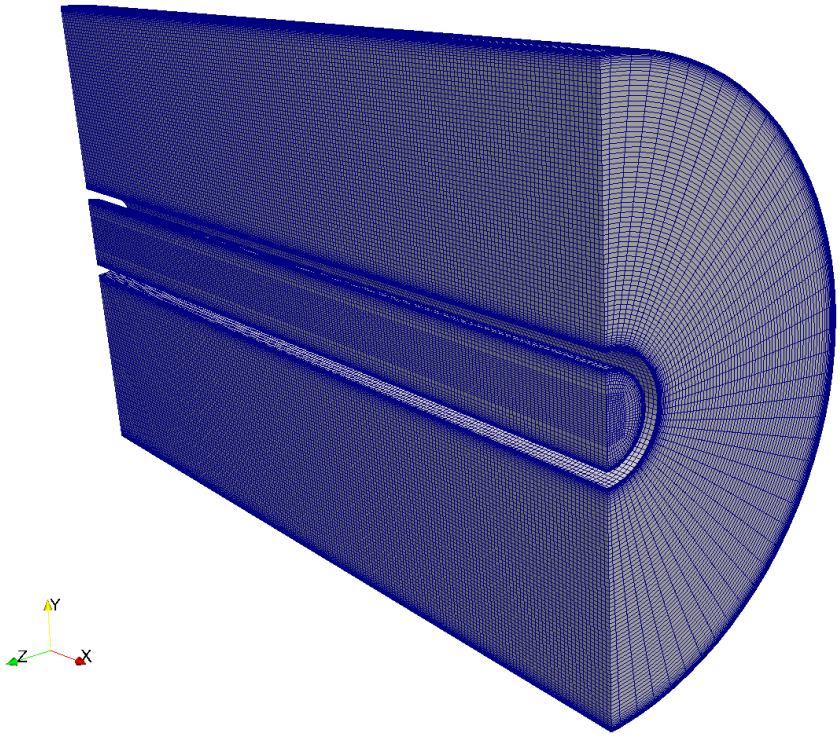

Figure 6.7: Mesh used to generate turbulence inlet data. Half of the mesh provided to show internal characteristics.

However, this corresponds to only four co-flow length scales, with the length scale given by the distance between the outer and inner co-flow surfaces. Since the interaction of the central and co-flow velocity fluctuations at the inner shear layer is not periodic this is deemed acceptable. The outer co-flow domain length is also restricted by memory considerations imposed by the cell count.

The extruded domains are filled with coherent structures using the method of Kempf et al. [64] described in Section 4.10. In order to generate at least three large eddy structures across a jet width the maximum length scale, L_{max}, is chosen to be 3mm, which is less than a third of the central jet exit diameter. A variable length scale formulation is employed to handle the presence of viscous walls, with parameter α_w in Equation 4.128 set to 0.4, as was used in [138]. Figure 6.8 shows the resulting turbulence profile, employing overall isotropic properties with R_{ii} set to $20\text{m}^2\text{s}^{-2}$.

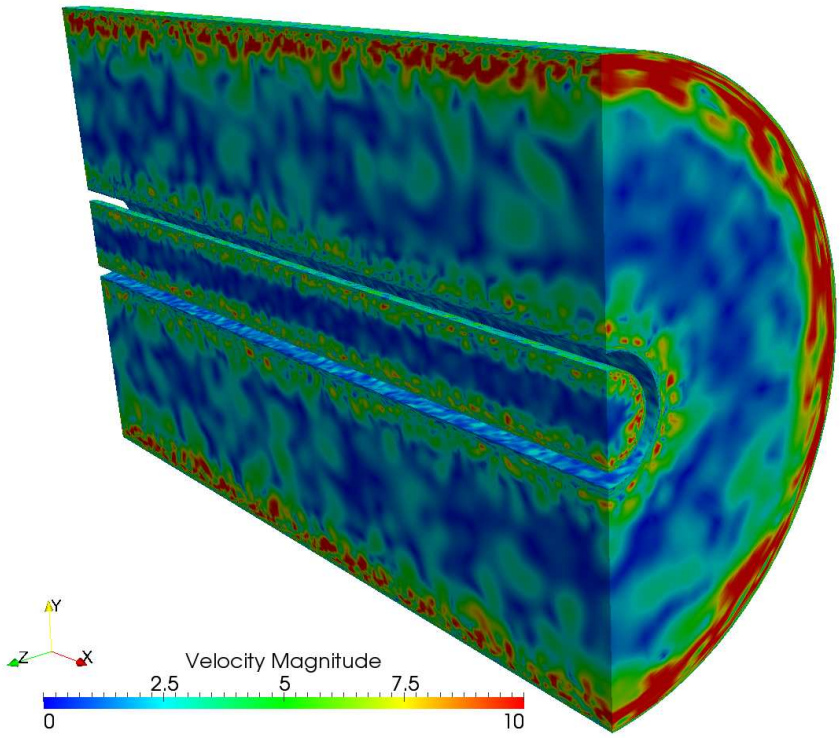

Figure 6.8: Generated inlet turbulence velocity data, in m/s. Half of the domain provided to show the internal profile.

Taylor's hypothesis [139] is used to impose planes of turbulent fluctuating data on the numerical fluxes at the mesh location described. From here on, any reference to inlet turbulence corresponds to the turbulent fluctuations imposed towards the jet exit.

6.2.2 Results

Figure 6.9 shows the turbulent structures convecting into the domain at the chosen location and their interaction with both the inner and outer shear layer can clearly be seen. Use of the z-velocity component (perpendicular to the page) to visualise the turbulent structures is somewhat unconventional, but enables their clear visualisation and shear layer interaction.

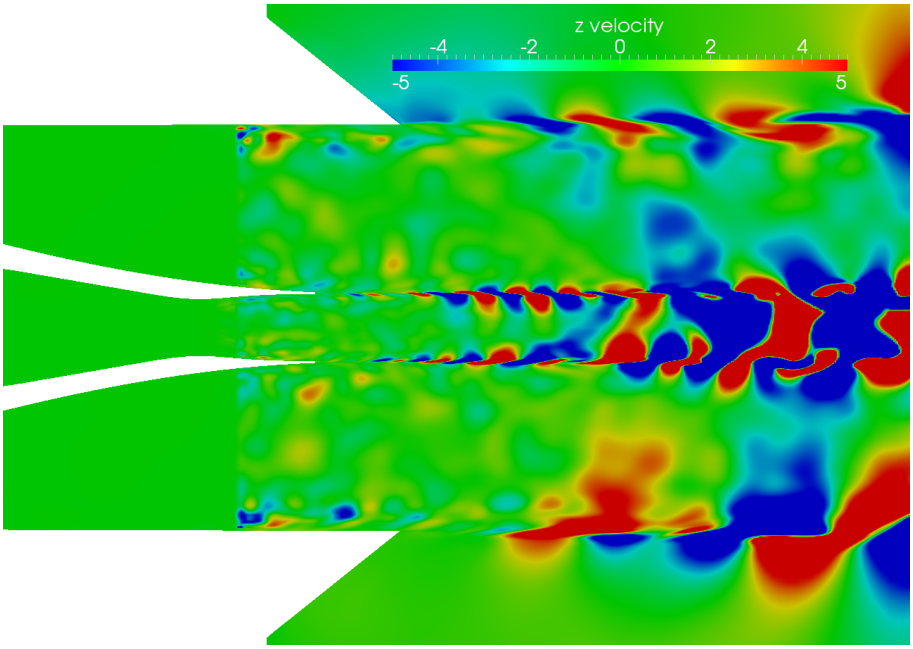

Figure 6.9: z-velocity component in m/s, showing injected coherent structures and shear layer interactions.

Figure 6.10 is an instantaneous image showing the resulting Helium mass fraction distribution. Significant jet breakup is achieved, removing the problematic transition delay from the simulation.

Figure 6.11 shows the resulting turbulent nature of the jet using positive Q iso-surfaces coloured by helium mass fraction, where Q is given by:

$$Q = \frac{1}{2}\left(\Omega_{ij}\Omega_{ij} - S_{ij}S_{ij}\right) \tag{6.1}$$

with

$$\Omega_{ij} = \frac{1}{2}\left(\frac{\partial u_i}{\partial x_j} - \frac{\partial u_j}{\partial x_i}\right) \tag{6.2}$$

Positive values of Q help to identify the low-pressure tubes which are associated with coherent vortices [140].

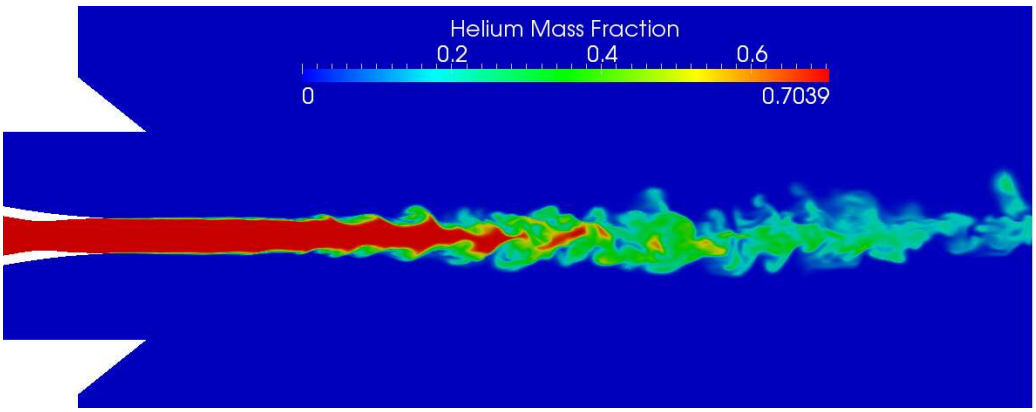

Figure 6.10: Instantaneous helium mass fraction profile for the coaxial jet DDES simulation with imposed turbulent fluctuations.

It can clearly be seen that the central jet has a fine turbulent structure whilst the outer shear layer is made up of larger coherent vortices.

In order to study the influence of the turbulent Prandtl and Schmidt numbers on LES results, three simulations are conducted employing the combination of parameters in Table 6.1. The isotropic turbulence profile in Figure 6.8 is used for the inlet fluctuations. Since no information on the experimental levels of turbulence is available, the value of $20\text{m}^2\text{s}^{-2}$ is chosen for the applied Reynolds stresses, R_{ii}, to provide peak inlet fluctuations on the order of 1-2% of the central jet exit velocity.

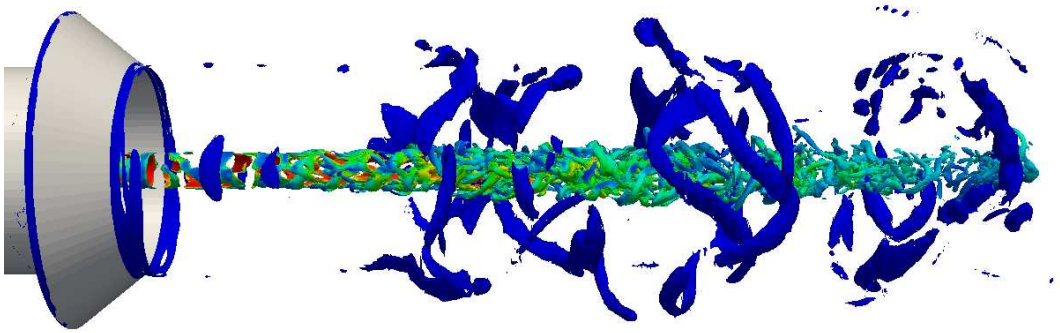

Figure 6.11: Positive Q iso-surfaces coloured by helium mass fraction.

	Pr_t	Sc_t
Simulation 1	0.9	1.0
Simulation 2	0.9	0.5
Simulation 3	0.5	1.0

Table 6.1: Turbulent Prandtl and Schmidt numbers for each simulation conducted.

The centre-line velocity profile from the RANS simulation employing the Sarkar compressibility correction with turbulent Prandtl and Schmidt numbers of 0.5 and 1.0, respectively, is used to define a flow-through time for the LES computational domain from the central-jet tip to the outlet. One flow-through time turns out to be 2.762×10^{-4}s, which corresponds to 89821 iterations. This can be used to estimate the number of iterations required to flush initial transients out of the system and then the number of iterations required to collect statistical data.

In order to compare computational results to experimental data the mean and rms values must be calculated. Since the co-flow exit velocity is significantly below that of the central jet, multiple flow through times are needed to gather the required statistics. Data collection is initiated after 225,000 iterations, corresponding to approximately 2.5 flow-through times, when initial transients have convected out of the domain. Ensemble averaged data are then collected over 765,000 iterations, corresponding to approximately 8.5 flow-through times, which are then employed to calculate the rms data over the period of another 8.5 flow-through times. Mean and rms values are therefore evaluated after 11 and 19.5

flow-through times, respectively. Statistical data are calculated for the velocity vector components and the pitot pressure, stagnation temperature and species mass fraction variables.

This simulation is conducted on 1440 cores of the HECToR cluster with 45,000 iterations achieved in just under 12 hours of run time. The total run time for each case is therefore approximately 19 days in real time or over 650,000 CPU hours. With this corresponding to over 74 years of run time for a serial code, parallel capabilities are obviously essential for such research.

Similarly to the study of solution convergence for a RANS simulation, the convergence of statistical data is observed through monitor points in the domain. Figure 6.12 shows both the instantaneous profile and ensemble average convergence history for the helium mass fraction, from 225,000 to 990,000 iterations on the centreline of the jet at an axial location of 0.27m.

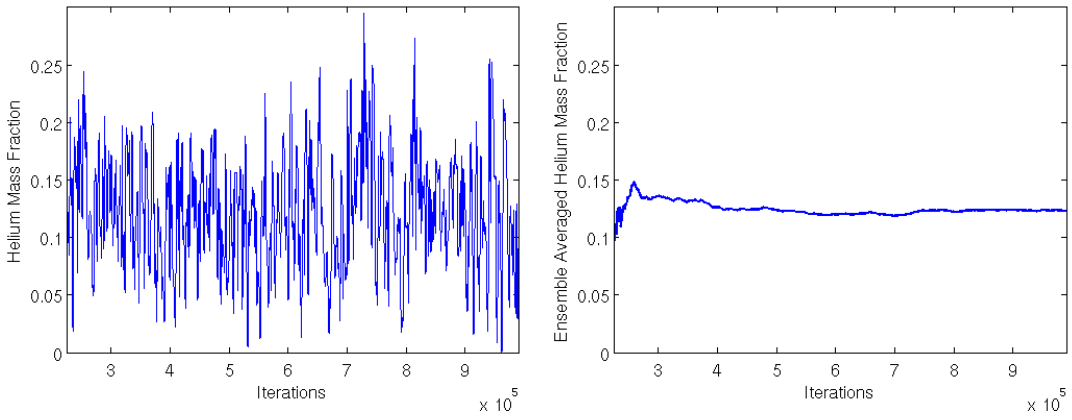

Figure 6.12: Helium mass fraction time history (left) and mean convergence (right) on the centreline at x=0.27m.

The turbulence energy spectrum from Simulation 1 is shown in Figure 6.13, evaluated using the time history of y-component of velocity over the iteration range from 225,000 to 1,755,000 on the centreline of the jet at an axial location of 0.27m. It can be seen that the mesh resolution is adequate, since evidence of the inertial range of the turbulence spectrum is visible. It appears that the inertial range is in agreement with Kolmogorov's $k^{-5/3}$ hypothesis, whilst the compressibility corrected gradient of $k^{-8/3}$ proposed by Ingenito and Bruno [19] appears to only agree after initiation of fall-off in the spectrum.

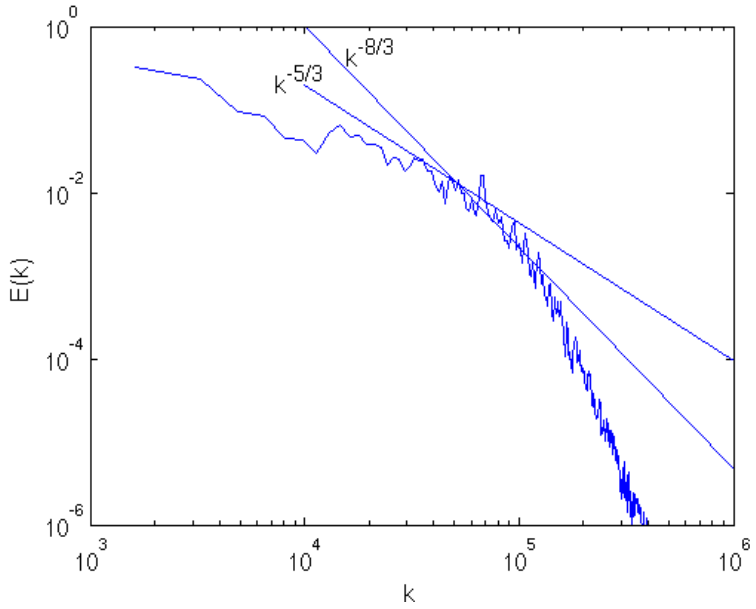

Figure 6.13: Turbulence energy spectrum for coaxial jet DDES

6.2.2.1 Helium Mass Fraction

It can be seen from Figure 6.14 that the LES results are indeed insensitive to the choice of values for the turbulent Prandtl and Schmidt numbers, significantly improving over the RANS method in this respect.

Although computational results for the helium mass fraction distribution are in good agreement with experimental data near to the jet exit, poor agreement is obtained further downstream. This could be due to the assumptions made for the intensity and length scales of the input turbulence fluctuations. It may also be due to the numerical diffusion supplied by the second order upwind scheme, adding to the spreading rate of the jet at downstream locations.

The over prediction obtained for the spreading rate can be further highlighted by the comparison in Figure 6.15 of the helium mass fraction distributions between the ensemble averaged data from the LES and from the RANS simulation employing the Sarkar compressibility correction with turbulent Prandtl and Schmidt number of 1.0 and 0.5, respectively, which was in good agreement with experimental data. The shorter core region and premature spreading of the jet in the LES simulation is clearly visible.

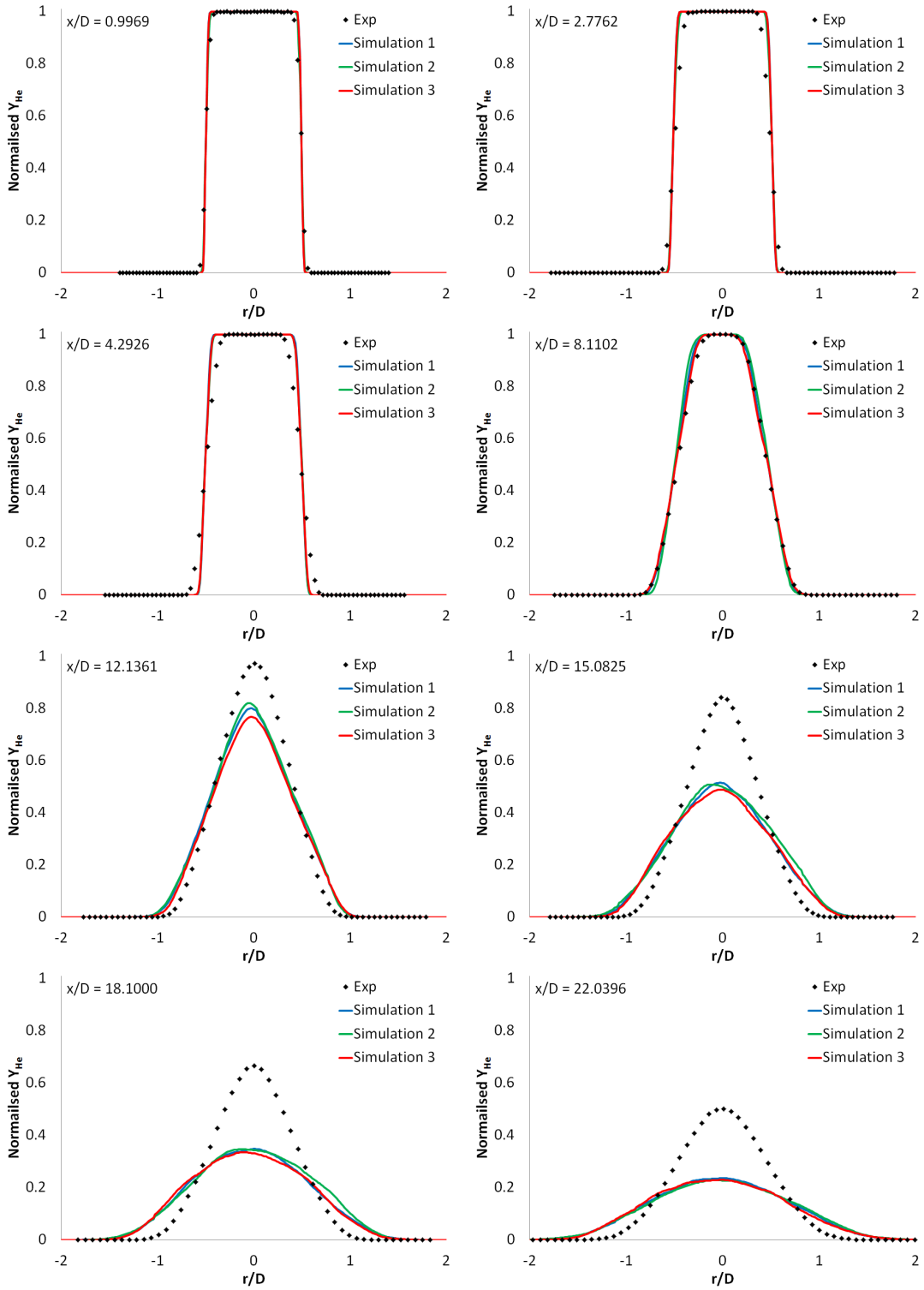

Figure 6.14: Radial (r) profiles of mean normalised helium mass fraction at several axial (x) locations, with varying Prandtl and Schmidt numbers

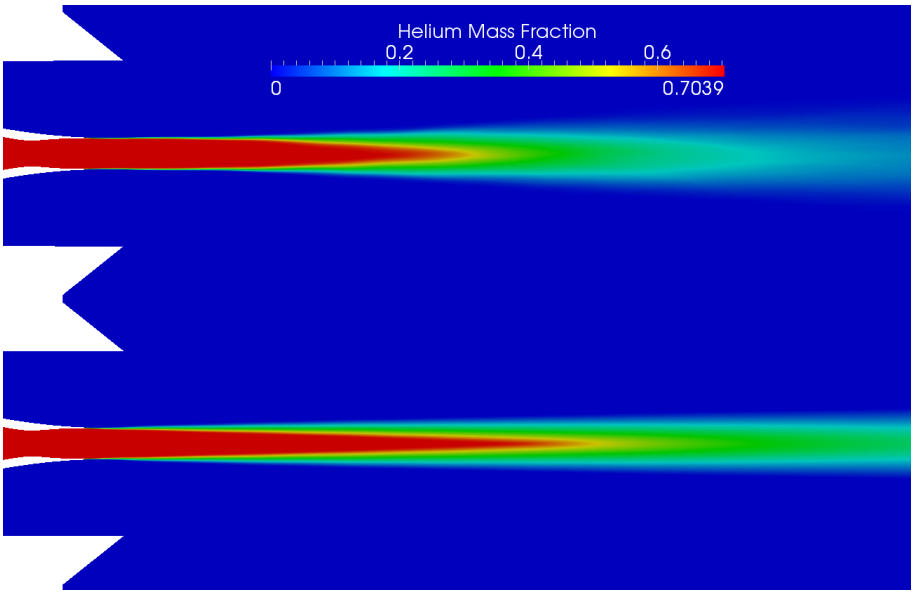

Figure 6.15: Comparison of ensemble averaged DDES (top) and RANS (bottom) helium mass fraction profiles.

6.2.2.2 Pitot Pressure

Similar results are obtained for the ensemble averaged pitot pressure profiles, where it can again be seen from Figure 6.16 that computational results are independent of the turbulent Prandtl and Schmidt numbers employed. However, the numerical results are again in poor agreement with the experimental data at downstream locations.

The poor agreement is particularly evident for the outer shear layer, with larger than expected losses in stagnation pressure and a larger spreading rate than found in the experimental data. This may be due to the large scale eddies in the outer shear layer causing more widespread mixing than experienced in practice. As can be seen in Figure 6.17, these large scale structures also have a significant influence on the inner shear layer. The unsteady behaviour of the outer shear layer is significant enough to generate shock waves which interact with the helium jet. It can be seen that significant distortion of the central jet results from the presence of large turbulent structures and shock wave interactions and hence an increased spreading rate for the helium mass fraction profile is obtained.

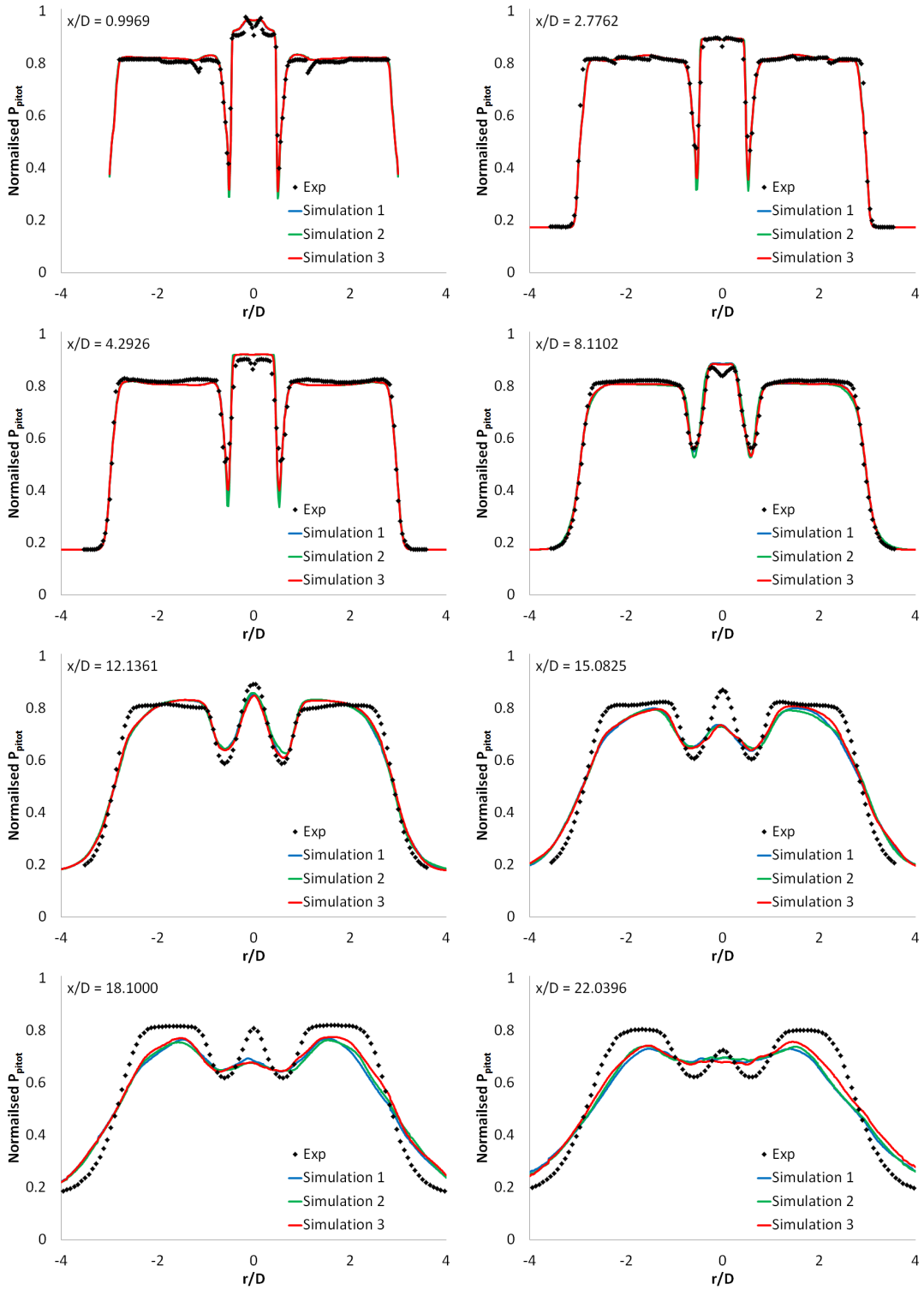

Figure 6.16: Radial (r) profiles of mean normalised pitot pressure at several axial (x) locations, with varying Prandtl and Schmidt numbers.

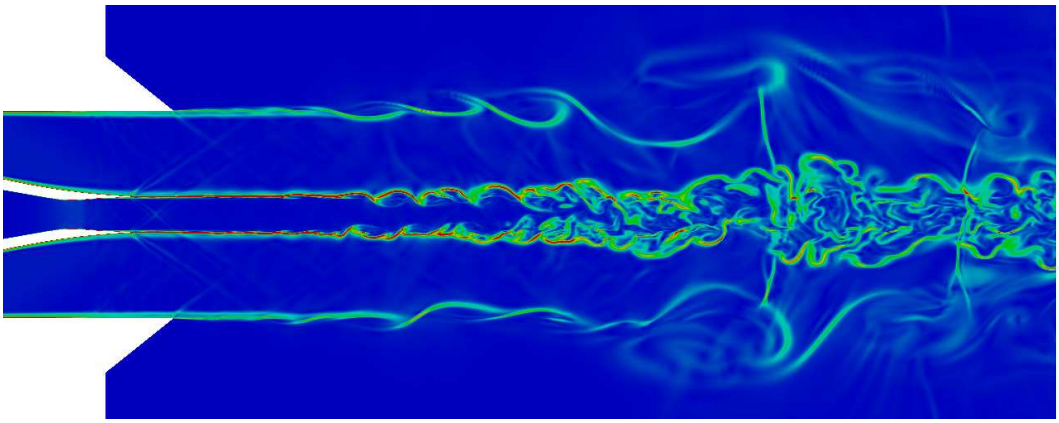

Figure 6.17: Numerical schlieren showing interactions between outer and inner shear layers.

Such severe unsteady behaviour for the outer shear layer and subsequent shock generation is not evident in the experimental schlieren of Figure 6.4 and hence this may play a significant role in the discrepancy between experimental and computational data. The outer shear layer breakdown is caused by the intense fluctuations in the inlet turbulence profile at the outer surface of the co-flow, as can be seen in Figure 6.8. These high intensities are caused by the Reynolds stress and length scale parameters chosen but also the volume normalisation of the turbulence initialisation method and gradient reconstruction approach employed. This is investigated in more detail in Section 6.4.

Lower than expected values for the pitot pressure are also evident in the inner shear layer for several diameters downstream of the exit plane. The shear layer is formed by the boundary layers separating from central jet and co-flow surfaces, which are solved using the RANS technique. Hence there is a lack of resolved turbulent content in the shear layer close to the exit plane, which if present would cause mixing with the high velocity fluid, increasing the stagnation pressure in this region.

6.2.2.3 Velocity

Experimental data for the mean and rms axial velocity are available, where the rms values are particularly valuable for the validation of the higher order statistics

available from LES.

Figures 6.18 and 6.19 confirm the independence of both mean and fluctuating axial velocity data from the values employed for the turbulent Prandtl and Schmidt numbers.

The mean axial velocity profiles follow a similar pattern to the helium mass fraction and pitot pressure, with poor agreement with experimental data obtained at downstream locations. Again this may be due to the large scale unsteadiness of the outer shear layer and the parameters used for the generation of inlet turbulence. Similarly to the pitot pressure profile, a region of lower than expected velocity is present in the inner shear layer for several diameters downstream of the jet exit, due to the lack of mixing.

Although the computational axial rms velocity results prove insensitive to model constant values, they over predict the turbulence intensity levels by approximately 50%. This disagreement with experimental data may again be due to the assumptions made for the imposed turbulence profile and the large outer shear layer eddies may impose significant velocity fluctuations on the central jet flow. The initial low turbulence intensities confirm the lack of mixing just downstream of the central jet tip. Although the magnitude of the fluctuations is poorly predicted, the correct profiles are obtained.

Figure 6.20 compares all three components of fluctuating velocity from Simulation 2, showing that the y and z components have a magnitude significantly below the axial rms velocity values. This is contradictory to the RANS results presented in Section 5.2.4, where the fluctuating velocity data in all three directions was found to be the same, since the Boussinesq approximation used in the modelling is dominated by the scalar turbulence kinetic energy. This implies that the Boussinesq approximation may not be suitable for modelling of the Reynolds stresses for this test case, although it was shown to produce good agreement with experimental data for the axial rms velocity in regions of high shear. This statement can not be confirmed due to a lack of experimental data for the y and z rms velocities, but is consistent with what was found by Baurle and Edwards [15].

Profiles of the inlet turbulence velocity components can be seen in Figure 6.21, confirming that an isotropic field is used, demonstrating that the disparity in rms velocity components is not caused by anisotropy in the inlet turbulence profile.

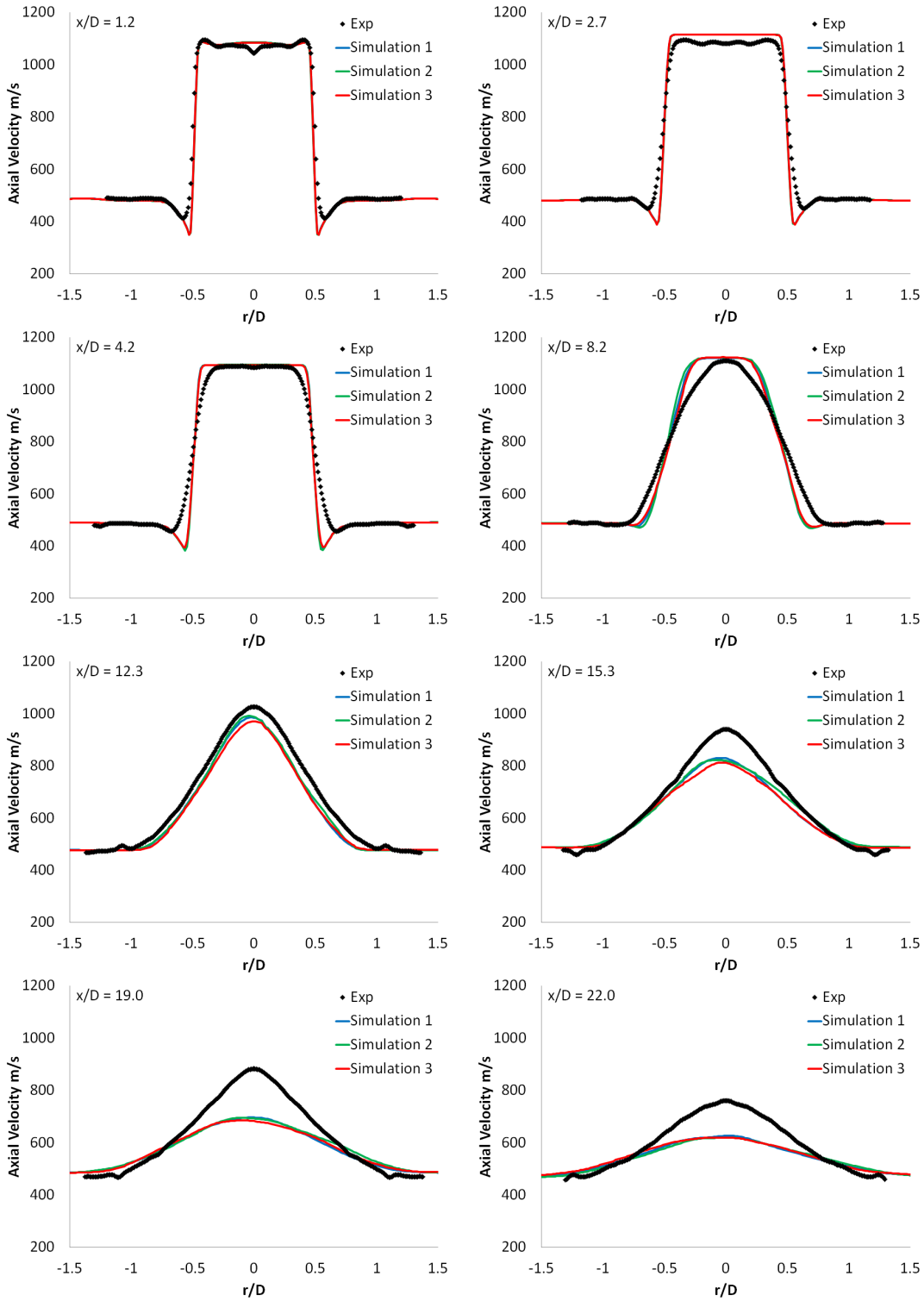

Figure 6.18: Radial (r) profiles of mean axial velocity at several axial (x) locations, with varying Prandtl and Schmidt numbers.

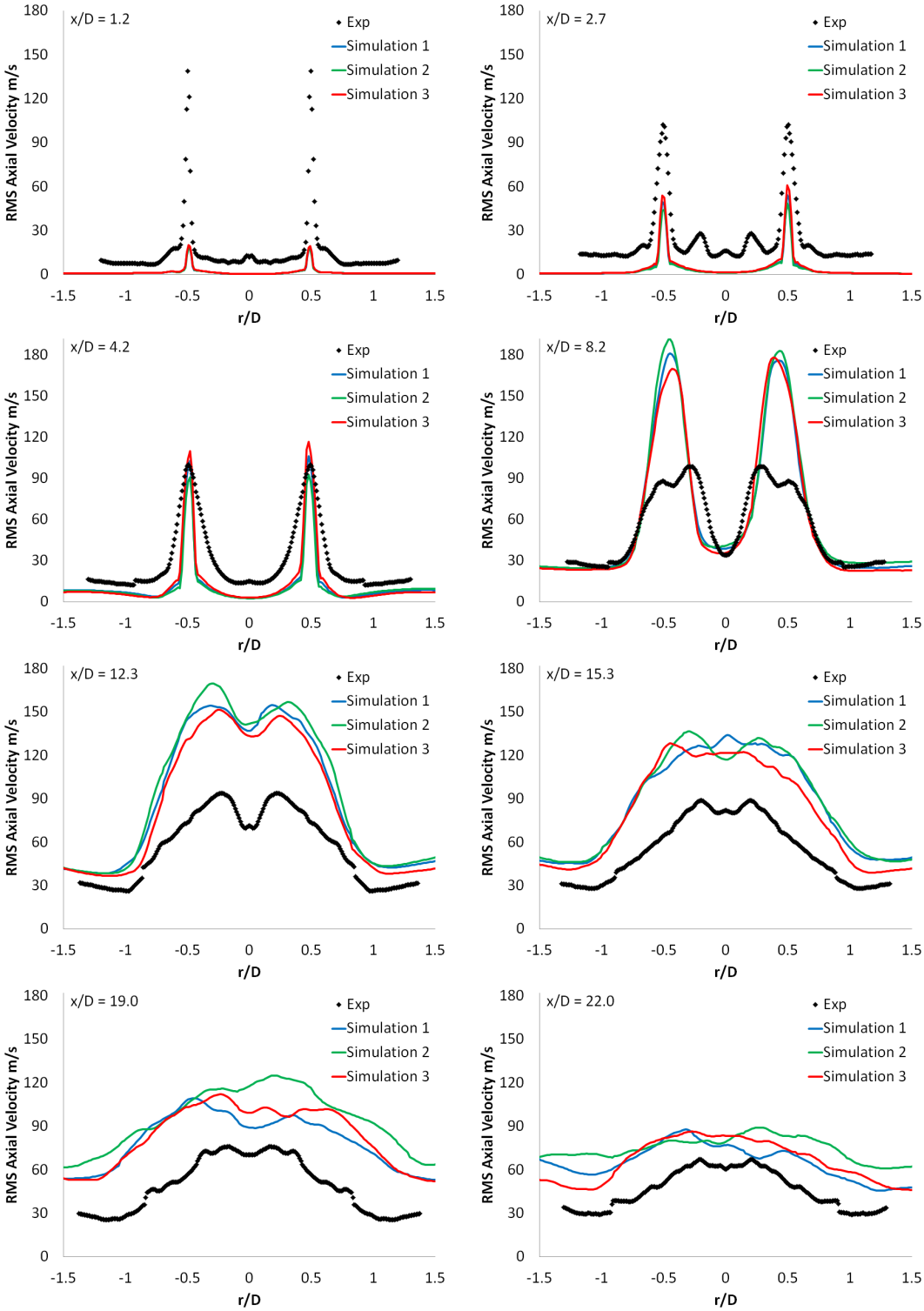

Figure 6.19: Radial (r) profiles of rms axial velocity at several axial (x) locations, with varying Prandtl and Schmidt.

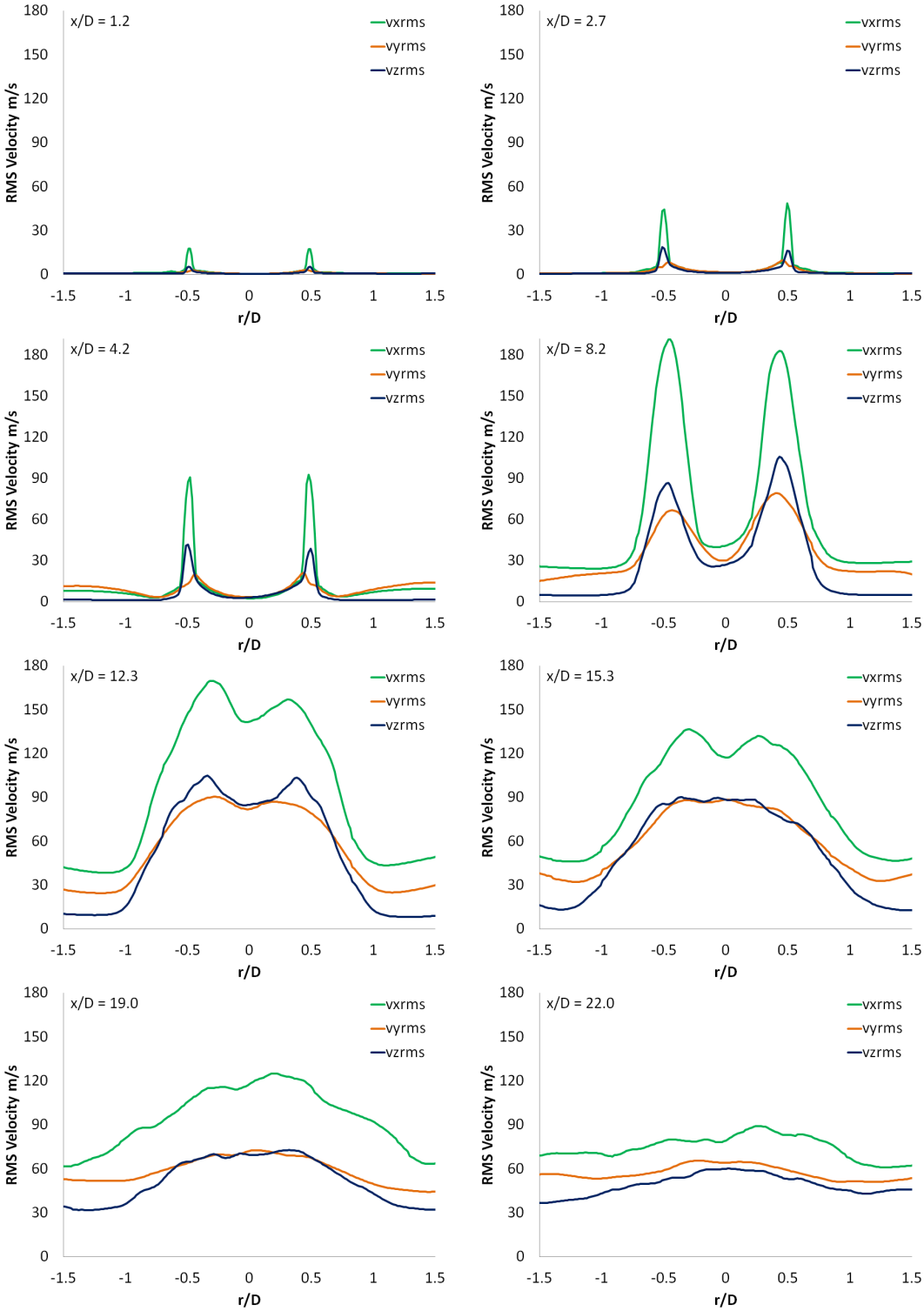

Figure 6.20: Radial (r) profiles of rms velocity components at several axial (x) locations, from Simulation 2.

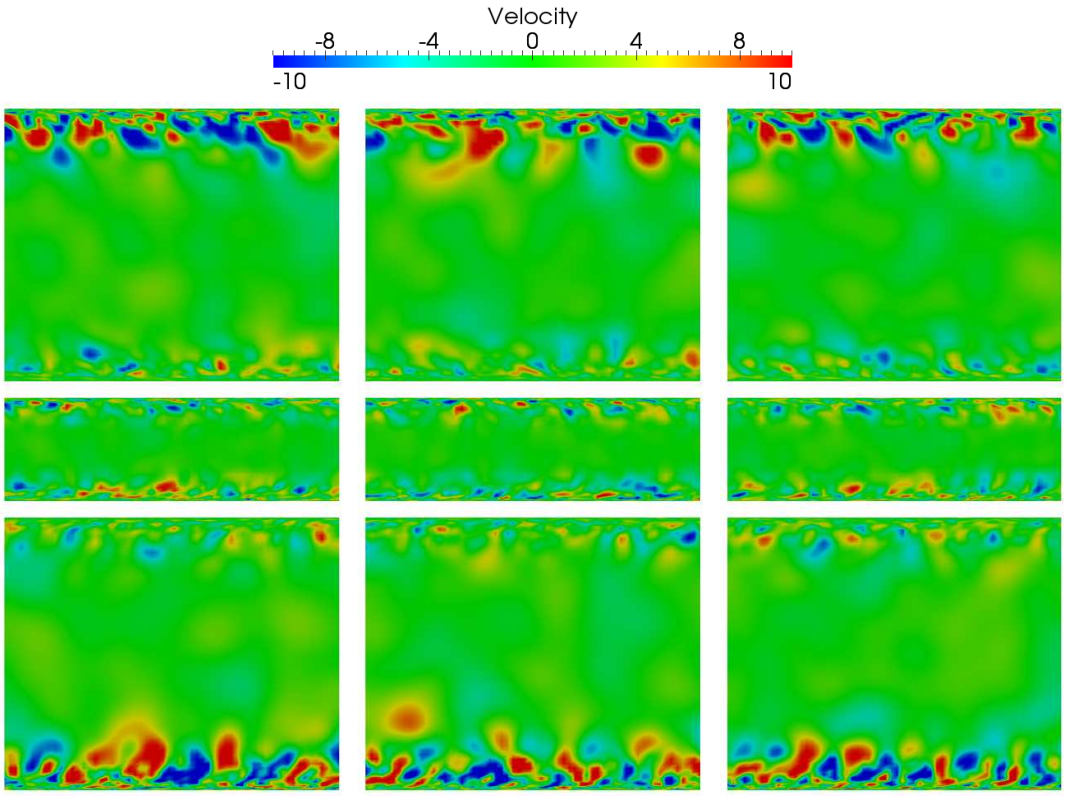

Figure 6.21: x (left), y (middle) and z (right) velocity profiles on a sample slice of the turbulence inlet data, in m/s.

6.2.2.4 Statistical Convergence

In order to further demonstrate convergence of the ensemble averaged data, computational results after 11 and 19.5 flow-through times are compared. The ensemble averaged values obtained at the end of the first cycle of 765,000 iterations are frozen and used to calculate the rms data over the next 765,000 iterations, but are also continually updated over this time and stored in a separate variable. It can be seen from Figures 6.22 and 6.23 that there is little difference between the two sets of ensemble averaged data for the species mass fraction and axial velocity and so confirmation of statistical convergence for the values used in rms calculations is confirmed.

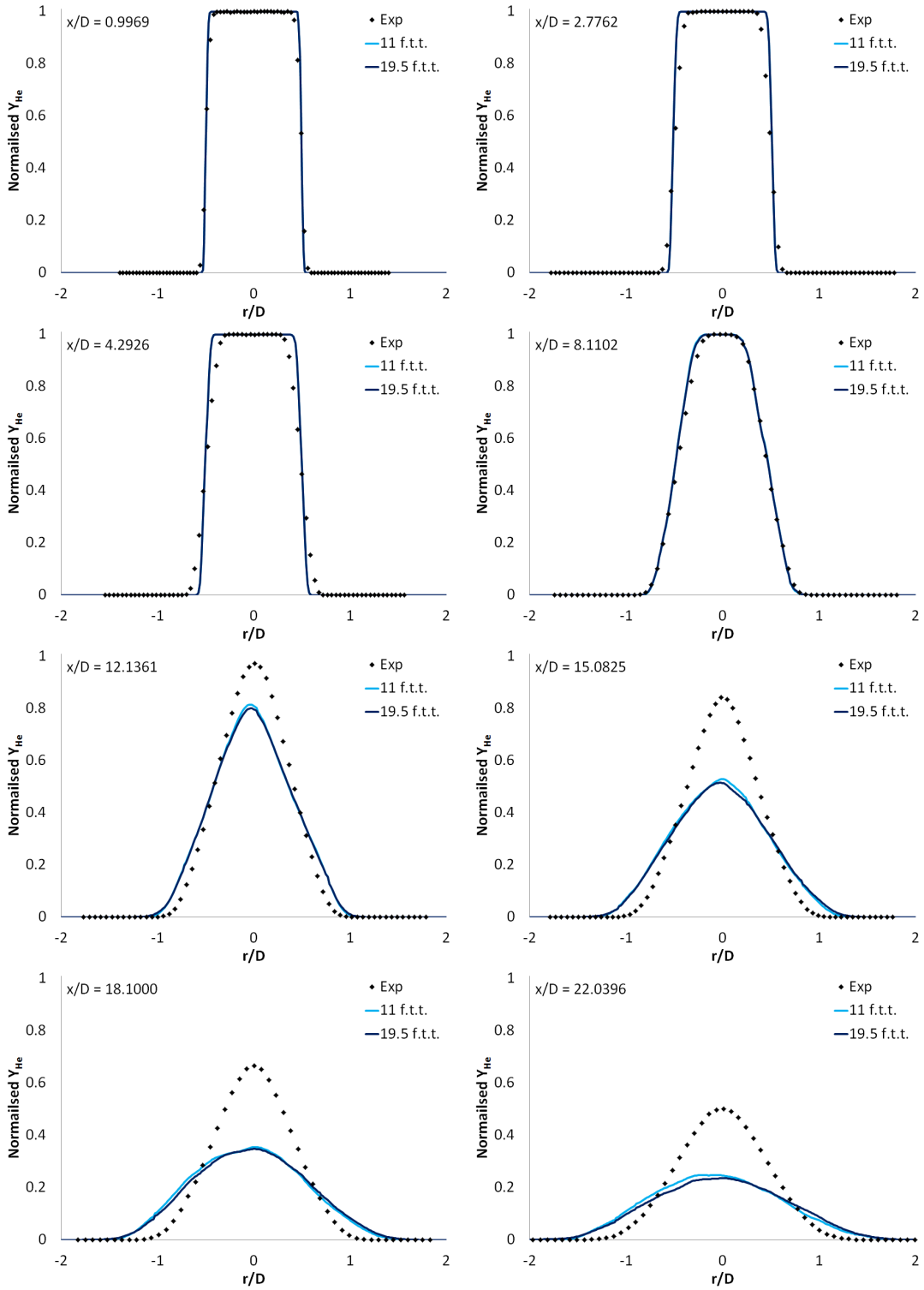

Figure 6.22: Radial (r) profiles of mean normalised helium mass fraction at several axial (x) locations, after 11 and 19.5 flow-through-times, for Simulation 1.

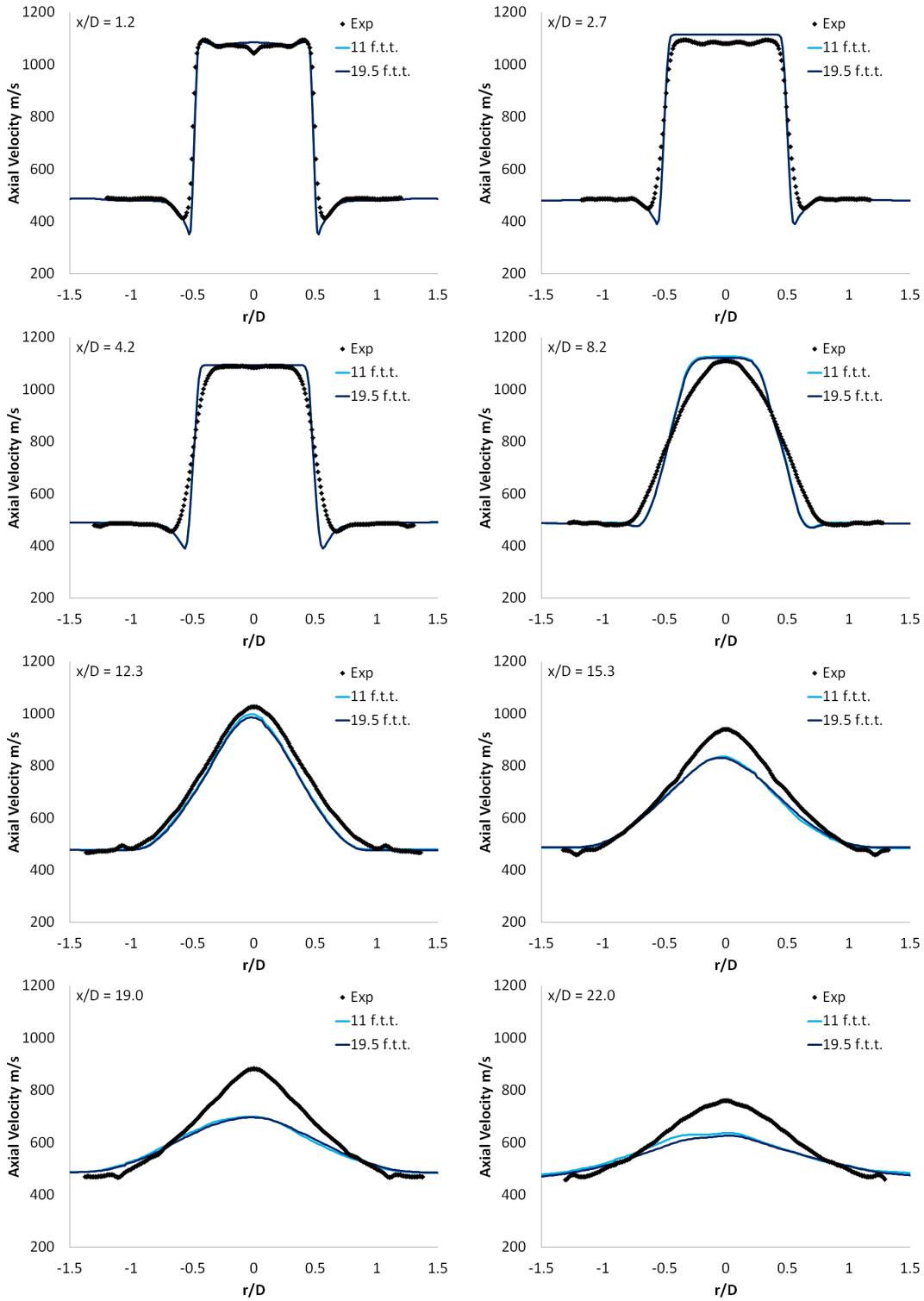

Figure 6.23: Radial (r) profiles of mean axial velocity at several axial (x) locations, after 11 and 19.5 flow-through-times, for Simulation 1.

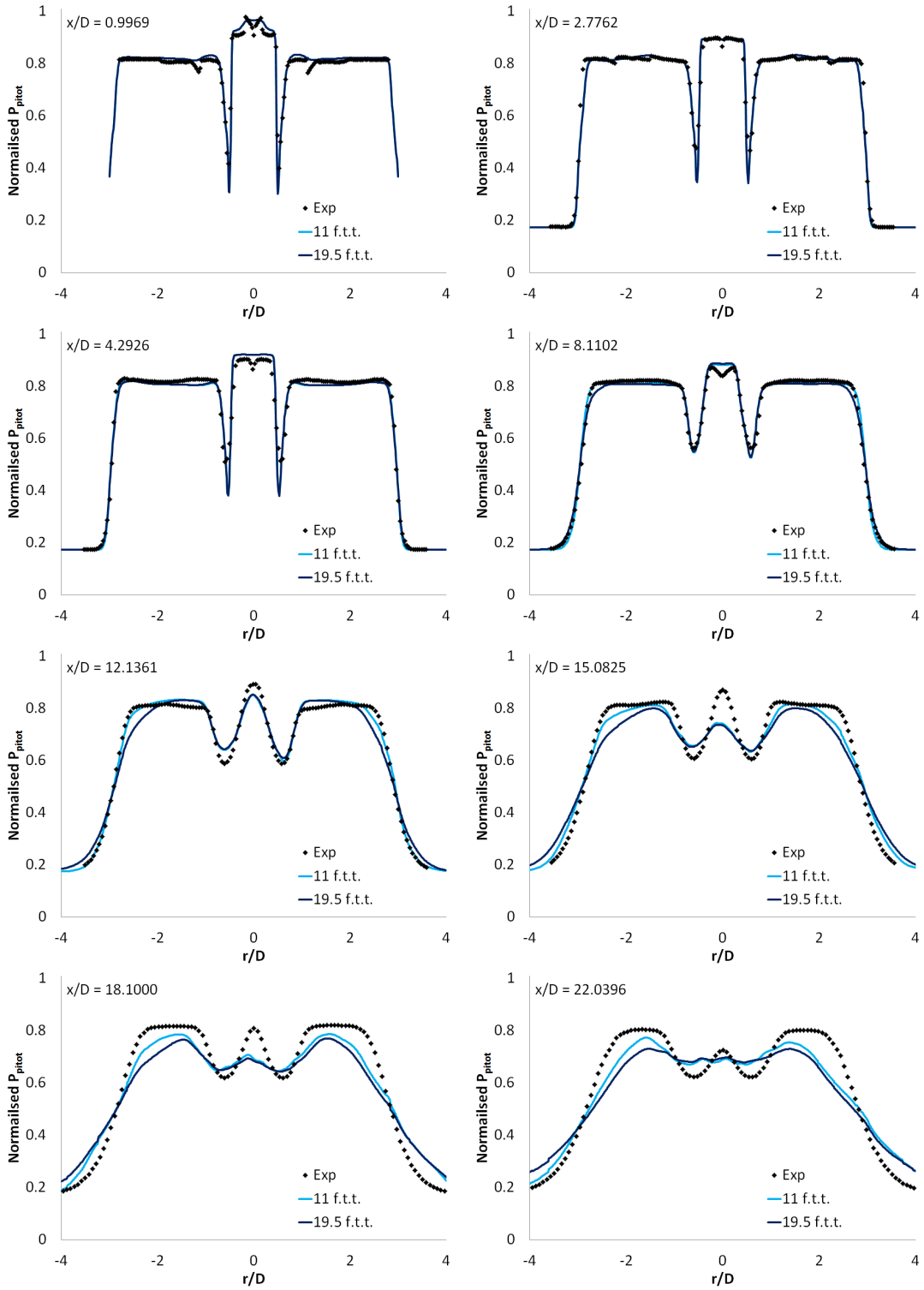

Figure 6.24: Radial (r) profiles of mean normalised pitot pressure at several axial (x) locations, after 11 and 19.5 flow-through-times, for Simulation 1.

It is a slightly different story for the pitot pressure profiles shown in Figure 6.24, however. Although convergence can be declared for the mean pitot pressure values in the central jet, there are distinct variations in the co-flow and outer shear layer, where the agreement with experimental data deteriorates over time. This is due to the large scale structures which cause an over prediction of the outer shear layer spreading. Since the outer shear layer separates the co-flow and ambient air, subsonic flow velocities are present and hence a larger number of iterations are required to fully develop this region and a larger number of iterations are required to obtain statistical convergence.

The downstream locations also confirm the severity of the outer and inner shear layer interactions, where they appear to merge; contradictory to experimental data.

Convergence of the axial rms velocity is displayed in Figure 6.25, which shows the time history for this value on the centreline of the jet at an axial location of 0.27m.

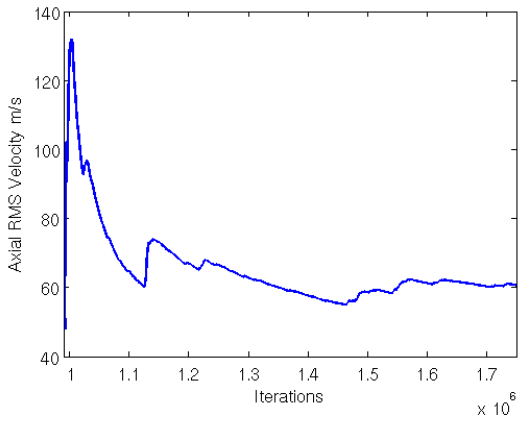

Figure 6.25: Axial rms velocity convergence

6.3 Parameter Sensitivities

Since the poor agreement between experimental and computational results at downstream locations may be due to the assumptions made for the length scales and Reynolds stresses of the imposed turbulence fluctuations, it is important

to investigate the sensitivities to these parameters. The choice of filter width calculation and mesh resolution may also have a significant influence on the computational results obtained.

6.3.1 Computational Mesh

Such an investigation requires multiple simulations to be conducted, varying the parameters in question between runs. In order to reduce the computational cost of such a study the computational domain is reduced in the axial direction from that presented in Section 6.1.1. The location to which the domain is truncated is chosen to ensure that important data points still remain within the bounds of the computational mesh. Recalling the results in Section 6.2, whatever computational setup is employed, reasonable agreement between experimental and computational data is obtained close to the nozzle exits. However, further downstream, significant differences arise and it is therefore important to evaluate the ensemble averaged data at these locations. The computational mesh is therefore terminated at an axial location of 0.158m, ensuring the data point at x/D = 15.0825 is still available.

An identical nozzle mesh is used to that described in Section 6.1.1, but the axial resolution in the free-stream is relaxed from 0.25mm, to 0.5mm. The resulting multi-block mesh consists of 9.35M hexahedral cells, which is still split into 1440 partitions and run on the HECToR cluster, with 90,000 iterations achieved in approximately 11 hours of run time. Since the near wall mesh resolution is unchanged, the time step remains at 3.075×10^{-9}s. Because the computational domain has been reduced in the axial direction, one flow-through time now turns out to be 1.437×10^{-4}s, which corresponds to 46731 iterations. In order to further reduce the computational cost, the collection of ensemble averaged data is initiated after 180,000 iterations, corresponding to approximately four flow-through times, and continues for 450,000 iterations, corresponding to approximately ten flow-through times. Due to the computational cost associated with additionally evaluating the rms data, only the influence of parameters on the mean values is to be studied in detail here.

6.3.2 Filter Width

The cube root of the cell volume filter width of Equation 2.57 is used in Sections 6.1 and 6.2 in order to reduce the level of subgrid viscosity in the simulation, in an attempt to compensate for use of an upwind method for the spatial discretisation and to encourage the growth of shear layer instabilities. However, it is possible the maximum length filter width of Equation 2.58 could reduce the high levels of velocity variance encountered in Section 6.2.2.3. It is therefore important to investigate the influence of the filter width calculation on the computational results obtained.

Two simulations employing the filter widths discussed are conducted and the turbulence inlet Reynolds stress, R_{ii}, is set to $50\text{m}^2\text{s}^{-2}$ and an L_{max} of 3mm and a near wall scaling coefficient, α_w, of 0.4, are used, as before.

Due to the minimal influence of variations in computational setup on numerical results at the first two axial locations previously presented, they will be ignored from now on with a concentration on behaviour at locations further downstream.

Figure 6.26 shows that the choice of filter width can have a significant impact on the computational results obtained, with the helium mass fraction profiles showing the maximum length filter width significantly reduces the spreading rate of the jet, for the given turbulence inlet conditions. From Figure 6.27 it can be seen that this is because of the higher levels of subgrid viscosity generated, due to the high aspect ratios cells present in the shear layer regions. However, this results in a very dissipative simulation, with the instantaneous helium mass fraction profile shown in Figure 6.28. It can be seen the high levels of subgrid viscosity kills the smallest resolved scales in the flow, when compared to a simulation employing the cube root filter width. It is therefore correct to employ the cube root of volume filter width, in order to obtain the jet behaviour expected in practice. Simulations employing the maximum length filter width would most likely be more sensitive to the values chosen for the turbulent Prandtl and Schmidt numbers, since the increased levels of subgrid viscosity would increase the role played by the turbulent diffusion terms in the filtered system of equations.

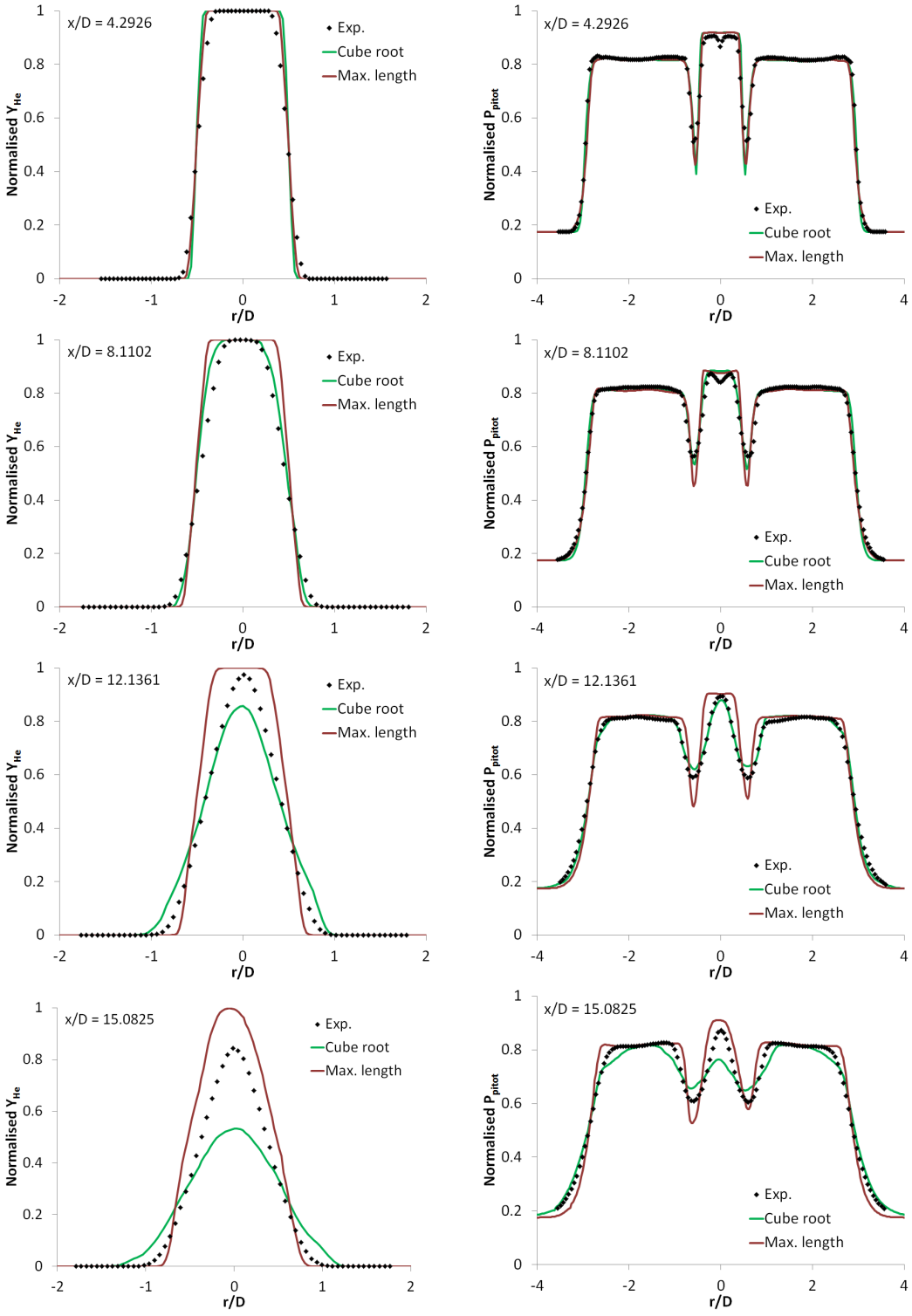

Figure 6.26: Radial (r) profiles of mean normalised helium mass fraction (left) and pitot pressure (right) at several axial (x) locations, comparing the cube root of volume and cell maximum length filter width calculations.

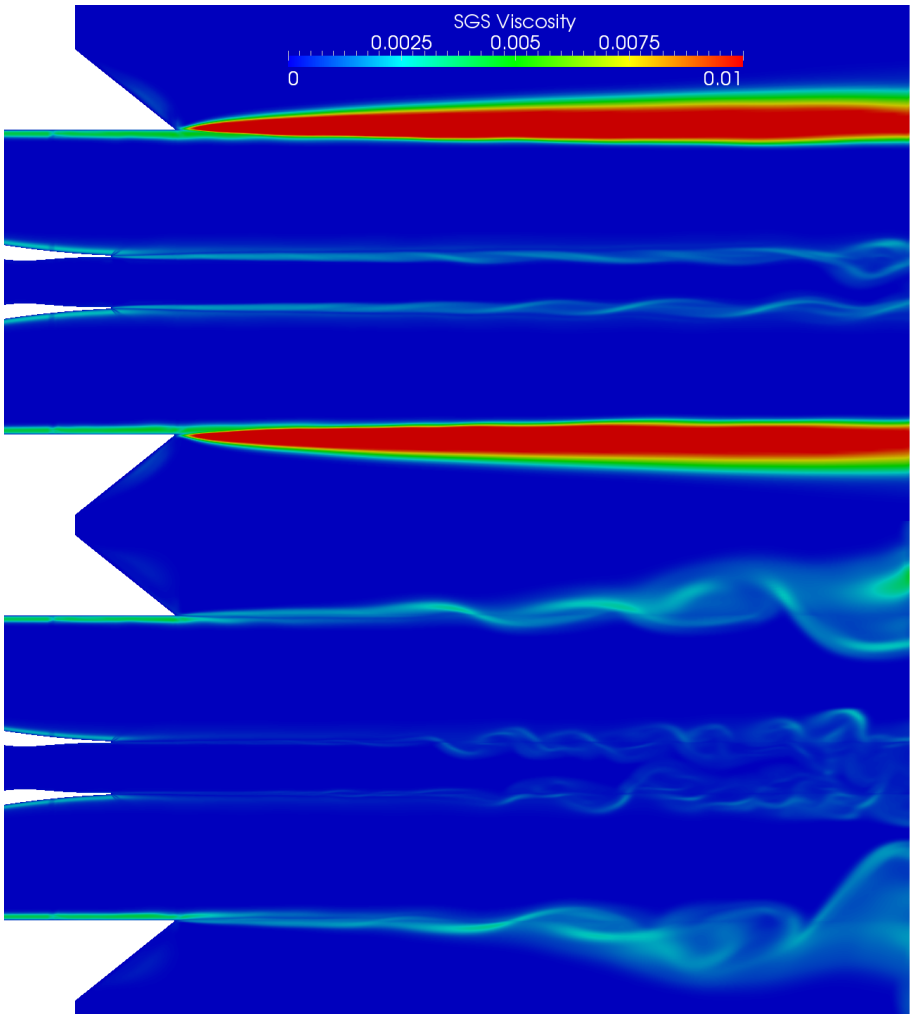

Figure 6.27: Instantaneous SGS viscosity profiles after 630,000 iterations, comparing the cell maximum length (top) and cube root of volume (bottom) filter width calculations.

It can also be seen from Figure 6.26 that the more dissipative filter width provides a sharper resolution of the co-flow pitot pressure profile. This is due to the high levels of subgrid viscosity in the outer shear layer killing all shear layer instabilities, leading to a constant smooth profile as shown in the numerical schlieren of Figure 6.29. However, the less dissipative filter width allows significant turbulent behaviour in the outer shear layer, which leads to a significant spreading of the ensemble averaged pitot pressure profile.

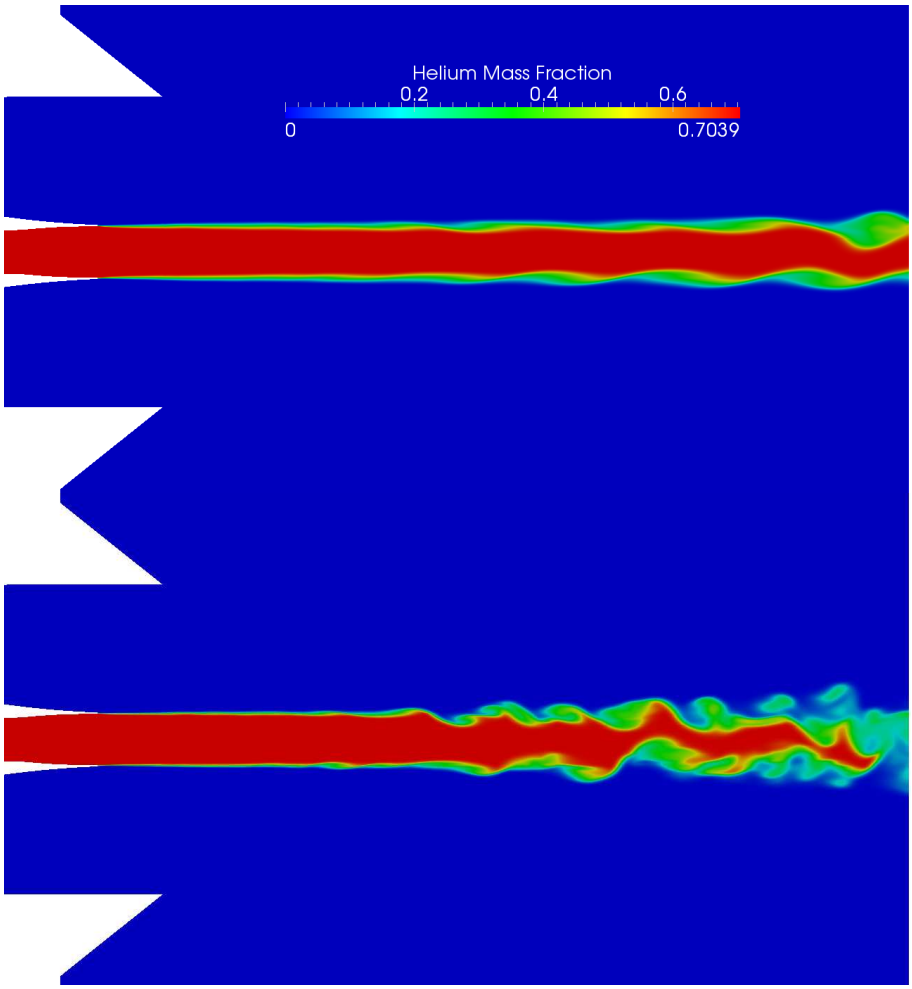

Figure 6.28: Instantaneous helium mass fraction profiles after 630,000 iterations, comparing the cell maximum length (top) and cube root of volume (bottom) filter width calculations.

Although it has been presented that velocity variance values from a simulation employing the cube root filter width are too high, it can be seen from Figure 6.4 that unsteadiness in the outer shear layer is present in practice and hence the level of subgrid viscosity provided by the maximum length filter width is too high. The high levels produced suggest the circumferential cell dimension dominates the filter width in this region, due to the o-grid meshing method employed.

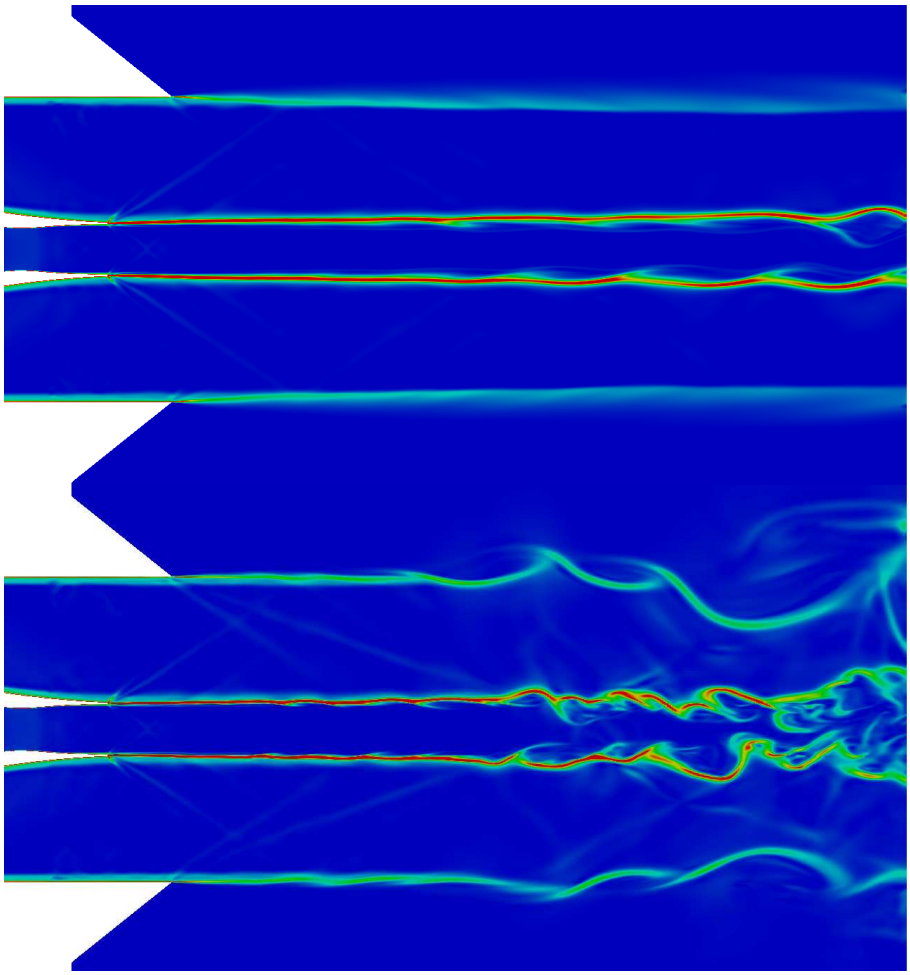

Figure 6.29: Instantaneous numerical schlieren images after 630,000 iterations, comparing the cell maximum length (top) and cube root of volume (bottom) filter width calculations.

Since use of the maximum length filter width is a strict requirement when using the DES method, it is also important to ensure use of the cube root filter width for DDES does not present any problems for the near wall modelling. If the cube root filter width is used in DES, transition to the LES regime incorrectly occurs deep inside the boundary layer, close to the wall. However, as can be seen in Figure 6.30, since the DDES method uses details of the flow variables to handle the RANS to LES transition there is no detrimental impact of employing the less dissipative cube root filter width in these simulations.

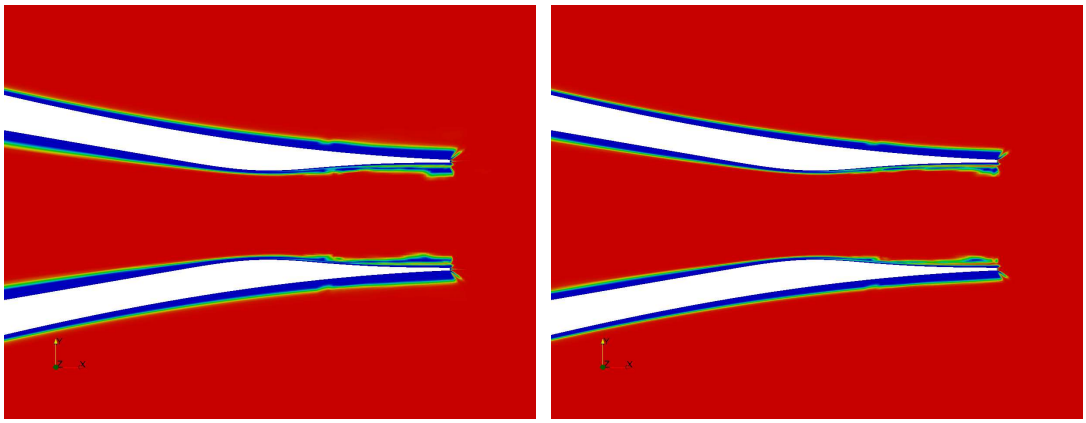

Figure 6.30: RANS-LES blending function for the DDES method, with blue and red corresponding to the RANS and LES regimes, respectively. Maximum length (left) and cube root of volume (right) filter widths are shown at the tip of the central jet nozzle.

In order to reduce the influence of the filter width calculation on the simulation, the computational cells in the LES regime should be made as isotropic as possible. Since the choice of filter width calculation alone can have a significant impact on the computational results, no effort is made to tune the C_{DES} constant employed in the subgrid-scale model.

6.3.3 Reynolds Stresses

The diagonal terms of the Reynolds stress tensor, R_{ii}, are set to $20\text{m}^2\text{s}^{-2}$ for the input turbulence in the DDES simulation presented in Section 6.2, while the off-diagonal Reynolds stresses are set to zero. It is important to investigate the influence of the Reynolds stress magnitude on the computational results obtained.

Figure 6.31 displays the influence on the helium mass fraction and pitot pressure distributions by comparing computational results using values for the Reynolds stress magnitude of $20\text{m}^2\text{s}^{-2}$, $50\text{m}^2\text{s}^{-2}$ and $100\text{m}^2\text{s}^{-2}$. It can be seen that the higher the Reynolds stress values, and hence the higher the magnitude of the velocity fluctuations and corresponding turbulence intensity, the more destructive the input turbulence, leading to a higher spreading rate for the central jet profiles.

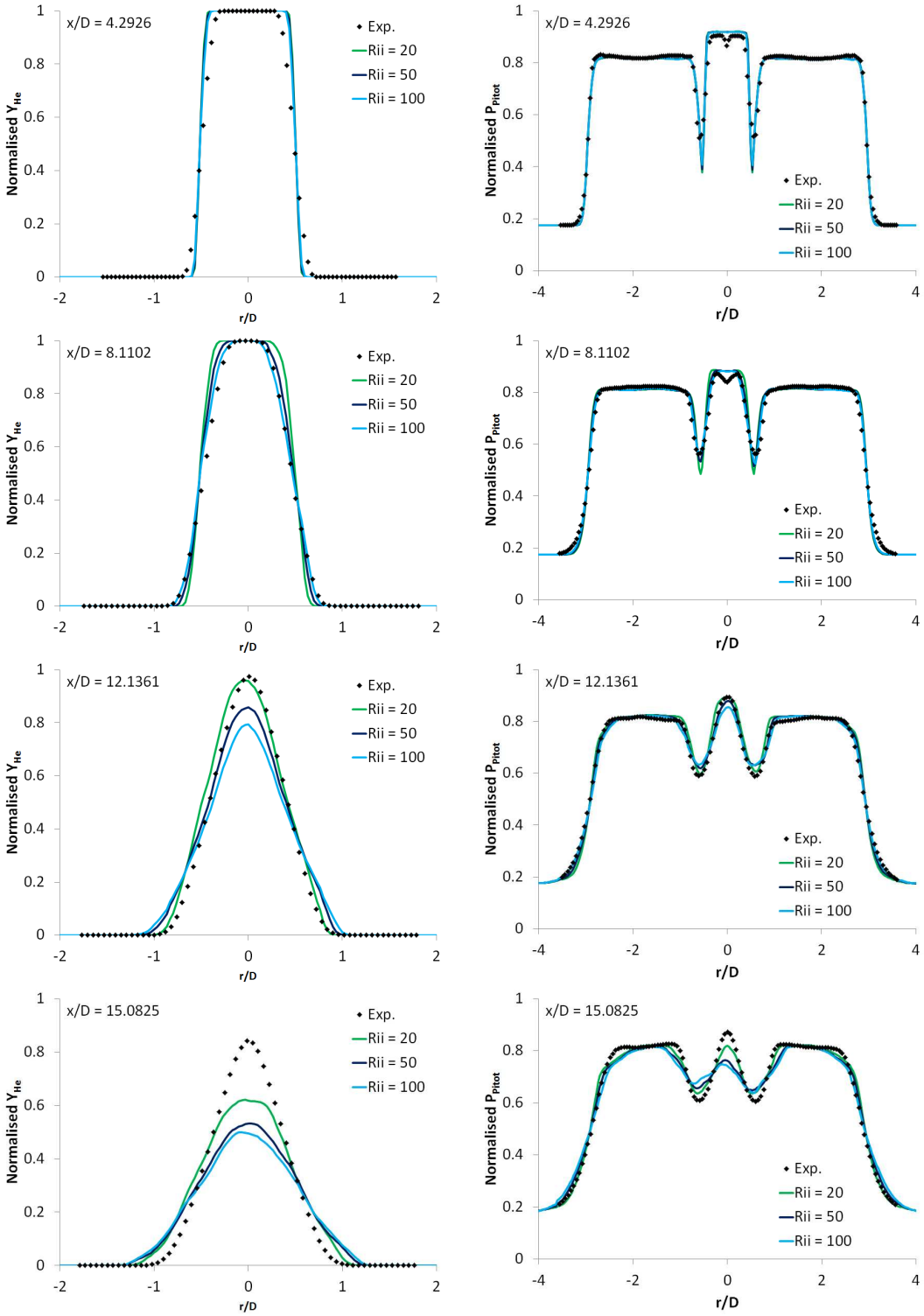

Figure 6.31: Radial (r) profiles of mean normalised helium mass fraction (left) and pitot pressure (right) at several axial (x) locations, with varying inlet turbulence Reynolds stress, in m^2s^{-2}.

However, the Reynolds stress magnitude appears to have a minimal impact on the co-flow and outer shear layer pitot pressure profiles. This may be due to the longer periods required to ensemble average this region of the flow, as discussed in Section 6.2.2.4.

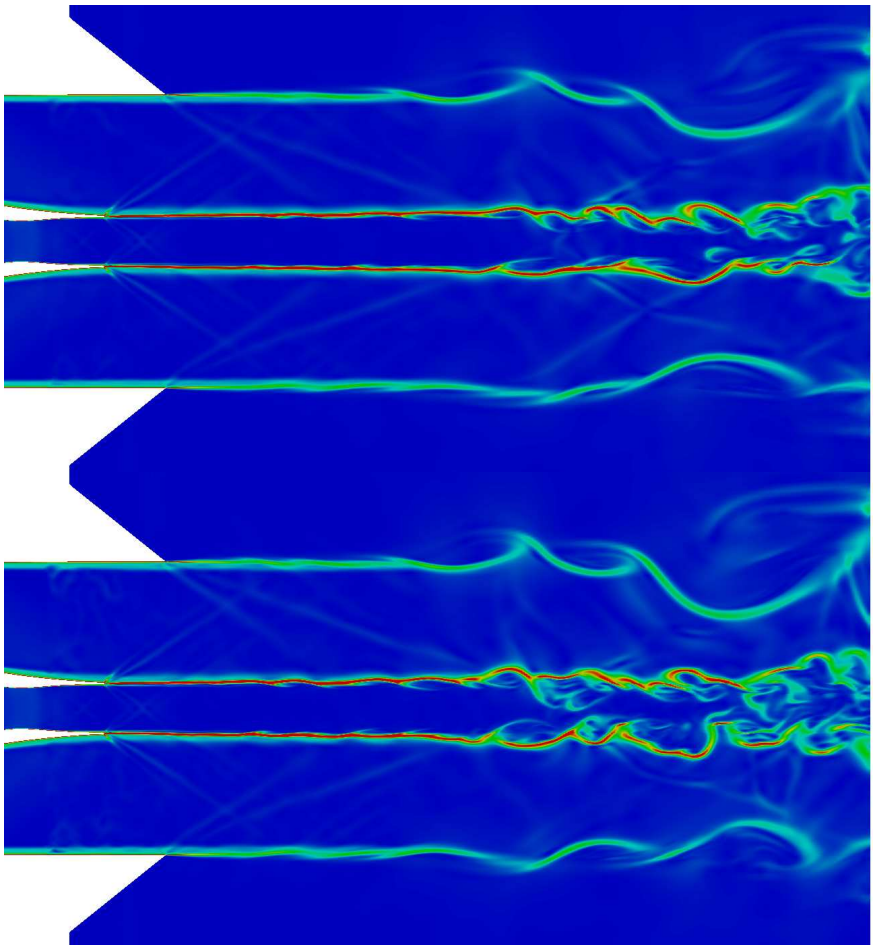

Figure 6.32: Instantaneous numerical schlieren images after 810,000 iterations, comparing inlet turbulence Reynolds stresses of $20\text{m}^2\text{s}^{-2}$ (top) and $100\text{m}^2\text{s}^{-2}$ (bottom).

The schlieren images in Figure 6.32 show the variation in shear layer structure with an increase in Reynolds stress. It can be seen that the severity of shear layer turbulence increases with the inlet turbulence intensity, confirming this as the reason for an increased spreading rate of the central jet profile. The schlieren images also confirm an influence of the Reynolds stress magnitude on the outer shear layer of the flow.

6.3.4 Near Wall Scales

The value employed for the near wall eddy scaling, α_w, may also impact the interaction of inlet turbulence with the jet shear layers. The region in which this scaling takes effect is controlled by the maximum eddy length scale, L_{max}, which is fixed at 3mm. Through manipulation of Equation 4.128 it can be shown that the near wall scaling defines the turbulence length scale in the region where $\alpha_w y_w < 3\text{mm}$. Since the diameter of the central jet inlet domain is approximately 9mm, the value of α_w would need to be greater than 0.67 for the constant L_{max} length scale to take effect anywhere within it.

The influence of the turbulence length scale is studied by applying values of 0.2, 0.4 and 0.6 to α_w for the generation of the imposed turbulence data. The impact on the fluctuating velocities of varying this parameter is presented in Figure 6.33, where it can be seen a reduced value leads to a distribution of finer scales near the wall.

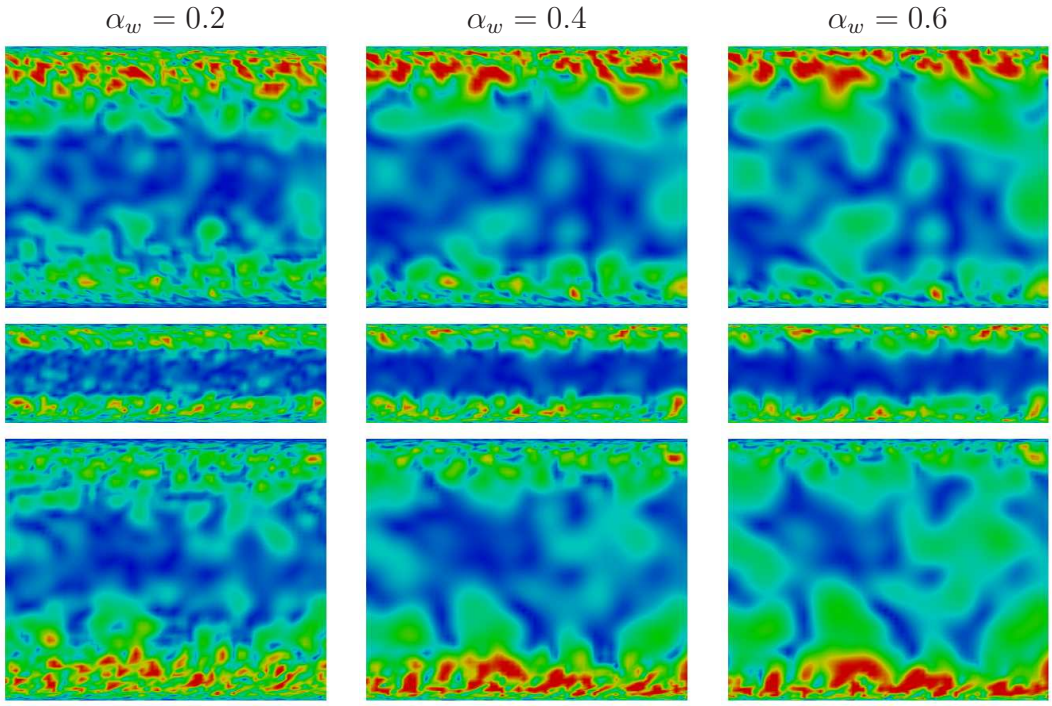

Figure 6.33: Comparing near wall scaling coefficients, α_w, of 0.2 (left), 0.4 (middle) and 0.6 (right) on a sample slice of the turbulence inlet data. Velocity magnitude shown, with scale 0 to 10 m/s.

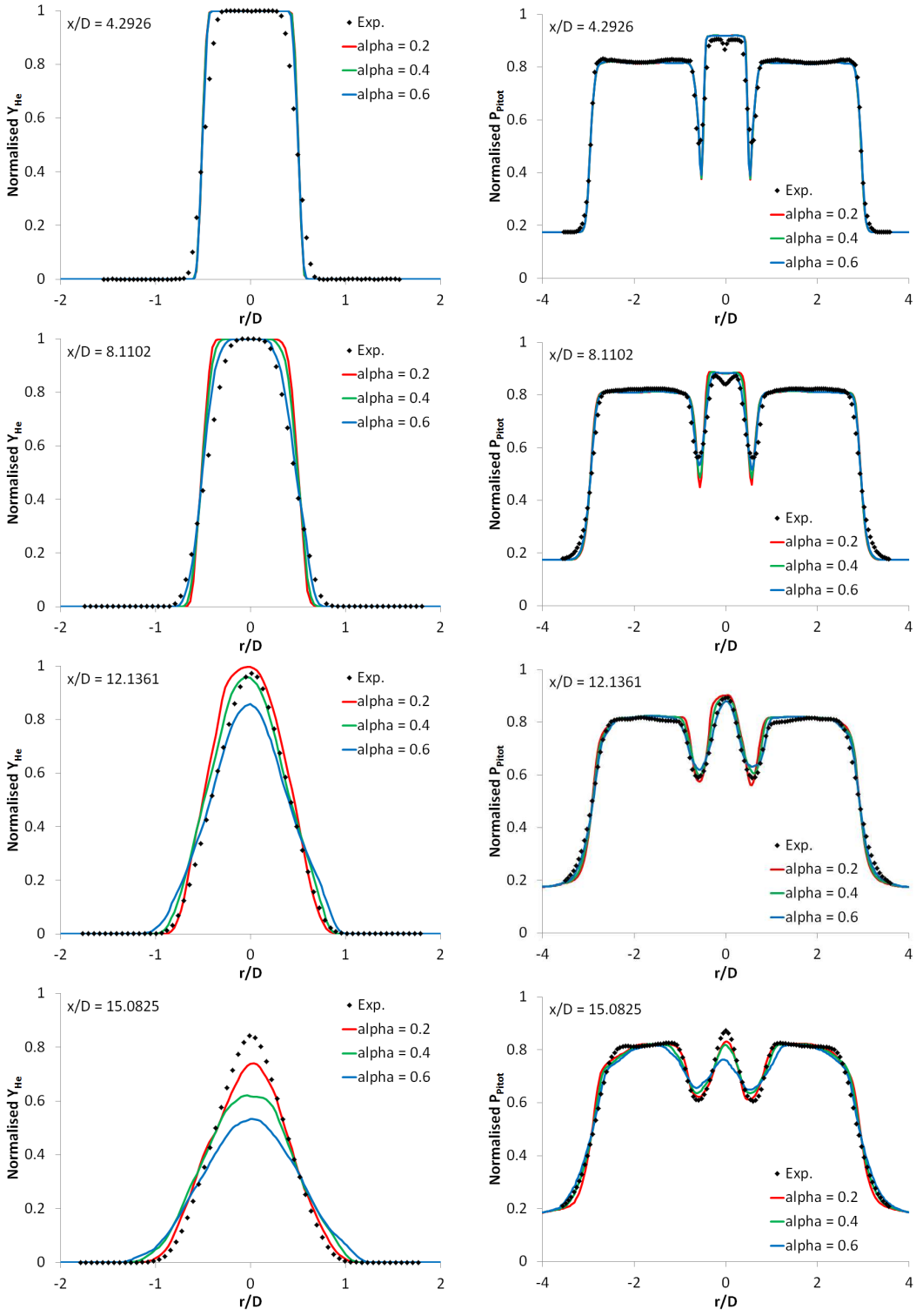

Figure 6.34: Radial (r) profiles of mean normalised helium mass fraction (left) and pitot pressure (right) at several axial (x) locations, with varying near wall scaling coefficient.

Figure 6.34 compares the resulting helium mass fraction and pitot pressure profiles, where it can be seen that the smaller near wall length scales lead to reduced spreading rate of the central jet. Since it is the near wall eddies which will interact with the jet shear layers, and since it is the larger scales which are the more energetic (as defined by the turbulence energy spectrum), the smaller the eddies the smaller the resulting perturbation applied and hence the smaller the resulting instability. Better agreement with experimental data is obtained for the lower near wall scaling values. Again, little influence is apparent for the outer shear layer pitot pressure profile.

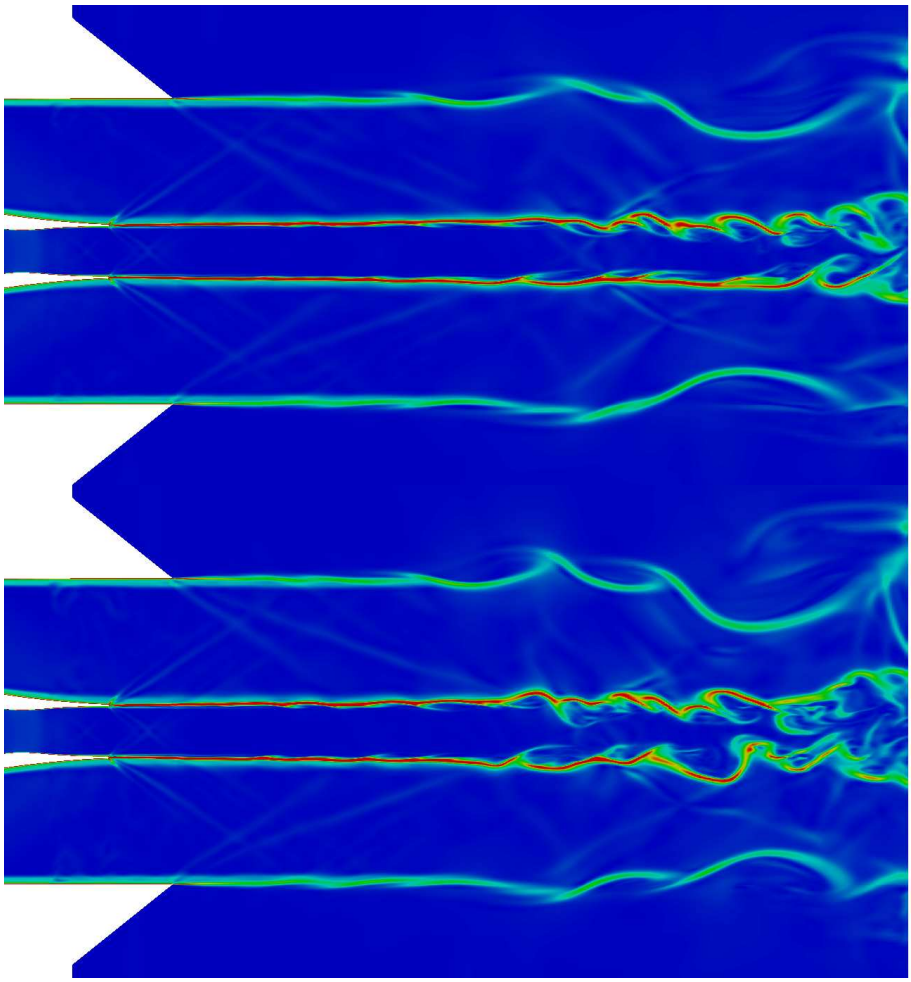

Figure 6.35: Instantaneous numerical schlieren images after 810,000 iterations, comparing inlet turbulence near wall scaling coefficients of 0.2 (top) and 0.6 (bottom).

This is supported by the numerical schlieren images in Figure 6.35 which show the larger the near wall length scales the higher the intensity of the shear layer fluctuations, increasing the spreading rate of the jet.

6.3.5 Mesh Resolution

Due to the implicit filtering applied by the computational grid, the mesh resolution can have an impact on the results obtained. The finer the mesh the higher the level of physics directly captured, and the coarser the mesh the larger the filter width and the larger the reliance on the SGS model. Here, results from the $R_{ii} = 20\text{m}^2\text{s}^{-2}$ and $\alpha_w = 0.4$ simulation are compared to data from the finer mesh calculations of Section 6.1.

It can be seen from Figure 6.36 that the coarser mesh predicts a reduced spreading rate for the central jet profile. This is due to the larger filter width providing higher levels of subgrid viscosity, as can be seen from Figure 6.37, which dampens the intensity of the turbulent fluctuations and hence decreases the severity of the jet breakup. However, the magnitude of this reduction is limited by the filter width used; if the maximum length filter width was employed an increase in the subgrid viscosity on the order of 100% would be incurred in the central jet region, through a doubling of the axial mesh spacing. A finer resolution of the turbulent structures is also evident with a higher mesh density.

It can also be seen from Figure 6.36, that for the turbulence inflow profile in question, the coarser mesh gives results in better agreement with experimental data for the central jet profiles. Better agreement is also obtained for the co-flow pitot pressure profile and this is partly due to the higher filter width providing higher levels of dissipation to control the large scale dynamics of the outer shear layer. However, the ensemble averaged data for the finer mesh has been collected over a significantly longer period and it was shown in Section 6.2.2.4 that due to the large scale instabilities in the outer shear layer and presence of subsonic velocities the statistics there take longer to converge, and hence this may not be a fair comparison.

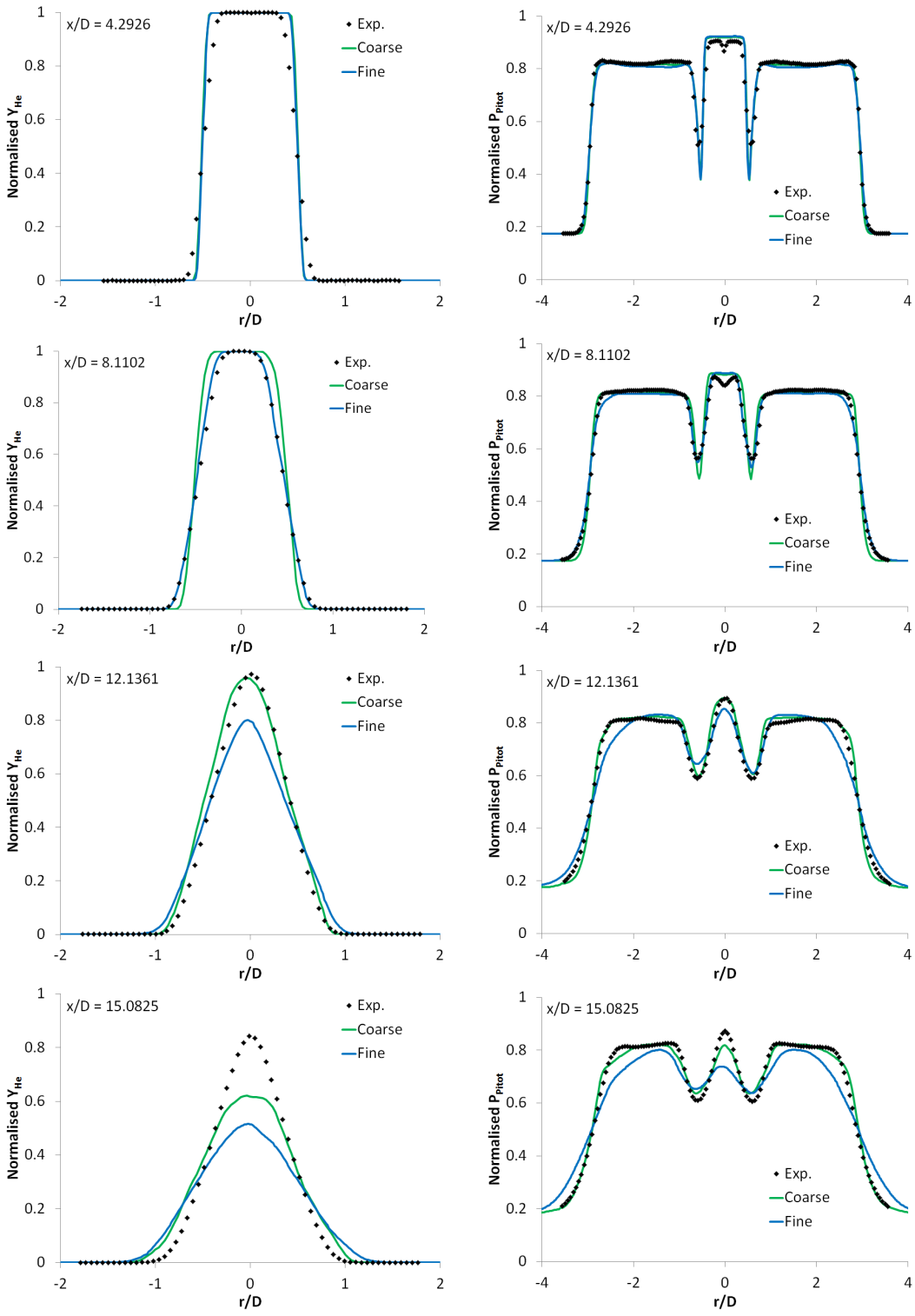

Figure 6.36: Radial (r) profiles of mean normalised helium mass fraction (left) and pitot pressure (right) at several axial (x) locations, on coarse and fine computational meshes.

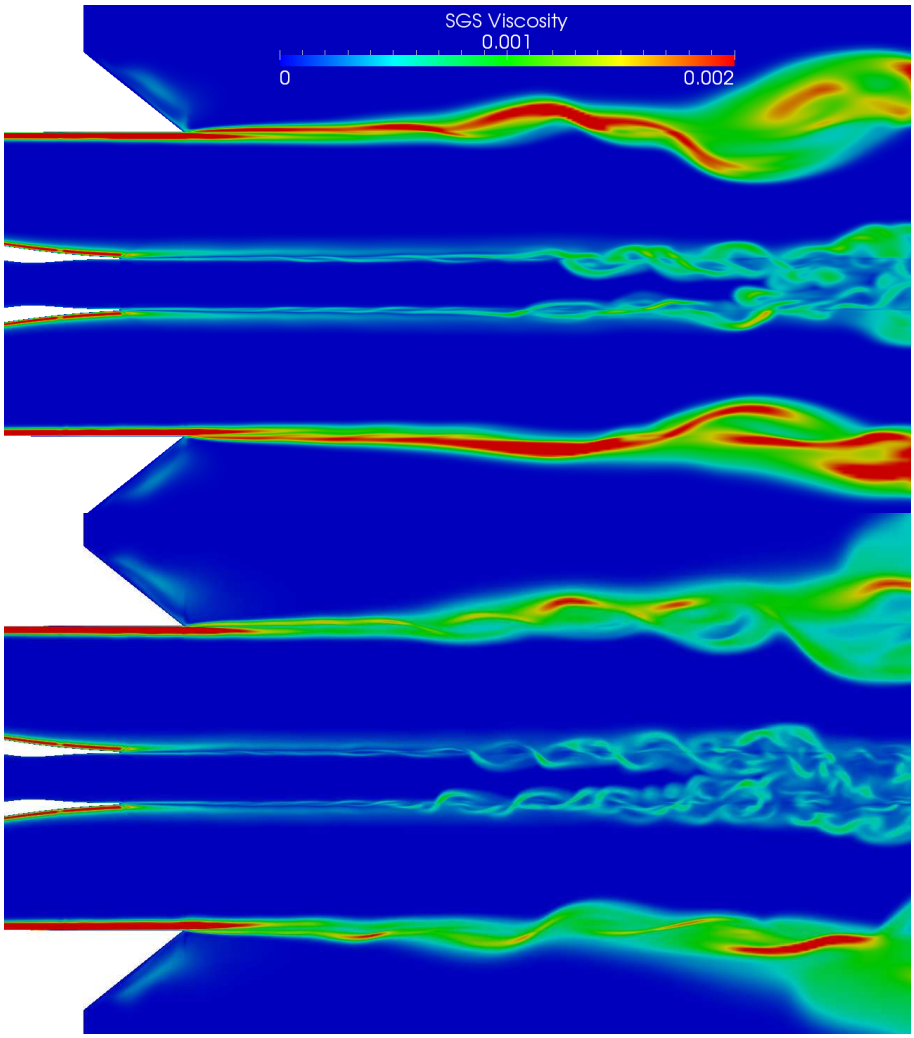

Figure 6.37: Instantaneous SGS viscosity profiles after 810,000 iterations on coarse (top) and fine (bottom) computational meshes.

The turbulence energy spectrum in Figure 6.38 confirms the resolution of the coarser computational mesh is high enough in all directions to provide a filter width within the inertial range. Spectra are evaluated using all three velocity components, with a time history from 270,000 to 810,000 iterations. Similarly to the spectrum in Figure 6.13 the velocity data is obtained at the centreline of the jet, but now at an axial location of x/D = 15.0825. It is difficult to tell with spectra calculated from velocity data at a single point, but again it appears the inertial range of the turbulence spectrum has a decay rate in agreement

with Kolmogorov's $k^{-5/3}$ law, rather than the steeper gradient of $k^{-8/3}$ due to compressibility effects proposed by Ingenito and Bruno [19].

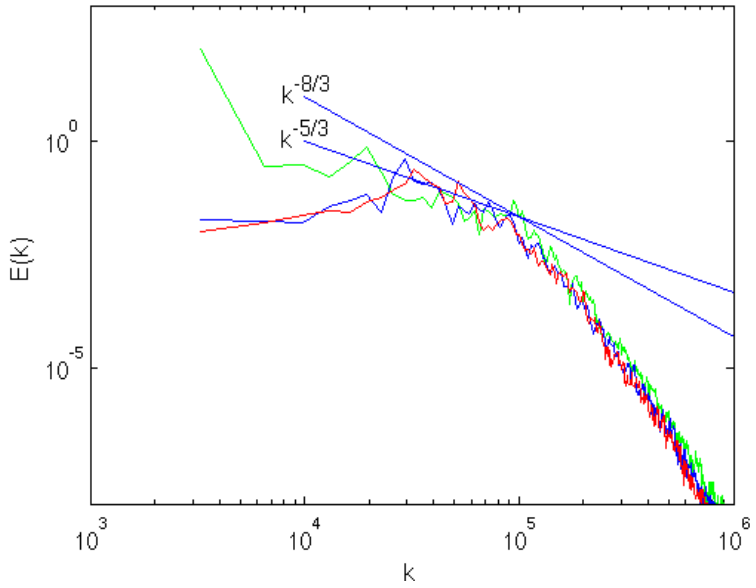

Figure 6.38: Turbulence energy spectrum for coarse mesh using x-velocity (green), y-velocity (blue) and z-velocity (red).

6.4 Modified Turbulence Initialisation

It has been suggested earlier that the poor agreement of the co-flow pitot pressure profile with experimental data is due to the large scale dynamics of the outer shear layer. It has also been seen from the numerical schlieren image in Figure 6.17 that this also leads to an interaction between the outer and inner shear layers, possibly encouraging central jet breakup at downstream locations.

The severe turbulent nature of the outer shear layer is due in part to the high levels of turbulence intensity for the imposed turbulent fluctuations at the outer surface of the co-flow jet, as can be seen in Figure 6.8, which is a product of the turbulence initialisation method employed.

As discussed in Section 4.10, the turbulence initialisation method [64] scales the velocities pre-diffusion by the cell volume. Figure 6.39 shows the influence of this cell volume scaling, where it can be seen the most uniform velocity magnitude profile is obtained when no scaling is employed. Scaling by the inverse of the cell volume significantly reduces the magnitude of velocity fluctuations in the majority of the domain but high velocities exist in the very near wall cells due to division by their low volume.

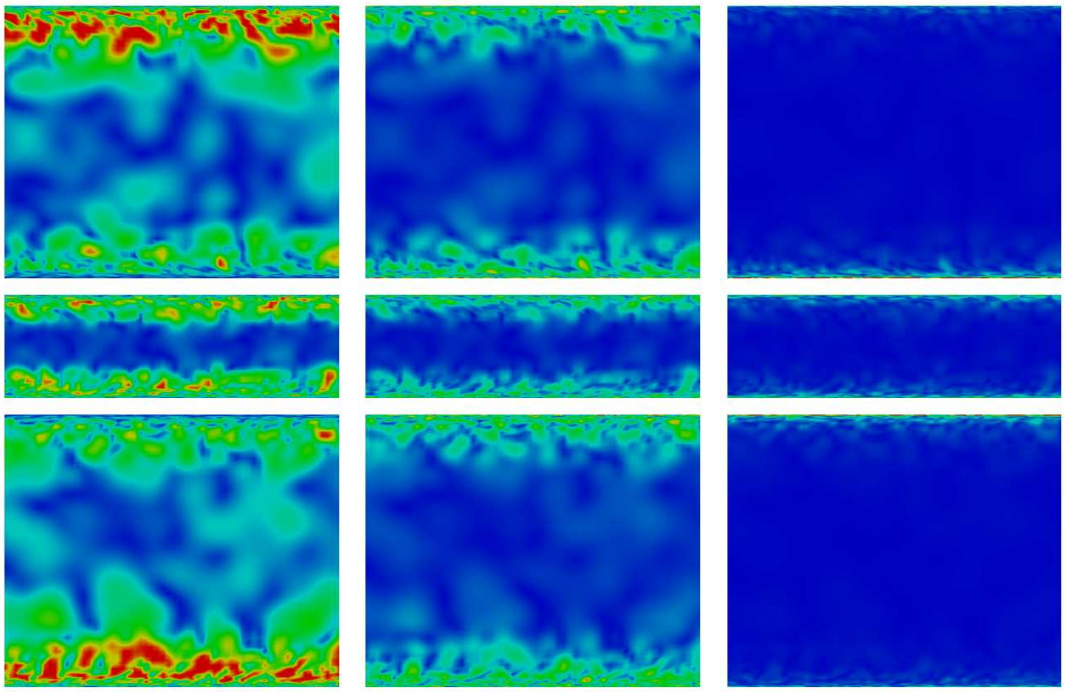

Figure 6.39: Showing influence of cell volume scaling on turbulence initialisation with volume multiplication (left), no volume scaling (middle) and volume division (right). Velocity magnitude shown, with scale 0 to 10 m/s.

It is possible that the weighted least squares method used for the gradient reconstruction in the turbulence initialisation calculation contributes to the higher turbulence intensity at the outer co-flow surface. Such methods can provide poor estimates of the gradient for highly stretched cells in regions of surface curvature [120], such as exists in this region of the mesh. Strong gradients requiring calculation may be initiated near the wall by the volume scaling process, due to the presence of cell stretching in the wall normal direction for boundary layer

capture.

A simulation neglecting the volume scaling for the imposed turbulence fluctuation calculation is conducted in an attempt to study the influence of the outer co-flow surface turbulence intensity on the outer shear layer and of the outer shear layer behaviour on computational results. Reynolds stresses R_{ii} are set to $20\text{m}^2\text{s}^{-2}$, with off diagonal terms fixed at zero, and the near wall length scaling term, α_w, is set to 0.4.

It can be seen from the schlieren image in Figure 6.40 that the unsteadiness experienced in the outer shear layer is somewhat reduced, but significant turbulent structures still remain and some interaction between the inner and outer shear layers is still evident.

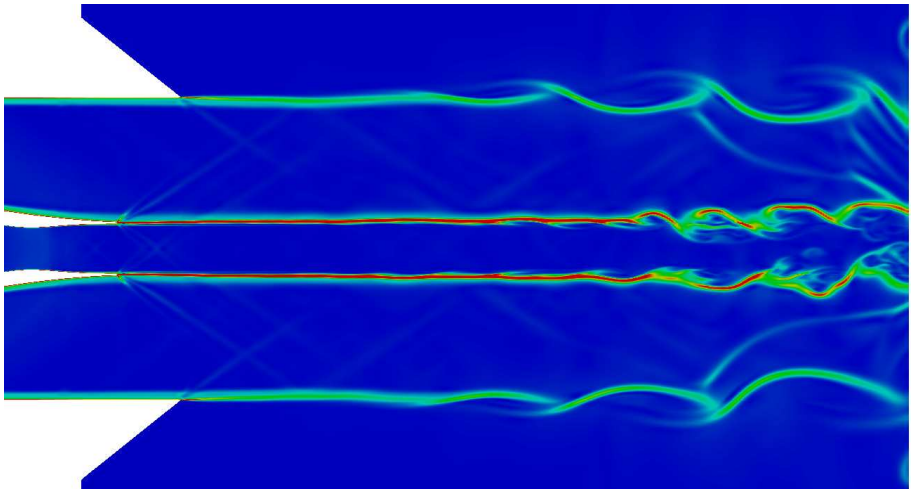

Figure 6.40: Instantaneous numerical schlieren image with no volume scaling applied to the inlet turbulence initialisation.

It can be seen from the helium mass fraction profiles in Figure 6.41 that at the x/D locations of 8.1102 and 12.1361 there is a mild reduction in the predicted spreading rate of the jet. This is most likely to be caused by the corresponding reduction in turbulence intensity of the central jet and inner co-flow surfaces caused by the removal of the volume scaling from the turbulence initialisation method (see Figure 6.39). However, at an x/D location of 15.0825 a significant improvement over the results obtained with volume scaling employed, is found. Since the interaction between inner and outer shear layers is more prominent at

downstream locations, the reduction in severity of the outer shear layer breakdown may be the reason for these improved results.

Although there is an improved agreement with experimental data at the most downstream location, it should be noted the predicted reduction in the spreading rate experienced closer to the jet exit provides a worse agreement than previously obtained.

The increased accuracy at downstream locations is reinforced by the pitot pressure profiles in Figure 6.41. However, the intensity of the shear layer turbulence is confirmed as too high by the discrepancy between computational and experimental results in the outer shear layer region, at the x/D location of 15.0825.

The computational cost involved in evaluating fully converged rms velocities is high. However, comparing the values after 90,000 and 180,000 iterations of rms calculations in Figure 6.42 it can be seen that the approximate magnitude of the mean fluctuating velocities can be evaluated, since there is no drastic change in the shear layer rms values between these two evaluations. However, the results show there is still a large disagreement with experimental data, despite the improvement in central jet profiles for mean values.

The low rms values experienced at the first three axial locations corresponds to the benign nature and corresponding delayed transition of the inner shear layer and corresponding under prediction of the central jet spreading rate. This reduced spreading rate leads to sharp peaks at a x/D location of 8.2, but the unsteady shear layer behaviour at this location leads to rms values larger than found in practice. The breakdown in the central jet leads to an agreement with experimental data for the width of the profile at locations further downstream, but the intensity of the velocity fluctuations still far exceeds what is required.

It is this transition from low levels of shear layer turbulence intensity to severe jet breakup which causes problems. As well as the interaction of inner and outer shear layers already discussed, the interaction of the turbulence structures in the central and co-flow jets at the inner shear layer interface further complicates the physics involved. To demonstrate the severity of this interaction, Figure 6.43 demonstrates the greatly reduced dynamics of the inner and outer shear layers when the turbulence structures imposed in the co-flow are removed.

The differences between rms values presented in Figures 6.19 and 6.42 are

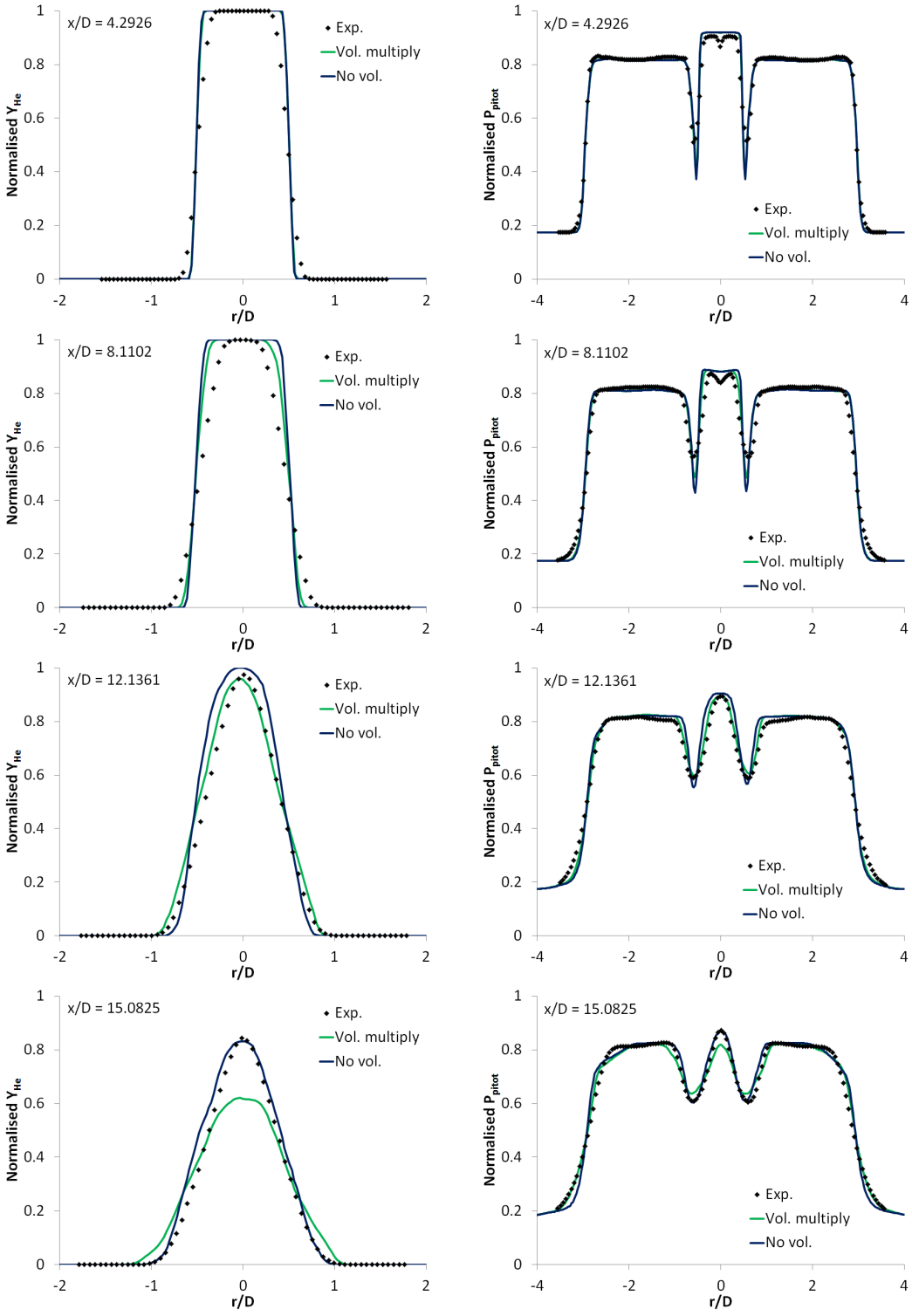

Figure 6.41: Radial (r) profiles of mean normalised helium mass fraction (left) and pitot pressure (right) at several axial (x) locations, with original and no volume scaling applied to the inlet turbulence initialisation.

partly due to mesh resolution effects and partly due to the reduced inlet turbulence intensities through removal of the volume scaling.

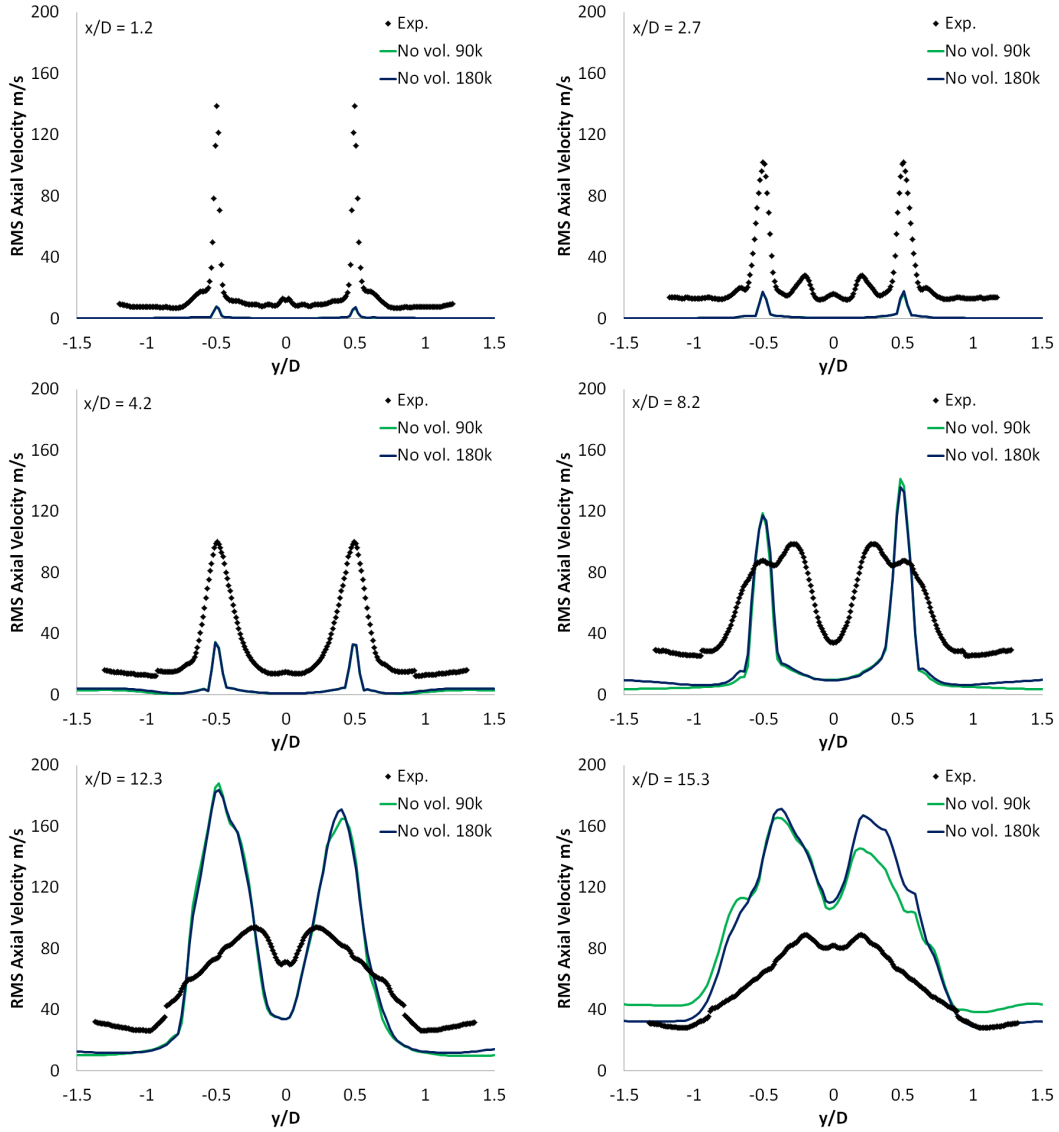

Figure 6.42: Radial (r) profiles of rms axial velocity at several axial (x) locations, with no volume scaling applied to the inlet turbulence initialisation, after 90,000 and 180,000 iterations of rms calculations.

It is possible that the downstream convection of inlet coherent structures causes a continual interaction with the jet shear layers, further increasing the

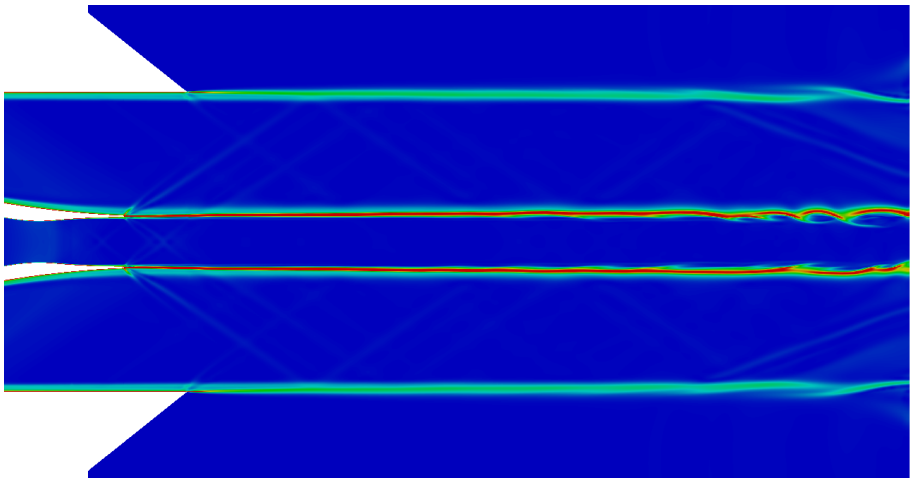

Figure 6.43: Instantaneous numerical schlieren image with the co-flow inlet turbulence removed.

severity of the jet breakup and resulting rms velocity magnitudes. Implementing the method of Keating and Piomelli [63] whereby stochastic forcing is employed at the RANS-LES interface, increasing the resolved stresses in this location, may be more suitable. The turbulence intensity in the shear layers near the jet exit might therefore be increased in line with the experimental data with no further interactions downstream to exacerbate the shear layer instabilities.

The same length scales and intensity levels have been employed in both the central and co-flow jets and this is another area of the computational setup which could be altered. There is no-end to the modifications which can be made to the simulation and imposed turbulence profiles in order to obtain good agreement with the experimental data, but it has already become a costly exercise. Of course the low levels of subgrid viscosity provided by the chosen filter width or chosen mesh design could also have a detrimental impact on the results obtained. The influence of the near wall scaling has been demonstrated but the maximum length scale, L_{max}, could also play a role in the dynamics of the simulation. However, it is obvious that the imposed turbulent structures play a significant role in the resulting jet behaviour and it is therefore very important for experimentalists to try and provide turbulence length scale and intensity data in order for accurate simulations to be possible.

It appears that, compared to RANS, LES is more computationally expensive

and still requires tuning of the simulation setup. However, LES is more physically meaningful and the parameters influencing the simulation are measurable properties rather than constants used in the modelling process. The high physical content of a large eddy simulation can be used to investigate the complex processes present in a supersonic combustor and therefore further improve the understanding of the physics involved in supersonic combustion.

Chapter 7

SCHOLAR Test Case

In order to validate the combustion modelling aspects of PULSAR, the SCHOLAR scramjet test case is to be simulated. Again, the capabilities of the RANS and LES approaches to turbulence modelling are compared and an investigation into the physics and regime of supersonic combustion is conducted.

7.1 Description

The SCHOLAR experiment [105] was designed with the validation of computational fluid dynamics software in mind, and in particular the validation of codes to be used for the simulation of supersonic combustion. This test case has been discussed in significant detail elsewhere [88; 105] and so only a basic overview is presented here.

Figure 7.1 is a schematic of the SCHOLAR experiment, showing the simple geometric configuration which makes up a scramjet combustor. Hot vitiated gas is supplied to the combustor nozzle at subsonic velocities, from a heater burning hydrogen with premixed oxygen and air. The enthalpy at the nozzle inlet corresponds to a flight Mach number of 7 and the nozzle has an exit Mach number of 2. Pure hydrogen is injected through the top wall of the combustor at an angle of 30 degrees to the horizontal, as shown in Figure 7.2, and the injector is designed to give an exit Mach number of 2.5.

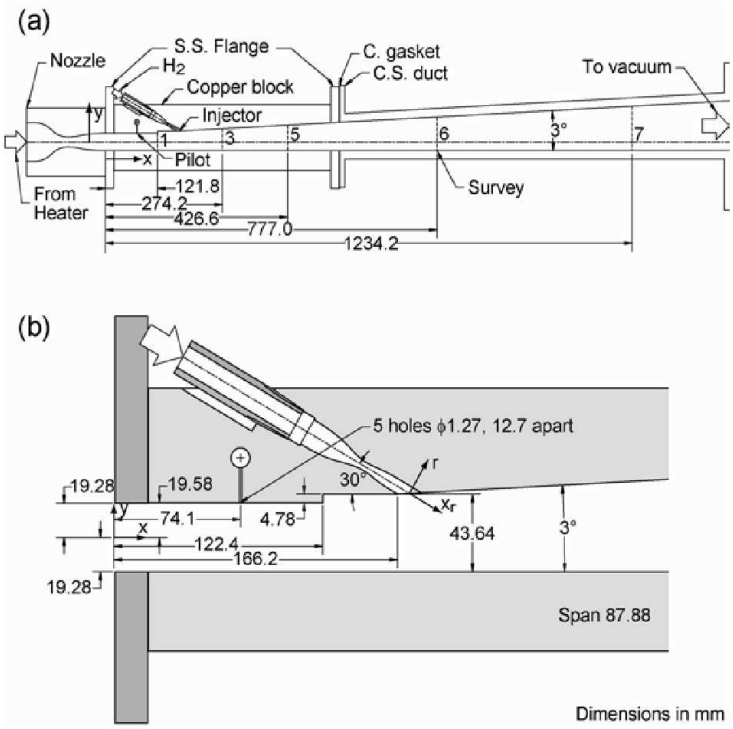

Figure 7.1: Schematic of the SCHOLAR experiment [105] (a) Detail of nozzle and combustor (b) Detail of combustor entrance and injector geometry

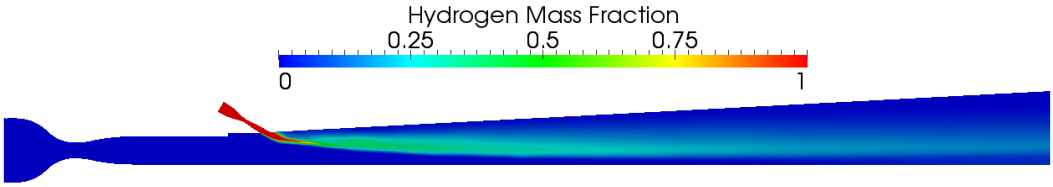

Figure 7.2: Hydrogen mass fraction distribution on the combustor centreline

The combustor is divided into three sections; a water cooled nozzle, a copper section containing the isolator and injector, and a downstream carbon steel section containing the remaining divergent section of the combustor. The sections are connected with stainless steel flanges and carbon gaskets. The thickness of the copper and steel sections allowed the combustor to run without cooling, however

this lack of cooling limited the possible run times of the experiment to just over 20 seconds, in order to prevent damage to the apparatus. After injection, the upper wall of the duct diverges at a constant angle of three degrees to the horizontal.

7.1.1 Experimental Data

Figure 7.1(a) shows 5 locations down the length of the combustor (labelled 1, 3, 5, 6 and 7) at which measurements are taken using the CARS technique, providing profiles of static temperature along with oxygen and nitrogen mole fraction distributions. The temperature and oxygen mole fraction data are presented in Figure 7.3.

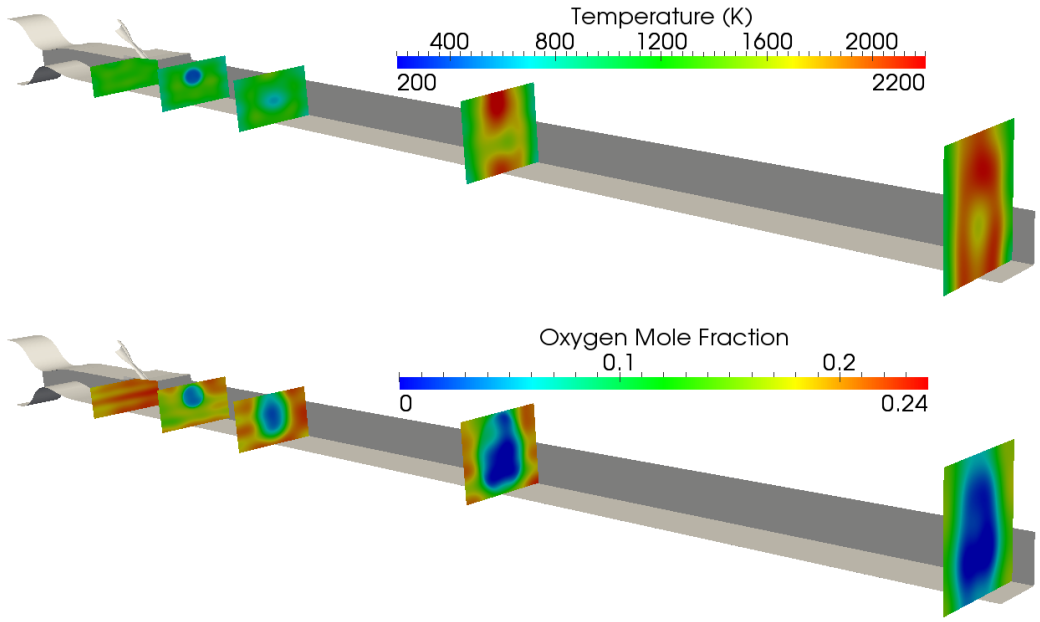

Figure 7.3: Planes of temperature and oxygen mole fraction experimental data down the axis of the SCHOLAR combustor

Static pressure taps are located on upper, lower and side walls of the combustor. Pressure measurements were taken at two second intervals during the experiment, starting at 10 seconds and ending after 24 seconds of run-time. Figure 7.4 compares the first and last set of pressure measurements with the mean

profile for the top and bottom walls, showing little change in the data. The mean profiles are to be compared to computational results.

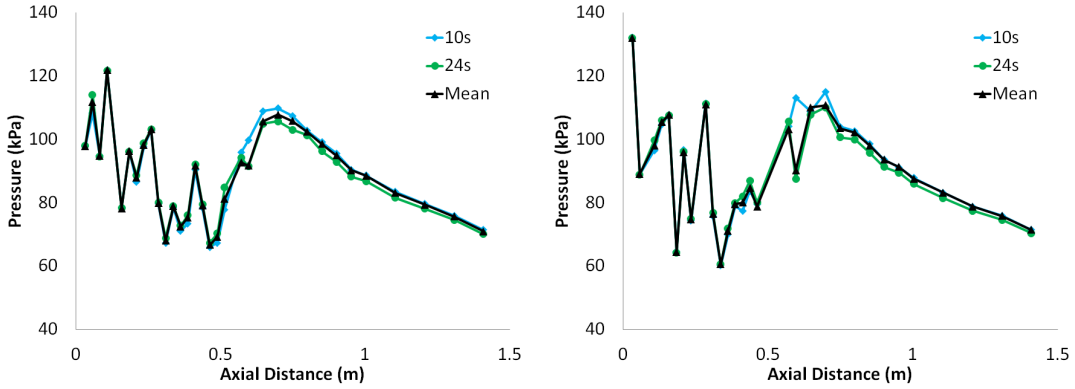

Figure 7.4: Experimental pressure distributions for the upper (left) and lower (right) walls of the combustor, after 10 and 24 seconds and the mean.

It should be noted that pressure taps in the copper section of the combustor are located along the centreline of the bottom wall, but at a location of z = -36.3mm for the top wall, where z is measured from the centreline [105]. For the steel duct, pressure taps are located along the centreline for both upper and lower walls. Thermocouples are also present on the top wall for surface temperature measurements, which are discussed in more detail in the next section.

7.1.2 Boundary Conditions

The nozzle and injector inlet boundary conditions are summarised in Table 7.1. The nozzle inlet species mass fractions are made up of H_2O, O_2 and N_2 since it was measured that these species make up 99% of the mixture molecular weight from the heater outlet [88], however the unmeasured 1% of radical species is a high concentration which could have a significant influence on ignition.

The wall temperature of the nozzle is set at 500 K, but the wall temperatures of the copper and steel sections varied from about 320 K to 500 K and 890 K, respectively. Due to the lack of cooling, the copper and steel sections did not reach a steady state temperature and so the respective wall temperatures for the simulations are set at 475 K and 700 K, as in [88]. However, it has been shown [88] that computational results are not sensitive to the wall temperature values.

Parameter	Nozzle	Injector
P_0 (MPa)	0.767	3.440
T_0 (K)	1828	302
Y_{H_2}	-	1.0
Y_{O_2}	0.2321	-
Y_{H_2O}	0.2041	-
Y_{N_2}	0.5638	-

Table 7.1: Inlet boundary conditions for nozzle and injector, showing stagnation pressure, stagnation temperature and species mass fraction values

7.2 RANS Simulations

As discussed in Section 3.4, it has been shown that the influence of turbulence-chemistry interaction modelling has a negligible impact on the results obtained when simulating a simple laboratory supersonic jet flame. Recent studies have therefore neglected these interactions and used simple laminar chemistry to handle the reaction rate calculations.

In order to see if turbulence chemistry interaction modelling plays a more significant role in a practical scramjet combustor geometry, computational results from simulations employing laminar chemistry and the assumed PDF combustion model are to be compared. These simulations are also to be used to tune the setup of an LES study by aiding the choice of combustion model and chemical mechanism.

7.2.1 Computational Mesh

The computational mesh is based on that from a previous study [88] and is a pure hexahedral multi-block mesh generated using ANSYS ICEM CFD. The mesh is fully three dimensional and contains 12.18M cells. Details of the mesh in the injector region can be seen in Figure 7.5, where an o-grid is employed to handle the circular injector cross-section.

In order to reduce the computational cost, rather than simulating the full length of the combustor the mesh is terminated at a length of 1.25m which is just downstream of the final plane of experimental data. Due to the supersonic flow

Figure 7.5: RANS mesh for the SCHOLAR test case. Detail around the step and injector shown.

conditions, the increased proximity of the domain outlet should not influence the computational results upstream.

A near wall mesh spacing of 1×10^{-5}m is uniformly applied to all surfaces, providing the y^+ distribution shown in Figure 7.6. It can be seen that the near wall mesh resolution is sufficient to ensure y^+ values of less than 5 over all combustor surfaces. However, the y^+ values on the surface of the injector are somewhat higher due to the low hydrogen density causing a higher speed of sound and hence higher velocities for a given Mach number. As the velocity increases through the injector throat the boundary layer thins and y^+ values increase, but are reduced again after the throat due to boundary layer growth, despite further flow acceleration.

The axial mesh spacing transitions from approximately 1mm in the region of injection, to 1.5mm in the steel section of the duct. A constant spacing of approximately 1mm is employed in the z-direction (perpendicular to the page as viewed in Figure 7.5), but due to the increasing height of the combustor the y-direction mesh spacing (between upper and lower walls) transitions to approximately 1.4mm at the outlet. A coarser mesh is employed in the nozzle section, in the axial direction.

Simulations are run on 64 cores of the Stokes cluster and convergence is measured through the monitoring of primary variables, as can be seen in Figure 7.7. Simulations are initialised with a non-reacting solution.

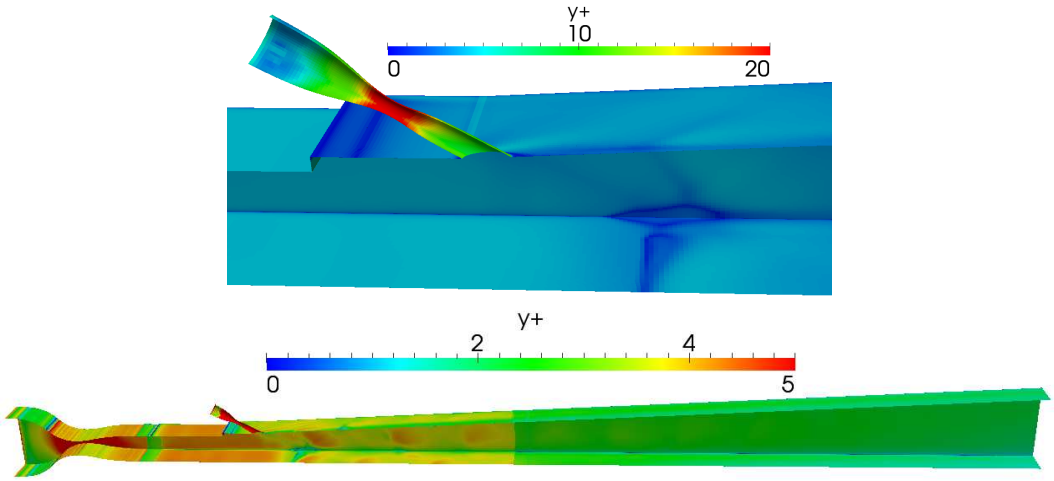

Figure 7.6: y^+ distribution for the SCHOLAR test case RANS simulations

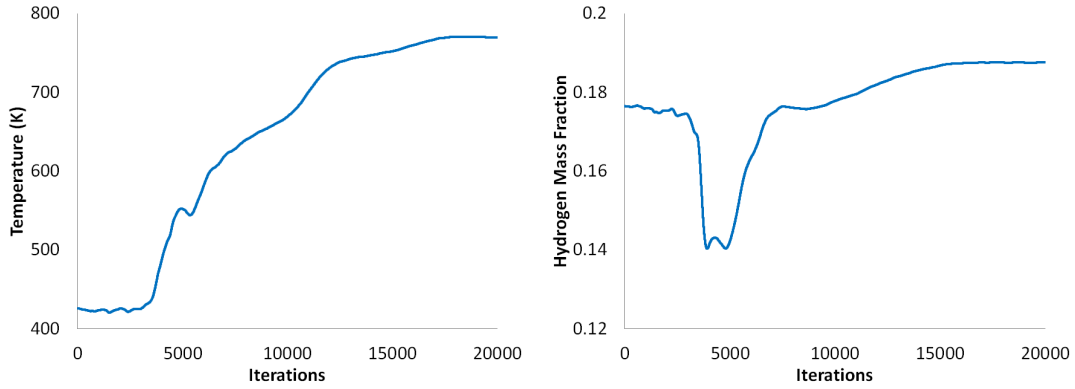

Figure 7.7: Convergence of the temperature and hydrogen mass fraction on the combustor centreline at x = 0.777m

7.2.2 Computational Methods

Again, the second order AUSM+UP scheme with the Van Rosendale gradient limiter is used for the spatial discretisation and the third order three step TVD

Runge-Kutta scheme for temporal integration. Since the assumed PDF combustion model is to be employed, it is important to use the two-equation Menter SST turbulence model in order to provide information about the turbulence length scales, for use in source terms of the combustion model variance equations. The k and ω variables are set in a way to enforce the turbulence intensity and ratio of turbulent to molecular viscosity at the nozzle exit (x = 0.0m) to be equal to 5% and 200, respectively, roughly in line with values used in [88].

Tabulated data is used for the forward and backward reaction rate calculations in the assumed PDF combustion model, which are calculated at the start of the simulation. The range of temperature and temperature variance intensity values used for the table are 300K to 3000K and 0.0001K to 0.8K, respectively, where the temperature variance intensity, I_{σ_T}, is defined as:

$$I_{\sigma_T} = \frac{\sqrt{\sigma_T}}{\widetilde{T}} \tag{7.1}$$

These ranges are each split into 300 equally spaced values, generating tables of 90,000 data points.

Since the purpose of these simulations is to investigate the influence of different modelling approaches on the computational results obtained, model constants will be fixed between simulations and will not be tuned to give excellent agreement with experimental data, as was done in Chapter 5. The turbulent Prandtl and Schmidt numbers are fixed at 0.9 and 0.7, respectively. No compressibility correction is employed

Although no information is provided on the concentration of radical species in the vitiated air at the inlet to the combustor, the high stagnation temperature of the flow combined with subsonic velocities causes reactions to proceed in the nozzle. These nozzle reactions are permitted in order to naturally generate highly reactive radical species, which are convected into the combustor to aid the ignition process.

7.2.3 Chemical Kinetics

As well as studying the influence of turbulence-chemistry interaction modelling it is also important to investigate the effect of the chemical mechanism on computa-

tional results. Therefore, two chemical kinetics models are to be compared, which are the full [91; 92] and reduced [94] Jachimowski mechanisms. As discussed in Section 3.5, these mechanisms are two of the most widely used in supersonic combustion research and have both been shown to give comparable results to the more complex O'Conaire mechanism. The full Jachimowski mechanism uses 9 species and 19 reactions while the reduced mechanism is significantly more cost effective, consisting of 7 species and 7 reactions. Details of each mechanism can be found in the Appendix.

7.2.4 Results

In order to investigate the influences of turbulence-chemistry interaction modelling and chemical kinetics, four simulations are conducted with the combination of computational setups displayed in Table 7.2.

	Reaction Rate	Chemical Mechanism
Simulation 1	Laminar chemistry	Reduced Jachimowski
Simulation 2	Assumed PDF model	Reduced Jachimowski
Simulation 3	Laminar chemistry	Full Jachimowski
Simulation 4	Assumed PDF model	Full Jachimowski

Table 7.2: Setup of four RANS simulations of the SCHOLAR test case

Figure 7.8 compares the experimental temperature profiles obtained using the CARS technique with computational data from the four simulations. The first point to note is the significant disagreement at the second location (x=0.4266m), where the high temperatures predicted in the simulations correspond to earlier ignition than found in the experiment. As can be seen from Figure 7.9, early ignition is caused by the presence of an oblique shock. The strong shock wave boundary layer interaction causes an increase in downstream temperature which is high enough to cause ignition to occur. It should be noted that the contours of static pressure are overlaid onto a static temperature profile. Ignition through this mechanism and flame anchoring at this location is evident in all simulations conducted. The physics present in this ignition process is very complex and presents a significant challenge to the computational methods employed. Due to the high kinetic energy of the flow, if a slightly stronger shock wave boundary

layer interaction is predicted than occurred in the experiment the subsequent deceleration would raise the local temperature sufficiently to cause ignition to occur.

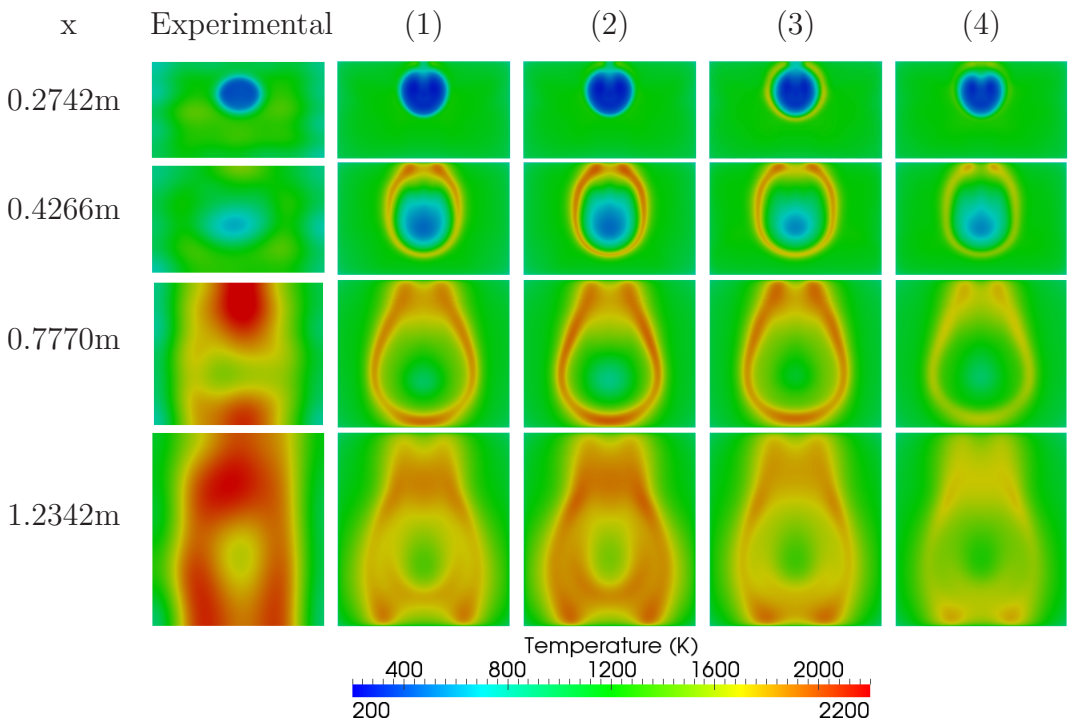

Figure 7.8: Comparison of mean temperature profiles from each RANS simulation to experimental data

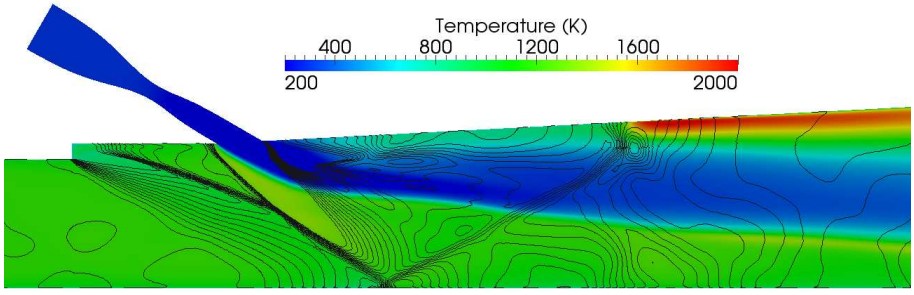

Figure 7.9: Shock induced ignition shown by contours of static pressure over a static temperature profile

Comparing results from the two chemical mechanisms, it appears the full mechanism in combination with the assumed PDF combustion model is not capable of predicting the high temperature levels found in the experimental data, but the profiles obtained are consistent with those from the other three simulations.

By comparing results from laminar chemistry and the assumed PDF combustion model for each mechanism, it is evident that minimal differences occur between temperature profiles, at all axial locations. Both laminar chemistry and turbulence chemistry interaction modelling results give reasonable agreement with experimental data, downstream of ignition. This suggests laminar chemistry does a reasonable job at simulating supersonic combustion for this particular test case, implying that interactions between turbulence and the reaction zone are minimal.

This conclusion can be reinforced through comparison of experimental and computational O_2 mole fraction profiles. It can again be seen from Figure 7.10 that when comparing results from laminar chemistry with those from the assumed PDF combustion model, for the same mechanism, minimal differences occur. There are however differences between results from the two chemical kinetics models, with a faster destruction of oxygen occurring with the full Jachimowski mechanism in the core region of the flow. However, with these simple visual comparisons it is difficult to say with any certainty which mechanism is in better agreement with experimental data.

Computational results for the wall pressure can also be compared to the mean experimental data presented in Figure 7.4. Figure 7.11 shows this comparison for the upper and lower combustor walls for all four simulations conducted, using wall centreline computational data. It can be seen that computational results are in reasonable agreement with experimental data, but the pressure peak in the ignition region is poorly captured. Part of the discrepancy is due to the early ignition predicted in the simulations, and hence the pressure profiles lie below the experimental data downstream. Severe oscillations due to the presence of shock waves are clearly visible in all computational profiles, but are absent in the experimental data. It is possible the shock wave boundary layer interaction points occur between the experimental pressure taps, but it is also possible the severity of the interaction predicted by the computational methods is too high.

These oscillations can be seen to reduce in magnitude down the length of the combustor due to natural and numerical diffusion effects.

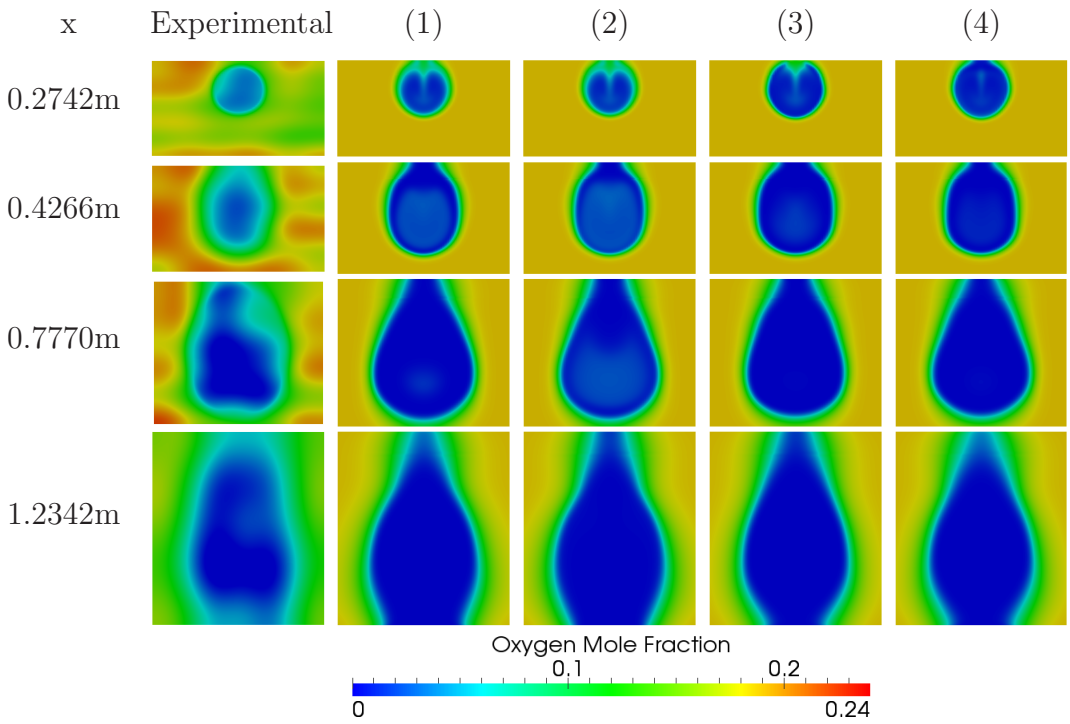

Figure 7.10: Comparison of mean oxygen mole fraction profiles from each RANS simulation to experimental data

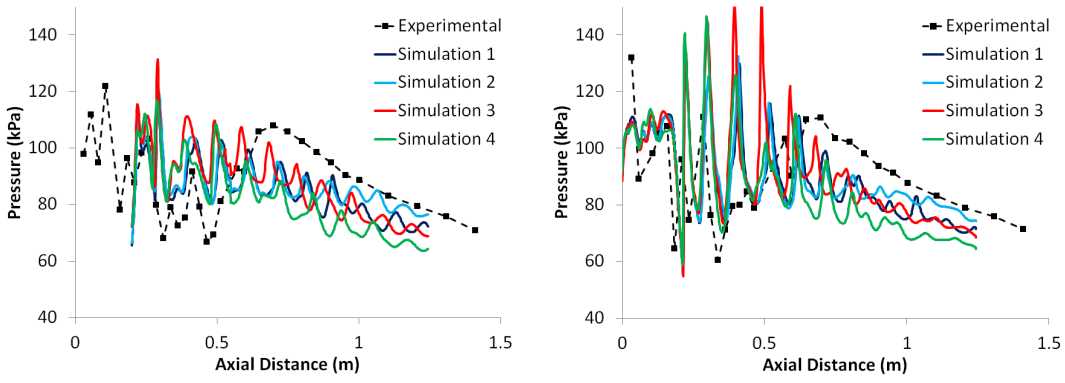

Figure 7.11: Comparison of upper (left) and lower (right) wall pressure distributions to experimental data, for each RANS simulation

It can also be seen from Figure 7.11 that there is little difference in the pressure profiles resulting from the four simulations, with Simulation 4 providing the poorest agreement with experimental data, corresponding to the low temperature levels presented in Figure 7.8. In order for a more robust and quantitative comparison of computational models to take place, more detailed experimental data are required.

The computational pressure profiles presented in Figure 7.11 are obtained along the centreline of the upper and lower combustor walls. However, the experimental data on the upper wall of the copper section is collected near to the side wall. Figure 7.12 compares pressure profiles taken on both the centreline and towards the side wall (at z = -36.3mm, measured from the centreline) for Simulation 1. It can be seen that no significant differences are apparent, other than slightly different shock wave boundary interaction locations, and so only the centreline pressures will be compared to experimental data from now on, for simplicity.

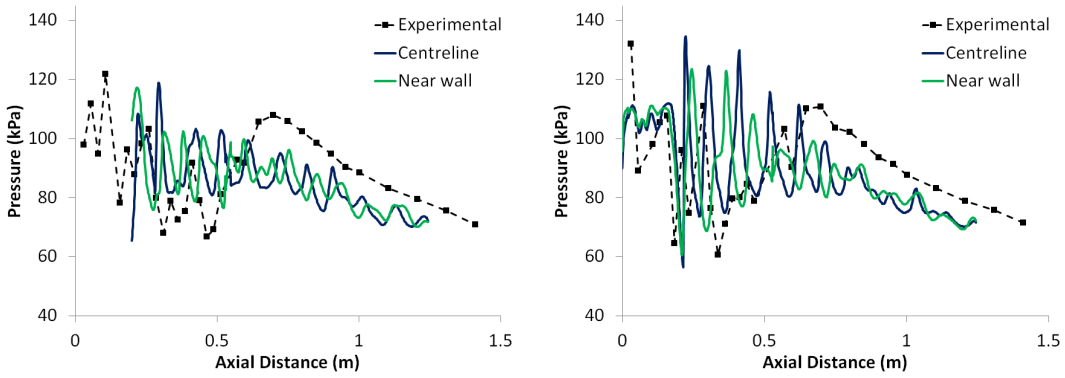

Figure 7.12: Comparison of upper (left) and lower (right) wall centreline and near wall pressure distributions, for Simulation 1

It would be sensible to suggest that the minimal difference between results from laminar chemistry and the assumed PDF combustion model may be down to the assumptions made in the modelling effort, through assumed statistical independence of temperature and composition, assumed shapes of PDFs and the neglection of source terms in variance transport equations. However, Möbus et al. [75] have also compared the transported PDF approach to laminar chemistry for a

laboratory jet flame, again displaying only a small difference between the results obtained, as discussed in Section 3.4. A deeper understanding of the physics involved in supersonic combustion and compressible turbulence is required in order to explain the behaviour observed.

7.2.5 Regime of Supersonic Combustion

Further insight into the regime of supersonic combustion can be gained by attempting to place the physics on the diagram of Figure 3.2. The non-dimensional Damköhler and turbulent Reynolds numbers, given by Equations 3.2 and 2.2, respectively, can be extracted from the computational data and used to help define the regime in which the reactions occur.

This analysis was conducted as a post processing exercise by Cocks et al. [141], by applying 1-step chemistry to the temperature profile of Simulation 1 in order to obtain the production rate of H_2O for use in Equation 3.4, to define the chemical time scale. Through this method, Damköhler numbers on the order of 50 to 200 are obtained, giving the combustion regime shown by the symbols in Figure 7.13. The low Damköhler numbers at x = 0.2742 are for the pre-ignition region where chemistry lags mixing, whilst the higher values obtained suggest operation in the flamelet regime.

As discussed in Section 2.1 it has been suggested [19] that baroclinic and dilatational effects lead to a steeper decay in the compressible turbulence energy spectrum than is given by classic Kolmogorov scaling. This, coupled with the high levels of molecular viscosity due to high temperatures damping the smallest scales of the flow may lead to a truncated spectrum where the smallest turbulent structures are larger than would be expected in the subsonic regime. This leads to a picture of the smallest eddies being larger than the flame thickness and hence only being able to provide wrinkling, rather than enter the flame and cause distributed reactions to occur. If this flame distortion is a large length scale phenomena, which can sufficiently be captured by a mesh of reasonable resolution, the laminar chemistry approach would be capable of providing an accurate description of the reaction rate terms.

It should be noted that 1-step chemistry was employed for this analysis in

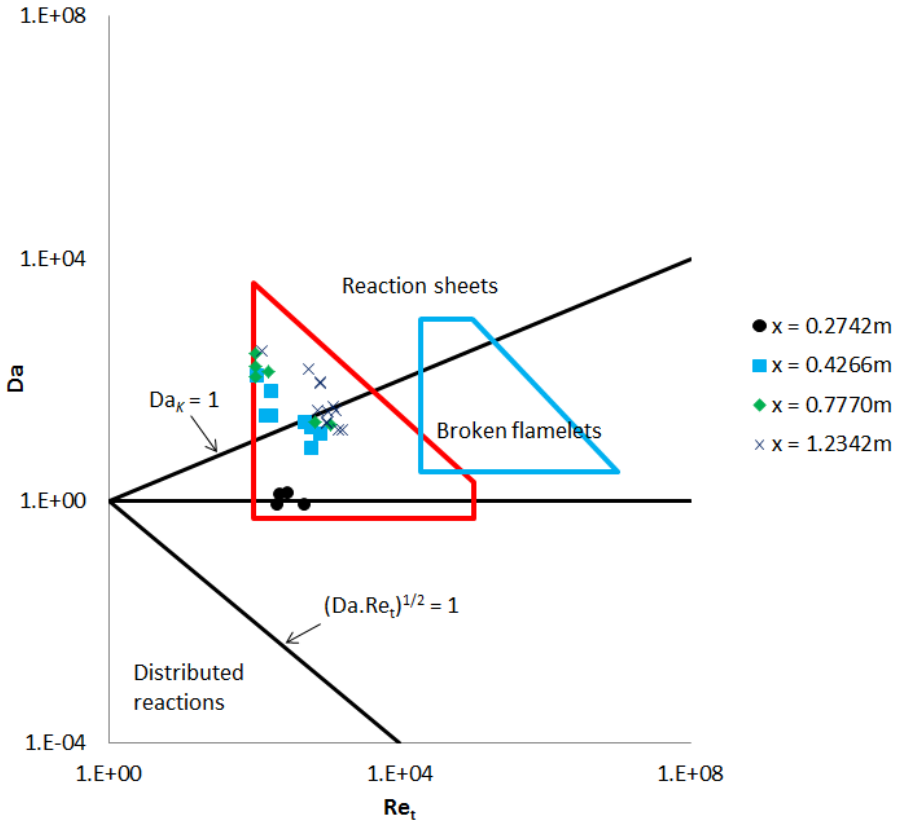

Figure 7.13: Regime diagram showing data from 1-step chemistry post-processing, at locations down the axis of the combustor

order for a direct comparison to be made to the work of Ingenito and Bruno [19]. Ingenito and Bruno conducted an LES simulation of the SCHOLAR test case using 1-step chemistry and subsequently proposed a regime for supersonic combustion, with which the data in Figure 7.13 can be seen to be in excellent agreement.

However, if the reaction rates for the production of H_2O are directly extracted from the complex chemistry RANS simulations, a very different picture is provided for the range of dimensionless Damköhler numbers. Figure 7.14 shows that Damköhler numbers on the order of unity are found for all four simulations. This suggests finite-rate effects play a more significant role than previously suggested, with turbulence and chemical times scales of a comparable magnitude. Figure 7.14 also shows that comparable reaction rates are provided by laminar chemistry and the assumed PDF combustion model.

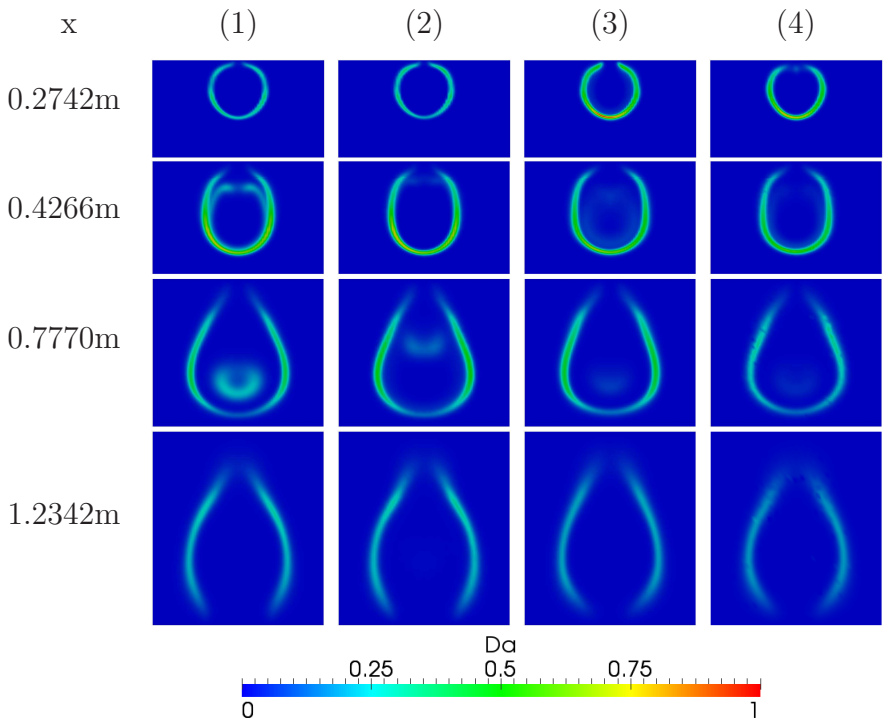

Figure 7.14: Damköhler profiles down the axis of the SCHOLAR combustor for each complex chemistry RANS simulation

The importance of finite rate chemistry can be reinforced by analysing the eddy turnover times calculated from Equation 3.3 using information from the two-equation turbulence model. It can be seen from Figure 7.15 that these are of the order of 5×10^{-4} seconds. Through analysis of the profile of axial velocity down the length of the combustor, a flow-through time from the backwards facing step to the domain outlet can be given as 7.5×10^{-4} seconds, showing that not only are the reaction rates comparable to the turbulence time scale but also to the residence time of reactants within the combustor.

The large discrepancy between the 1-step chemistry analysis and reaction rate information extracted from the complex chemistry simulations is due to the poor suitability of this 1-step mechanism to the simulation of supersonic combustion, as discussed in Section 3.5. Through analysis of ignition delay and induction times, both Gerlinger et al. [98] and Berglund et al. [68] observed that the reaction rates provided by this mechanism are far too fast. It was

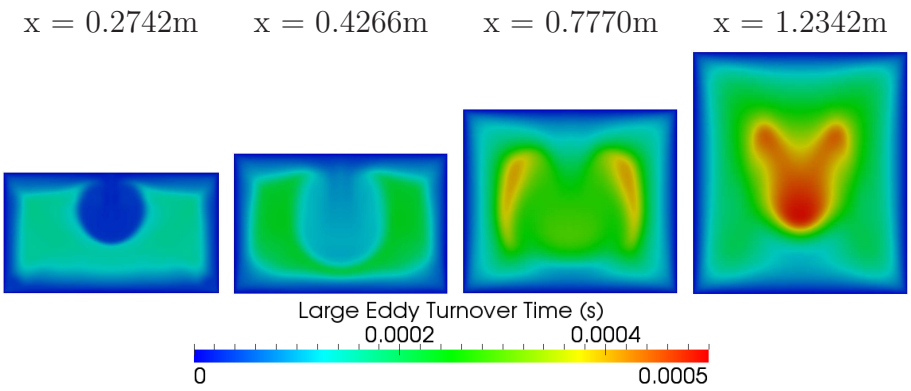

Figure 7.15: Distribution of large eddy turnover time for Simulation 3

found that significant improvements in the reaction rate predictions are obtained through the use of more complex chemical kinetics models. Therefore, the results of Ingenito and Bruno obtained through the use of the 1-step mechanism may be somewhat questionable, with the complex mechanism data presented here being more reliable. This suggests that a distributed reaction regime may be more likely, for this particular test case, with finite rate effects of paramount importance. However, the increased likelihood of distributed reactions occurring suggests the interaction between turbulence and chemistry is more significant than previously discussed, making it harder to explain why laminar chemistry is capable of providing results in reasonable agreement with experimental data.

It is possible the physics encountered in supersonic combustion is sufficiently different to that studied under subsonic conditions that the simple extension of current combustion modelling techniques is not capable of capturing the interactions present. A deeper understanding of the physics involved in supersonic combustion and the interaction of turbulence and chemistry is sorely required. Methods such as direct numerical simulation (DNS) are ideal for these investigations, but the question is whether such simulations of high Reynolds number flows are affordable.

The turbulence encountered (and hence it's interaction with chemistry) is also very case dependent, with the backwards facing step and large diameter injector likely to generate large coherent structures in the flow. Combustors employing hydrocarbon fuels or multiple injectors may experience smaller scales at the low

wavenumber end of the spectrum. The turbulent Reynolds number used to define a region on the regime diagram is also highly dependent on the characteristics of the turbulence at the combustor inlet. Hence the regime in which supersonic combustion occurs is likely to also be case dependent, as discussed in Section 3.1.

7.2.6 Inlet Turbulence Influence

It was shown by Rodriguez and Cutler [88] that the levels of turbulence at the nozzle exit can have a significant impact on the wall pressure results obtained. This is to be confirmed here, whilst also investigating the sole influence of implied turbulence length scales on a RANS solution.

Through use of Equation 2.28, the turbulence intensity, I, can be defined as:

$$I = \frac{\widetilde{u'}}{\widetilde{u}} = \frac{1}{\widetilde{u}}\sqrt{\frac{2k}{3}} \tag{7.2}$$

and by combining Equations 2.45 and 2.47 the turbulence length scale is given by:

$$L_{turb} = \frac{k^{\frac{1}{2}}}{\beta^{\star}\omega} \tag{7.3}$$

Therefore, keeping the turbulence intensity constant and increasing the ratio of turbulent to molecular viscosity through a reduction in ω corresponds to an increase in the turbulence length scale. Figure 7.16 shows the pressure distributions resulting from modifications to the turbulence levels at the nozzle exit, for both the laminar chemistry and assumed PDF combustion model simulations using the reduced chemical mechanism. The low turbulence data corresponds to no inlet turbulence, allowing it to be self-generated by the physics of the problem in question. The high turbulence data corresponds to simulations where the turbulence intensity is kept at 5%, but the ratio of turbulent to molecular viscosity is increased to 500, through a reduction in ω at the nozzle exit.

It can be seen that the higher the levels of turbulence at the nozzle exit, the higher the wall pressure values at both the upper and lower surfaces of the combustor. This confirms the findings of Rodriguez and Cutler, whilst additionally showing that both the turbulence intensity and implied turbulence length scales

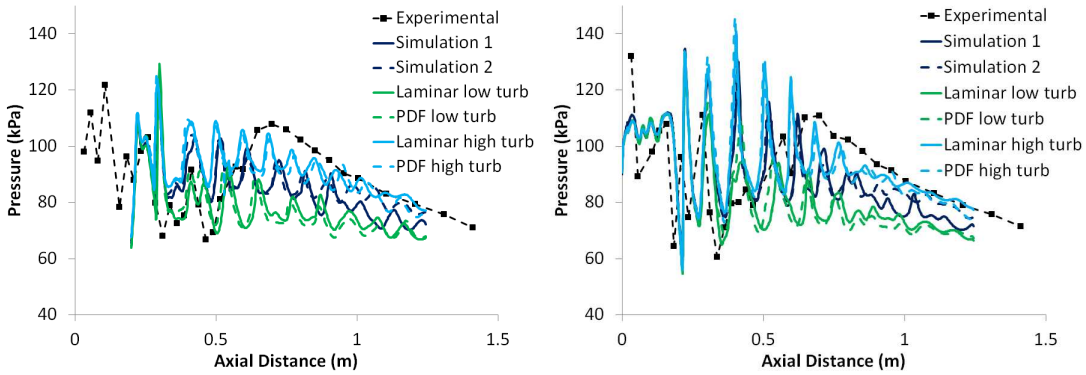

Figure 7.16: Influence of inflow turbulence on the upper (left) and lower (right) wall pressure distributions for Simulations 1 and 2.

can have a significant influence on the computational results obtained from a RANS simulation. This reinforces the conclusions of Chapter 6, providing further support to the need for experimentalists to measure turbulence parameters and also displays it is not only LES that can suffer from a lack of this data.

It should also be noted that even at higher turbulence levels laminar chemistry and the assumed PDF combustion model provide comparable results. In fact, the turbulence intensity and levels of eddy viscosity have a larger impact on the results obtained than the method chosen for the reaction rate calculations.

In order to demonstrate the dependence of the wall pressure measurements on the temperature rise from combustion, the computational results from Simulation 1 are compared to those from a non-reacting simulation in Figure 7.17, where the influence of combustion is clearly visible. The 'Cold' simulation has the same nozzle exit turbulence profile as Simulation 1, whilst the 'Cold low turb' simulation allows self-generation of k and ω. It can be seen that the inlet turbulence profile has no impact on the pressure distribution for the non-reacting simulations, suggesting that the main influence of increased turbulence levels is an increase in mixing and hence increased reaction rates and corresponding heat release from combustion.

This can be confirmed through analysis of the temperature profiles resulting from the low and high turbulence reacting simulations, where it can be seen from Figure 7.18 that the high turbulence test case does indeed result in a much wider distribution of elevated temperatures due to mixing.

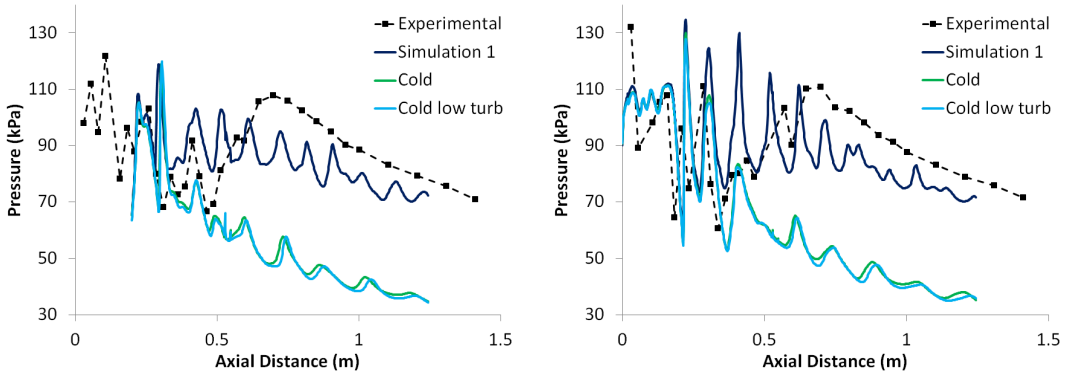

Figure 7.17: Influence of heat release on the upper (left) and lower (right) wall pressure distributions and influence of turbulence inflow on results from a non-reacting simulation

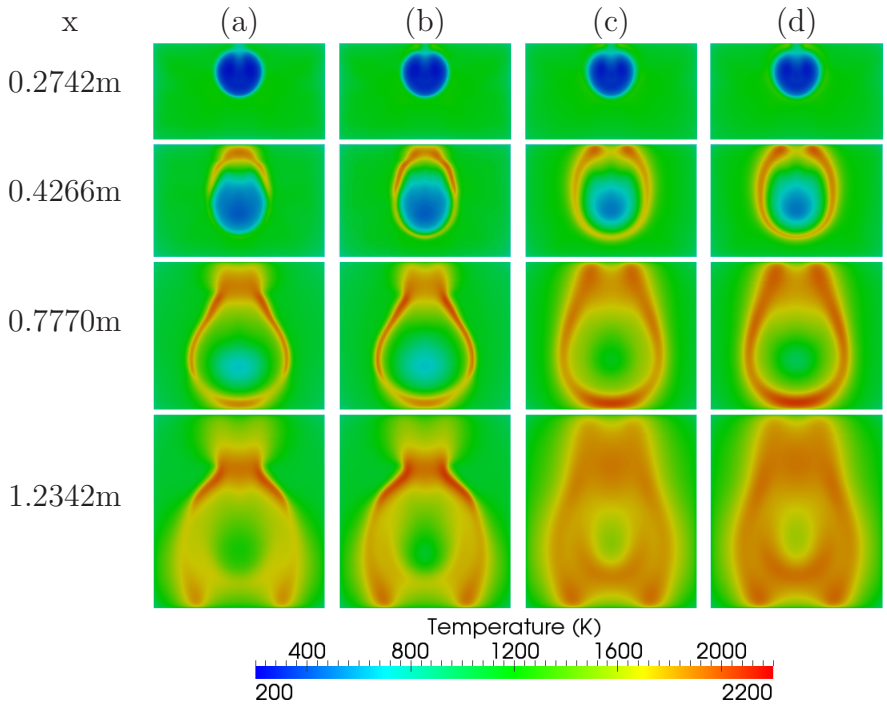

Figure 7.18: Influence of turbulence inflow on temperature profiles down the axis of the SCHOLAR combustor, showing reduced mechanism results with (a) laminar chemistry and low turbulence, (b) assumed PDF combustion model and low turbulence, (c) laminar chemistry and high turbulence and (d) assumed PDF combustion model and high turbulence

Correspondingly, it can be seen in Figure 7.19 that the high turbulence test case results in a more significant destruction of oxygen, both in the core of the combustor and surrounding region.

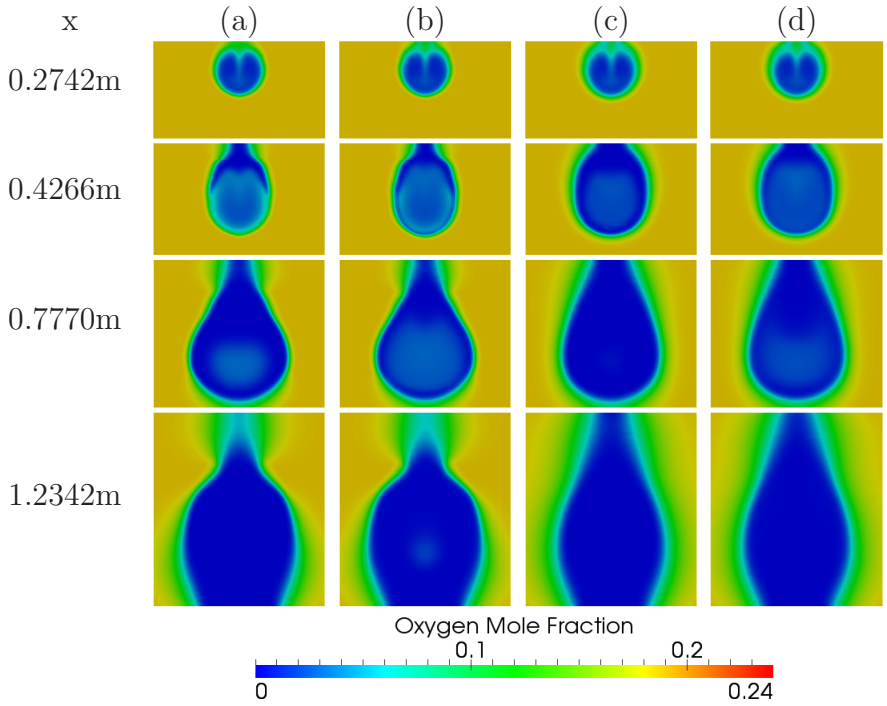

Figure 7.19: Influence of turbulence inflow on oxygen mole fraction profiles down the axis of the SCHOLAR combustor, showing reduced mechanism results with (a) laminar chemistry and low turbulence, (b) assumed PDF combustion model and low turbulence, (c) laminar chemistry and high turbulence and (d) assumed PDF combustion model and high turbulence

7.2.7 Radicals Influence

Since the mass fractions of radical species entering the nozzle from the heater are not measured, it is important to investigate their influence on the computational results obtained. As discussed in Section 7.1.2, the radical species are allowed to evolve in the high temperature nozzle region before the throat and are then convected into the combustor to aid ignition. Figure 7.20 compares the top and bottom wall pressure distributions from a simulation where the nozzle chemistry

is frozen, preventing radical formation, to the results from Simulation 1. Laminar chemistry and the reduced chemical mechanism are employed.

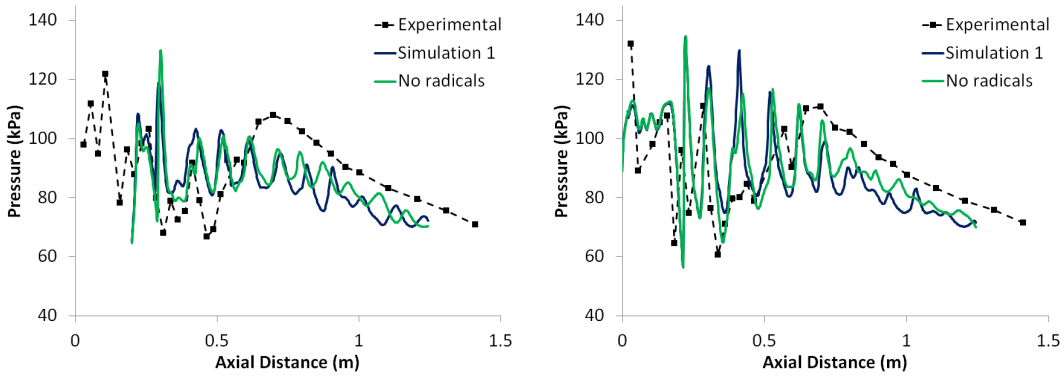

Figure 7.20: Influence of inlet radical species concentration on upper (left) and lower (right) wall pressure distributions for Simulation 1

From the pressure distributions it is apparent that the presence of radicals at the inlet has a negligible impact on the computational results obtained. This is because it is not the radicals which are influencing ignition, but the presence of a shock wave. However, the temperature profiles in Figure 7.21 show that ignition is actually slightly delayed in the no radicals case, even though the shock still acts as the ignition mechanism. This is due to the increased time required for radical formation.

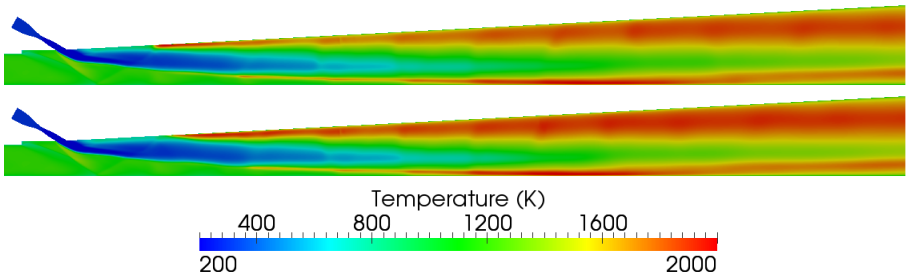

Figure 7.21: Centreline static temperature profiles for Simulation 1 with nozzle reactions (top) and without (bottom)

Slightly elevated temperatures also appear to be present in the case with frozen nozzle chemistry, suggesting that the presence of radicals at the inlet can have an influence on the results obtained, albeit a small one for this test case.

The interaction between the reaction zone and shock waves which reflect down the length of the combustor can be seen by the flame distortion and patches of higher temperature downstream of the discontinuities.

Of course, if ignition is not caused by shock waves in practice, the concentration of radical species at the inlet may play a more significant role in the ignition process.

7.2.8 Mesh Convergence

It was hoped that mesh convergence could be proved by conducting a RANS simulation on the fine LES mesh to be presented in Section 7.3.1, but due to restraints on computational resources this is not possible. However, since the mesh is of a comparable resolution to that used by Rodriguez and Cutler [88] and since comparable computational results are obtained, a detailed mesh convergence study is not deemed essential in order to demonstrate their validity. Through a comparison of results to those obtained on a coarser computational grid Rodriguez and Cutler found the influence of mesh resolution to be smaller than the influence of parameters such as turbulence intensity at the combustor entrance.

7.2.9 Computational Cost

It is worth mentioning the additional computational costs incurred by both the combustion modelling process and increase in complexity of the chemical kinetics. Average times per iteration for the four baseline simulations are presented in Table 7.3.

	Time per iteration (s)
Simulation 1	10.53
Simulation 2	11.92
Simulation 3	14.43
Simulation 4	15.46

Table 7.3: Time per iteration for each simulation, calculated over 100 time steps

Compared to the laminar chemistry simulations, the increase in computational cost through use of the assumed PDF combustion model is on the order

of 7% and 13% for the full and reduced Jachimowski mechanisms, respectively. The percentage increase in computational cost for the full mechanism is below that for the reduced mechanism since the percentage increase in additional transport equations is lower. The percentage increase in computational cost incurred through using the full mechanism, compared to employing the reduced mechanism, is 30% and 37% for assumed PDF combustion model and laminar chemistry simulations, respectively.

Of course, since the times per iteration are calculated over a period of 100 time steps there is a degree of error in their comparisons, but the increased computational cost induced by combustion modelling and complex chemical mechanisms is clear.

7.3 DDES Study

Since LES is computationally expensive in comparison to RANS, the results from Section 7.2 can be used to tune the setup of a large eddy simulation of the SCHOLAR scramjet test case in order to limit the number of runs required.

Again the DDES method is employed to bring the computational cost associated with the LES of this high Reynolds number wall bounded flow down to acceptable levels, since wall resolved LES of a supersonic combustor is beyond the computational capabilities of today. The Menter SST two-equation turbulence model is used to calculate the subgrid viscosity and fluid mechanical properties of the flow.

The capabilities of LES for the study of supersonic reacting flows is to be evaluated and an attempt to gain a deeper understanding into the physics involved in the SCHOLAR test case is to be made.

7.3.1 Computational Mesh

Due to the high mesh resolution requirements, coupled with the significant length of the nozzle-combustor assembly and number of iterations required to obtain converged statistical data, the computational mesh is truncated at an axial location of 0.81m in order to make the simulation affordable with available resources. This

effectively removes the final plane of experimental data from the simulation, with the domain outlet now a small distance downstream of the 0.777m experimental data location.

The RANS mesh described in Section 7.2.1 is refined in all directions in order to generate a grid which can support the resolved turbulence content inherent in LES. The chosen mesh density is comparable to that used by others [90]. The majority of the domain contains cells of an isotropic nature, but high aspect ratio elements are present in the upper half of the combustor in the injector region due to both the continuation of the pre-step boundary layer mesh and concentration of cells downstream of the step which expand with the combustor divergence, as can be seen in Figure 7.5.

The combustor axial mesh spacing is set at 0.6mm around the region of injection, stretching to 0.75mm for the remainder of the copper and steel sections. Mesh spacing in the z-direction is set constant to 0.6mm whilst the outlet mesh spacing is fixed at 0.6mm in the y-direction. It should be noted that these are the maximum values in the core region of the domain, with near wall stretching employed to capture the boundary layer.

This generates a pure hexahedral mesh with 36.8M elements, which is partitioned to run on 2640 cores of the HECToR cluster. The same near wall mesh spacing used in the RANS simulations is employed, which leads to a solution time step of 4.03×10^{-9} seconds. Using data from the centreline velocity profile of a RANS simulation, the combustor flow-through time (from the step location to domain outlet) is calculated as 4.6×10^{-4} seconds, corresponding to just over 114,000 iterations.

7.3.2 Computational Methods

Since it is concluded from the RANS simulations that the neglect of turbulence-chemistry interaction modelling through the use of simple laminar chemistry is capable of providing a reasonable agreement with experimental data, the additional cost involved in modelling is not warranted and so need not be used here. Since modelling requirements are lower in LES than RANS it is expected the influence of a combustion model on the computational results would be even lower

than already demonstrated.

The reduced Jachimowski mechanism was shown to provide results in better agreement with experimental data than the full Jachimowski chemical kinetics model, with significant computational cost savings, and so is employed here.

It has also been shown that the levels of turbulence entering the combustor can have a significant impact on the computational results obtained. However, since no experimental data is available for the turbulence intensity and length scales it is difficult to know what turbulence profile to prescribe. Since fuel injection into a supersonic cross-flow is expected to be a significantly more violent process than the region of separation encountered around the thin central tip of the coaxial jet simulated in Chapter 6, it is possible the combustor turbulence could be sufficiently self generating. Peterson et al. [90] conducted a LES of a test case similar to the SCHOLAR experiment, but with fuel injection normal to the wall rather than at a significantly less intrusive 30 degrees to the horizontal, as studied here. It was concluded that the normal jet is capable of breaking down without the addition of synthetic turbulence in the boundary layer upstream of injection. However, the computational results obtained in Section 7.2.6 when allowing turbulence to self-generate in the combustor ('low turbulence' test case) suggest this method is not suitable here.

It possible turbulence emanating from both the nozzle and injector could have a significant influence on the levels of mixing experienced. Since available computational resources do not allow a large number of simulations to be conducted in order to investigate the influence of various inflow parameters and simulation configurations, it is decided that a single turbulence inflow is to be provided just upstream of the combustor entrance, in an attempt to excite the shear layer generated over the backwards facing step.

Experience from Chapter 6 is used to describe what is a reasonable turbulence inflow profile, which is imposed (somewhat arbitrarily) only 4.1mm upstream of the combustor entrance, where the combustor entrance is defined as the step location. It is worth pointing out that this location is further downstream than the nozzle exit (x = 0.0m) where the levels of turbulence were imposed in the RANS simulations conducted previously. Isotropic inflow turbulence with Reynolds stresses, R_{ii}, of $50\text{m}^2\text{s}^{-2}$, maximum length scale of 9mm and near wall

scaling factor, α_w, of 0.4 is generated. The resulting turbulence field can be seen in Figure 7.22, where positive Q isosurfaces are coloured by velocity magnitude. As with the coaxial jet test case, the smallest structures and highest intensities can be seen to exist in the near wall region.

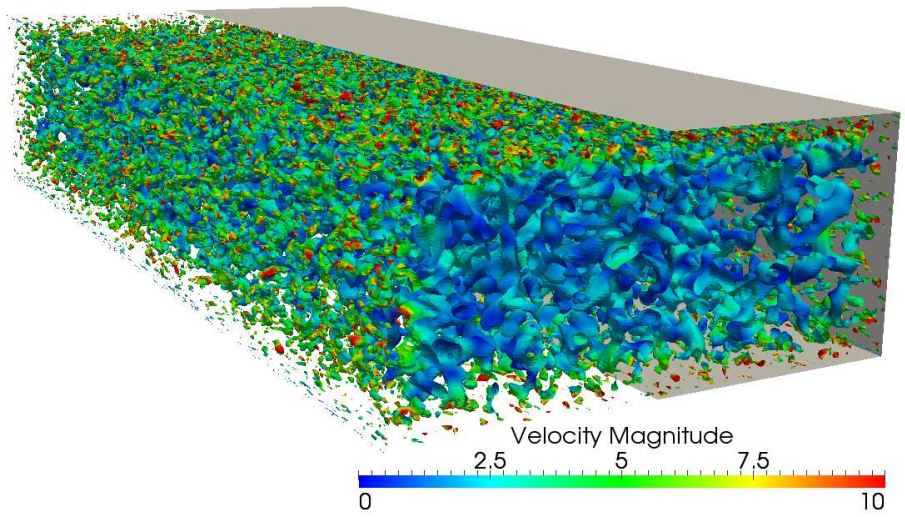

Figure 7.22: Positive Q isosurfaces coloured by velocity magnitude in m/s, showing the inflow turbulence profile

The inlet turbulence is generated on a domain which extends 0.2m in the axial direction and consists of 200 layers of 1mm cells, totalling 4.86M hexahedral elements.

7.3.3 Results

Ensemble averaged data are collected for the velocity, pressure, temperature and species mole fractions, but the additional computational cost involved in evaluating the rms values is too high and so they are not calculated here. The simulation is started from a RANS solution mapped onto the fine LES mesh and 180,000 iterations are used to flush initial transients out of the domain, which corresponds to just over one and a half flow-through times. Due to the lack of subsonic regions in the domain, it is not expected to take the flow any longer than this to develop. The ensemble averaged data are then collected over an additional 990,000 iterations, corresponding to over eight and a half flow-through times. The simulation

therefore runs for a total of 1.23M time steps, or 4.95×10^{-3} seconds.

The ensemble averaged oxygen mole fraction profiles are compared to experimental data in Figure 7.23. It can be seen that a reasonable agreement is obtained just downstream of injection, at the x=0.2742m location. However, as moving further downstream, a mole fraction profile emerges which appears somewhat more elongated than presented in the experimental data. This continues to the x=7770m plane, where it can also be seen that significant oxygen depletion is present closer to the lower wall and further from the upper wall than found in the experiment. The reasons for the results obtained are to be investigated later, through a detailed analysis of the physics involved.

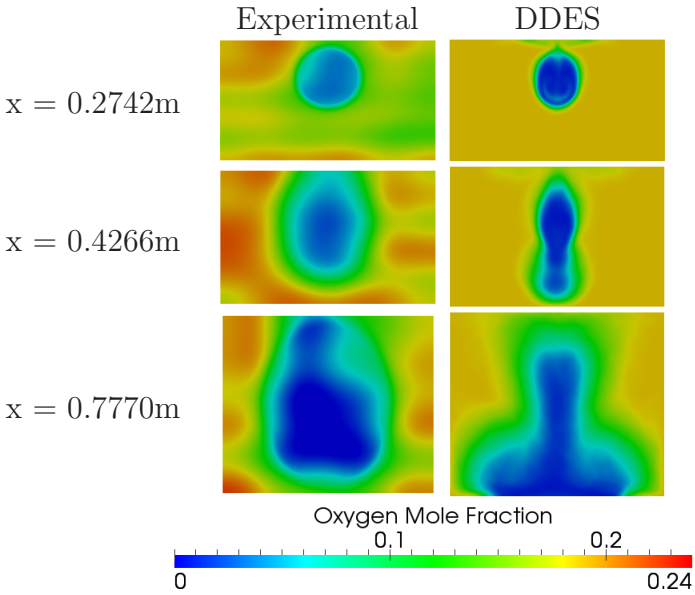

Figure 7.23: Comparison of the ensemble averaged oxygen mole fraction to experimental data

Figure 7.24 compares the ensemble averaged temperature profiles. It can be seen that the mean temperature values are significantly below those provided in the experimental data and significant modification of the temperature scale in column (b) is required in order to highlight the temperature distribution calculated. This was also found by Peterson et al. [90] with their detached eddy simulation of a similar test case with normal fuel injection. The low values are due to the significant motion of the flame, which is due to the turbulent nature

of the simulation, with the high temperature regions not at a single location long enough to contribute significantly to the ensemble averaged values. It should be noted that the experimental data are not time averaged, but are polynomial fits through data at a given location [105].

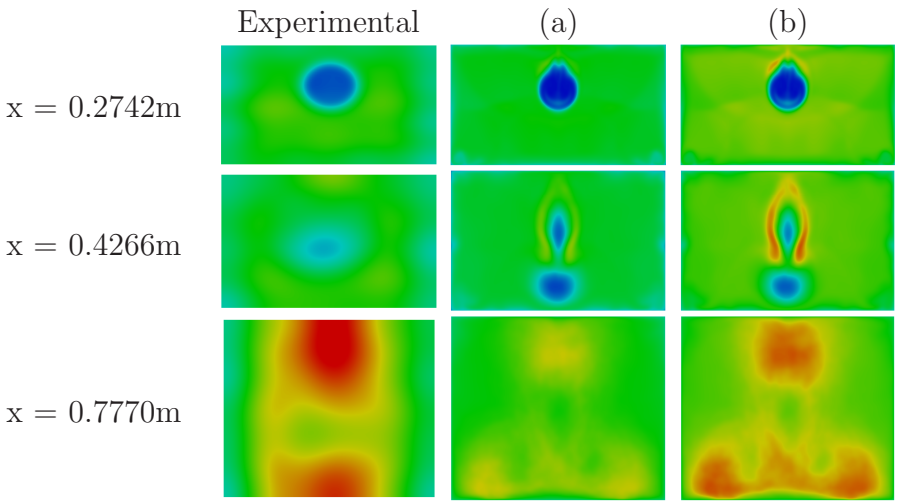

Figure 7.24: Comparison of the ensemble averaged temperature to experimental data. Experimental data and (a) are scaled from 200K (blue) to 2200K (red), whilst (b) is scaled from 200K (blue) to 1700K (red). (a) and (b) are the same computational data.

The poor agreement with experimental data for the upper and lower wall pressure distributions presented in Figure 7.25 is in line with the low values calculated for the ensemble averaged temperatures. However, as will be shown, the instantaneous flame temperatures are of the order of 2200K but the instantaneous pressure profiles are in agreement with the ensemble averaged data. It is possible the level of imposed turbulence may have an influence on the results obtained since it has been shown in Figure 7.16 that the nature of the inflow turbulence can have a significant impact on the wall pressure profiles when using RANS.

Reducing the turbulence intensity may lead to a more concentrated flame and hence higher ensemble averaged values, but an increase in the intensity may lead to higher mixing and a more widely distributed flame and hence higher heat release and wall pressure values. Also, even though the roles of the combustion model and chemical mechanism were investigated in the RANS simulations pre-

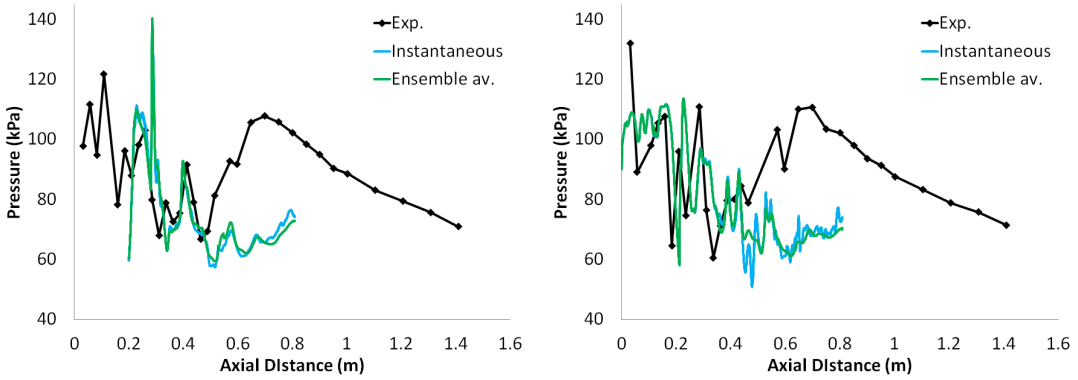

Figure 7.25: Comparison of upper (left) and lower (right) wall pressure distributions to experimental data, showing instantaneous and ensemble averaged data

sented at the start of this Chapter, it is possible they have an impact on the results obtained here. In order to investigate the influence of the inflow turbulence and combustion model in the LES, two additional simulations are conducted. The first simulation removes the turbulence inflow but keeps using laminar chemistry for the reaction rate calculations, and the second simulation keeps the turbulence inflow but uses the assumed PDF combustion model to handle subgrid turbulence-chemistry interactions. Results from all three simulations are to be compared.

Only a simple modification is made to the assumed PDF formulation to convert it to a subgrid combustion model for handling the turbulence chemistry interactions in LES. The subgrid viscosity and fluid mechanical properties provided by the two-equation subgrid-scale model are now used in the variance transport equations in place of the properties previously provided by RANS modelling. Due to both the limitation in computational resources and additional cost involved in evaluating the reaction rates using the assumed PDF combustion model, statistical data is collected over only 600,000 iterations, compared to 990,000 for the two laminar chemistry simulations.

An example of the time taken per iteration is presented in Table 7.4, where the additional cost of using a combustion model compared to simple laminar chemistry is clearly visible. The additional cost incurred by employing a turbulence inflow appears to be below 1%, which is somewhat negligible, and this small

difference could even be attributed to other effects such as cluster load (e.g. I/O).

Simulation	Time per iteration (s)
Laminar with turbulence	1.294
Laminar without turbulence	1.284
Assumed PDF with turbulence	1.481

Table 7.4: Time per iteration in seconds, averaged over 30,000 time steps.

It can be seen from Figure 7.26 that the presence of inflow turbulence has a significant impact on the ensemble averaged oxygen mole fraction profiles, with a wider region of oxygen depletion caused by increased mixing in case (a) compared to case (b). However, the influence of including turbulence-chemistry interaction modelling appears to have a minimal impact on the results obtained. Both of these observations support the conclusions of the RANS results presented previously.

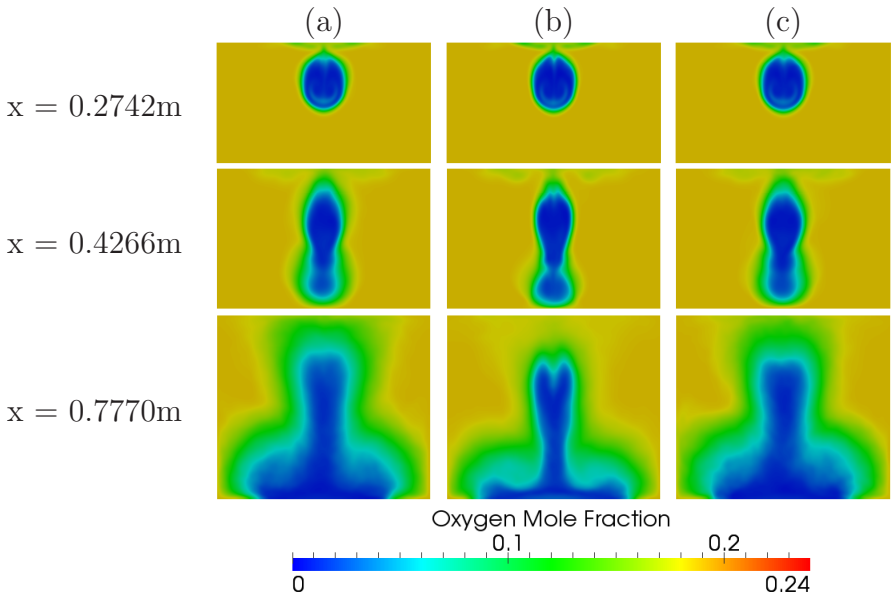

Figure 7.26: Comparison of ensemble averaged oxygen mole fraction profiles for simulations using (a) laminar chemistry and a turbulence inflow, (b) laminar chemistry and no turbulence inflow and (c) the assumed PDF combustion model and a turbulence inflow

Figure 7.27 compares the ensemble averaged temperature profiles for the three simulations, which are scaled to a maximum temperature of 1700K in order to be visible. Again it appears the influence of the turbulence inflow is far greater than the influence of subgrid turbulence-chemistry interaction modelling. The assumed PDF combustion model appears to predict slightly lower average temperatures than the laminar chemistry simulation with a turbulence inflow, but this may simply be due to the significantly fewer number of iterations over which the assumed PDF statistics are calculated. The argument of significant flame unsteadiness leading to lower mean temperatures is supported by the higher values provided by the laminar chemistry simulation without the turbulence inflow, than with; particularly at the x = 0.4266m location. Further downstream, at x = 0.7770m, the temperature profiles are significantly more concentrated when no turbulence inflow is present.

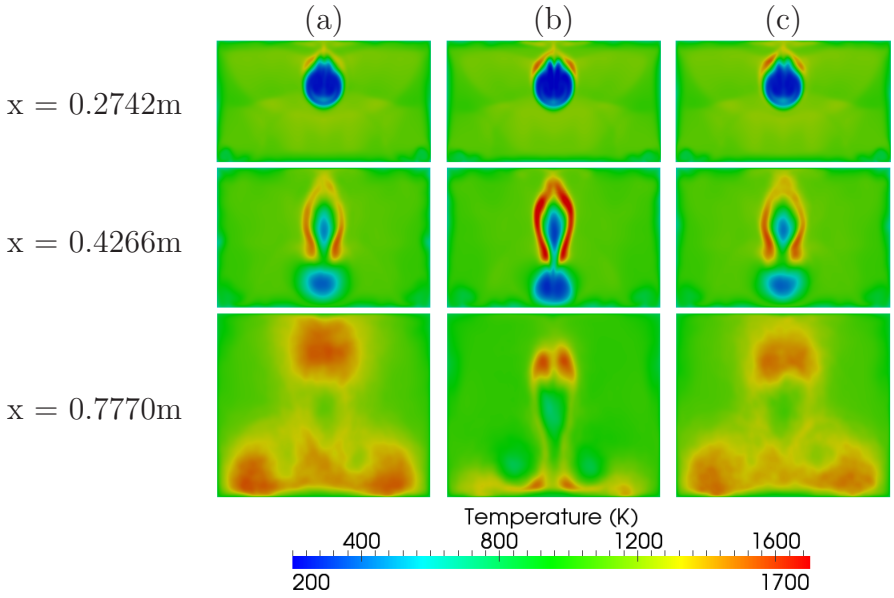

Figure 7.27: Comparison of ensemble averaged temperature profiles for simulations using (a) laminar chemistry and a turbulence inflow, (b) laminar chemistry and no turbulence inflow and (c) the assumed PDF combustion model and a turbulence inflow

The influence of the turbulence inflow and combustion modelling on the computational results can also be analysed through a comparison of the respective upper and lower wall pressure distributions presented in Figure 7.28. As with the

RANS results, it is apparent that the inflow turbulence has a much more significant impact on the pressure profiles obtained than the addition of turbulence-chemistry interaction modelling. The increase in pressure with the addition of turbulence suggests that a significantly higher inlet turbulence intensity is required for the computational results to be in agreement with experimental data.

In order to demonstrate convergence of the statistical results obtained, the time history of the ensemble averaged hydrogen mole fraction calculation is presented in Figure 7.29.

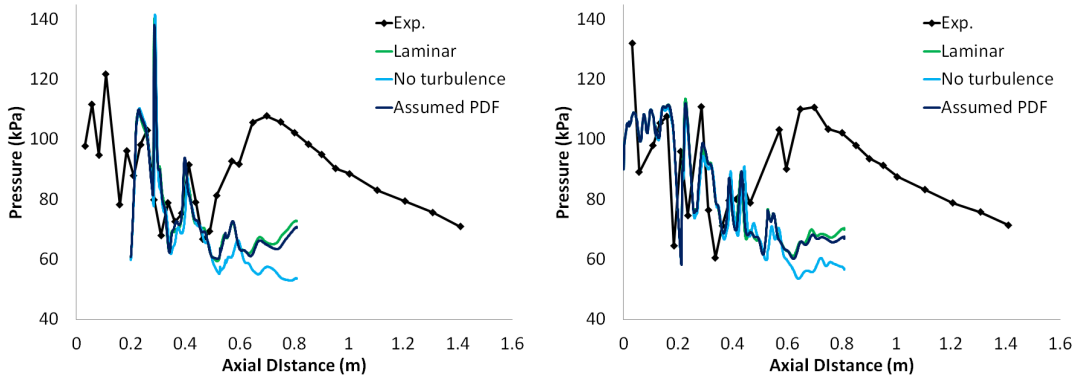

Figure 7.28: Comparison of upper (left) and lower (right) wall pressure distributions for the three DDES simulations

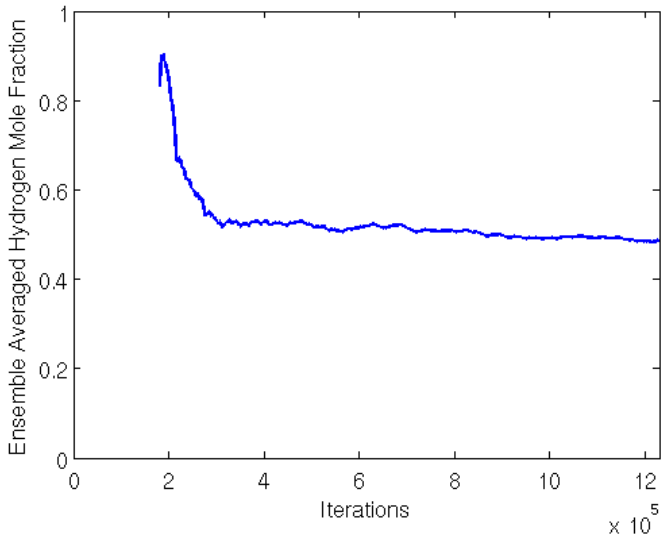

Figure 7.29: Convergence of ensemble averaged hydrogen mole fraction on the centreline of the combustor at x=0.777m

Additionally, the ensemble averaged oxygen mole fraction and temperature profiles after 780,000 and 1,230,000 iterations are presented in Figure 7.30. Whilst the profiles after 1,230,000 iterations are significantly smoother, there is no drastic change in the shape obtained. This confirms statistical convergence for the laminar chemistry simulations, and also sufficient convergence for the assumed PDF simulation for the visual comparisons conducted here.

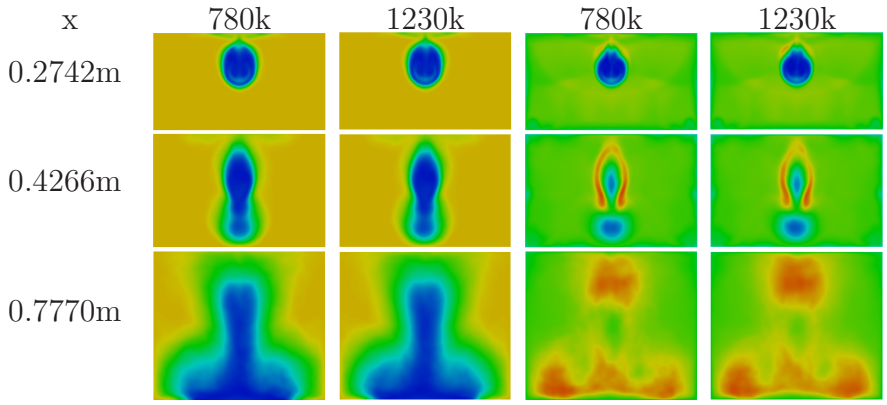

Figure 7.30: Comparison of ensemble averaged oxygen mole fraction and temperature profiles after 780,000 and 1,230,000 iterations for the laminar chemistry simulation with a turbulence inflow

In order to demonstrate that the simulations have sufficiently evolved after 180,000 iterations for the commencement of statistics calculations, positive Q isosurfaces for all three simulations are presented in Figure 7.31, after both 180,000 and 780,000 iterations, and are coloured by hydrogen mass fraction. It can be seen that even in the case where no turbulence inflow is present and the physics is left to self-evolve, significant turbulent structures are present after 180,000 iterations, which are also comparable to those found after 780,000 time steps. Although hairpin vortices from the boundary layer appear to contribute significantly to the mixing at downstream locations, it is clear that the turbulence content for the simulation with no turbulence inflow is below that of the other two.

In order to better understand the dynamics of the flow it is important to further study the instantaneous data. Figure 7.32 shows the instantaneous temperature profiles for the three simulations in question, at three locations down

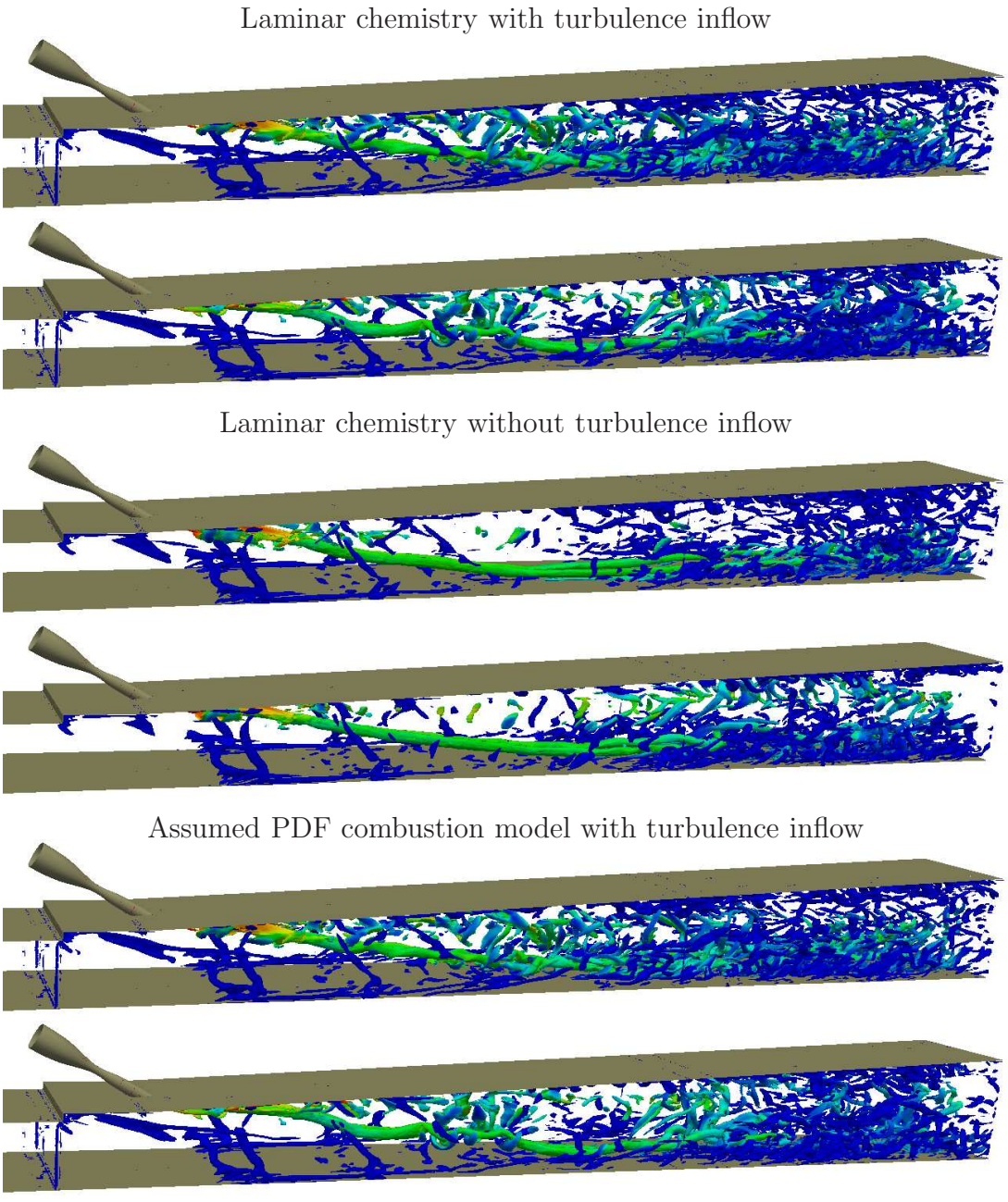

Figure 7.31: Positive Q isosurfaces coloured by hydrogen mass fraction for the three DDES simulations after 180,000 (top) and 780,000 (bottom) iterations, for each case

the axis of the combustor. Three instances in time are also presented in order to study the evolution of the flow profile over a period of 600,000 iterations. The first thing to note is the high levels of symmetry present in case (b), the simulation with no turbulence inflow. This corresponds to the lack of turbulent mixing, which is three dimensional and asymmetric by nature. However, the flow does appear to further develop over time, with more asymmetries introduced. This suggests that although the initial transients from the RANS initialisation may have disappeared after 180,000 iterations, the full development of the flow field may take significantly longer, particularly when a turbulence inflow is not present to aid this process.

In contrast, the dynamic nature of the flame in cases (a) and (d) is clearly visible, corresponding to the wider distribution of temperature in the ensemble averaged profiles.

Figures 7.33 and 7.34 show the instantaneous profiles of oxygen mole fraction and hydrogen mass fraction, respectively. Again, the higher degree of asymmetry and longer times required for flow evolution for case (b) are clearly visible. The increased levels of turbulence in cases (a) and (c) corresponds to high mixing which leads to a higher depletion of both oxygen and hydrogen. The lack of mixing in case (b) causes a high concentration of hydrogen to still be present at an axial location of 0.7770m.

The dominant flow feature which can clearly be seen in Figure 7.31, and are also visible in the instantaneous images of Figures 7.32, 7.33 and 7.34, are the two streamwise vortices emanating from the jet. Such vortices are classical of the physics resulting from transverse injection into a moving fluid [142] and it is likely their breakdown plays a significant role in the mixing process. However, the vortices appear very persistent and a significant delay in their breakdown is evident. This may be a large contributor to the discrepancies displayed between computational and experimental data. It can be seen from Figure 7.31 that the inflow turbulence is likely to have a significant impact on the vortex breakdown, since the vortices appear to be more persistent when no turbulence inflow is present.

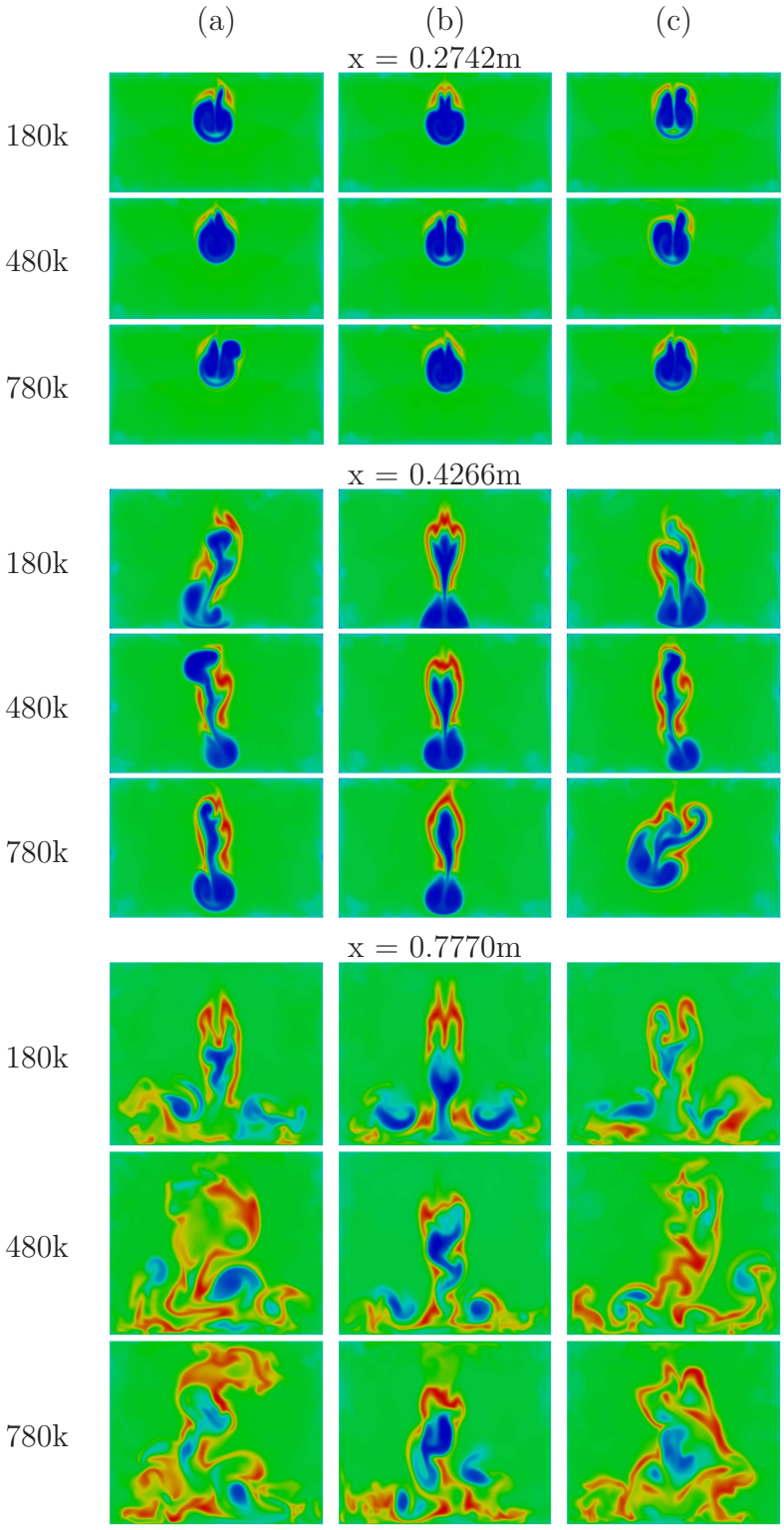

Figure 7.32: Instantaneous temperature profiles for the (a) laminar chemistry with a turbulence inflow, (b) laminar chemistry with no turbulence inflow and (c) assumed PDF combustion model with a turbulence inflow, simulations, at three axial locations and at three instances in time. Scaled from 200K (blue) to 2200K (red).

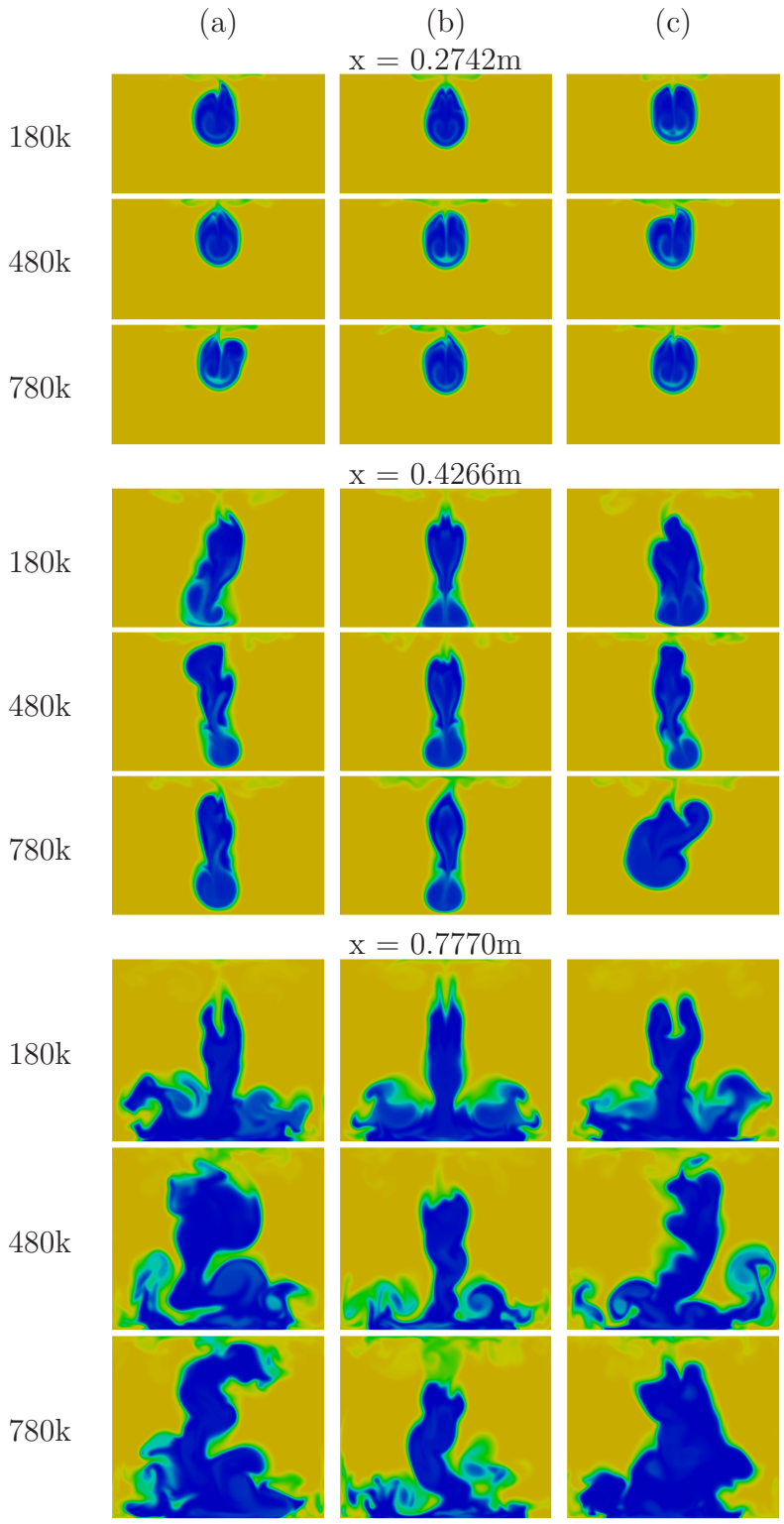

Figure 7.33: Instantaneous oxygen mole fraction profiles for the (a) laminar chemistry with a turbulence inflow, (b) laminar chemistry with no turbulence inflow and (c) assumed PDF combustion model with a turbulence inflow, simulations, at three axial locations and at three instances in time. Scaled from 0 (blue) to 0.24 (red).

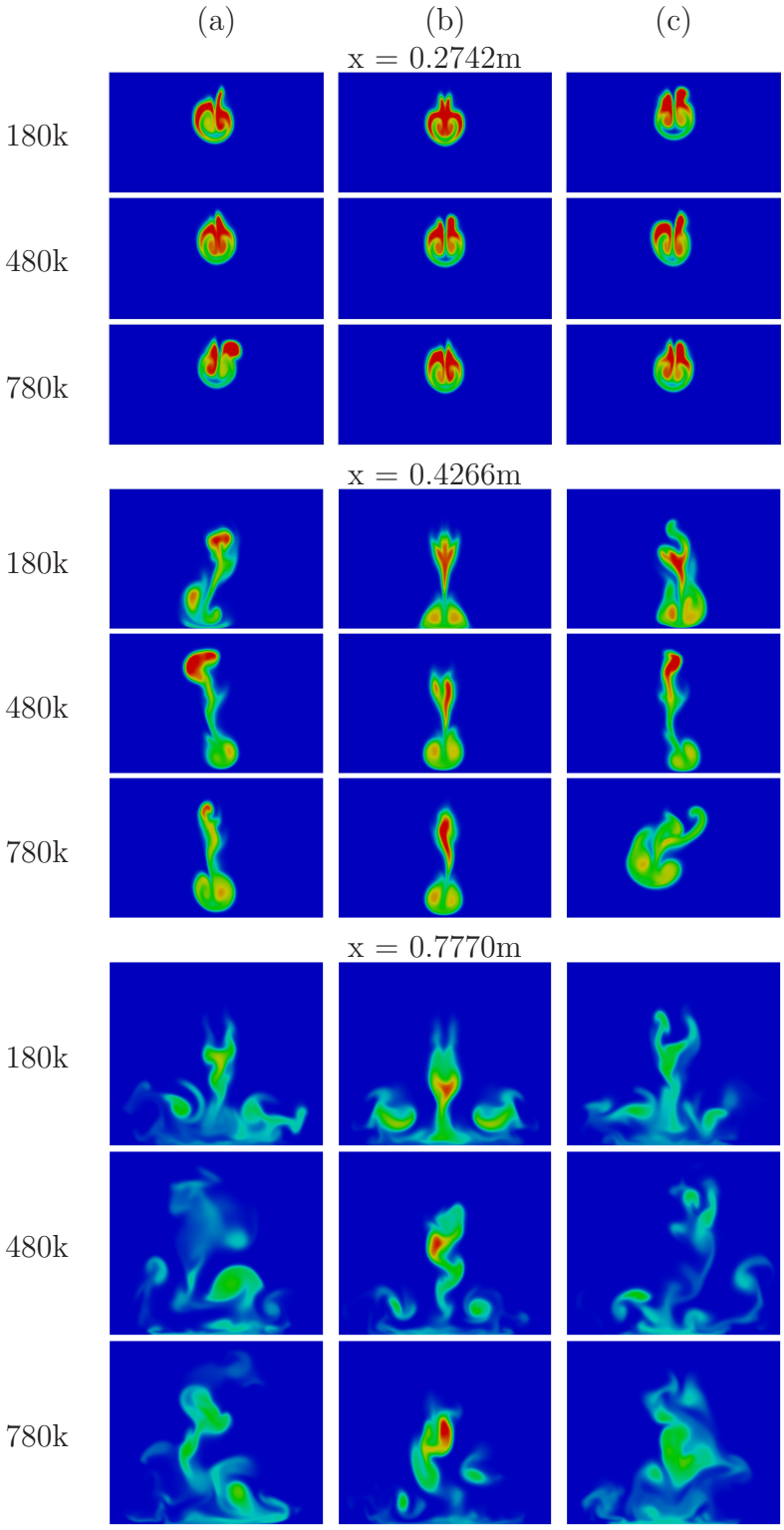

Figure 7.34: Instantaneous hydrogen mass fraction profiles for the (a) laminar chemistry with a turbulence inflow, (b) laminar chemistry with no turbulence inflow and (c) assumed PDF combustion model with a turbulence inflow, simulations, at three axial locations and at three instances in time. Scaled from 0 (blue) to 0.7 (red).

However, the location at which vortex breakdown occurs appears to be a transient phenomena, as can be seen by the images in Figure 7.35 which shows positive Q isosurfaces for the laminar chemistry simulation with a turbulence inflow at 300,000 iteration intervals. Significant vortex breakdown is presented after 600,000 iterations, but after both 300,000 and 900,000 iterations their behaviour appears significantly more benign.

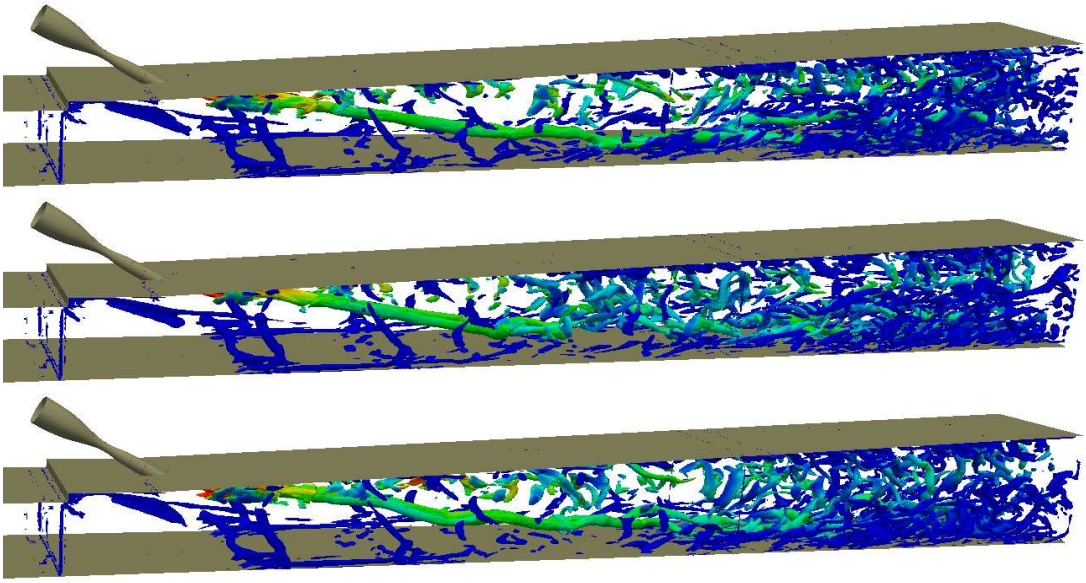

Figure 7.35: Positive Q isosurfaces coloured by hydrogen mass fraction after 300,000 (top), 600,000 (middle) and 900,000 (bottom) time steps, for the laminar chemistry simulation with a turbulence inflow.

Figure 7.36 presents slices down the axis of the combustor showing profiles of vorticity magnitude, which can be used to highlight the behaviour of these dominant streamwise vortices. It should be noted that these profiles are for the laminar chemistry simulation with a turbulence inflow, and only results from this simulation will presented from here onwards due to the poorer results from the simulation without a turbulence inflow and negligible difference in results from the assumed PDF combustion model simulation. Starting from the top left image in Figure 7.36 and working along a row at a time, significant insight can be gained into the development of the physics encountered in the combustor.

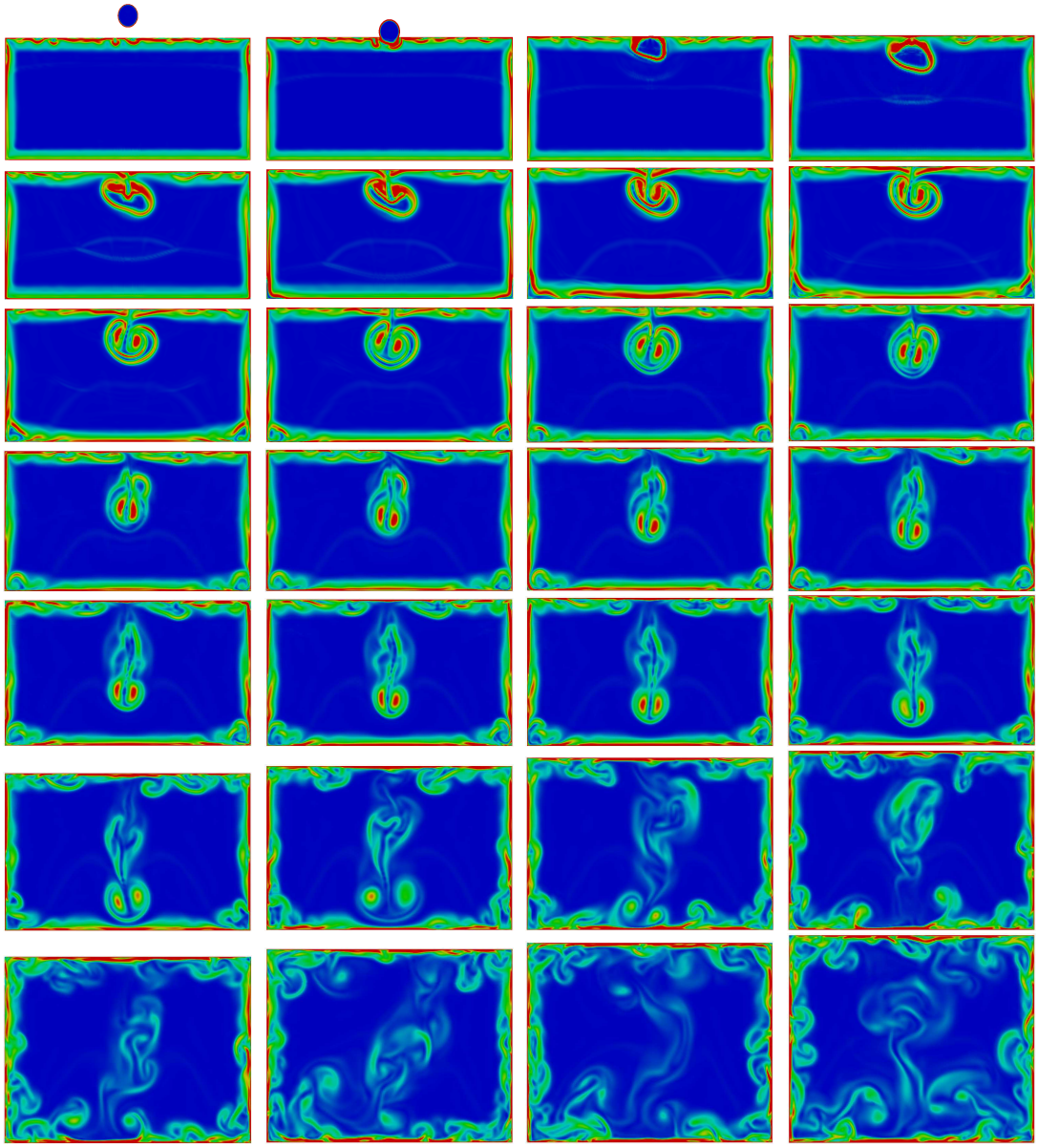

Figure 7.36: Profiles of vorticity magnitude down the axis of the combustor for the laminar chemistry simulation with a turbulence inflow, after 1.2M iterations. The images on the first five rows are in 0.01m steps, starting at x=0.16m and ending at x=0.35m. The images on the last two rows are in 0.05m steps, from x=0.40m to x=0.75m.

The unsteady boundary layer visible on the upper wall of the combustor pre-injection is due to the presence of the backwards facing step further upstream. As the fuel is injected a ring of high vorticity develops, which originates from the injector boundary layer. Two counter-rotating vortices begin to form within this ring of vorticity and develop further as they proceed downstream. Two corner vortices become visible on the lower wall of the combustor (in the third row of images), which are a product of a shock wave boundary layer interaction. On the fourth row of images it is apparent that the two dominant vortices begin to move away from the upper wall and break through the ring of vorticity, which remains above the vortex pair but is drawn downwards by their entrainment. The corner vortices grow in size and two small vortices become apparent on the upper wall of the combustor, which become clearer further downstream (on the fifth row of images). Rows six and seven take larger steps between planes and show the significant interaction of the dominant counter-rotating vortices with the lower combustor wall. This interaction has a significant influence on the whole combustor and it can be seen in the final image that significant turbulent structures are present on all walls as well as in the centre of the domain.

The flow physics encountered around the region of injection can be studied in more detail by analysing the three-dimensional positive Q contours. Figure 7.37 shows the structures present, coloured by hydrogen mass fraction, with the top wall of the combustor removed for clarity. It should also be noted that the contours on each side wall of the combustor have be clipped away, in order to aid visualisation.

The main flow features are labelled in the first image with (1) being the the wake of the backwards facing step and resulting streaks in the boundary layer. (2) corresponds to a horseshoe vortex wrapping around the jet, which is caused by the adverse pressure gradient upstream of injection, leading to boundary layer separation [142]. (3) corresponds to a region of shock wave boundary layer interaction induced separation and (4) are the dominant counter-rotating vortex pair. (5) are the vortices on the upper surface, which are a pair of secondary vortices arising due the flow field imposed on the upper wall by the counter-rotating vortex pair and (6) appears to be a second horseshoe vortex which may be generated by the presence of a bow shock, as will be discussed later. (7) and (8) are additional

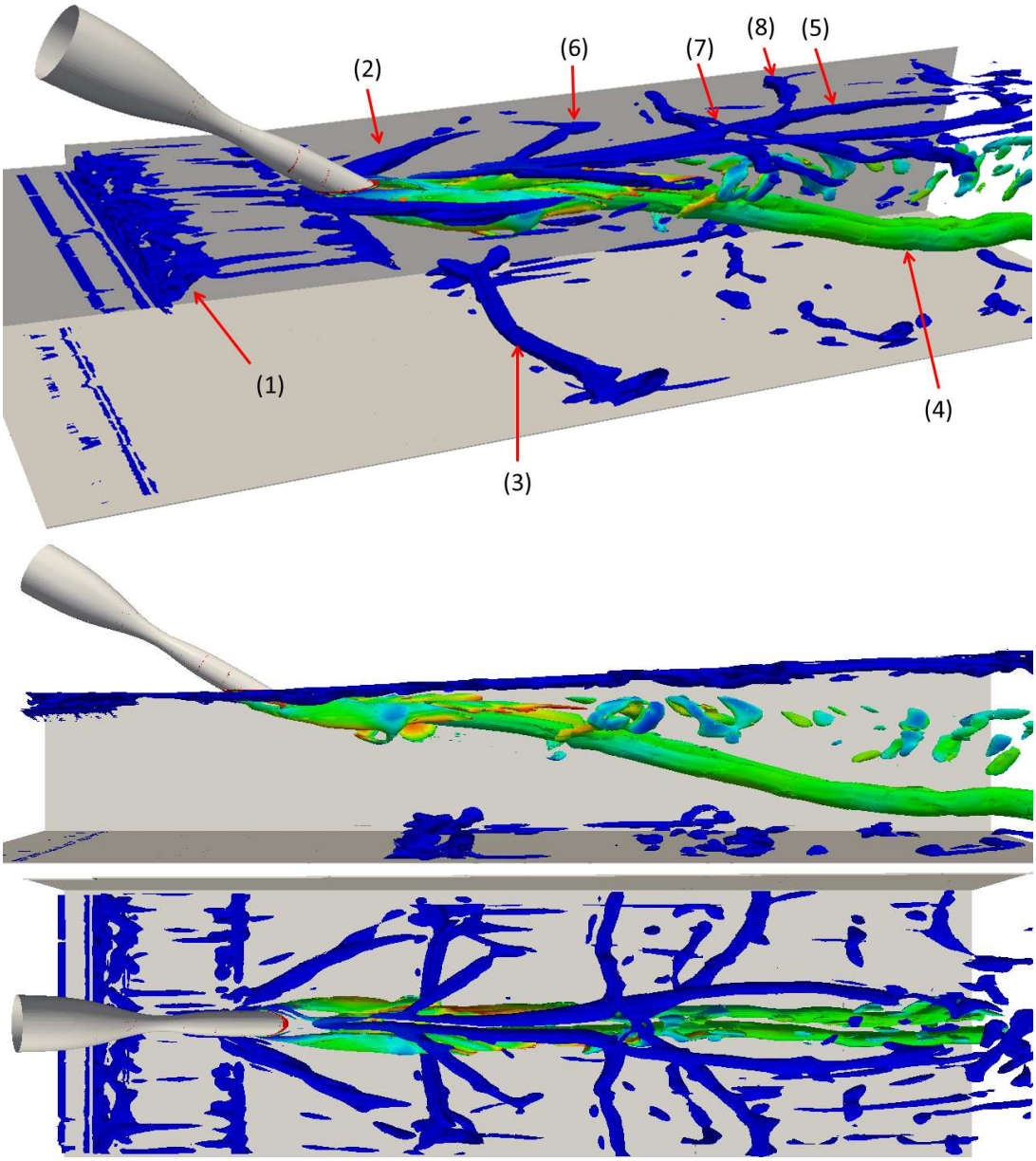

Figure 7.37: Positive Q isosurfaces around the region of injection coloured by hydrogen mass fraction, showing views from an angle (top), the side (middle) and above (bottom).

regions of shock wave boundary layer interactions, caused by the reflection and generation of shocks at (3). The importance of these interactions is also to be highlighted.

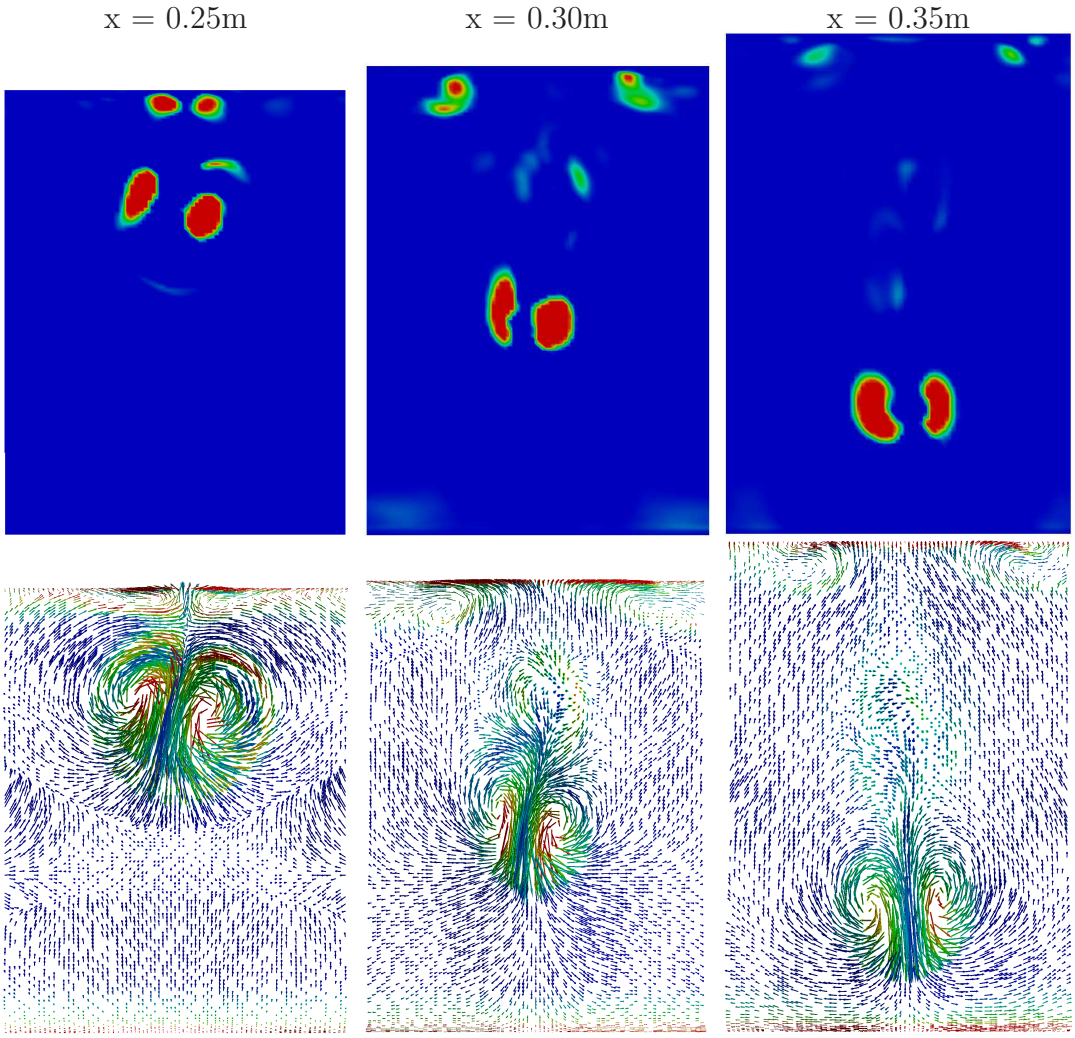

Figure 7.38: Profiles of positive Q (top) and velocity vectors coloured by vorticity magnitude (bottom) at three axial locations, showing the counter-rotating and secondary vortices.

The generation of the secondary vortices on the upper wall of the combustor can be analysed by studying the velocity vector fields in Figure 7.38, which are coloured by vorticity magnitude. The top images in this figure are profiles of positive Q, which are used to highlight the location of the coherent structures. The

positive Q profile at x = 0.25m shows the presence of four dominant structures, corresponding to the counter-rotating vortex pair emanating from the jet and the induced secondary vortices on the upper surface of the combustor. It can be seen that the left and right large vortices rotate in a clockwise and anti-clockwise manner, respectively. Due to the close proximity of the upper wall to this velocity field a spanwise boundary layer is generated, with respective velocities in the two halves of the combustor converging at the centreline of the wall. This convergence generates an adverse pressure gradient which causes the boundary layers to separate and form the two secondary vortices seen. These vortices rotate in the opposite sense to the larger vortices which generated them. It can also be seen that the secondary vortices are still present after the larger vortices have moved towards the bottom wall, but are separated by a larger distance.

One reason the secondary vortices may move apart can be seen in Figure 7.39, which is a duplicate of the positive Q contours in Figure 7.37 but now coloured by static pressure. It can be seen from the view above the combustor that a significant shock-shock-boundary layer interaction causes a small region of high pressure. It will be shown that it is this region of high pressure, and hence high temperature, which causes ignition. The spot of high pressure and subsequent expansion due to heat release from combustion may be the cause of the two secondary vortices moving apart downstream of this location.

A high pressure region can also be seen on the lower wall of the combustor, which corresponds to a significant shock wave boundary layer interaction and subsequent separation and reattachment of the flow.

In order to further demonstrate the complex shock system arising in the combustor, a three dimensional schlieren image is shown in Figure 7.40, which is coloured by static pressure. The dominant flow features are numerically labelled, with (1) corresponding to the expansion fan generated by flow acceleration around the backwards facing step. When this flow meets the wall it must turn back on itself, which is enabled through the oblique shock at (2). (3) is the bow shock which is typical of injection into a supersonic cross-flow [101; 102] and a significant interaction and combination of the oblique and bow shocks takes place. This resulting shock causes a significant shock wave boundary layer interaction and corresponding region of separation at (4). In order for the flow to climb over

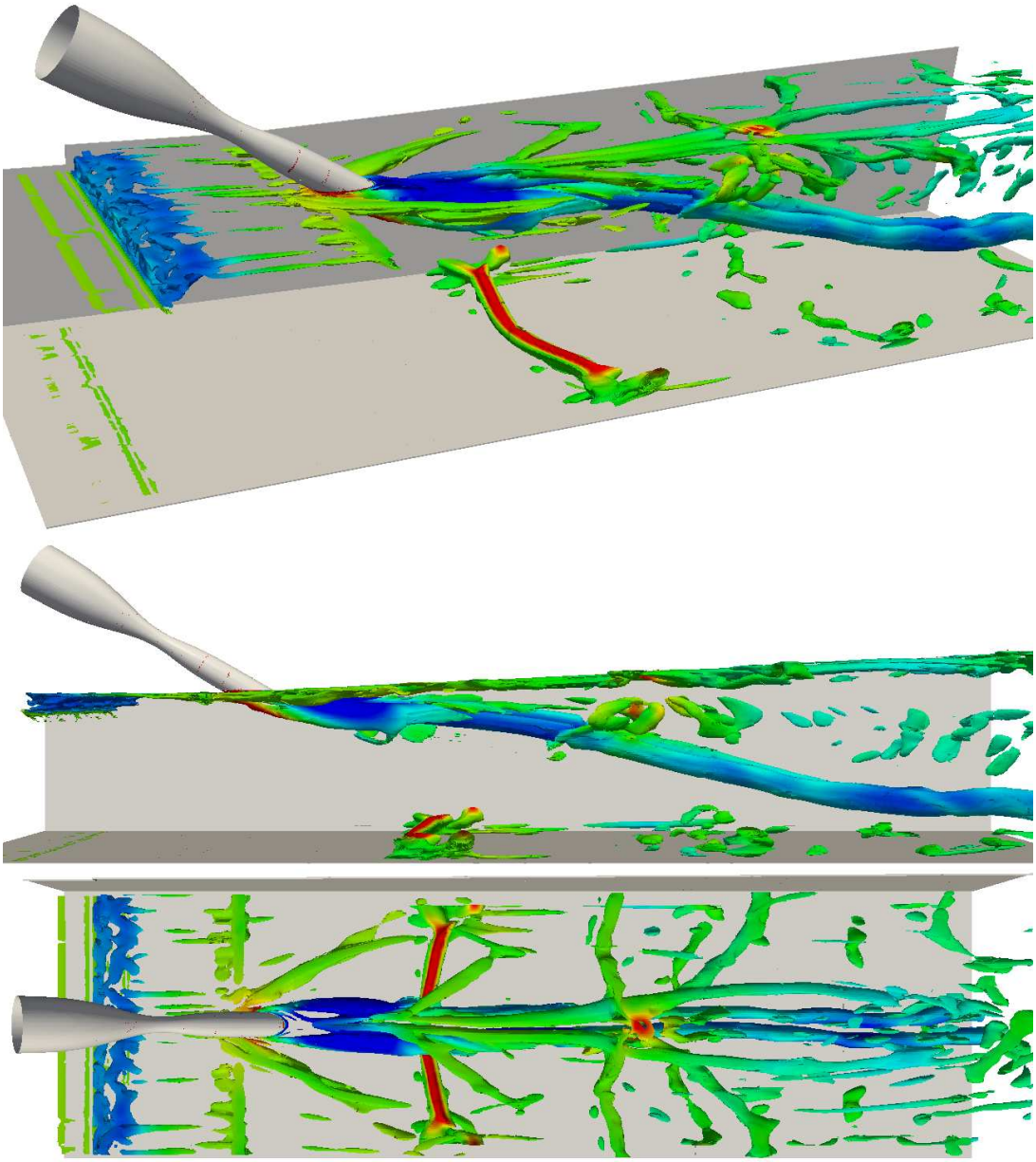

Figure 7.39: Positive Q isosurfaces around the region of injection coloured by static pressure, showing views from an angle (top), the side (middle) and above (bottom).

this separation bubble it must turn into itself and hence a second oblique shock is generated at (5). The strong shock causing the lower wall separation reflects to generate the shock at (6). Two more shock wave boundary layer interactions occur on the upper wall at (7) and (8). Such reflections continue down the length of the combustor, generating a very complex flow field with interactions that present a significant challenge to computational techniques. As well as shock wave boundary layer interactions, shock-shock, shock-vortex, shock-turbulence and shock-flame interactions are also present. An additional bow shock appears to be present at (9), which could explain the additional horseshoe vortex at (6) in Figure 7.37.

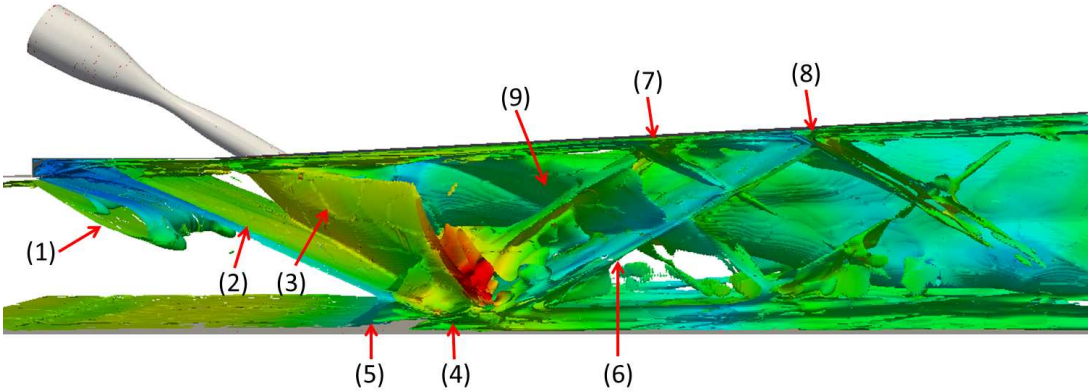

Figure 7.40: Three dimensional schlieren image coloured by static pressure

The shock wave causing the upper wall boundary layer interaction labelled (8) in Figure 7.37 is obviously not flat, but combines with the flat oblique shock generated by the region of separation on the lower wall, at the combustor centre-line; causing the high pressure spot discussed. This is demonstrated further in Figure 7.41, which shows pressure contours either side of the combustor centre-line (top and bottom images) and one on the combustor centreline, coloured by static pressure. From the off-centreline contour plots it is clear that two separate shocks emanate from the separation bubble on the lower wall of the combustor. However, at the centreline these shocks appear to merge causing both a significant interaction with the jet and upper wall boundary layer, leading to a high pressure region downstream. It is likely the curved shock is a product of the jet bow shock reflecting off the lower wall and it is also likely that the combination

of the two shocks may be sensitive to both the inflow boundary conditions and geometrical setup, since any alteration in these parameters is likely to influence shock angles and the location of the lower wall separation bubble and therefore whether this shock combination and hence high pressure region on the upper wall exists.

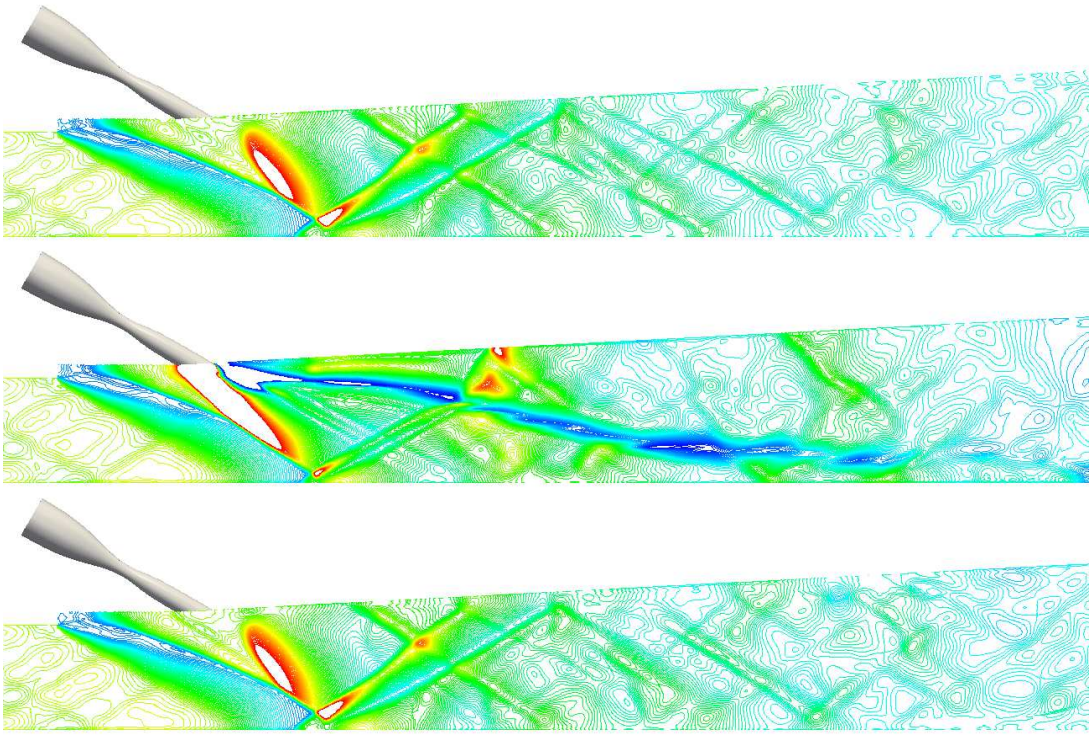

Figure 7.41: Pressure contours coloured by static pressure either side of the centreline (top and bottom) and on the centreline (middle).

The contours of temperature and radical species mass fraction in Figure 7.42 show the location at which ignition occurs, which, from the two-dimensional static pressure contours on the centreline, is clearly due to the strong shock wave boundary layer interaction on the upper wall.

It appears from Figures 7.37 and 7.39 that the vortex pair emanating from the jet follow the upper wall downstream of injection before tending to the lower surface of the combustor. Due to the downwards momentum of the injected fuel there is a tendency for the jet to move away from the upper wall, however the rate at which this happens is significantly reduced by the entrained cross-flow fluid

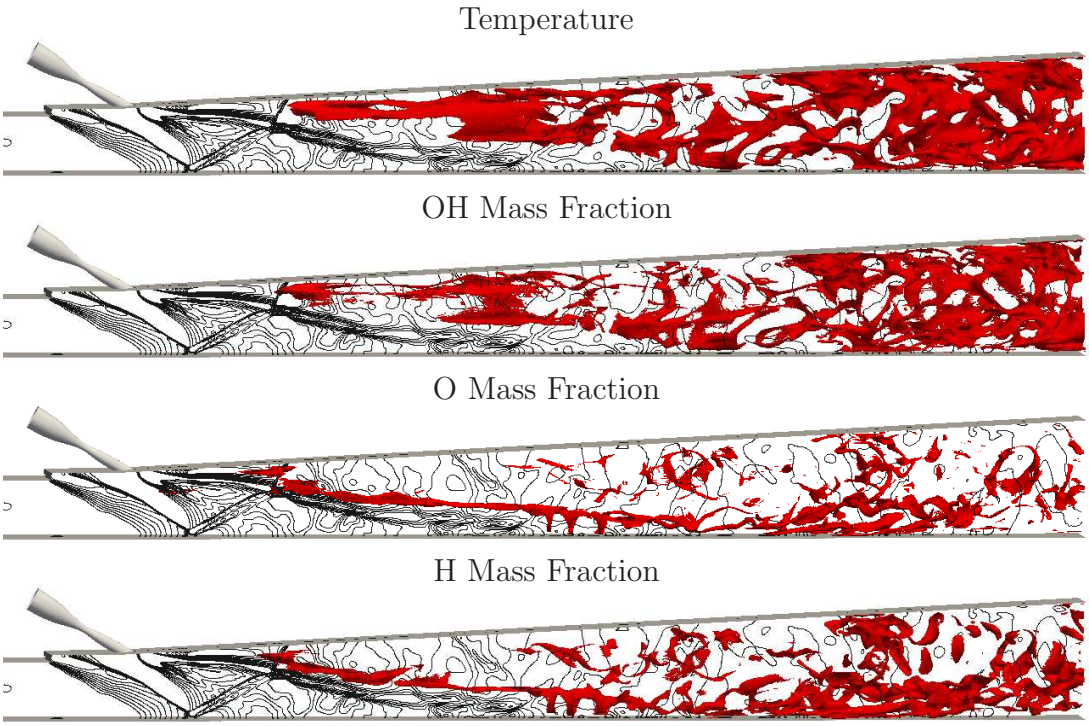

Figure 7.42: Three-dimensional contours of: Temperature = 1900K, $Y_{OH} = 0.015$, $Y_O = 0.008$ and $Y_H = 0.004$, with a two-dimensional pressure contour on the combustor centreline.

[142] and the vortices appear to stay close to the upper surface. The velocity field generated may also cause a low pressure region above the vortices, further reducing their downward motion. However, as can be seen even more clearly in Figure 7.43 the motion of the vortices down the length of the combustor does not appear monotonic and there is a distinctive change of direction towards the lower wall, along with subsequent disturbances to the flow path. It is most likely that this behaviour is the result of shock-vortex interactions, with a turning effect imposed on the streamwise structures.

However, it should be noted that no such influence is imposed on the structures breaking off in the upper half of the domain. It is possible the coherent vortices would also be less susceptible to shock manipulation after breakdown has occurred and hence a delay in vortex bursting may play a significant role in the resulting elongated profiles exhibited in the ensemble averaged data.

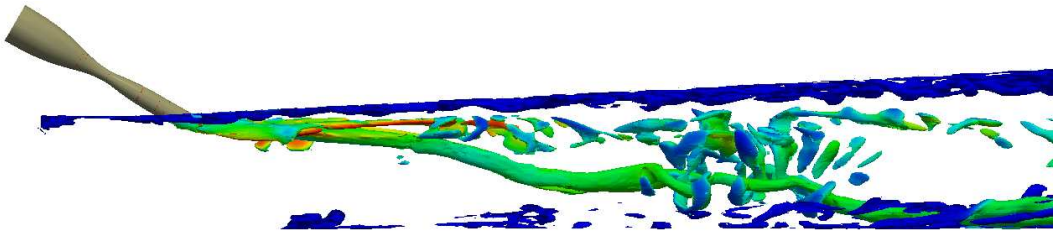

Figure 7.43: Side view of positive Q contours coloured by hydrogen mass fraction

As well as increasing the intensity of the turbulence inflow upstream of the combustion chamber, the introduction of coherent structures in the injector may also have an influence on the vortex dynamics. It can be seen from the instantaneous image in Figure 7.44 that no shear layer instabilities are present immediately after injection, but are often experienced with transverse injection into a cross-flow [142].

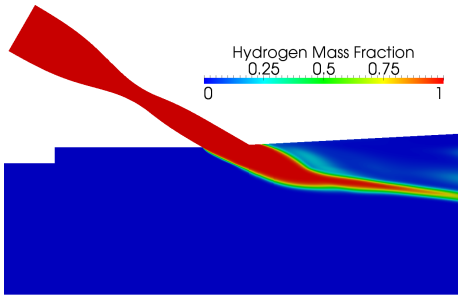

Figure 7.44: Instantaneous hydrogen mass fraction profile on the centreline after 1.2M iterations.

In contrast, Figure 7.45 shows the distribution of species mass fraction variance from Simulation 2 of the RANS study, which employed the assumed PDF combustion model for the reaction rate calculation. The high mass fraction variance displayed in the jet shear layer immediately after injection corresponds to significant fluctuations in composition in that region, which are not exhibited in the LES study and hence the addition of injector turbulence may be required.

Finally, in order to demonstrate that the mesh resolution is high enough to support the resolved content inherent in LES a turbulence energy spectrum is presented in Figure 7.46, where it can be seen an inertial range is indeed present. The spectrum is calculated from a time history of the y-velocity over a period of

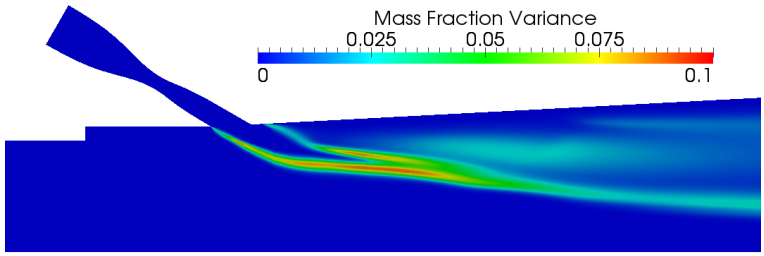

Figure 7.45: Centreline σ_Y profile from Simulation 2 of the RANS study.

765,000 iterations of the laminar chemistry simulation with a turbulence inflow, at centre of the combustor and an axial location of 0.777m. Again, it is difficult to confirm or disprove the presence of a steeper decay than found in low Mach number turbulence, with both the standard Kolmogorov scaling of $k^{-5/3}$ and steeper decay of $k^{-8/3}$ appearing to be in better agreement with different parts of the spectrum.

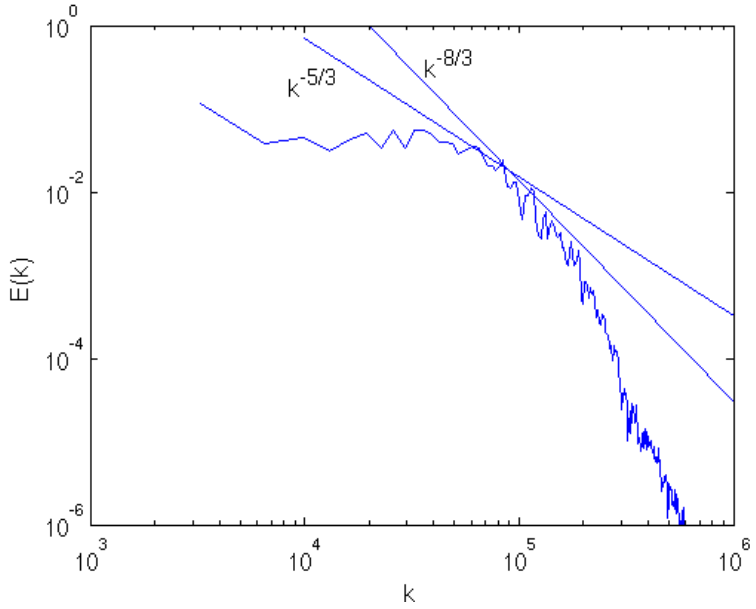

Figure 7.46: Turbulence energy spectrum using data for the y-velocity from 225,000 to 990,000 iterations on the centreline of the combustor at x=0.777m.

The extremely complex physics encountered in a scramjet combustor has been demonstrated through use of the LES technique. The importance of vortex dynamics, shock-shock, shock boundary layer, shock-combustion and shock-vortex

interactions along with turbulence and its associated interactions have been highlighted. The influence of turbulence chemistry interaction modelling has again been shown to have a minimal influence on the results obtained, with other aspects of the computational setup having a more significant impact. The domination of inflow turbulence has again been demonstrated, highlighting the importance for experimentalists to provide this information in order for accurate simulations to be conducted.

Chapter 8

Conclusions

8.1 Conclusions

8.1.1 Overview

This work had two aims: First, to compare the capabilities of RANS and LES approaches as a tool for the simulation of supersonic combustion; second, that insight would be gained into the physics involved in supersonic combustion, in order to aid the development of turbulence and combustion modelling in this regime.

A new code, PULSAR, has been successfully developed for both Reynolds averaged and large eddy simulations of supersonic reacting flows. Significant attention has been paid to the discretisation of convective fluxes, ensuring a monotonic solution is achieved with limited numerical dissipation. In order to avoid the restrictive reduction to first order of accuracy in discontinuous regions through use of flux limiters, a gradient limiter based on that by Van Rosendale [117] has been developed, allowing second order of accuracy under all flow conditions.

PULSAR is fully parallel through the implementation of MPI, with good scaling performance demonstrated over thousands of processor cores. Such parallel capabilities have been shown to be of paramount importance for high fidelity simulations due to the significant computational costs involved.

The DDES method in combination with the Menter SST turbulence model

is implemented in order to conduct LES of high Reynolds number wall bounded flows, with near wall modelling handled by the RANS technique. Due to the lack of resolved content in the RANS-LES blending region the turbulence generation method of Kempf et al. [64] is employed, which can be used to provide turbulence inflow data for a simulation.

Finite rate combustion calculations are enabled through the implementation of complex chemistry reactions, using multiple transport equations for the reactive scalars. PULSAR is capable of neglecting turbulence-chemistry interactions through the use of the laminar chemistry approach, or including them through use of an assumed PDF combustion model.

8.1.2 Non-Reacting Flow

The non-reacting elements of PULSAR were validated through the simulation of a supersonic coaxial jet, using helium for the central jet gas and air for the co-flow in order to simulate compressible mixing of a light fuel. It was found that RANS methods are capable of providing results for mean properties of the flow which are in good agreement with experimental data, but only after significant tuning of model constants. The high levels of eddy viscosity encountered in RANS due to modelling of the whole turbulence spectrum causes the turbulent flux terms in the system of governing equations to play a dominant role. The turbulent Prandtl and Schmidt numbers were shown to have a significant influence on the results obtained and compressibility corrections for the Menter SST turbulence model were required to reduce the levels of eddy viscosity generated. However, results were also observed to be dependent on the compressibility correction employed.

Such dependence on model parameters makes the accuracy of RANS results unreliable, especially if no experimental data is available for tuning. Even if tuning is possible, it can be a computationally expensive exercise due to the number of simulations required and still the accuracy of extrapolation to flight conditions is uncertain.

A tuned RANS simulation was capable of providing results for the rms axial velocity in reasonable agreement with experimental data. However, due to the use of the Boussinesq approximation, poor agreement is obtained in the core region

of the jet because of the lack of mean velocity gradients there. Also, due to the use of the Boussinesq approximation for the calculation of the Reynolds stresses and the dominance of the turbulence kinetic energy scalar in high speed flows, the rms velocities in all three directions were found to be the same. The accuracy of this result could not be confirmed due to the lack of experimental rms velocity data in the two transverse directions.

Through simulation of the same non-reacting coaxial jet it was found that LES results are insensitive to variations in the turbulence Prandtl and Schmidt numbers, improving on this significant deficiency of the RANS technique. Since the large scales of the flow are directly captured in LES and only the small scales modelled, the levels of eddy viscosity are much lower than in RANS. The turbulent flux terms in the governing system of equations, which are scaled by these model constants, therefore play a significantly less dominant role. However, their level of influence was found to be sensitive to the filter width used, with the cube root of the volume providing the least dissipative results.

If the physics in the LES is left to develop by itself it was found that a significant delay in the turbulent transition of the jet existed. This could be due to the RANS-LES method employed for the simulation since no resolved content is present in the near wall region and hence no turbulence information is present to perturb the jet shear layer upon separation from the central jet tip. It is also possible the levels of resolved turbulence in the nozzle LES region are not in agreement with that present in the experiment, which is unknown since no measurements were made. These effects are magnified by the high axial velocity of the central jet, since any perturbation to the inner shear layer is convected far downstream before it has time to cause turbulence transition to occur. The purely dissipative nature of the subgrid scale model may also play a role, since the presence of backscatter is not allowed for, which would provide energy to the large scale disturbances in the flow.

In order to encourage jet breakup and to help solve the problems due to lack of resolved content in both the near wall regions and free stream, the method of Kempf et al. [64] was used to generate turbulence inflow data for the simulation. However, this data was imposed towards the jet exit rather than at the domain inlet due to the time scales of the flow making the latter computationally ex-

pensive. Turbulence length scales in both the near wall region and free stream, along with Reynolds stresses, can be prescribed using this turbulence generation technique. It was found that the ensemble averaged data are highly sensitive to the nature of the inflow turbulence, through the prescription of both of these parameters. Again, tuning of the simulation was required in order to get results in reasonable agreement with the mean experimental data.

It was found that the breakdown of the shear layer between the co-flow and ambient air can cause significant interactions with the shear layer between the co-flow and core helium jet, having a major impact on the results obtained. This interaction was avoided by Baurle and Edwards [15] by using a RANS method for the outer region and applying LES to only the inner jet, but this approach neglects an important aspect of the complex physics present. In order to reduce the severity of the outer shear layer breakdown the turbulence initialisation method was modified, through removal of the volume scaling, in order to reduce the turbulence intensity generated on the outer wall of the co-flow. This was found to reduce the inner and outer shear layer interactions although significant breakdown of the outer shear layer still occurred.

Despite the reasonable agreement of the mean flow parameters, the magnitudes of the rms velocities calculated were in poor agreement with experimental data, although the correct profiles were obtained. However, the two transverse components of rms velocity data were shown to be significantly smaller than the axial component, contradictory to the results obtained using the RANS technique. Although experimental data for the transverse components are not available, this result is in agreement with the LES results of Baurle et al. [15].

Tuning of LES is significantly more problematic than the tuning of RANS due to the high computational costs involved. Due to the mesh resolution requirements and number of iterations needed to achieve converged statistical data, massive parallel computing is required. However, tuning in LES concerns physical data, rather than model parameters as in RANS, meaning the tuning effort can be significantly reduced if experimental data for the turbulence intensity and length scales are available.

8.1.3 Reacting Flow

In order to validate the reacting aspects of PULSAR and to also conduct an investigation into the regimes and physics of supersonic combustion, the SCHOLAR scramjet test case was simulated. The RANS and LES approaches were again compared, with results from the RANS simulations used to tune the LES setup. Although RANS has been shown to be sensitive to the choice of model constants, it can be used to investigate trends in computational results brought about through modification of the modelling process.

Using RANS, the laminar chemistry and assumed PDF combustion model approaches to the simulation of reacting flows were compared in an attempt to evaluate the influence of turbulence-chemistry interactions in supersonic combustion. It was found that only minimal differences in results arise between the two techniques, suggesting the influence of turbulence-chemistry interactions is minimal. The current trend in supersonic combustion modelling appears to be a movement to more complex and computationally expensive methods, such as the transported PDF and LEM models. However, since the influence of the turbulence-chemistry interactions appears to be small, it is possible the physics involved could be captured by a simpler mathematical description.

The influence of chemistry was evaluated through the use of two complex chemical mechanisms. Although the differences between results from the reduced and full mechanisms was found to be small, they were more significant than the differences between combustion modelling approaches. Slower oxygen depletion in the core region of the combustor was evident when the reduced Jachimowski mechanism is employed, and the full Jachimowski mechanism in combination with the assumed PDF combustion model was unable to predict the temperature levels evident in the experimental data.

The level of turbulence at the combustor entrance was found to have a significant impact on the results obtained, evaluated through comparisons of computational wall pressure distributions and both planes of temperature and oxygen mole fraction to experimental data. Increased levels of turbulence were found to enhance mixing in the combustion chamber, leading to increased heat release and subsequent increased pressure levels on the walls of the combustor. Results

were independently influenced by turbulence intensity and implied turbulence length scales, demonstrating that turbulence inflow data can have a significant impact on reacting RANS simulations, as well as the LES dependencies found with the coaxial jet. This reinforces the need for experimentalists to measure the turbulence intensities and length scales present.

Whatever mechanism or combustion modelling approach was employed, early ignition was found in the computational results when compared to experimental data. This is due to a strong shock wave boundary layer interaction, causing sufficient deceleration of the flow and subsequent rise in temperature to cause ignition to occur. Influence of the radical species concentration in the facility nozzle on this ignition process was investigated. With chemistry frozen in the nozzle region, preventing the generation of radical species to be convected into the combustion chamber, a small delay in ignition was found when compared to a simulation with radicals present. However, the ignition mechanism is still the shock wave boundary layer interaction, with the small delay due to the longer time required for radical production. It is expected that if ignition is not caused by such a violent process the radical species concentration at the combustor inlet would play a much more significant role in this process and hence it important for experimentalists to also attempt to provide such measurements.

The RANS results were used to conduct an investigation into the regime of supersonic combustion, where both Damköhler and turbulent Reynolds numbers were evaluated in an attempt to better understand the physics involved. As a post-processing exercise 1-step chemistry was applied to the temperature profile of a complex chemistry simulation in order to evaluate the production rate of H_2O, for use as the chemical time scale in the Damköhler number calculations. This was done in order for a direct comparison to be made to the LES results of Ingenito and Bruno [19], who employed 1-step chemistry for the simulation in question. It was found that the results from this exercise were in excellent agreement with the combustion regime proposed by Ingenito and Bruno, suggesting a flamelet like behaviour. However, significantly lower Damköhler numbers were found when the production rate of H_2O was directly taken from the complex chemistry simulations, presenting the importance of finite rate reactions and suggesting operation between the flamelet and distributed reaction regimes. The

slower reaction rates provided by the complex chemical mechanisms are in agreement with the work of Gerlinger et al. [98] and Berglund et al. [68], where 1-step chemistry was found to produce chemical time scales which are much too short, with complex chemistry in much better agreement with available data. This suggests the regime predicted by the complex chemical mechanisms is more reliable.

A LES study was also carried out on the SCHOLAR test case, through use of the DDES method to make such a simulation of this wall bounded flow affordable. The results of the RANS simulations were used to specify use of laminar chemistry and the reduced Jachimowski mechanism, along with a single turbulence inflow upstream of the combustor entrance. The additional computational cost involved in using the full Jachimowski mechanism or assumed PDF combustion model make their use unwarranted. Poor agreement was found between the ensemble averaged temperature profiles and experimental data, due to the lower mean temperatures calculated from the LES. It was shown that this is not due to the use of laminar chemistry, with very comparable results obtained when including modelling for the turbulence-chemistry interactions, confirming the results from the RANS investigation. However, it was shown that the ensemble averaged results are significantly influenced by the level of mixing in the combustor through use of a laminar chemistry simulation without a turbulence inflow.

The influence of inflow turbulence on the wall pressure profiles and poor agreement of computational results with experimental data even when a turbulence inflow is employed suggests a significantly higher level of mixing is required. The lack of unsteadiness in the shear layer between fuel and oxidizer immediately after injection suggests a turbulence inflow in the injector may also be needed. This is supported through analysis of the species mass fraction variance variable from a RANS simulation employing the assumed PDF combustion model, which shows a high variance intensity in this region.

8.1.4 Revealed Physics

Since LES directly captures the large scales of the flow, greater insight can be gained into the physical processes present. Despite the non-reacting coaxial jet

appearing to be a simple test case, the physics involved are very complex. The presence of both inner and outer shear layers significantly complicates the dynamics due to the significant interactions which can arise. It was found that shocks could be formed between the two shear layers, severely disrupting their turbulent breakdown. The turbulence length scales of the outer shear layer were found to be much larger than those in the region between the central jet and co-flow and the magnitude of the velocity fluctuations in the axial direction were found to be higher than for the two transverse components.

Through simulation of the SCHOLAR test case, it was found that the dominant feature of oblique wall injection is a pair of counter-rotating vortices, whose breakdown plays an important role in the mixing process. This breakdown is in turn influenced by the presence of turbulence at the combustor entrance, but appears to be a dynamic process. The degree of mixing present was found to have a significant impact on the wall pressure distributions due to strong mixing, leading to higher heat release. However, due to the shallow injection angle and hence smaller disturbance to the flow than would be encountered with wall normal injection, the vortices appear persistent, limiting their mixing capabilities.

Although mixing was found to play a dominant role in the combustion process, both RANS and LES results displayed that interactions between turbulence and chemistry are minimal. The low Damköhler numbers provided by complex chemistry calculations suggest some of the smaller turbulent scales may be able to enter and disrupt the reaction zone, possibly causing extinction, whilst the largest eddies wrinkle the flame. Since combustion modelling had a minimal influence on the results obtained, it is suggested that the effects on compressibility on the turbulence spectrum, causing the smallest eddies to be larger than would be expected under incompressible conditions, may limit the disruptive nature of the smaller scales of the flow.

The behaviour of the dominant vortex pair is also influenced by the complex shock system present, through alterations in their flow direction. It was found that the ignition mechanism is due to the combination of two shock waves on the combustor centreline and their subsequent strong interaction with the boundary layer on the upper wall. It is therefore suggested that this ignition mechanism could be influenced through alterations in geometry or boundary conditions. This

may explain why such ignition was not experienced in the experiment, due to possible differences in these parameters.

Despite the streamwise vorticity present in the coherent vortex pair playing the dominant role in fuel-air mixing, the injection of vorticity from the boundary layer through the presence of hairpin vortices also plays a significant role in mixing at downstream locations.

The velocity field generated by the vortices was found to induce a pair of secondary vortices on the upper wall of the combustor. A bow shock and horseshoe vortex are also found to exist, which are common occurrences with wall injection into a supersonic crossflow. The horseshoe vortex is a result of the adverse pressure gradient generated upstream of injection, distorting the incoming vorticity field.

The turbulence energy spectra obtained were not able to prove or disprove the suggestion of a steeper inertial range due to compressibility effects, since the difference in $k^{-5/3}$ and $k^{-8/3}$ slopes is relatively small. Further work is required in order to better understand the nature of turbulence in a highly compressible flow.

8.2 Future Work

Several areas of future work are evident from the research presented, from experimental to computational aspects and from turbulence to combustion modelling.

8.2.1 Experimental Data

From an experimental point of view, there is a distinct need for both detailed measurements of a supersonic reacting flow and for measurements of turbulence intensity and length scales.

Despite the SCHOLAR test case and similar experiments providing a realistic replication of combustion in a scramjet engine, it is very difficult to make detailed measurements in such wall bounded flows. Data sets comparable to that available for the non-reacting coaxial jet presented in this thesis are required, where both

mean and fluctuating data are available. As well as fluctuating data for the velocity, for which transverse component measurements are required in order to further evaluate the deficiencies of the Boussinesq approximation employed in RANS turbulence modelling, fluctuating data for temperature and species mass fractions are vital for the evaluation of combustion model accuracy and chemical mechanism suitability.

Using LES to conduct investigations into mildly separated flows is currently a challenge due to the significant sensitivities of computational results to the nature of the turbulence inflow and lack of experimental measurements for this data. Both the non-reacting and reacting test cases simulated in this thesis present a significant challenge to the computational techniques employed due to the limited existence of massively separated regions. Although the SCHOLAR test case was designed to simplify modelling, through a reduction in large regions of separation and re-circulation, this in fact introduces problems in LES due to the limited generation of large scale instabilities. Hybrid RANS-LES studies of normal wall or strut injection may be more successful due to the inherent turbulent nature of the flow and hence reduced sensitivities to inflow turbulence [90].

Since the physics involved in the fuel injection process has a dominant influence on the resulting combustor flow, it may be sensible to study both the physics and behaviour of computational techniques on smaller wall injection test cases, such as [101; 103], before simulating the computationally expensive combustor as attempted here.

8.2.2 Turbulence Modelling

Since the Boussinesq approximation leads to identical predictions for the axial and transverse Reynolds stresses, which are not realistic according to results from LES, the Reynolds stress model may provide a more accurate representation of the physics involved, although such a turbulence model is computationally expensive due to the large number of additional transport equations required.

It has been discussed that the purely dissipative nature of the Smagorinsky SGS model employed in the DES method may contribute to the lack of turbulence generation in the LES of mildly separated flows. A dynamic SGS model should

be incorporated into the method in order to modify the levels of subgrid viscosity in both space and time, but to also introduce the modelling of backscatter into the simulation. Both of these influences may aid the transition of shear layers to the turbulence regime. The sole influence of backscatter can be evaluated by allowing the generation of negative model constants in one simulation, but restricting them to positive values in another.

8.2.3 Turbulence Inflow

The current method of choice for encouraging shear layer transition when using LES is the application of a turbulence inflow, where slices of turbulence data from a domain of previously calculated fluctuations are imposed at a given location. This method applies coherent structures across the whole inflow, rather than just in the boundary layer region as is done with some techniques.

It is possible this approach is not suitable for the non-reacting coaxial jet studied, although this is hard to evaluate in the absence of experimental turbulence data. The computational rms results suggest too little interaction near the nozzle exit, but too large an interaction further downstream. This could be caused by the downstream convection of coherent structures in the core region of the flow. In practice there may be limited turbulence in the core region of the jet, with the shear layer breakdown mostly caused by the resolved content in the separating boundary layer. Other methods, such as the near wall stochastic forcing approach developed by Keating and Piomelli [63] may be more suitable, which increases the levels of resolved stress at the RANS-LES interface. This removes the presence of free stream turbulence from the simulation whilst providing the shear layer disturbances required.

The downstream convection of free stream turbulence may however be important for the SCHOLAR test case, with this statement supported by the improvement of the RANS results when a significant turbulence inflow is employed. It is important to study the influence of turbulence in the injector on the shear layer immediately downstream of injection and subsequent influence on the dominant vortices and impact on mixing and ensemble averaged results obtained.

8.2.4 Supersonic Combustion

In order for the turbulence-chemistry interactions in supersonic combustion to be correctly modelled, even if they are small, a deeper understanding of these interactions and the physics involved is required. This knowledge can then be used to develop new methods for incorporating this physics into the RANS and LES frameworks, rather than moving to more complex and more expensive combustion models as currently appears to be the trend. DNS is the obvious choice for such investigations, but further work is required to evaluate whether the simulation of the high Reynolds number flow in question is affordable. A certain aspect of the physics would need to be chosen for the investigation, such as the reacting shear layer between fuel and oxidiser, since DNS of a whole jet or combustor is not possible with today's computational resources.

Appendix A: Jachimowski Reaction Mechanisms

Reaction No.	Reaction	A	n	E
1	$H_2 + O_2 \Leftrightarrow H_2O + H$	1.00×10^{14}	0.00	56000
2	$H + O_2 \Leftrightarrow OH + O$	2.60×10^{14}	0.00	16800
3	$O + H_2 \Leftrightarrow OH + H$	1.80×10^{10}	1.00	8900
4	$OH + H_2 \Leftrightarrow H_2O + H$	2.20×10^{13}	0.00	5150
5	$OH + OH \Leftrightarrow H_2O + O$	6.30×10^{12}	0.00	1090
6	$H + OH + M \Leftrightarrow H_2O + M$	2.20×10^{22}	-2.00	0
7	$H + H + M \Leftrightarrow H_2 + M$	6.40×10^{17}	-1.00	0
8	$H + O + M \Leftrightarrow OH + M$	6.00×10^{16}	-0.60	0
9	$H + O_2 + M \Leftrightarrow HO_2 + M$	2.10×10^{15}	0.00	-1000
10	$HO_2 + H \Leftrightarrow OH + OH$	1.40×10^{14}	0.00	1080
11	$HO_2 + H \Leftrightarrow H_2O + O$	1.00×10^{13}	0.00	1080
12	$HO_2 + O \Leftrightarrow O_2 + OH$	1.50×10^{13}	0.00	950
13	$HO_2 + OH \Leftrightarrow H_2O + O_2$	8.00×10^{12}	0.00	0
14	$HO_2 + HO_2 \Leftrightarrow H_2O_2 + O_2$	2.00×10^{12}	0.00	0
15	$H + H_2O_2 \Leftrightarrow H_2 + HO_2$	1.40×10^{12}	0.00	3600
16	$O + H_2O_2 \Leftrightarrow OH + HO_2$	1.40×10^{13}	0.00	6400
17	$OH + H_2O_2 \Leftrightarrow H_2O + HO_2$	6.10×10^{12}	0.00	1430
18	$H_2O_2 + M \Leftrightarrow OH + OH + M$	1.20×10^{17}	0.00	45500
19	$O + O + M \Leftrightarrow O_2 + M$	6.00×10^{13}	0.00	-1800

Table 1: Full Jachimowski mechanism [91; 92]. Units are seconds, moles, cubic centimeters, calories and Kelvin. Third-body efficiencies relative to $N_2 = 1$ are as follows: For reaction 6, $H_2O = 6.0$; for reaction 7, H2 = 2 and $H_2O = 6.0$; for reaction 8, $H_2O = 5.0$; for reaction 9, H2 = 2 and $H_2O = 16.0$; and for reaction 18, $H_2O = 15.0$.

Reaction No.	Reaction	A	n	E
1	$H_2 + O_2 \Leftrightarrow OH + OH$	1.70×10^{13}	0.00	48000
2	$H + O_2 \Leftrightarrow OH + O$	1.20×10^{17}	-0.91	16500
3	$OH + H_2 \Leftrightarrow H_2O + H$	2.20×10^{13}	0.00	5150
4	$O + H_2 \Leftrightarrow OH + H$	5.06×10^{04}	2.67	6290
5	$OH + OH \Leftrightarrow H_2O + O$	6.30×10^{12}	0.00	1090
6	$H + OH + M \Leftrightarrow H_2O + M$	2.21×10^{22}	-2.00	0
7	$H + H + M \Leftrightarrow H_2 + M$	7.30×10^{17}	-1.00	0

Table 2: Reduced Jachimowski mechanism [94]. Units are seconds, moles, cubic centimeters, calories and Kelvin. Third-body efficiencies relative to $N_2 = 1$ are $H2 = 2.5$ and $H_2O = 16.0$.

References

[1] M. Smart, "Scramjets," *The Aeronautical Journal*, vol. 111, no. 1124, pp. 605–619, 2007.

[2] C. Cockrell, A. Auslender, R. Guy, C. McClinton, and S. Welch, "Technology Roadmap for Dual-Mode Scramjet Propulsion to Support Space-Access Vision Vehicle Development," in *11th AIAA/AAAF International Space Planes and Hypersonic Systems and Technologies Conference*, 29 September - 4 October 2002. AIAA-2002-5188.

[3] J. Drummond, G. Diskin, and A. Cutler, "Fuel-Air Mixing and Combustion in Scramjets," in *38th AIAA/ASME/SAE/ASEE Joint Propulsion Conference and Exhibit*, 7-10 July 2002. AIAA-2002-3878.

[4] P. Gerlinger, P. Stoll, M. Kindler, F. Schneider, and M. Aigner, "Numerical investigation of mixing and combustion enhancement in supersonic combustors by strut induced streamwise vorticity," *Aerospace Science and Technology*, vol. 12, pp. 159–168, 2008.

[5] D. M. Peterson and G. V. Candler, "Supersonic Combustor Fuel Injection Simulations Using a Hybrid RANS/LES Approach," in *48th AIAA Aerospace Sciences Meeting and Exhibit*, 4-7 January 2010. AIAA-2010-411.

[6] A. Ben-Yakar, *Experimental Investigation of Mixing and Ignition of Transverse Jets in Supersonic Crossflows*. PhD thesis, Stanford University, 2000.

[7] M. Nishioka, S. Sakaue, K. Komada, H. Sakoshi, and I. Furukawa, "Mixing Transition in Supersonic Streamwise Vortices," in *IUTAM Symposium on Elementary Vortices and Coherent Structures: Significance in Turbulence Dynamics* (S. Kida, ed.), pp. 249–258, Springer, 2006.

[8] M. Oevermann, "Numerical investigation of turbulent hydrogen combustion in a SCRAMJET using flamelet modeling," *Aerospace Science and Technology*, vol. 4, pp. 463–480, 2000.

[9] D. M. Van Wie, S. M. D-Alessio, and M. E. White, "Hypersonic Airbreathing Propulsion," *John Hopkins APL Technical Digest*, vol. 26, no. 4, pp. 430–437, 2005.

[10] R. Kazmar, "Airbreathing Hypersonic Propulsion at Pratt & Whitney - Overview," in *AIAA/CIRA 13th International Space Planes and Hypersonics Systems and Technologies Conference*, 16-20 May 2005. AIAA-2005-3256.

[11] USAF, "X-51 Waverider makes historic hypersonic flight." http://www.af.mil/news/story.asp?id=123206525, 26 May 2010.

[12] M. Berglund and C. Fureby, "LES of supersonic combustion in a scramjet engine model," in *Proceedings of the Combustion Institute*, 31, pp. 2497–2504, 2007.

[13] D. C. Haworth, R. J. Blint, B. Cuenot, and T. J. Poinsot, "Numerical Simulation of Turbulent Propane-Air Combustion with Nonhomogeneous Reactants," *Combustion and Flame*, vol. 121, pp. 395–417, 2000.

[14] U. Piomelli, "Large-eddy simulation of turbulent flows," in *Large Eddy Simulation and Related Techniques: Theory and Applications*, Von Karman Institute Lecture Series, 10-14 March 2008.

[15] R. A. Baurle and J. R. Edwards, "Hybrid Reynolds-Averaged/Large-Eddy Simulations of a Coaxial Supersonic Freejet Experiment," *AIAA Journal*, vol. 48, no. 3, pp. 551–571, 2010.

[16] K. N. C. Bray, P. A. Libby, and F. A. Williams, "High speed turbulent combustion," in *Turbulent Reacting Flows* (P. A. Libby and F. A. Williams, eds.), Academic Press, 1994.

[17] R. W. Stewart, J. R. Friedman, and W. Hansard, "Turbulence." National Committee for Fluid Mechanics Films, 1969.

[18] M. Lesieur, *Turbulence in Fluids*. Springer, fourth ed., 2008.

[19] A. Ingenito and C. Bruno, "Physics and Regimes of Supersonic Combustion," *AIAA Journal*, vol. 48, no. 3, pp. 515–525, 2010.

[20] L. Romagnosi, A. Ingenito, D. Cecere, E. Giacomazzi, and C. Bruno, "The role of the baroclinic term in supersonic fuel/air mixing enhancement," in *49th AIAA Aerospace Sciences Meeting and Exhibit*, 4-7 January 2011. AIAA-2011-0401.

[21] U. Piomelli, W. H. Cabot, P. Moin, and S. Lee, "Subgrid-scale backscatter in turbulent and transitional flows," *Physics of Fluids A*, vol. 3, no. 7, pp. 1766–1771, 1991.

[22] R. S. Cant and E. Mastorakos, *An Introduction to Turbulent Reacting Flows*. Imperial College Press, 2008.

[23] A. N. Kolmogorov, "The local structure of turbulence in incompressible viscous fluid for very large Reynolds numbers," vol. 434 of *Proceedings of the Royal Society of London, Series A - Mathematical and Physical Sciences*, pp. 9–13, 1991. Translation.

[24] S. G. Saddoughi and S. V. Veeravalli, "Local isotropy in turbulent boundary layers at high Reynolds number," *Journal of Fluid Mechanics*, vol. 268, pp. 333–372, 1994.

[25] D. Veynante and L. Vervisch, "Turbulent Combustion Modeling," *Progress in Energy and Combustion Science*, vol. 28, pp. 193–266, 2002.

[26] A. Favre, "Équations des gaz turbulents compressible. I. Formes générales," *Journal Mecanique*, vol. 4, pp. 361–390, 1965.

[27] A. Favre, "Équations des gaz turbulents compressible. II. Méthode des vitesses moyennes; méthode des vitesses macroscopiques pondérés par la masse volumique," *Journal Mecanique*, vol. 4, pp. 391–421, 1965.

[28] T. Poinsot and D. Veynante, *Theoretical and Numerical Combustion*. Edwards, second ed., 2005.

[29] C. Rumsey, "Compressibility Considerations for $k - \omega$ Turbulence Models in Hypersonic Boundary-Layer Applications," *Journal of Spacecraft and Rockets*, vol. 47, no. 1, pp. 11–20, 2010.

[30] R. A. Baurle, "Modeling of High Speed Reacting Flows: Established Practices and Future Challenges," in *42nd AIAA Aerospace Sciences Meeting and Exhibit*, 5-8 January 2004. AIAA-2004-0267.

[31] W. Rodi, *Turbulence Models and Their Application in Hydraulics*. A. A. Balkema, 1993.

[32] P. R. Spalart and S. R. Allmaras, "A one-equation turbulence model for aerodynamic flows," *La Recherche Aerospatiale*, vol. 1, no. 1, pp. 5–21, 1994.

[33] H. K. Versteeg and W. Malalasekera, *An Introduction to Computational Fluid Dynamics: The Finite Volume Method*. Pearson Education Limited, second ed., 2007.

[34] P. R. Spalart, "Trends in Turbulence Treatments," in *Fluids 2000 Conference and Exhibit*, 19-22 June 2000. AIAA-2000-2306.

[35] W. P. Jones and B. E. Launder, "The Prediction of Laminarization with a Two-Equation Model of Turbulence," *International Journal of Heat and Mass Transfer*, vol. 15, pp. 301–314, 1972.

[36] B. E. Launder and B. I. Sharma, "Application of the Energy Dissipation Model of Turbulence to the Calculation of Flow Near a Spinning Disc," *Letters in Heat and Mass Transfer*, vol. 1, no. 2, pp. 131–138, 1974.

[37] D. C. Wilcox, "Reassessment of the Scale-Determining Equation for Advanced Turbulence Models," *AIAA Journal*, vol. 26, no. 11, pp. 1299–1310, 1988.

[38] K.-Y. Chien, "Predictions of Channel and Boundary-Layer Flows with a Low-Reynolds Number Turbulence Model," *AIAA Journal*, vol. 20, no. 1, pp. 33–38, 1982.

[39] D. C. Wilcox, "Formulation of the $k - \omega$ Turbulence Model Revisited," *AIAA Journal*, vol. 46, no. 11, pp. 2823–2838, 2008.

[40] F. R. Menter, M. Kuntz, and R. Langtry, "Ten Years of Industrial Experience with the SST Turbulence Model," in *Turbulence, Heat and Mass Transfer 4* (Y. N. K. Hanjalić and M. Tummers, eds.), 2003.

[41] B. E. Launder, G. J. Reece, and W. Rodi, "Progress in the Development of a Reynolds-Stress Turbulence Closure," *Journal of Fluid Mechanics*, vol. 68, no. 3, pp. 537–566, 1975.

[42] K. D. Squires, "Detached-Eddy Simulation of Turbulent Flows," in *Large Eddy Simulation and Related Techniques: Theory and Applications*, Von Karman Institute Lecture Series, 10-14 March 2008.

[43] D. A. Lyn, S. Einav, W. Rodi, and J.-H. Park, "A laser-Doppler velocimetry study of ensemble-averaged characteristics of the turbulent near wake of a square cylinder," *Journal of Fluid Mechanics*, vol. 304, pp. 285–319, 1995.

[44] S. Ghosal and P. Moin, "The Basic Equations for the Large Eddy Simulation of Turbulent Flows in Complex Geometry," *Journal of Computational Physics*, vol. 118, no. 1, pp. 24–37, 1995.

[45] M. Strelets, "Detached Eddy Simulation of Massively Separated Flows," in *39th AIAA Aerospace Sciences Meeting and Exhibit*, 8-11 January 2001. AIAA-2001-0879.

[46] P. R. Spalart, "Detached Eddy Simulation," *Annual Review of Fluid Mechanics*, vol. 41, pp. 181–202, 2009.

[47] J. Smagorinsky, "General circulation experiments with the primitive equations," *Monthly Weather Review*, vol. 91, no. 3, pp. 99–164, 1963.

[48] M. Germano, U. Piomelli, P. Moin, and W. H. Cabot, "A dynamic subgrid-scale eddy viscosity model," *Physics of Fluids A*, vol. 3, no. 7, pp. 1760–1765, 1991.

[49] P. Moin, K. Squires, W. Cabot, and S. Lee, "A dynamic subgrid-scale model for compressible turbulence and scalar transport," *Physics of Fluids A*, vol. 3, no. 11, pp. 2746–2757, 1991.

[50] E. Garnier, M. Mossi, P. Sagaut, P. Comte, and M. Deville, "On the use of shock-capturing schemes for large-eddy simulation," *Journal of Computational Physics*, vol. 153, pp. 273–311, 1999.

[51] J. P. Boris, F. F. Grinstein, E. S. Oran, and R. L. Kolbe, "New insights into large eddy simulation," *Fluid Dynamics Research*, vol. 10, pp. 199–228, 1992.

[52] C. Fureby and F. F. Grinstein, "Monotonically Integrated Large Eddy Simulation of Free Shear Flows," *AIAA Journal*, vol. 37, no. 5, pp. 544–556, 1999.

[53] C. Fureby, "Large Eddy Simulation of Rearward-Facing Step Flow," *AIAA Journal*, vol. 37, no. 11, pp. 1401–1410, 1999.

[54] U. Piomelli, "Wall layer models for LES," in *46th AIAA Aerospace Sciences Meeting and Exhibit*, 7-10 January 2008. AIAA-2008-603.

[55] W. Cabot and P. Moin, "Approximate Wall Boundary Conditions in the Large-Eddy Simulation of High Reynolds Number Flow," *Flow, Turbulence and Combustion*, vol. 63, pp. 269–291, 1999.

[56] J. W. Deardorff, "A numerical study of three-dimensional turbulent channel flow at large Reynolds numbers," *Journal of Fluid Mechanics*, vol. 41, pp. 453–480, 1970.

[57] U. Schumann, "Subgrid-scale model for finite difference simulation of turbulent flows in plane channels and annuli," *Journal of Computational Physics*, vol. 18, pp. 376–404, 1975.

[58] E. Balaras and C. Benocci, "Subgrid-scale models in finite-difference simulations of complex wall bounded flows," in *AGARD CP 551*, 1994.

[59] U. Piomelli and E. Balaras, "Wall-Layer Models for Large-Eddy Simulations," *Annu. Rev. Fluid Mechanics*, vol. 34, pp. 349–374, 2002.

[60] P. R. Spalart, W.-H. Jou, M. Strelets, and S. R. Allmaras, "Comments on the feasibility of LES for wings, and on a hybrid RANS/LES approach," in *Advances in DNS/LES* (C. Liu and Z. Liu, eds.), Greyden Press, 1997.

[61] P. R. Spalart, "Young-Person's Guide to Detached-Eddy Simulation Grids," tech. rep., NASA, 2001. CR-2001-211032.

[62] P. R. Spalart, S. Deck, M. L. Shur, K. D. Squires, M. K. Strelets, and A. Travin, "A New Version of Detached-eddy Simulation, Resistant to Ambiguous Grid Densities," *Theoretical and Computational Fluid Dynamics*, vol. 20, pp. 181–195, 2006.

[63] A. Keating and U. Piomelli, "A dynamic stochastic forcing method as a wall-layer model for large-eddy simulations," *Journal of Turbulence*, vol. 7, no. 12, pp. 1–24, 2006.

[64] A. Kempf, M. Klein, and J. Janicka, "Efficient Generation of Initial- and Inflow-Conditions for Transient Turbulent Flows in Arbitrary Geometries," *Flow, Turbulence and Combustion*, vol. 74, pp. 67–84, 2005.

[65] G. Balakrishnan and F. A. Williams, "Turbulent Combustion Regimes for Hypersonic Propulsion Employing Hydrogen-Air Diffusion Flames," *Journal of Propulsion and Power*, vol. 10, no. 3, pp. 434–437, 1994.

[66] P. A. Libby and F. A. Williams, "Fundamental aspects and a review," in *Turbulent Reacting Flows* (P. A. Libby and F. A. Williams, eds.), Academic Press, 1994.

[67] M. Berglund and C. Fureby, "LES of supersonic combustion in a scramjet engine model," *Proceedings of the Combustion Institute*, vol. 31, pp. 2497–2504, 2007.

[68] M. Berglund, E. Fedina, C. Fureby, J. Tegnér, and V. Sabel'nikov, "Finite Rate Chemistry Large-Eddy Simulation of Self-Ignition in a Supersonic Combustion Ramjet," *AIAA Journal*, vol. 48, no. 3, pp. 540–550, 2010.

[69] I. Glassman, *Combustion*. Academic Press, third ed., 1996.

[70] L. L. Zheng and K. N. C. Bray, "The Application of New Combustion and Turbulence Models to H_2-Air Nonpremixed Supersonic Combustion," *Combustion and Flame*, vol. 99, pp. 440–448, 1994.

[71] J. S. Evans, C. J. Schexnayder, and H. J. Beach, "Application of a Two-Dimensional Parabolic Computer Program to Prediction of Turbulent Reacting Flows," tech. rep., NASA, 1978. TP-1169.

[72] S. B. Pope, "Simple models of turbulent flows," *Physics of Fluids*, vol. 23, 2011. Paper 011301.

[73] S. B. Pope, "PDF Methods for Turbulent Reactive Flows," *Progress in Energy and Combustion Science*, vol. 11, 1985.

[74] S. B. Pope, "A Monte Carlo Method for the PDF Equations of Turbulent Reactive Flow," *Combustion Science and Technology*, vol. 25, 1981.

[75] H. Möbus, P. Gerlinger, and D. Brüggemann, "Scalar and joint scalar-velocity-frequency Monte Carlo PDF simulation of supersonic combustion," *Combustion and Flame*, vol. 132, 2003.

[76] P. Gerlinger, H. Möbus, and D. Brüggemann, "An Implicit Multigrid Method for Turbulent Combustion," *Journal of Computational Physics*, vol. 167, 2001.

[77] P. Gerlinger, "Investigation of an Assumed PDF Approach for Finite-Rate Chemistry," *Combustion Science and Technology*, vol. 175, 2003.

[78] R. A. Baurle and S. S. Girimaji, "Assumed PDF turbulence-chemistry closure with temperature-composition correlations," *Combustion and Flame*, vol. 134, 2003.

[79] S. S. Girimaji, "Assumed β-pdf Model for Turbulent Mixing: Validation and Extension to Multiple Scalar Mixing," *Combustion Science and Technology*, vol. 78, 1991.

[80] S. S. Girimaji, "A Simple Recipe for Modeling Reaction-Rate in Flows with Turbulent-Combustion," in *22nd Fluid Dynamics, Plasma Dynamics and Lasers Conference*, 24-26 June 1991. AIAA-1991-1792.

[81] N. Peters, *Turbulent Combustion*. Cambridge University Press, 2000.

[82] T. S. Cheng, J. A. Wehrmeyer, R. W. Pitz, O. J. Jarrett, and G. B. Northam, "Raman Measurement of Mixing and Finite-Rate Chemistry in a Supersonic Hydrogen-Air Diffusion Flame," *Combustion and Flame*, vol. 99, 1994.

[83] C. Ghodke, J. Choi, and S. Menon, "Large Eddy Simulation of Supersonic Combustion in a Cavity-Strut Flameholder," in *49th AIAA Aerospace Sciences Meeting and Exhibit*, 4-7 January 2011. AIAA-2011-0323.

[84] V. Sankaran and S. Menon, "LES of scalar mixing in supersonic mixing layers," *Proceedings of the Combustion Institute*, vol. 30, pp. 2835–2842, 2005.

[85] F. Génin and S. Menon, "Simulation of Turbulent Mixing Behind a Strut Injector in Supersonic Flow," *AIAA Journal*, vol. 48, no. 3, pp. 526–539, 2010.

[86] F. Génin, B. Chernyavsky, and S. Menon, "Large Eddy Simulation of Scramjet Combustion Using a Subgrid Mixing/combustion Model," in *12th AIAA International Space Planes and Hypersonic Systems and Technologies*, 15-19 December 2003. AIAA-2003-7035.

[87] P. G. Keistler, H. A. Hassan, and X. Xiao, "Role of Turbulence/Chemistry Interaction in 3-D Supersonic Combustion," in *46th AIAA Aerospace Sciences Meeting and Exhibit*, 7-10 January 2008. AIAA-2008-89.

[88] C. G. Rodriguez and A. D. Cutler, "Computational Simulation of a Supersonic-Combustion Benchmark Experiment," in *41st AIAA/ASME/SAE/ASEE Joint Propulsion Conference and Exhibit*, 10-13 July 2005. AIAA-2005-4424.

[89] S.-H. Won, I.-S. Jeung, B. Parent, and J.-Y. Choi, "Numerical Investigation of Transverse Hydrogen Jet into Supersonic Crossflow Using Detached-Eddy Simulation," *AIAA Journal*, vol. 48, no. 9, pp. 1047–1058, 2010.

[90] D. M. Peterson, G. V. Candler, and T. W. Drayna, "Detached Eddy Simulation of a Generic Scramjet Inlet and Combustor," in *47th AIAA Aerospace Sciences Meeting and Exhibit*, 5-8 January 2009. AIAA-2009-130.

[91] C. J. Jachimowski, "An Analytical Study of the Hydrogen-Air Reaction Mechanism With Application to Scramjet Combustion," tech. rep., NASA, 1988. TP-2791.

[92] G. J. Wilson and R. W. MacCormack, "Modeling Supersonic Combustion Using a Fully Implicit Numerical Method," *AIAA Journal*, vol. 30, no. 4, pp. 1008–1015, 1992.

[93] C. J. Jachimowski, "An Analysis of Combustion Studies in Shock Expansion Tunnels and Reflected Shock Tunnels," tech. rep., NASA, 1992. TP-3224.

[94] R. A. Baurle, G. A. Alexopoulos, and H. A. Hassan, "Assumed Joint Probability Density Function Approach for Supersonic Turbulent Combustion," *Journal of Propulsion and Power*, vol. 10, no. 4, pp. 473–484, 1994.

[95] M. Ó'Conaire, H. J. Curran, J. M. Simmie, W. J. Pitz, and C. K. Westbrook, "A Comprehensive Modeling Study of Hydrogen Oxidation," *Internation Journal of Chemical Kinetics*, vol. 26, no. 11, pp. 603–622, 2004.

[96] N. M. Marinov, C. K. Westbrook, and W. J. Pitz, "Detailed and Global Chemical Kinetics Model for Hydrogen," in *Proceedings of the Eighth International Symposium on Transport Phenomena in Combustion* (S. H. Chan, ed.), pp. 118–129, Taylor & Francis: London, 1995.

[97] R. C. Rogers and W. Chinitz, "On the use of a global hydrogen-air combustion model in the calculation of turbulent reacting flows," in *20th AIAA Aerospace Sciences Meeting*, 11-14 January 1982. AIAA-1982-112.

[98] P. Gerlinger, K. Nold, and M. Aigner, "Influence of reaction mechanisms, grid spacing, and inflow conditions on the numerical simulation of lifted supersonic flames," *Internation Journal for Numerical Methods in Fluids*, vol. 62, no. 12, p. 13571380, 2010.

[99] C. L. Dancey, "The turbulent flow field downstream of an axisymmetric Mach 2 supersonic burner - LDA measurements," in *32nd ASME, SAE, and ASEE, Joint Propulsion Conference and Exhibit*, 1-3 July 1996. AIAA-1996-3073.

[100] A. D. Cutler, G. S. Diskin, J. P. Drummond, and J. A. White, "Supersonic Coaxial Jet Experiment for Computational Fluid Dynamics Code Validation," *AIAA Journal*, vol. 44, no. 3, pp. 585–592, 2006.

[101] J. G. Santiago and J. C. Dutton, "Velocity Measurements of a Jet Injected into a Supersonic Crossflow," *Journal of Propulsion and Power*, vol. 13, no. 2, pp. 264–273, 1997.

[102] W. M. VanLerberghe, J. G. Santiago, J. C. Dutton, and R. P. Lucht, "Mixing of a Sonic Transverse Jet Injected into a Supersonic Flow," *AIAA Journal*, vol. 38, no. 3, pp. 470–479, 2000.

[103] A. Ben-Yakar, M. G. Mungal, and R. K. Hanson, "Time Evolution and Mixing Characteristics of Hydrogen and Ethylene Transverse Jets in Supersonic Crossflows," *Physics of Fluids*, vol. 18, no. 2, pp. 470–479, 2006. Paper 026101.

[104] S. A. Tedder, S. O. Byrne, P. M. Danehy, and A. D. Cutler, "CARS Temperature and Species Concentration Measurements in a Supersonic Combustor with Normal Injection," in *43rd AIAA Aerospace Sciences Meeting and Exhibit*, 10-13 January 2005. AIAA-2005-616.

[105] A. D. Cutler, P. M. Danehy, R. R. Springer, S. O'Byrne, D. P. Capriotti, and R. DeLoach, "Coherent Anti-Stokes Raman Spectroscopic Thermometry in a Supersonic Combustor," *AIAA Journal*, vol. 41, no. 12, pp. 2451–2459, 2003.

[106] A. D. Cutler, G. Magnotti, R. Baurle, D. Bivolaru, S. Tedder, and P. M. Danehy, "Development of Supersonic Combustion Experiments for CFD Modeling," in *45th AIAA Aerospace Sciences Meeting and Exhibit*, 8-11 January 2007. AIAA-2007-978.

[107] D. Bivolaru, J. W. Lee, S. B. Jones, S. Tedder, P. M. Danehy, M. C. Weikl, G. Magnotti, and A. D. Cutler, "Mobile CARS - IRS Instrument for Simultaneous Spectroscopic Measurement of Multiple Properties in Gaseous Flows," in *22nd International Congress on Instrumentation in Aerospace Simulation Facilities*, pp. 1–9, 10-14 June 2007.

[108] B. Diskin and J. L. Thomas, "Comparison of Node-Centered and Cell-Centered Unstructured Finite-Volume Discretizations: Inviscid Fluxes," in *48th AIAA Aerospace Sciences Meeting and Exhibit*, 4-7 January 2010. AIAA-2010-1079.

[109] B. Diskin, J. L. Thomas, E. J. Nielsen, H. Nishikawa, and J. A. White, "Comparison of Node-Centered and Cell-Centered Unstructured Finite-Volume Discretizations: Viscous Fluxes," *AIAA Journal*, vol. 48, no. 7, pp. 1326–1338, 2010.

[110] C. Hirsch, *Numerical Computation of Internal & External Flows*. Elsevier, second ed., 2007.

[111] T. K. Sengupta, G. Ganerwal, and A. Dipankar, "High Accuracy Compact Schemes and Gibbs' Phenomenon," *Journal of Scientific Computing*, vol. 21, no. 3, pp. 253–268, 2004.

[112] P. L. Roe, "Approximate Riemann solvers, parameter vectors, and difference schemes," *Journal of Computational Physics*, vol. 43, no. 2, pp. 357–372, 1981.

[113] M.-S. Liou, "A Sequel to AUSM: AUSM+," *Journal of Computational Physics*, vol. 129, no. 2, pp. 364–382, 1996.

[114] M.-S. Liou and C. J. J. Steffen, "A New Flux Splitting Scheme," *Journal of Computational Physics*, vol. 107, no. 1, pp. 23–39, 1993.

[115] M.-S. Liou, "A Continuing Search for a Near-Perfect Numerical Flux Scheme. Part I: AUSM+," tech. rep., NASA, 1994. Technical Memorandum 106524.

[116] M.-S. Liou, "A sequel to AUSM, Part II: AUSM+-up for all speeds," *Journal of Computational Physics*, vol. 214, no. 1, pp. 137–170, 2006.

[117] J. Van Rosendale, "Floating Shock Fitting via Lagrangian Adaptive Meshes," tech. rep., NASA, 1994. CR-1994-194997,ICASE 94-89.

[118] A. Harten, B. Engquist, S. Osher, and S. R. Chakravarthy, "Uniformly high order accurate essentially non-oscillatory schemes, III," *Journal of Computational Physics*, vol. 71, no. 2, pp. 231–303, 1987.

[119] J. Blazek, *Computational Fluid Dynamics: Principles and Applications*. Elsevier, 2005.

[120] D. J. Mavriplis, "Revisiting the Least-squares Procedure for Gradient Reconstruction on Unstructured Meshes," tech. rep., NASA, 2003. CR-2003-212683.

[121] A. Haselbacher and J. Blazek, "Accurate and Efficient Discretization of Navier-Stokes Equations on Mixed Grids," *AIAA Journal*, vol. 38, no. 11, pp. 2094–2102, 2000.

[122] C. M. Rhie and W. L. Chow, "Numerical Study of the Turbulent Flow Past an Airfoil With Trailing Edge Separation," *AIAA Journal*, vol. 21, no. 11, pp. 1525–1532, 1983.

[123] F. R. Menter, "Improved Two-Equation $k-\omega$ Turbulence Models for Aerodynamic Flows," tech. rep., NASA, 1992. Technical Memorandum 103975.

[124] P. G. Tucker, "Differential equation-based wall distance computation for DES and RANS," *Journal of Computational Physics*, vol. 190, no. 1, pp. 229–248, 2003.

[125] D. C. Wilcox, *Turbulence Modeling for CFD*. DCW Industries, third ed., 2006.

[126] F. R. Menter, "Two-Equation Eddy-Viscosity Turbulence Models for Engineering Applications," *AIAA Journal*, vol. 32, no. 8, pp. 1598–1605, 1994.

[127] T. von Karman, "The Analogy Between Fluid Friction and Heat Transfer," in *Transactions of ASME*, vol. 61, pp. 705–710, 1939.

[128] D. B. Spalding, "A Single Formula for the Law of the Wall," in *Journal of Applied Mechanics, Transactions of ASME*, E, pp. 455–458, 1961.

[129] B. L. Smith, "Adaption of the law of the wall boundary treatment to include volumetric heating effects," *Applied Mathematical Modelling*, vol. 33, pp. 1306–1322, 2009.

[130] C. L. V. Jayatilleke, "The influence of Prandtl number and surface roughness on the resistance of the Laminar sublayer to momentum and heat transfer," in *Progress in Heat and Mass Transfer 1*, pp. 193–201, 1969.

[131] F. Menter, J. C. Ferreira, T. Esch, and B. Konno, "The SST Turbulence Model with Improved Wall Treatment for Heat Transfer Predictions in Gas Turbines," in *Proceedings of the International Gas Turbine Congress*, 2003. IGTC2003-TS059.

[132] R. S. Cant, *SENGA2 Direct Numerical Simulation of Combustion: User Guide*.

[133] F. C. Lockwood and A. S. Naguib, "The Prediction of the Fluctuations in the Properties of Free, Round-Jet, Turbulent, Diffusion Flames," *Combustion and Flame*, vol. 24, pp. 109–124, 1975.

[134] S. Gottlieb and C.-W. Shu, "Total Variation Diminishing Runge-Kutta Schemes," *Mathematics of Computation*, vol. 67, no. 221, pp. 73–85, 1998.

[135] T. S. Lund, X. Wu, and K. D. Squires, "Generation of Turbulent Inflow Data for Spatially-Developing Boundary Layer Simulations," *Journal of Computational Physics*, vol. 140, no. 2, pp. 233–258, 1998.

[136] G. Karypis, K. Schloegel, and V. Kumar, *ParMeTiS: Parallel Graph Partitioning and Sparse Matrix Ordering Library*, 2003.

[137] X. Xiao, H. A. Hassan, and R. A. Baurle, "Modeling Scramjet Flows with Variable Turbulent Prandtl and Schmidt Numbers," *AIAA Journal*, vol. 45, no. 6, pp. 1415–1423, 2007.

[138] A. Kempf, R. P. Lindstedt, and J. Janicka, "Large-eddy simulation of a bluff-body stabilized nonpremixed flame," *Combustion and Flame*, vol. 144, pp. 170–189, 2006.

[139] G. I. Taylor, "The spectrum of turbulence," in *Proceedings of the Royal Society of London*, vol. 164 of *Series A, Mathematical and Physical Sciences*, pp. 476–490, 1938.

[140] M. Lesieur, O. Métais, and P. Comte, *Large-Eddy Simulations of Turbulence*. Cambridge University Press, 2005.

[141] P. A. T. Cocks, W. N. Dawes, and R. S. Cant, "The Influence of Turbulence-Chemistry Interaction Modelling for Supersonic Combustion," in *49th AIAA Aerospace Sciences Meeting and Exhibit*, 4-7 January 2011. AIAA-2011-0306.

[142] T. F. Fric and A. Roshko, "Vortical structure in the wake of a transverse jet," *Journal of Fluid Mechanics*, vol. 279, pp. 1–47, 1994.